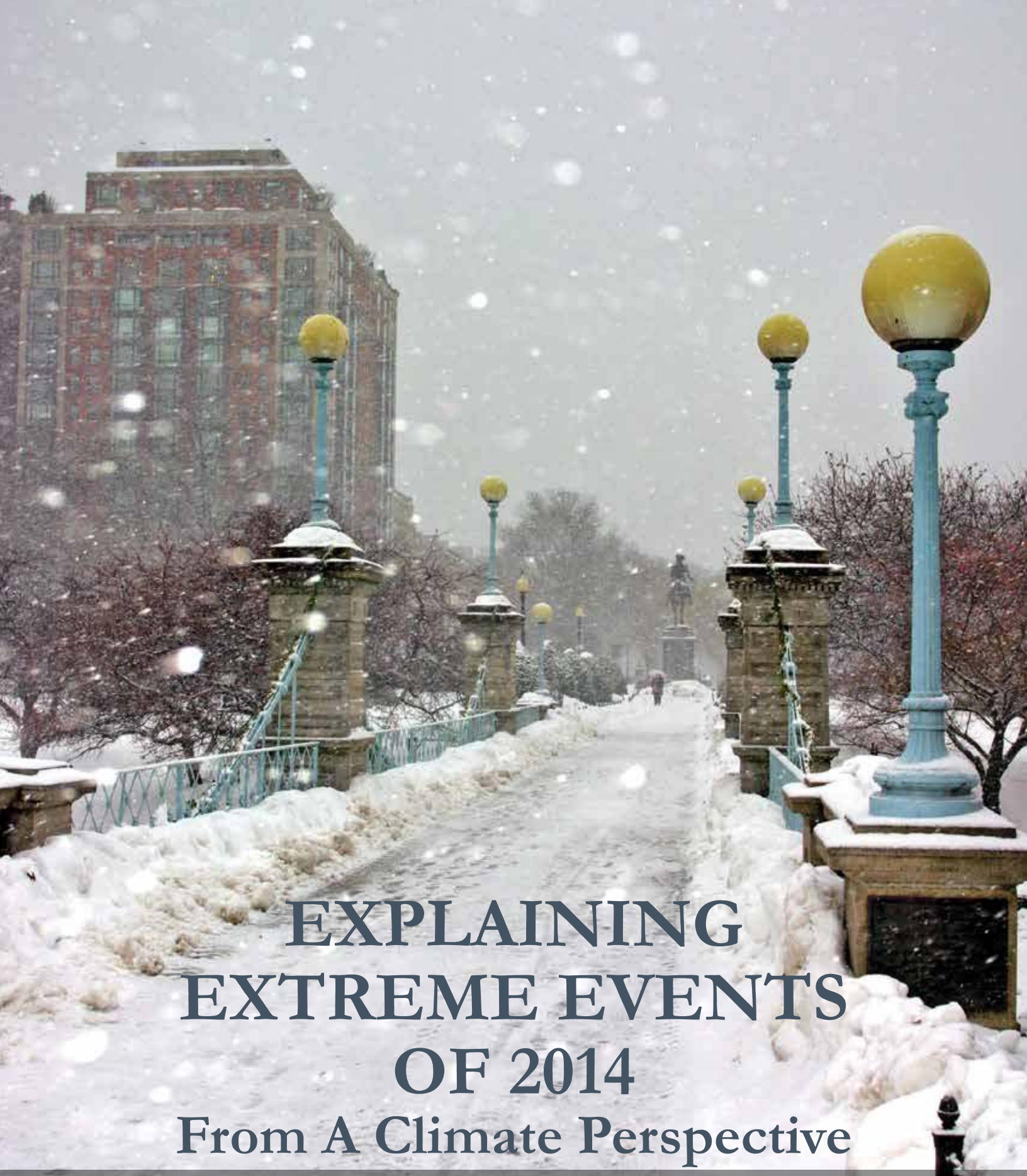

EXPLAINING EXTREME EVENTS OF 2014

From A Climate Perspective

Special Supplement to the
Bulletin of the American Meteorological Society
Vol. 96, No. 12, December 2015

EXPLAINING EXTREME EVENTS OF 2014 FROM A CLIMATE PERSPECTIVE

Editors

Stephanie C. Herring, Martin P. Hoerling, James P. Kossin, Thomas C. Peterson, and Peter A. Stott

Special Supplement to the

Bulletin of the American Meteorological Society

Vol. 96, No. 12, December 2015

American Meteorological Society

Corresponding Editor:

Stephanie C. Herring, PhD
NOAA National Centers for Environmental Information
325 Broadway, E/CC23, Rm 1B-131
Boulder, CO 80305-3328
E-mail: stephanie.herring@noaa.gov

Cover credits:

Front: ©iStockphotos.com/coleong—Winter snow, Boston, Massachusetts, United States.

Back: ©iStockphotos.com/nathanphoto—Legget, California, United States – August 13, 2014: CAL FIRE helicopter surveys a part of the Lodge Fire, Mendocino County.

HOW TO CITE THIS DOCUMENT

Citing the complete report:

Herring, S. C., M. P. Hoerling, J. P. Kossin, T. C. Peterson, and P. A. Stott, Eds., 2015: Explaining Extreme Events of 2014 from a Climate Perspective. *Bull. Amer. Meteor. Soc.*, **96** (12), S1–S172.

Citing a section (example):

Yoon, J. H., S.-Y. S. Wang, R. R. Gillies, L. Hipps, B. Kravitz, and P. J. Rasch, 2015: Extreme fire season in California: A glimpse into the future? [in "Explaining Extremes of 2014 from a Climate Perspective"]. *Bull. Amer. Meteor. Soc.*, **96** (12), S5–S9.

EDITORIAL AND PRODUCTION TEAM

Riddle, Deborah B., Lead Graphics Production, NOAA/NESDIS National Centers for Environmental Information, Asheville, NC

Love-Brotak, S. Elizabeth, Graphics Support, NOAA/NESDIS National Centers for Environmental Information, Asheville, NC

Veasey, Sara W., Visual Communications Team Lead, NOAA/NESDIS National Centers for Environmental Information, Asheville, NC

Griffin, Jessicca, Graphics Support, Cooperative Institute for Climate and Satellites-NC, North Carolina State University, Asheville, NC

Maycock, Tom, Editorial Support, Cooperative Institute for Climate and Satellites-NC, North Carolina State University, Asheville, NC

Misch, Deborah J., Graphics Support, LMI Consulting, Inc., NOAA/NESDIS National Centers for Environmental Information, Asheville, NC

Osborne, Susan, Editorial Support, LMI Consulting, Inc., NOAA/NESDIS National Centers for Environmental Information, Asheville, NC

Schreck, Carl, Editorial Support, Cooperative Institute for Climate and Satellites-NC, North Carolina State University, and NOAA/NESDIS National Centers for Environmental Information, Asheville, NC

Sprain, Mara, Editorial Support, LAC Group, NOAA/NESDIS National Centers for Environmental Information, Asheville, NC

Young, Teresa, Graphics Support, STG, Inc., NOAA/NESDIS National Centers for Environmental Information, Asheville, NC

TABLE OF CONTENTS

ABSTRACT—Stephanie C. Herring, Martin P. Hoerling, James P. Kossin, Thomas C. Peterson, and Peter A. Stott

Understanding how long-term global change affects the intensity and likelihood of extreme weather events is a frontier science challenge. This fourth edition of explaining extreme events of the previous year (2014) from a climate perspective is the most extensive yet with 33 different research groups exploring the causes of 29 different events that occurred in 2014. A number of this year's studies indicate that human-caused climate change greatly increased the likelihood and intensity for extreme heat waves in 2014 over various regions. For other types of extreme events, such as droughts, heavy rains, and winter storms, a climate change influence was found in some instances and not in others. This year's report also included many different types of extreme events. The tropical cyclones that impacted Hawaii were made more likely due to human-caused climate change. Climate change also decreased the Antarctic sea ice extent in 2014 and increased the strength and likelihood of high sea surface temperatures in both the Atlantic and Pacific Oceans. For western U.S. wildfires, no link to the individual events in 2014 could be detected, but the overall probability of western U.S. wildfires has increased due to human impacts on the climate.

Challenges that attribution assessments face include the often limited observational record and inability of models to reproduce some extreme events well. In general, when attribution assessments fail to find anthropogenic signals this alone does not prove anthropogenic climate change did not influence the event. The failure to find a human fingerprint could be due to insufficient data or poor models and not the absence of anthropogenic effects.

This year researchers also considered other human-caused drivers of extreme events beyond the usual radiative drivers. For example, flooding in the Canadian prairies was found to be more likely because of human land-use changes that affect drainage mechanisms. Similarly, the Jakarta floods may have been compounded by land-use change via urban development and associated land subsidence. These types of mechanical factors re-emphasize the various pathways beyond climate change by which human activity can increase regional risk of extreme events.

1. INTRODUCTION TO EXPLAINING EXTREME EVENTS OF 2014 FROM A CLIMATE PERSPECTIVE

Stephanie C. Herring, Martin P. Hoerling, James P. Kossin, Thomas C. Peterson, and Peter A. Stott

The field of event attribution faces challenging questions. Can climate change influences on single events be reliably determined given that observations of extremes are limited and implications of model biases for establishing the causes of those events are poorly understood? The scientific developments in this report—now in its fourth year—as well as in the broader scientific literature, suggest that "event attribution" that detects the effects of long-term change on extreme events is possible. However, because of the fundamentally mixed nature of anthropogenic and natural climate variability, as well as technical challenges and methodological uncertainties, results are necessarily probabilistic and not deterministic.

As the science advances, other questions are emerging. For what types of events can event attribution provide scientifically robust explanations of causes? Is near-real-time attribution possible? And, how useful are science-based explanations of extremes for society? We consider these questions in more detail.

The Science. When launched in 2012, an original aim of this report was to encourage the development of the science of event attribution. In this endeavor, we continue to be encouraged by the response from the climate community. The report has grown again and this year includes 32 papers looking at 28 different events from all seven continents (Fig. 1.1).

The exact analysis that goes into each of the attribution statements in this report is dependent on the event in question and the available data and models. Take for example the attribution statement, "High global water vapor content of the atmosphere likely caused the very heavy Pyrenees rainfall event in September." In this case, the science must address the physical processes relating water vapor to heavy precipitation over the Pyrenees in September. Additional extreme event features are also important to explain, including event magnitude and likelihood, against which societal resilience, vulnerability, and preparedness are judged. Magnitude and likelihood are not mutually exclusive characteristics of extremes, though explanations for how long-term change affected one feature can differ from how it affected others (e.g., Dole et al. 2012; Otto et al. 2012).

The sophistication of the contributions continues to develop. For instance, the resources provided by the Weather@home group, which generates regional modeling experiments, have been increasingly employed to study how climate change affects regional-scale weather (e.g., Rosier et al. 2015; Black et al. 2015). The strengths and limitations of Weather@home and other methods are increasingly being scrutinized. With rapid turn-around and space constraints, the possibilities for exhaustive analysis in this report are more limited than in the general literature; the studies here generally rely on well-developed and vetted methodologies.

In addition to an increasing number of submissions, we are also seeing new types of events being examined. In general, temperature and precipitation extremes have dominated event attribution literature since this field emerged in the early 2000s. Confidence in the role of human-caused climate change in temperature extremes remains the highest due to the detectability of a climate change signal. Event types represented for the first time in this year's report include forest fires, tropical cyclones, sea surface temperature, and sea level pressure anomalies. This report is not a random selection of extreme events from the past year, so it does not facilitate broad claims about trends for any extreme event type.

Another significant challenge is near-real-time event attribution. One reason this is important is that extreme events often elicit immediate public policy responses, such as building code modifications (Peterson et al. 2008). In these cases, near-real-time attribution can help science inform discussion about

AFFILIATIONS: Herring—NOAA/National Centers for Environmental Information, Boulder, Colorado; Hoerling—NOAA/Earth System Research Laboratory, Boulder, Colorado; Kossin—NOAA/National Centers for Environmental Information, Madison, Wisconsin; Peterson—NOAA/National Centers for Environmental Information, Asheville, North Carolina; Stott—Met Office Hadley Centre, Exeter, United Kingdom

DOI: 10.1175/BAMS-D-15-00157.1

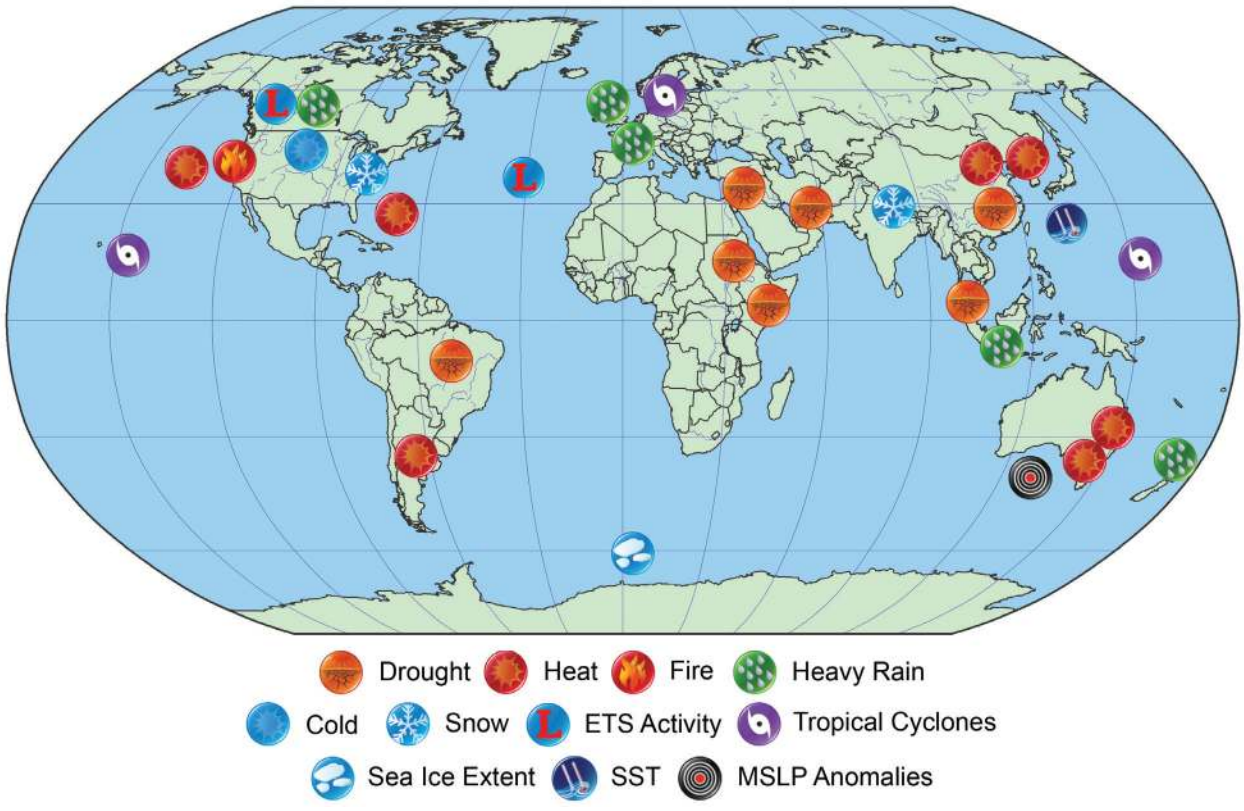

Fig. 1.1. Location and types of events analyzed in this publication.

about policy. Major efforts in real-time event attribution include the World Weather Attribution (WWA; www.climatecentral.org/what-we-do/our-programs/climate-science#wwa) project based in the United States and led by Climate Central as well as the European Climate and Weather Events: Interpretation and Attribution (EUCLEIA; www.eucleia.eu) project based in Europe and led by the UK Met Office.

The Stakeholders. Both the EUCLEIA and WWA initiatives reflect a growing interest in connecting attribution science to decision making. In a European context, stakeholders involved in decision making that could be affected by climate variability and change have shown a strong interest in the science of event attribution (Stott and Walton 2013). There is also some literature emerging that illustrates how attribution work is being applied by stakeholders, including a case study using the hot and dry summer of 2012 in southeast Europe (Sippel et al. 2015). However, interest from a wide variety of sectors including policy making, litigation, regional planning, and public communication does not mean that the requirements from the different groups are the same, and tailored approaches to communication between scientists and stakeholders are likely to be required (Stott and Walton 2013). We are looking forward to the results of efforts such as WWA and EUCLEIA over the next several years.

In the absence of robust literature exploring decision-maker needs for event attribution information, we have taken an anecdotal look at how the science in these reports could be relevant beyond the research community. From our initial look, it is clear that event attribution is more than just a tool to communicate the impacts of the changing climate to the public. Some decision makers do value knowing how specific events were impacted by the changing climate and what this means for their future (e.g., Hoerling et al. 2013). The science of event attribution can thus be viewed as critical progress toward building a "situational awareness" that supports informed decision making. From the science perspective, this involves providing information about global environmental elements and explaining their connections to regional conditions. From a stakeholder perspective, a robust and reliable situational awareness informs risk reduction. The science is evolving, but the vision is to provide users with an improved understanding of how changes in extremes can be relevant and applied to improved decision making.

Certain sectors appear to have a greater interest in event attribution than others do. For example, we asked several contacts in the reinsurance sector about how they might use event attribution. While the attribution of changing trends in extreme events was relevant to their business and bottom line, our contacts all indicated they do not currently find great value in the attribution of specific events. This is primarily because relatively short time scales are of greatest relevance to them, and these tend to be dominated by year-to-year variability and persistence rather than climate change on longer time scales.

In contrast, discussions with participants of the National Integrated Drought Information Service (NIDIS; www.drought.gov) revealed that water resource managers and others dealing with drought in the U.S. West find event attribution work useful. The attribution work helps show why long-term planning should account for changing climate. Also, since all droughts are different, decision makers are interested in what ingredients went into any particular drought, how it evolved, and whether it could have been predicted. This is especially beneficial for improving early warning for drought. Attribution science provides situational awareness of our weather and climate system, which can lead to informed planning decisions. Decision makers have also shown interest in attribution for floods. For example, NOAA was asked by the U.S. Army Corps of Engineers to do an in-depth assessment of the 2011 Missouri River Basin flood to inform their planning (Hoerling et al. 2013).

Stakeholder perspectives will undoubtedly vary around the world depending on the specific local contexts in which event attribution science is applied. The extent to which hazardous weather and climate extremes affect people depends on their exposure and vulnerability as well as the meteorology (e.g., Peduzzi et al. 2012). Therefore, much more work needs to be done on attribution of the impacts of extreme events (Stott 2015). A continuing ambition for this report is to increase the geographical coverage of regions examined and geographical representation of authors contributing their regional expertise as we'd like this report to serve stakeholders throughout the world.

Conclusions. As attribution science continues to mature, effectively communicating the results becomes increasingly important. So this year, authors have been asked to try and clearly state whether climate change influenced the event's intensity, frequency, or both. These distinctions are important because changes in intensity versus frequency have very different implications for communities, businesses, and governments trying to adapt to the impacts of a changing climate.

Looking to the future, it will be important to continue to assess whether and how effectively decision makers apply attribution science. Expectations about what will have value needs to be developed by the user community in collaboration with scientists. Close interactions between attribution scientists and the user community will be essential to fully exploit the value of this research to society.

REFERENCES

Black, M. T., D. J. Karoly, and A. D. King, 2015: The contribution of anthropogenic forcing to the Adelaide and Melbourne, Australia, heatwaves of January 2014 [in "Explaining Extreme Events of 2014 from a Climate Perspective"]. *Bull. Amer. Meteor. Soc.*, **96** (12), S145–S148, doi:10.1175 /BAMS-D-15-00098.1.

Dole, R. M., and Coauthors, 2011: Was there a basis for anticipating the 2010 Russian heat wave? *Geophys. Res. Lett.*, **38**, L06702, doi:10.1029/2010GL046582.

Hoerling, M., J. Eischeid, and R. Webb, 2013: Understanding and explaining climate extremes in the Missouri River Basin associated with the 2011 flooding. National Oceanic and Atmospheric Administration, 28 pp. [Available online at www.esrl .noaa.gov/psd/csi/factsheets/pdf/noaa-mrb-climate -assessment-report.pdf.]

Otto, F. E. L., N. Massey, G. J. vanOldenborgh, R. G. Jones, and M. R. Allen, 2012: Reconciling two approaches to attribution of the 2010 Russian heat wave. *Geophys. Res. Lett.*, **39**, L04702, doi:10.1029/2011GL050422.

Peduzzi, P., B. Chatenoux, H. Dao, A. De Bono, C. Herold, J. Kossin, F. Mouton, and O. Nordbeck, 2012: Tropical cyclones: Global trends in human exposure, vulnerability and risk. *Nat. Climate Change*, **2**, 289–294, doi:10.1038/nclimate1410.

Peterson, T. C., and Coauthors, 2008: Why weather and climate extremes matter. *Weather and Climate Extremes in a Changing Climate. Regions of Focus: North America, Hawaii, Caribbean, and U.S. Pacific Islands*, T. R. Karl et al., Eds., U.S. Climate Change Science Program and the Subcommittee on Global Change Research, 11–33.

Rosier, S., S. Dean, S. Stuart, T. Carey-Smith, M. T. Black, and N. Massey, 2015: Extreme rainfall in early July 2014 in Northland, New Zealand—Was there an anthropogenic influence? [in "Explaining Extreme Events of 2014 from a Climate Perspective"]. *Bull. Amer. Meteor. Soc.*, **96** (12), S136–S140, doi:10.1175 / BAMS-D-15-00105.1.

Sippel, S., P. Walton, and F. E. L. Otto, 2015: Stakeholder perspectives on the attribution of extreme weather events: An explorative enquiry. *Wea. Climate Soc.*, **7**, 224–237, doi:10.1175/WCAS-D-14-00045.1.

Stott, P. A., 2015: Weather risks in a warming world. *Nat. Climate Change*, **5**, 517–518, doi:10.1038/nclimate2640.

——, and P. Walton, 2013: Attribution of climate-related events: Understanding stakeholder needs. *Weather*, **68**, 274–279, doi:10.1002/wea.2141.

2. EXTREME FIRE SEASON IN CALIFORNIA: A GLIMPSE INTO THE FUTURE?

Jin-Ho Yoon, S.-Y. Simon Wang, Robert R. Gillies, Lawrence Hipps, Ben Kravitz, and Philip J. Rasch

The fire season in northern California during 2014 was the second largest in terms of burned areas since 1996. An increase in fire risk in California is attributable to human-induced climate change.

Introduction. California has been under drought conditions since 2012, and the drought worsened considerably in the winter of 2013/14 (e.g., Wang et al. 2014), which fueled an extreme fire season in 2014 (Hart et al. 2015). The early onset of the 2014 dry season (Supplemental Fig. S2.1) fueled an extraordinary jump in wildfires. Between 1 January and 20 September, the California Department of Forestry and Fire Protection reported thousands more fires than the five-year average (www.fire.ca.gov). In early August, a state of emergency was declared for a single wildfire that had burned 32 000 acres (http://gov.ca.gov/news.php?id=18645). This unusual fire season is expected to continue well through 2015.

The connection between a warming climate and lengthened fire seasons may seem intuitive, given the general tendency toward a hot-and-dry climate scenario and an earlier snowmelt (Westerling et al. 2006). However, what is not yet fully understood is the extent to which the projected wetter climate in California towards the latter part of the 21st century (Neelin et al. 2013) could affect wildfire risk in the future; this historical drought and unusual fire season also calls attention to possible impacts from human-induced climate change.

Satellite merged data of burned area from the fourth generation of the Global Fire Emissions Database (GFED4; Giglio et al. 2013) was analyzed (online supplemental material). Because the GFED4 product may underestimate wildfire extent due to its limit in the minimum detectable burned area and obscuration by cloud cover, the Keetch–Byram Drought index (KBDI; Janis et al. 2002; Keetch and Byram 1968), routinely used by the United States Forest Service for monitoring fire risk, was included as well. The KBDI is computed with both the observational and simulated daily precipitation and maximum surface temperature. Observational dataset is from the North American Land Data Assimilation phase 2 (NLDAS2; Xia et al. 2012).

Fire extent of 2014. Figure 2.1 shows the annual mean KBDI, the fractional area under extreme fire risk (online supplemental material), and the burned area averaged for entire California (Fig. 2.1a) and northern California—north of 39°N (Fig. 2.1b). Both the KBDI and the extreme fire risk exhibit a steady increase over California since 1979 despite the rather large interannual fluctuation. In terms of area burned in GFED4, 2014 ranks the sixth largest in the entire state and second in northern California; but in terms of the KBDI and the extreme fire risk, 2014 ranks first in both the entire state and northern California. Also noteworthy is that the two largest burned areas in northern California, over the 18-year record of GFED4, occurred in 2012 and 2014. Spatially, the area of higher fire risk in 2014, that is, a KBDI value higher than 400, extends further north compared to that of 2012 (Figs. 2.1e,f), consistent with the burned area (Figs. 2.1c,d).

Attribution and projection. Wildfire simulations and projections are generally performed using stand-alone vegetation models (e.g., Brown et al. 2004; Cook et al. 2012; Luo et al. 2013; Scholze et al. 2006; Yue et al. 2013) driven by global climate model output. While the advantage of using a stand-alone vegetation model lies in its application to high spatial resolution through downscaling, disadvantages include added uncertainty produced from downscaling (e.g., Shukla and Lettenmaier 2013; Yoon et al. 2012). In this study,

AFFILIATIONS: Yoon, Kravitz, and Rasch—Atmospheric Sciences and Global Change Division, Pacific Northwest National Laboratory, Richland, Washington; Wang, Gillies, and Hipps—Utah Climate Center/Dept. Plants, Soils and Climate, Utah State University, Logan, Utah

DOI:10.1175/BAMS-D-15-00114.1

A supplement to this article is available online (10.1175/BAMS-D-15-00114.2)

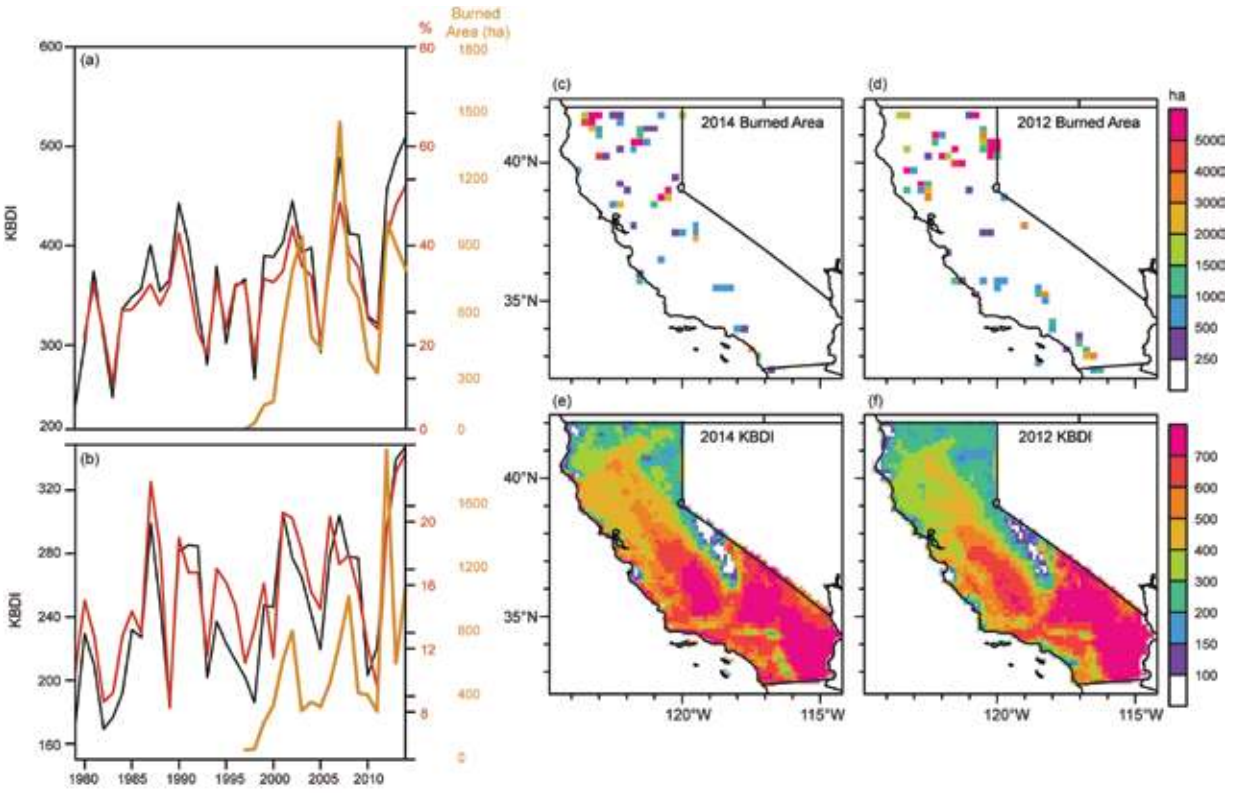

Fig. 2.1. Annual mean of the KBDI in black, fraction of the area that are under the extreme fire risk in red, which is defined as KBDI > 600, and burned area from GFED4 in orange averaged for (a) California and (b) Northern California. Spatial distribution of burned area in hectare (ha) from GFED4 averaged for (c) 2014 and (d) 2012, and corresponding the annual mean KBDI in (e) and (f).

we analyzed both the KBDI and wildfire probabilities computed directly within the Community Earth System Model version 1 (CESM1), which are primarily driven by the dryness of the surface soil and the availability of fuel load, that is, vegetation (Thonicke et al. 2001). Although CESM1's spatial resolution of 1-degree is relatively coarse, the model does simulate well the climate drivers of fire, such as precipitation and surface air temperature of California (Wang et al. 2014). Further, the CESM1 has produced 30 members (online supplemental material) spanning historical (1920–2005) and future periods (2006–80; based on RCP8.5 scenario), together with a pre-industrial simulation of 1800 years. These model outputs provide a unique opportunity for the detection and attribution study conducted here to assess wildfire probabilities under climate change.

Projections for California did show a steady increase of the fire risk based solely upon the KBDI (Fig. 2.2a) and are consistent with recent studies (Dennison et al. 2014; Lin et al. 2014; Luo et al. 2013; van Mantgem et al. 2013) that indicate increased occurrence of area burned and wildfire intensity and duration over the western United States. The CESM1 projects only a slight increase in annual precipitation accompanied with increasing surface warming after 1990 through 2070 (Supplemental Figs. S2.2b,c), consistent with those produced by the Coupled Model Intercomparison Project Phase 5 (CMIP5) ensembles (Neelin et al. 2013). At face value, these simulations of a slightly wetter climate from 1990 onward could explain the cessation of the simulated fire probability increase at the end of 20th century (Supplemental Fig. S2.2c). However, the KBDI and the extreme fire risk measures, computed here in terms of the fractional area and the extreme fire danger days (Figs. 2.2b,c), do show a steady and rapid increase from early 1990s and 2000s.

To what extent can the change of the extreme fire risk over California be attributed to global warming? First, we need to understand how much fluctuation is caused by natural climate variability alone (e.g., Kitzberger et al. 2007). Analyzing the 1800-year pre-industrial simulation of the CESM1 by treating the simulation as 18 member ensembles of 100-year simulation, the pre-industrial simulations envelops entirely both the KBDI and the extreme fire risk measures fluctuation for the period spanning 1920–80

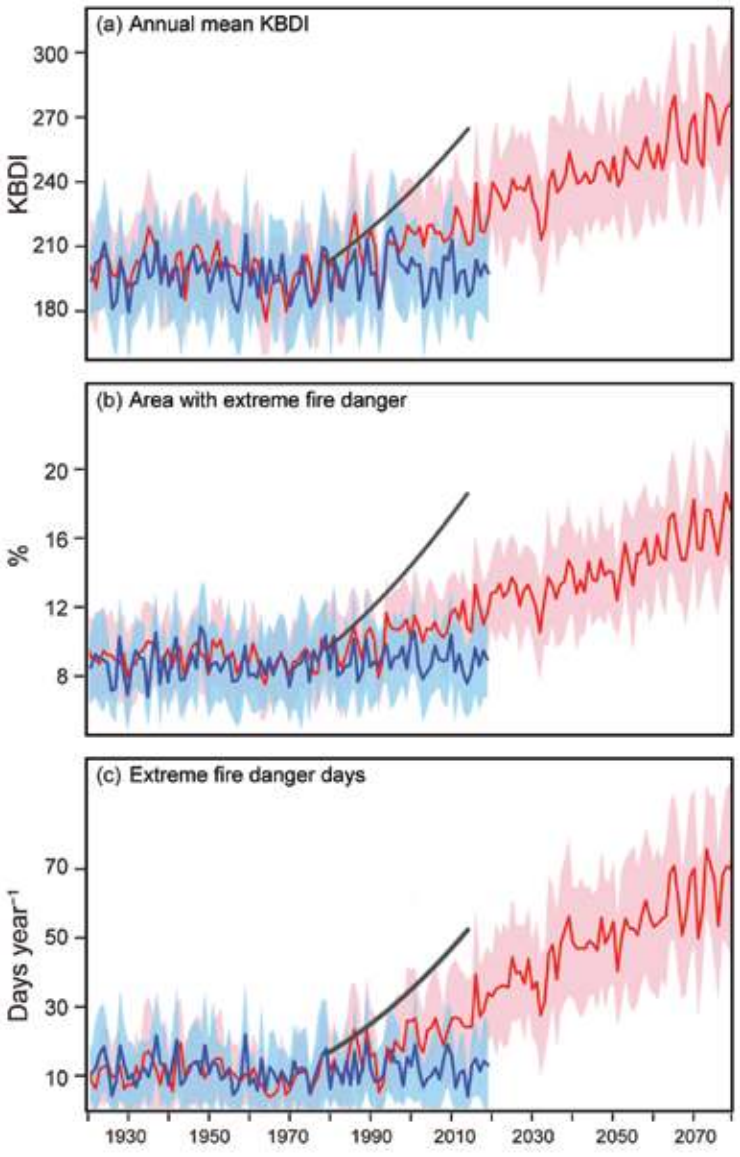

Fig. 2.2. (a) Annual mean of the KBDI from the large ensemble simulation of the CESM1, (b) fractional area (%) under the extreme fire risk, and (c) the extreme fire danger (days year^{-1}) over California. Red (blue) indicates the historical and RCP8.5 (pre-industrial) runs. Gray lines indicate 50% of the 2nd order trend of the KBDI and the extreme fire risk measures based on the NLDAS2. To remove the climatological bias, starting points are adjusted to be the same as the modeled ensemble mean of year 1979.

(Fig. 2.2). Beginning in the 1990s—the later part of the historical simulation—a clear separation emerges between the extreme fire risks driven by the anthropogenic climate forcing and that of natural climate variability. However, 2014 occurred in a period of rapidly increasing extreme fire risk. The pace of increasing extreme fire risk according to simulation has accelerated since the early 21st century and is expected to surpass the range of natural climate variability. Observations show much faster increases of the KBDI and extreme fire risk measures (gray lines in Fig. 2.2).

The accelerated increase in the KBDI and the extreme fire risk in relation to the projected wetter climate in California is intriguing. To increase extreme fire risk, two basic situations need to be present: one is abundant fuel load (i.e., surface vegetation coverage enhanced through precipitation), and the other is the occurrence of a hot-and-dry climate regime or drought to dry the vegetation. A process called CO_2 fertilization (Donohue et al. 2013) tends to increase vegetation activity simply through the uptake of an increasing atmospheric CO_2. Under such a scenario along with a wetter climate, vegetation growth would increase and subsequently supply sufficient fuel load. Though population growth and associated urban area change are accounted for in the model, the CESM1 produced fire probability does not account for incidence of human-caused fire ignition, which correlate with population growth.

The extent to which man-made global warming has increased the risk or strength of the recent drought in California has been an active area of research. For example, the severity of the 2014 drought in California was previously analyzed and its potential link to anthropogenic warming was suggested (Diffenbaugh et al. 2015; Wang et al. 2015, 2014) despite presence of natural climate variability (Wang and Schubert 2014). However, it is important to point out from this study that, the increase in extreme fire risk is expected within the coming decade to exceed that of natural variability and this serves as an indication that anthropogenic climate warming will likely play a significant role in influencing California's fire season.

Conclusions. The 2014 fire season saw the second largest burned area in northern California since 1997, next only to 2012, and ranks the highest since 1979 in the case of extreme fire risk over the entire state.

Although both fire measures are based upon observations, these derived variables do exhibit uncertainty (Giglio et al. 2013; Xia et al. 2012). The recent extreme fire seasons have occurred in a time of drought. Some measures of extreme fire risk are also expected to increase in the future despite the overall lack of change in the mean fire probability and annual precipitation simulated by climate models for the next 50 years. Our result, based on the CESM1 outputs, indicates that man-made global warming is likely one of the causes that will exacerbate the areal extent and frequency of extreme fire risk, though the influence of internal climate variability on the 2014 and the future fire season is difficult to ascertain.

ACKNOWLEDGEMENTS. Research by Yoon, Kravitz, and Rasch was supported by the Earth System Modeling program in the Office of Science/DOE and Wang, and Gillies by the WaterSMART grant from the Bureau of Reclamation. Computation was done at the National Energy Research Scientific Computing Center and the Environmental Molecular Sciences Laboratory at PNNL. CESM1 is supported by the NSF and DOE. PNNL is operated for the Department of Energy by Battelle Memorial Institute under Contract DEAC05-76RLO1830.

REFERENCES

Brown, T., B. Hall, and A. Westerling, 2004: The impact of twenty-first century climate change on wildland fire danger in the western United States: An applications perspective. *Climatic Change*, **62**, 365–388.

Cook, B., N. Zeng, and J.-H. Yoon, 2012: Will Amazonia dry out? Magnitude and causes of change from IPCC climate model projections. *Earth Interact.*, **16**, 1-27, doi:10.1175/2011EI398.1.

Dennison, P. E., S. C. Brewer, J. D. Arnold, and M. A. Moritz, 2014: Large wildfire trends in the western United States, 1984–2011. *Geophy. Res. Lett.*, **41**, 2928–2933, doi:10.1002/2014GL059576.

Diffenbaugh, N. S., D. L. Swain, and D. Touma, 2015: Anthropogenic warming has increased drought risk in California. *Proc. Natl. Acad. Sci. USA*, **112**, 3931–3936, doi:10.1073/pnas.1422385112.

Donohue, R. J., M. L. Roderick, T. R. McVicar, and G. D. Farquhar, 2013: Impact of CO_2 fertilization on maximum foliage cover across the globe's warm, arid environments. *Geophys. Res. Lett.*, **40**, 3031–3035, doi:10.1002/grl.50563.

Giglio, L., J. T. Randerson, and G. R. van der Werf, 2013: Analysis of daily, monthly, and annual burned area using the fourth-generation global fire emissions database (GFED4). *J. Geophys. Res. Biogeosci.*, **118**, 317–328, doi:10.1002/jgrg.20042.

Hart, S. J., T. Schoennagel, T. T. Veblen, and T. B. Chapman, 2015: Area burned in the western United States is unaffected by recent mountain pine beetle outbreaks. *Proc. Natl. Acad. Sci. USA*, **112**, 4375–4380, doi:10.1073/pnas.1424037112.

Janis, M. J., M. B. Johnson, and G. Forthun, 2002: Near-real time mapping of Keetch-Byram drought index in the south-eastern United States. *Int. J. Wildland Fire*, **11**, 281–289.

Keetch, J. J., and G. M. Byram, 1968: A drought index for forest fire control. U.S.D.A. Forest Service Res. Paper SE-38, 32 pp. [Available online at www.srs.fs.usda.gov/pubs/rp/rp_se038.pdf.]

Kitzberger, T., P. M. Brown, E. K. Heyerdahl, T. W. Swetnam, and T. T. Veblen, 2007: Contingent Pacific–Atlantic Ocean influence on multicentury wildfire synchrony over western North America. *Proc. Natl. Acad. Sci. USA*, **104**, 543–548.

Lin, H.-W., J. L. McCarty, D. Wang, B. M. Rogers, D. C. Morton, G. J. Collatz, Y. Jin, and J. T. Randerson, 2014: Management and climate contributions to satellite-derived active fire trends in the contiguous United States. *J. Geophys. Res. Biogeosci.*, **119**, 645–660, doi:10.1002/2013JG002382.

Luo, L., Y. Tang, S. Zhong, X. Bian, and W. E. Heilman, 2013: Will future climate favor more erratic wildfires in the western United States? *J. Appl. Meteor. Climatol.*, **52**, 2410–2417, doi:10.1175/JAMC-D-12-0317.1.

Mo, K. C., and R. W. Higgins, 1998a: Tropical convection and precipitation regimes in the western United States. *J. Climate*, **11**, 2404–2423.

—— and ——, 1998b: Tropical influences on California precipitation. *J. Climate*, **11**, 412–430.

Neelin, J. D., B. Langenbrunner, J. E. Meyerson, A. Hall, and N. Berg, 2013: California winter precipitation change under global warming in the Coupled Model Intercomparison Project Phase 5 Ensemble. *J. Climate*, **26**, 6238–6256, doi:10.1175/JCLI-D-12-00514.1.

Scholze, M., W. Knorr, N. W. Arnell, and I. C. Prentice, 2006: A climate-change risk analysis for world ecosystems. *Proc. Natl. Acad. Sci. USA*, **103**, 13116–13120.

Shukla, S., and D. P. Lettenmaier, 2013: Multi-RCM ensemble downscaling of NCEP CFS winter season forecasts: Implications for seasonal hydrologic forecast skill. *J. Geophys. Res. Atmos.*, **118**, 10770–10790, doi:10.1002/jgrd.50628.

Thonicke, K., S. Venevsky, S. Sitch, and W. Cramer, 2001: The role of fire disturbance for global vegetation dynamics: Coupling fire into a Dynamic Global Vegetation Model. *Global Ecol. Biogeogr.*, **10**, 661–677.

van Mantgem, P. J., J. C. B. Nesmith, M. Keifer, E. E. Knapp, A. Flint, and L. Flint, 2013: Climatic stress increases forest fire severity across the western United States. *Ecol. Lett.*, **16**, 1151–1156, doi:10.1111/ele.12151.

Wang, H., and S. Schubert, 2014: Causes of the extreme dry conditions over California during early 2013 [in "Explaining Extreme Events of 2013 from a Climate Perspective"]. *Bull. Amer. Meteor. Soc.*, **95** (9), S7–S11.

Wang, S.-Y. S., W.-R. Huang, and J.-H. Yoon, 2015: The North American winter 'dipole' and extremes activity: A CMIP5 assessment. *Atmos. Sci. Lett.*, **16**, 338–345, doi:10.1002/asl2.565.

——, L. Hipps, R. R. Gillies, and J.-H. Yoon, 2014: Probable causes of the abnormal ridge accompanying the 2013-2014 California drought: ENSO precursor and anthropogenic warming footprint. *Geophys. Res. Lett.*, **41**, 3220–3226, doi:10.1002/2014GL059748.

Westerling, A. L., H. G. Hidalgo, D. R. Cayan, and T. W. Swetnam, 2006: Warming and earlier spring increase western US forest wildfire activity. *Science*, **313**, 940–943.

Xia, Y. L., and Coauthors, 2012: Continental-scale water and energy flux analysis and validation for the North American Land Data Assimilation System project phase 2 (NLDAS-2): 1. Intercomparison and application of model products. *J. Geophys. Res.*, **117**, D03109, doi:10.1029/2011JD016048.

Yoon, J. H., K. Mo, and E. F. Wood, 2012: Dynamic-model-based seasonal prediction of meteorological drought over the contiguous United States. *J. Hydrometeor.*, **13**, 463–482, doi:10.1175/JHM-D-11-038.1.

Yue, X., L. J. Mickley, J. A. Logan, and J. O. Kaplan, 2013: Ensemble projections of wildfire activity and carbonaceous aerosol concentrations over the western United States in the mid-21st century. *Atmos. Environ.*, **77**, 767–780, doi:10.1016/j.atmosenv.2013.06.003.

3. HOW UNUSUAL WAS THE COLD WINTER OF 2013/14 IN THE UPPER MIDWEST?

Klaus Wolter, Martin Hoerling, Jon K. Eischeid, Geert Jan van Oldenborgh, Xiao-Wei Quan, John E. Walsh, Thomas N. Chase, and Randall M. Dole

The frigid 2013/14 Midwestern winter was 20–100 times less likely than in the 1880s due to long-term warming, while winter temperature variability has shown little long-term change.

Introduction. Below-normal temperatures covered the Upper Midwest and Great Lakes region from November 2013 through April 2014, the longest such consecutive monthly stretch since 1995–96, culminating in the coldest winter since 1978/79.[1] The U.S. economy suffered a severe setback,[2] in part due to the harsh winter (Boldin and Wright 2015; Bloesch and Gourio 2015). Direct economic losses due to wintry weather totaled at least $4 billion (U.S. dollars).[3] The largest Great Lakes ice extent since 1979[4] hindered shipping exceptionally long into spring.[5] The frigid weather after two decades of mostly mild winters surprised many, who were not warned by seasonal forecasts either (see Supplemental Figs. S3.1, S3.2).

The severity of individual daily and weekly cold spells was not exceptional compared to previous cold waves, especially during the 1980s (Peterson et al. 2013; van Oldenborgh et al. 2015), despite the media commotion about the so-called "polar vortex".[6] However, the full winter temperature anomaly exceeded two standard deviations, the only land region to do so globally (Supplemental Fig. S3.3).

Our paper poses three questions: How extreme was the cold winter of 2013/14 in its core region? Have winter temperatures been getting more variable? What are the odds of a cold winter this extreme, in the past, present, and future? We analyze observations and models to address these questions.

Data and Methods. Gridded monthly mean temperature data (Lawrimore et al. 2011) were analyzed for 1880–2014. The region from 40°–50°N and 75°–100°W (box in Fig. 3.1a) represents the core of the cold anomaly, and has temperature records since the late 19th century. We refer to this domain as the "greater Upper Midwest" (GUM).

Gridded satellite-based snow cover data from 1966/67 onwards (Robinson and Dewey 1990) was used to establish a snow cover history for the GUM, given potential snow contributions to cold conditions through snow-albedo feedbacks (e.g., Wagner 1973; Namias 1985; Leathers and Robinson 1993).

To isolate the role of radiative forcing, coupled climate model simulations were investigated with NCAR's Community Earth System Model version 1 (CESM1), for transient runs from 1920 onwards (Kay et al. 2014). The simulations consist of 30 ensemble members driven by anthropogenic greenhouse gases, aerosols, and natural external radiative forcing during the historical record, and with the RCP8.5 emissions scenario after 2005. In addition, single runs from 30 different CMIP5 models (Taylor et al. 2012) were examined that have been forced in a similar manner as CESM1, but over a longer period (from 1880/81 onwards).

Results. a. The observed 2013/14 event and its historical context. The winter 2013/14 temperature anomaly was −4.1°C for the full GUM area compared to

[1]www.ncdc.noaa.gov/sotc/national/2014/2
[2]http://blogs.wsj.com/economics/2014/11/26/the-weather-really-can-hold-back-the-economy-its-not-just-an-excuse/
[3]www.munichre.com/en/reinsurance/magazine/topics-online/2015/03/harsh-winter
[4]www.glerl.noaa.gov/data/ice/imgs/IceCoverAvg1973_2014.jpg
[5]www.nrcc.cornell.edu/newsletter/GL2014-06.pdf
[6]http://en.wikipedia.org/wiki/2013–14_North_American_cold_wave

AFFILIATIONS: Wolter, Eischeid, Quan, and Chase—Cooperative Institute for Research in the Environmental Sciences, University of Colorado Boulder, Boulder, Colorado; Hoerling and Dole—NOAA/Earth System Research Laboratory/Physical Sciences Division, Boulder, Colorado; van Oldenborgh—Royal Netherlands Meteorological Institute (KNMI), De Bilt, Netherlands; Walsh—University of Alaska Fairbanks, Fairbanks, Alaska

DOI: 10.1175/BAMS-D-15-00126.1

A supplement to this article is available online (10.1175/BAMS-D-15-00126.2)

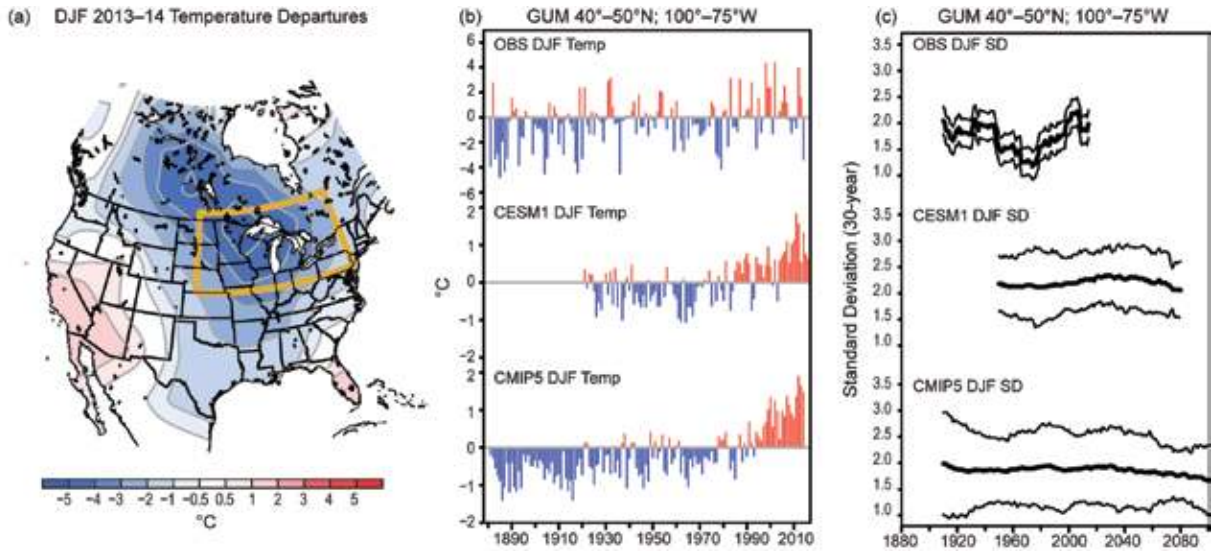

Fig. 3.1. (a) DJF 2013/14 temperature anomalies (°C) for NCDC gridded data (1981–2010 base period). Spherical rectangle delineates the GUM (40°–50°N, 100°–75°W). (b) Time series for GUM DJF temperature anomalies (°C) for (top) NCDC 1881–2013 base period, (middle) transient 1921–2013 CESM1 30-member ensemble average, and (bottom) 1881–2013 CMIP5 30-model ensemble member averages. (c) Standard deviations (sliding 30-year periods) in °C for GUM in (top) observations, (middle) CESM1, and (bottom) CMIP5. 95% confidence intervals (dashed lines) were estimated based on resampling for the observational record (top), and the actual sliding distribution of 30-ensemble member standard deviations for the model results (middle, bottom).

1981–2010 means (Fig. 3.1a). It was the coldest winter since 1978/79 in this region, and ranked 10th coldest since 1880/81 (Fig. 3.1b, top). Aside from 1978/79 and 1935/36, all other colder winters occurred before 1919. A wider seasonal average from December 2013 through March 2014 was even the coldest since 1903/04. Snow cover was ample (seventh highest since 1966/67), but not at record-levels. The enhanced snow cover is consistent with a strong negative correlation ($r = -0.75$) of GUM winter temperatures and snow cover anomalies observed over 1966/67 to 2013/14 (Supplemental Fig. S3.4). This association is reproduced in CESM1 (Supplemental Fig. S3.5).

b. Externally forced variability of GUM winter temperatures. Two independent estimates of the externally forced variability in winter temperatures for the period of record are shown in Fig. 3.1b (middle for CESM1, bottom for CMIP5). The dominant feature of this forced variability is a warming trend, especially post-1980. The preponderance of observed warm winters in the last few decades is thus consistent with an emergent radiatively forced warm signal, making the 2013/14 cold event even more unusual.

The risk assessment of a cold winter must also account for changes in variability. The long-term observed standard deviation for GUM winter temperatures is 1.9°C. Over the last century, the range of observed standard deviations (30-year values) has been between 1.2°C for the mid-20th century and 2.2°C for the late 20th century (Fig. 3.1c), showing a significant increase prior to 2005, but only to levels slightly higher than in the early 20th century. During the same period, 30-year standard deviations for individual model runs have varied from about 1.0°C to about 3.0°C (Fig. 3.1c), a larger range than for the observations. However, *average* CESM1 and CMIP5 standard deviations show very little long-term trend over the last century, and even into the future. Observations and models agree that the risk of seasonal extremes is largely dictated by changes in long-term mean temperatures.

Observed winter temperatures have increased +1.0°C (+2.3°C) during 1921–2013 (1881–2013) over the GUM based on linear trend analysis. These warming rates fit into the range of modeled trends for these two periods in CESM1 (Fig. 3.2a) and CMIP5 (Fig. 3.2b), respectively. Admittedly, the observed temperature increase since the late 19th century is on the high end of the modeled temperature increases, while the observed warming since 1921 is right in the middle of the CESM1 trend distribution. However, the range of modeled temperature increases is more than 2°C for both periods, illustrating the considerable unforced component of long-term trends in this region. In the case of the CESM1 distribution, the range in trends

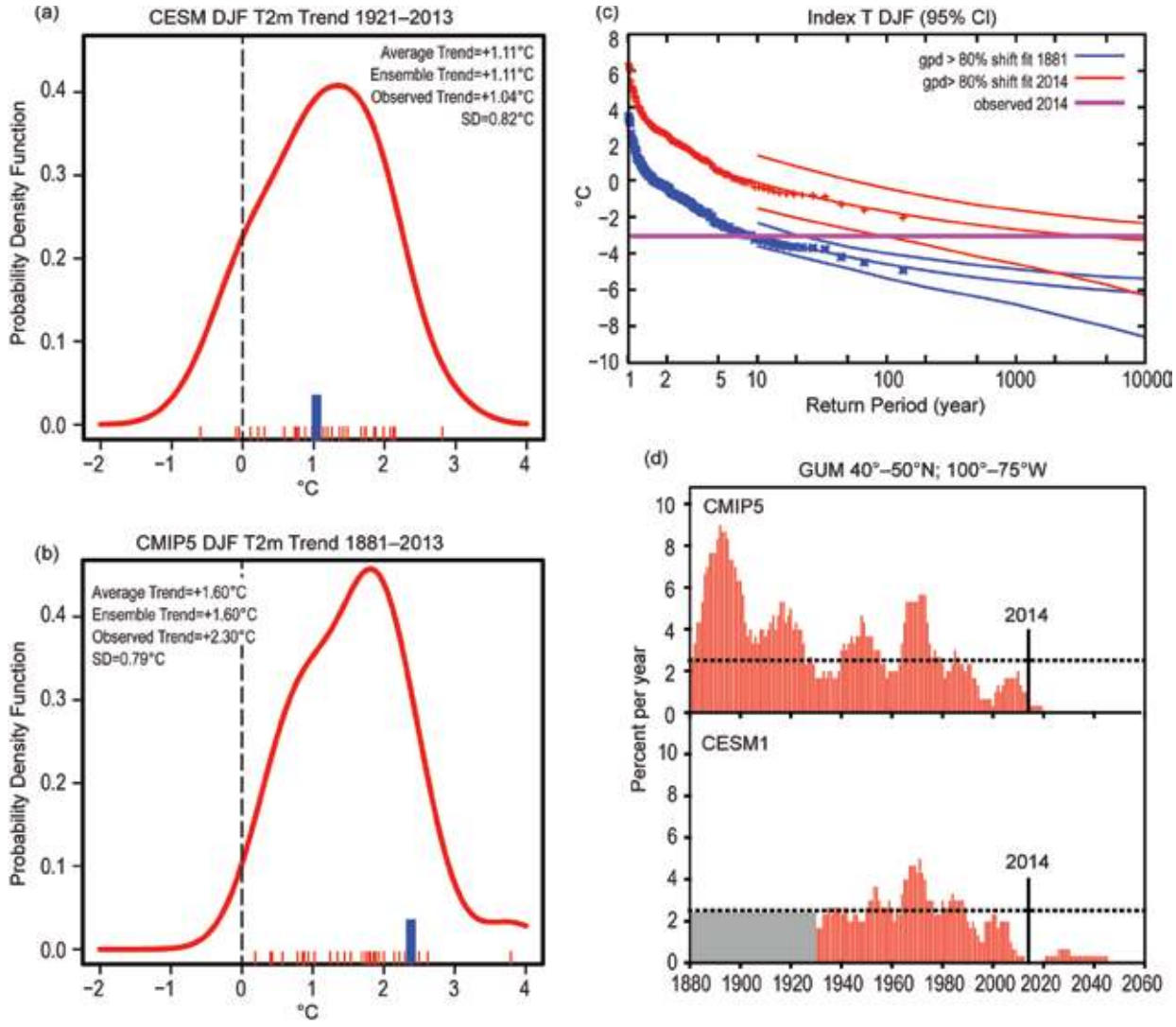

Fig. 3.2. (a) Temperature trends (°C) for CESM1 30 ensemble members since 1921 versus observations in GUM (blue tick). (b) Temperature trends (°C) for CMIP5 30-model ensemble member since 1881 versus observations in GUM (blue tick). (c) GPD fit to observed GUM temperature anomalies (°C, 95% confidence interval) with the effects of NCDC global temperature linearly subtracted from the position parameter, referenced at 1881 (blue) and 2014 (red), similar to van Oldenborgh et al. (2015). (d) Frequency distribution of −2 std dev winter temperatures in GUM from 10-year samples among 30 ensemble members since 1881 (CMIP5; top), and since 1921 (CESM1; bottom).

is entirely due to internal coupled ocean–atmosphere variability. In the case of the CMIP5 distribution, different model sensitivities to similar external forcing also contribute to the range, as discussed in Hawkins and Sutton (2009).

c. Late 19th century versus current odds. The observational GUM winter temperature time series was analyzed with a generalized Pareto distribution (GPD) fit (Fig. 3.2c) in order to assess extreme event probabilities through time. In this statistical modeling of tail events, we assumed no change in the scale and shape parameter of extreme cold events over time, supported in part by Fig. 3.1c. Our empirically derived change in cold event probability (expressed as a change in return periods) is thus driven by the mean warming of +2.3°C since 1881. The blue symbols in Fig. 3.2c represent conditions at the beginning of the record (1881), while the red symbols refer to present conditions. While a winter comparable to 2013/14 would have been roughly a once-a-decade event in 1881 (return periods from 5–20 years), it has become roughly a once-in-a-thousand years event in 2014 (return periods from 90 to over 10 000 years). This implies that extremely cold winters are two orders of magnitude less frequent in today's climate than in that of around 1881. Using a

Gaussian fit rather than GPD, the change in probability for such a cold winter would go from once-in-14 years in 1881 to once-in-200 years in 2014 (Supplemental Fig. S3.6). Due to the area-averaging, these changes in odds are more extreme than those found by van Oldenborgh et al. (2015) for individual stations since 1951, but match the drastic reduction in odds that Christidis et al. (2014) computed for cold springs in the United Kingdom.

An alternative approach to estimating the change in odds for an extreme cold winter is through diagnosis of the historical climate simulations. By pooling all ensemble members for moving 10-year windows, we computed the frequencies of two-sigma cold events since 1881 (1921) for CMIP5 (CESM1), shown in Fig. 3.2d. The CMIP5 results (Fig. 3.2d, top) confirm close to once-per-decade odds for the late 19th century, while 2014 is close to the "point of no return" by not showing this kind of severity again for the next half-century. The CESM1 results (Fig. 3.2d, bottom) are a little less extreme with a few "outlier" winters reaching the same severity as 2013/14 until about 2040, suggesting return periods around once-in-300 years. In sum, the model results are consistent with empirically derived results since both analyses rely on similar long-term warming trends, while the model data affirm little change in the scale parameter over time.

Conclusions. Our analysis of a 134-year record of winter season temperatures indicates that a cold winter of the severity observed over the GUM region in 2013/14 would have been a once-a-decade phenomenon at the end of the 19th century, but has become extraordinarily unlikely in the early 21st century. The reason for this reduced risk lies in overall warming since 1881, the principal cause for which appears to be the long-term change in external radiative forcing. Our results for this cold event are consistent with numerous other assessments of changing odds for cold winters and the role of climate change (e.g., Perlwitz et al. 2009; IPCC 2013; Christidis et al. 2014; van Oldenborgh et al. 2015). A new aspect of our analysis is the demonstration that the 2013/14 cold was not a symptom of a more variable climate, supported by a large ensemble of historical simulations that show little detectable change in winter season temperature variability over the GUM.

Both observed and modeled GUM winter temperatures are strongly related to snow cover. Observed snow cover has exhibited no long-term decline over this region (Hughes and Robinson 1996; Frei et al. 1999), with the last 20 years even showing an increase. If the modeled future reduction in snow cover does not materialize, cold winters may remain possible a little longer.

ACKNOWLEDGEMENTS. We wish to thank David Robinson and Thomas Estilow at Rutgers University for access to their gridded northern hemispheric snow cover data. Three anonymous reviews helped to improve our manuscript. This work was supported by the NASA MAP program under the funded MAP12-0072 project. It was also supported by the EUCLEIA project funded by the European Union's Seventh Framework Programme (FP7/2007-2013) under Grant Agreement No. 607085.

REFERENCES

Bloesch, J., and F. Gourio, 2015: The effect of winter weather on U.S. economic activity. *Econ. Perspect.*, **39** (1Q), 1–20. [Available online at https://chicagofed.org/publications/economic-perspectives/index.]

Boldin, M., and J. H. Wright, 2015: Weather-adjusting employment data. Working Paper No.15-05, Federal Reserve Bank of Philadelphia, 24 pp. [Available online at www.philadelphiafed.org/research-and-data/publications/working-papers/2015/wp15-05.pdf.]

Christidis, N., P. A. Stott, and A. W. Ciavarella, 2014: The effect of climate change on the cold spring of 2013 in the United Kingdom [in "Explaining Extreme Events of 2013 from a Climate Perspective"]. *Bull. Amer. Meteor. Soc.*, **95** (9), S79–S82.

Frei, A., D. A. Robinson, and M. G. Hughes, 1999: North American snow extent: 1900–1994. *Int. J. Climatol.*, **19**, 1517–1534.

Hawkins, E., and R. Sutton, 2009: The potential to narrow uncertainty in regional climate predictions. *Bull. Amer. Meteor. Soc.*, **90**, 1095–1107.

Hughes, M. G., and D. A. Robinson, 1996: Historical snow cover variability in the Great Plains region of the USA: 1910 through to 1993. *Int. J. Climatol.*, **16**, 1005–1018.

IPCC, 2013: Summary for policymakers. *Climate Change 2013: The Physical Science Basis*, T. F. Stocker et al., Eds., Cambridge University Press, 3–29.

Kay, J. E., and Coauthors, 2014: The Community Earth System Model (CESM) large ensemble project: A community resource for studying climate change in the presence of internal climate variability. *Bull. Amer. Meteor. Soc*., doi:10.1175/BAMS-D-13-00255.1, in press.

Lawrimore, J. J., M. J. Menne, B. E. Gleason, C. N. Williams, D. B. Wuertz, R. S. Vose, and J. Rennie, 2011: An overview of the Global Historical Climatology Network monthly mean temperature data set, Version 3. *J. Geophys. Res.,* **116**, D19121, doi:10.1029/2011JD016187.

Leathers, D. J., and D. A. Robinson, 1993: The association between extremes in North American snow cover extent and United States temperatures. *J. Climate*, **6**, 1345–1355.

Namias, J., 1985: Some empirical evidence for the influence of snow cover on temperature and precipitation. *Mon. Wea. Rev.*, **113**, 1542–1553.

Perlwitz, J., M. Hoerling, J. Eischeid, T. Xu, and A. Kumar, 2009: A strong bout of natural cooling in 2008. *Geophys. Res. Lett*., **36**, L23706, doi:10.1029/2009GL041188.

Peterson, T. C., and Coauthors, 2013: Monitoring and understanding changes in heat waves, cold waves, floods and droughts in the United States: State of knowledge. *Bull. Amer. Meteor. Soc*., **94**, 821–834, doi:10.1175/BAMS-D-12-00066.1.

Robinson, D. A., and K. F. Dewey, 1990: Recent secular variations in the extent of Northern Hemisphere snow cover. *Geophys. Res. Lett*., **17**, 1557–1560.

Taylor, K. E., R. J. Stouffer, and G. A. Meehl, 2012: an overview of CMIP5 and the experiment design. *Bull. Amer. Meteor. Soc*., **93**, 485–498, doi:10.1175/BAMS-D-11-00094.1.

van Oldenborgh, G. J., R. Haarsma, H. de Vries, and M. R. Allen, 2015: Cold extremes in North America vs. mild weather in Europe: The winter 2013–14 in the context of a warming world. *Bull. Amer. Meteor. Soc*., **96**, 707–714, doi:10.1175/BAMS-D-14-00036.1.

Wagner, A. J., 1973: The influence of average snow depth on monthly mean temperature anomaly. *Mon. Wea. Rev.*, **101**, 624–626.

4. WAS THE COLD EASTERN US WINTER OF 2014 DUE TO INCREASED VARIABILITY?

Laurie Trenary, Timothy DelSole, Michael K. Tippett, and Brian Doty

The near-record number of extremely cold days during winter 2014 in the eastern United States cannot be attributed to trends or variability changes. Daily temperature variability is actually decreasing, in contrast to CMIP5 simulations and projections.

Introduction. The eastern United States endured persistent below normal temperatures during the winter of 2014 (Fig. 4.1a), with many states experiencing monthly temperatures ranked amongst the 15th coldest on record (NOAA National Climatic Data Center 2014). Insured U.S. losses from weather damage during winter 2014 (2.4 billion U.S. dollars) were more than double the annual average of the previous decade (Bevere et al. 2015).

The intensity and duration of cold temperatures during winter 2014 sparked considerable discussion about whether the behavior of cold air outbreaks was changing. The prevailing view among climate scientists is that the earth is warming primarily due to emissions of greenhouse gases from fossil fuel burning. Such warming will tend to make frigid winters less likely (Bindoff et al. 2013). On the other hand, extreme cold air outbreaks in the United States are associated with southward meandering of the midlatitude jet stream, which has a complex behavior. To the extent that jet stream variability arises from fluid dynamical instabilities associated with the pole-to-equator temperature difference (Holton 2004), such variability might be expected to decrease as the Arctic warms faster than other parts of the earth. In contrast, Francis and Vavrus (2012) argue that this reduced gradient leads to a slower and more north–south meandering jet stream. They conjecture that continued global warming will increase the "waviness" of the jet stream and lead to more frequent weather extremes.

Apparent trends in the latitudinal extent of atmospheric waves, which Francis and Vavrus (2012) used to support their hypothesis, have been found to be sensitive to methodology (Barnes 2013; Screen and Simmonds 2013). Moreover, van Oldenborgh et al. (2014) analyzed North American cold extremes of both seasonal and daily minimum temperature during the winter of 2014 and concluded that the cold temperatures were not unusual relative to the past, although extreme cold events are occurring less frequently. Finally, numerous studies report a reduction in daily cold temperature extremes over the United States in response to global warming (Hartmann et al. 2013).

Global warming is often conceptualized as a shift of the probability distribution function (PDF) toward warmer temperatures. The width of the PDF characterizes the variability of those temperatures. If cold extremes are becoming more likely in response to climate change, as suggested by Francis and Vavrus (2012), and warm extremes are becoming more likely, as many studies have shown, then the width of the PDF should increase. There is no strong indication of a systematic change in the width of the PDF for monthly mean U.S. temperatures (Kunkel et al. 2015). A goal of this study is to check this implicit consequence of the Francis and Vavrus hypothesis for daily winter temperatures. We also document changes in daily winter temperatures along the U.S. east coast and compare them to climate model simulations. The eastern United States is chosen for study because of its high vulnerability to extreme winter weather [60% of the reported loses from the 2014 winter came from states along the U.S. eastern seaboard (NOAA National Centers for Environmental Information 2014)]

AFFILIATIONS: Trenary, DelSole, and Doty—George Mason University and Center for Ocean-Land-Atmosphere Studies, Fairfax, Virginia; Tippett—Department of Applied Physics and Applied Mathematics, Columbia University, New York, New York, and Center of Excellence for Climate Change Research, Department of Meteorology, King Abdulaziz University, Jeddah, Saudi Arabia

DOI:10.1175/BAMS-D-15-00138.1

A supplement to this article is available online (10.1175/BAMS-D-15-00138.2)

and because of its dense population [nearly a third of the U.S. population (U.S. Census 2010)].

Data and Methods. Daily temperature is estimated as the average of the maximum and minimum surface temperatures from the United States Historical Climatology Network (Menne et al. 2015), for the days 1 January–31 March between 1950 and 2014. Anomalies are found for each station by removing a third order polynomial fit to the January–March seasonal cycle. Regional estimates for the mid-Atlantic (Fig. 4.1a, states outlined in black), the north Atlantic (Fig. 4.1a, states outlined in green), and the south Atlantic (Fig. 4.1a, states outlined in red), are found by averaging station anomalies in each region.

We also analyze climate model simulations from phase 5 of the Coupled Model Intercomparison Project (CMIP5; Taylor et al. 2012). We use historical runs between 1950 and 2005, which contain both anthropogenic and natural forcing, and pre-industrial control runs, whose forcings do not change. Twelve models with daily surface temperature data and with at least 100 years of daily data from a pre-industrial control run were selected (see Supplemental Table S4.1 for model list). The historical runs were extended using the Representative Concentration Pathways (RCP) 8.5, since the projected greenhouse gas forcing smoothly transitions from the historic runs (Taylor et al. 2012) and is most consistent with present values relative to other RCPs (Peters et al. 2013). To allow for comparison with observations, time series of daily land temperature for January–March were computed from averages in the mid-Atlantic (35°–40°N, 83°–72°W), north Atlantic (40°–48°N, 83°–65°W), and south Atlantic (25°–35°N, 89°–75°W).

Two measures of variability were used: sample standard deviation and the difference between the 95th and 5th percentiles. Confidence intervals for trends in standard deviation were assessed using ordinary least squares and the bias-corrected, accelerated bootstrap (Efron and Tibshirani 1994). The resulting intervals were practically the same so only those produced by ordinary least squares are shown.

Results. The minimum of average daily temperature for each winter in the north (green), mid- (black), and south (red) Atlantic states is shown in Fig. 4.1b. The figure shows that the magnitudes of minimum temperatures along the eastern seaboard during winter 2014 (Fig. 4.1b, green, black, and red dots) were not unusual. The entire eastern seaboard has experienced much colder winters in each of the six preceding decades.

The frequency of extremely cold winter days for the three Atlantic regions is shown in Fig. 4.1c. We define extremely cold days as ones in which the average daily temperature falls below the 10th percentile of winter daily temperatures (relative to 1961–90), for each region respectively. In 2014, the north Atlantic endured the greatest number of extremely cold days on record. In the mid-Atlantic, the frequency of extremely cold days was the second largest since 1978. As a result, the seasonal average of daily temperatures in both the north and mid-Atlantic states yielded the second most frequently cold season since 1978 for each region (not shown).

Lastly, the standard deviation of daily winter temperature anomalies for the mid-Atlantic is shown in Fig. 4.1d. Our analysis focuses on only one region, since variations in average daily winter temperatures are consistent along the eastern seaboard (not shown). The winter temperature variability in 2014 is well within the range of previous observed values. Autocorrelation in daily time series may mask changes in variability. A second order autoregressive model is fit to January–March daily temperature, and its residuals are called "whitened anomalies". No significant or systematic changes in autoregressive model parameters were detected, indicating that there are no detectable changes in the persistence of cold winter temperatures. However, the standard deviation of the whitened anomalies, shown as the dashed blue line in Fig. 4.1d, decreases at a rate of ~0.72°C century^{-1} over the 1950–2014 period. Thus, in contrast to Francis and Vavrus (2012), we find that daily winter temperatures along the U.S. eastern seaboard are becoming less variable. Measuring variability as the difference between the 95th and 5th percentiles of the whitened temperature anomalies confirms that the range of winter temperature fluctuations is decreasing (see red curve in Fig. 4.1d).

Whether the above change in variability is natural or human-forced cannot be ascertained from purely observational analysis. Accordingly, we compute corresponding trends from the CMIP5 climate simulations. The trend in standard deviation of whitened daily winter temperature for three eastern seaboard regions, along with the 95% confidence intervals, are shown in Fig. 4.2 for historic runs (red) and observations (blue) between 1950 and 2014, and pre-industrial controls (black). The observed trend is negative and significantly different from zero in all three regions. In nearly all model projections, there is no significant

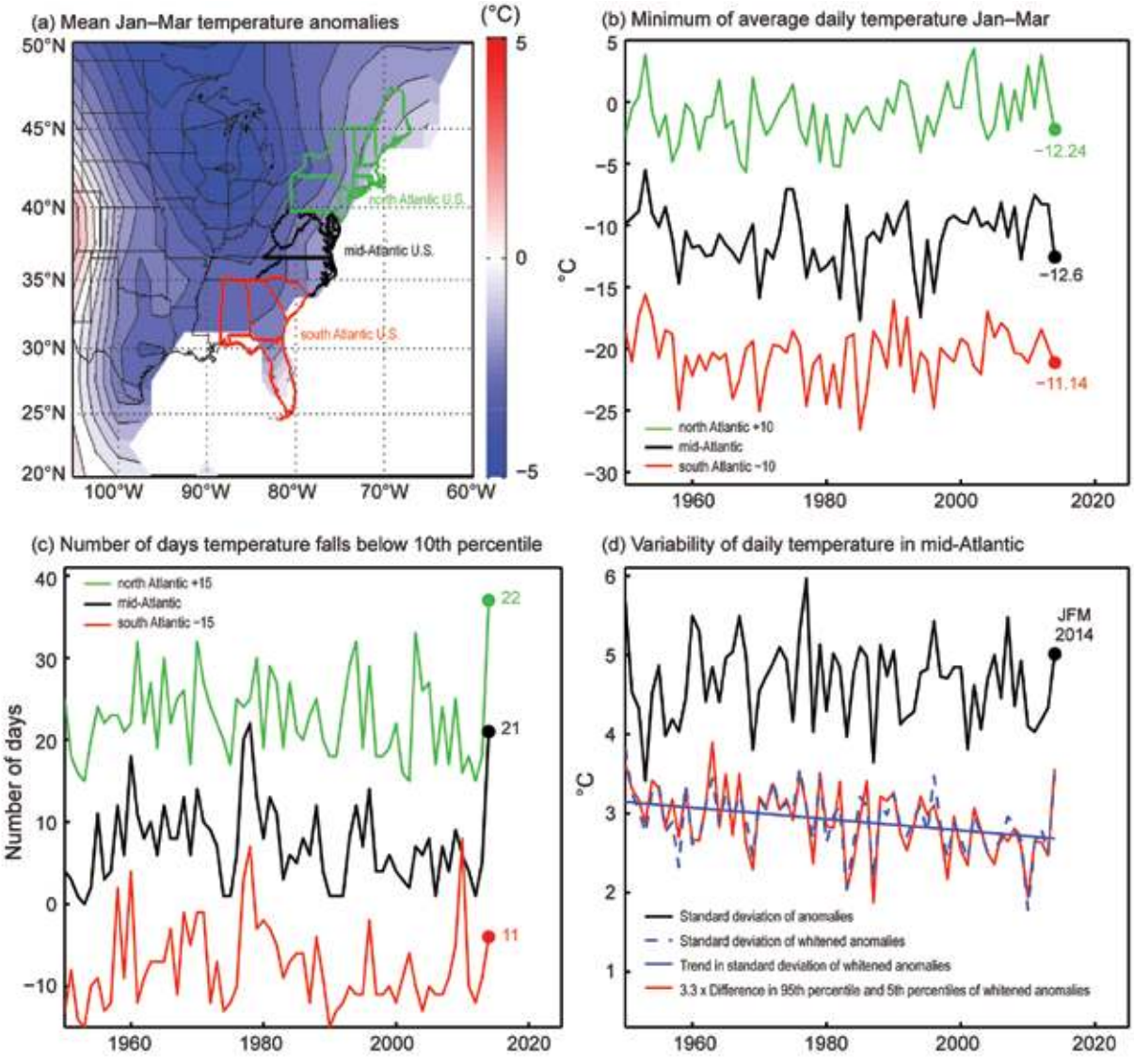

Fig. 4.1. (a) Mean temperature anomaly (°C) from NCEP/NCAR reanalysis for Jan–Mar 2014 (anomalies are computed point wise relative to the Jan–Mar seasonal cycle between 1950 and 2014, which is estimated as a 3rd order polynomial). The different colored states indicate the U.S. regions analyzed in the rest of the paper. All time series analysis is based on station data. (b) Minimum in Jan–Mar average daily temperature anomaly (°C) in the north (green), mid- (black), and south (red) Atlantic regions for the years 1950–2014. The north (south) Atlantic time series have been shifted by +10 (−10). The dot marks the year 2014 and the associated text reports the observed minimum in average daily temperature for that year. (c) Number of days in which the daily temperatures during Jan–Mar fall below the 10th percentile in the north (green), mid- (black), and south (red) Atlantic regions. The north (south) time series have been shifted by +15 (−15). The dot marks the year 2014 and the associated text reports the observed number of days with temperatures below the 10th percentile. (d) Standard deviation of Jan–Mar daily temperature anomalies (black), and the standard deviation of daily whitened temperature anomalies (blue dash) in the mid-Atlantic region. Whitened anomalies are computed as the residual of a second order autoregressive model fit to the Jan–Mar temperature anomalies. The solid blue line shows the least squares line fit to the standard deviation of the whitened anomalies over 1950–2014. The red curve shows the difference between the 95th and 5th percentiles of Jan–Mar whitened daily temperature anomalies, multiplied by 3.3 to convert to standard deviation for a Gaussian distribution.

negative trend. This does not mean that models and observations are inconsistent. All model estimates in mid-/north Atlantic states and half of those from the south Atlantic are consistent with observations, as indicated by the overlap in blue and red confidence intervals. Given the consistency between pre-

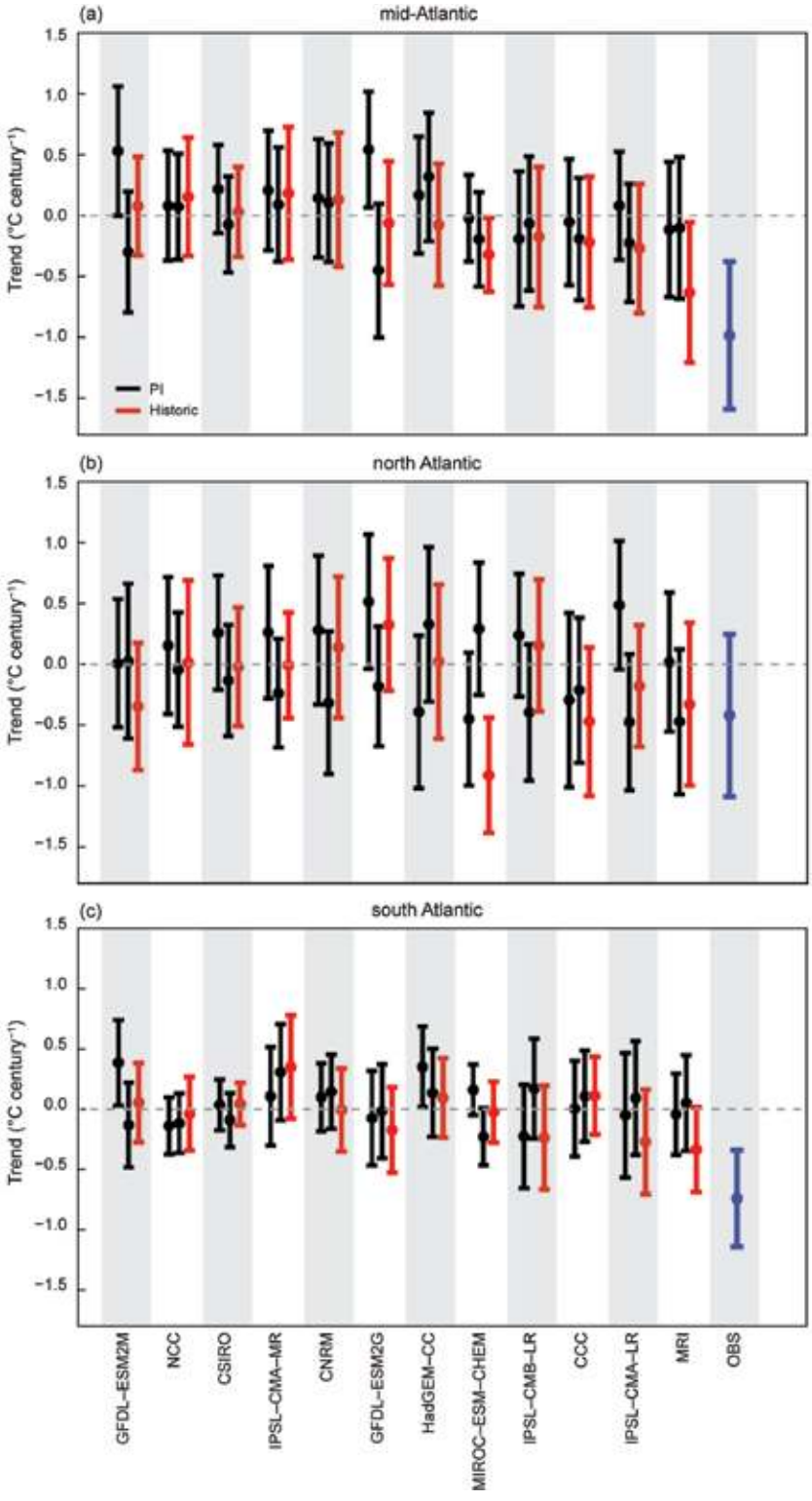

Fig. 4.2. Trends in the standard deviation of Jan–Mar whitened daily temperature anomalies (°C century^{-1}) for observations (blue dots) and historical runs (red) over the period 1950–2014, and the first and last 65 years for CMIP5 pre-industrial control runs (black dots), for three different U.S. regions: (a) the mid-Atlantic , (b) north Atlantic , and (c) the south Atlantic. The bars indicate the 95% confidence intervals.

industrial controls and historic runs across a majority of models (note overlap in the black and red confidence intervals), we conclude that the models do not attribute a significant change in daily winter temperature variability to anthropogenic forcing.

Summary. The north and mid-Atlantic states endured a record number of days with below average temperatures during January–March 2014. In contrast, the variability of winter daily temperature, and therefore of the range of realized temperature, has been decreasing for the past six decades. The decrease in variance is a plausible consequence of polar amplification of global warming, since a decrease in the pole-to-equator temperature gradient reduces the strength of fluid dynamical instabilities (Schneider et al. 2014; Screen 2014). Model simulations suggest that human-induced forcing does not significantly influence the range of daily winter temperatures (with noted exceptions). In any case, we find no evidence that daily winter temperatures are becoming more variable in the eastern United States or that such increased variability could explain the cold winter of 2014.

ACKNOWLEDGEMENTS. This work was sponsored by the National Science Foundation (ATM1338427), National Aeronautics and Space Administration (NNX14AM19G), National Oceanic and Atmospheric Administration (NA09OAR4310058), and Department of Energy (ER65095). We acknowledge the World Climate Research Programme's

Working Group on Coupled Modelling, which is responsible for CMIP.

REFERENCES

Barnes, E. A., 2013: Revisiting the evidence linking arctic amplification to extreme weather in midlatitudes. *Geophys. Res. Lett.*, **40**, 4734–4739, doi:10.1002/grl.50880.

Bevere, L., K. Orwig, and R. Sharan, 2015: Natural catastrophes and man-made disasters in 2014: Convective and winter storms generate most losses. Swiss Re Sigma No. 2, 47 pp. [Available online at www.actuarialpost.co.uk/downloads/cat_1/sigma2_2015_en.pdf.]

Bindoff, N. L., and Coauthors, 2013: Detection and attribution of climate change: From global to regional. *Climate Change 2013: The Physical Science Basis*, T. Stocker et al., Eds., Cambridge University Press, 867–952.

Efron, B., and R. J. Tibshirani, 1994: *An Introduction to the Bootstrap*. Chapman and Hall, 456 pp.

Francis, J. A., and S. J. Vavrus, 2012: Evidence linking arctic amplification to extreme weather in mid-latitudes. *Geophys. Res. Lett.*, **39**, L06801, doi:10.1029/2012GL051000.

Hartmann, D. L., and Coauthors, 2013: Observations: Atmosphere and surface. *Climate Change 2013: The Physical Science Basis*, T. F. Stocker et al., Eds., Cambridge University Press, 159–254.

Holton, J. R., 2004: *An Introduction to Dynamic Meteorology*. International Geophysics Series, Vol. 88, 4th ed., Academic Press, 535 pp.

Kunkel, K. E., R. S. Vose, L. E. Stevens, and R. W. Knight, 2015: Is the monthly temperature climate of the United States becoming more extreme? *Geophys. Res. Lett.*, **42**, 629–636, doi:10.1002/2014GL062035.

Menne, M. J., C. N. Williams, and R. S. Vose, 2015: United States Historical Climatology Network Daily temperature, precipitation, and snow data (USHCN–Daily). Carbon Dioxide Information Analysis Center, digital media, http://cdiac.ornl.gov/epubs/ndp/ushcn/access.html.

NOAA National Centers for Environmental Information, 2014: Billion-dollar weather and climate disasters: Table of events. [Available online at www.ncdc.noaa.gov/billions/events.]

NOAA National Climatic Data Center, 2014: State of the climate in 2014: National overview for March 2014. [Available online at www.ncdc.noaa.gov/sotc/national/2014/3.]

Peters, G. P., and Coauthors, 2013: The challenge to keep global warming below 2°C. *Nat. Climate Change*, **3**, 4–6, doi:10.1038/nclimate1783.

Schneider T., T. Bischoff, and H. Płotka, 2015: Physics of changes in synoptic midlatitude temperature variability. *J. Climate*, **28**, 2312–2331, doi:10.1175/JCLI-D-14-00632.1.

Screen, J. A., 2014: Arctic amplification decreases temperature variance in north mid- to high-latitudes. *Nat. Climate Change*, **4**, 577–582, doi:10.1038/nclimate2268.

——, ——, and I. Simmonds, 2013: Exploring links between Arctic amplification and mid- latitude weather. *Geophys. Res. Lett.*, **40**, 959–964, doi:10.1002/grl.50174.

Taylor, K. E., R. J. Stouffer, and G. A. Meehl, 2012: An overview of CMIP5 and the experiment design. *Bull. Amer. Meteor. Soc.*, **93**, 485–498, doi:10.1175/BAMS-D-11-00094.1.

U.S. Census, 2010: United State Census 2010: Interactive population map. [Available online at www.census.gov/2010census/popmap/.]

van Oldenborgh, G. J., R. Haarsma, H. de Vries, and M. R. Allen, 2014: Cold extremes in North America vs. mild weather in Europe: The winter 2013/2014 in the context of a warming world. *Bull. Amer. Meteor. Soc.*, **96**, 707–714, doi:10.1175/BAMS-D-14-00036.1.

5. THE 2014 EXTREME FLOOD ON THE SOUTHEASTERN CANADIAN PRAIRIES

Kit Szeto, Julian Brimelow, Peter Gysbers, and Ronald Stewart

The collective effects of anthropogenic climate change and artificial pond drainage may have played an important role in producing the extreme flood that occurred during early summer 2014 on the southeastern Canadian Prairies.

Introduction. Being located at the confluence of the Assiniboine and the Red Rivers, the southeastern Canadian Prairies is one of the most flood-prone regions in Canada. Although spring floods are a fact of life for many residents of the Assiniboine River Basin (ARB, Fig. 5.1a), the flood that occurred during July 2014 was exceptional in terms of its magnitude and impacts. Preliminary assessments of damages from the flooding are estimated at $1 billion (Canadian dollars) for the agricultural sector alone, with other damages yet to be assessed (Environment Canada 2015). In addition, this extreme event occurred only three years after the record-breaking flood of 2011 (Brimelow et al. 2015). This short span between the two extreme events has raised concerns as to whether or not climate and land use changes in the area (such as pond drainage for agricultural purposes) have increased the potential for extreme floods in the ARB; and this is the question we attempt to address in this paper.

The 2014 extreme flood. Snow accumulation and melt critically affect runoff and flooding in the region (Fang and Pomeroy 2008). Initial conditions in 2014 were not favorable for major flooding over the ARB. The precipitation in the preceding fall and winter, and thus snow accumulations, were all close to normal values. However, developments in April increased concerns for potential flooding. First, based on the 55-year Japanese Reanalysis (JRA-55, Kobayashi et al. 2015)—the dataset used for the analysis in this section unless noted otherwise—the basin experienced a very cool spring in 2014 which delayed the onset of snowmelt, and the spring melt was not complete until late April in many areas. Consequently, the soils were unable to dry out before the region experienced one of the stormiest and wettest May–June periods on record (Fig. 5.1a).

Specifically, during May–June, 12 synoptic disturbances affected the area, double the 1960–2013 average. This resulted in 35 days with a basin-average daily accumulation greater than 1 mm and 33 days with consecutive rain (compared to an average of 14). This suggests that, in addition to more systems affecting the region, some of them were likely moving slower than usual.

Widespread flooding started in early July after a slow-moving major rainstorm brought record rainfall to many locations in the region during the last four days of June. The seasonal volume of water measured near the outlet of the ARB between June and August (Fig. 5.1b) was the second highest on record (after 2011), with some gauges observing record monthly discharges.

The large-scale atmospheric conditions that spawned the frequent and slow-moving synoptic disturbances in June 2014, and which produced the exceptional rainfall in the ARB, are shown in Figs. 5.1c–e. Most of northern Canada experienced significantly above normal surface temperatures, with the largest anomalies in the vicinity of Hudson Bay (Fig. 5.1c). Consequently, the mean north–south 1000–500 hPa thickness gradient was reduced, and this resulted in a much weaker than average zonal flow at 500 hPa (Fig. 5.1e). The associated upper-level circulation anomalies (Fig. 5.1d) were characterized by a stalled trough over the Great Plains and a blocking ridge over northeastern Canada and the Labrador Sea. This configuration favored the persistent tracking of surface lows (and attendant precipitation) in the vicinity of the ARB. In addition, the weak zonal flow could have been partly responsible for the slow propagation of some of these systems.

Climate change in the ARB. Results from lagged correlations between precipitation and streamflow data (not shown) suggest that May–June (MJ) rainfall ex-

AFFILIATIONS: Szeto and Gysbers—Environment Canada, Downsview, Ontario, Canada; Brimelow—Environment Canada, Edmonton, Alberta, Canada; Stewart—University of Manitoba, Winnipeg, Manitoba, Canada

DOI: 10.1175/BAMS-D-15-00110

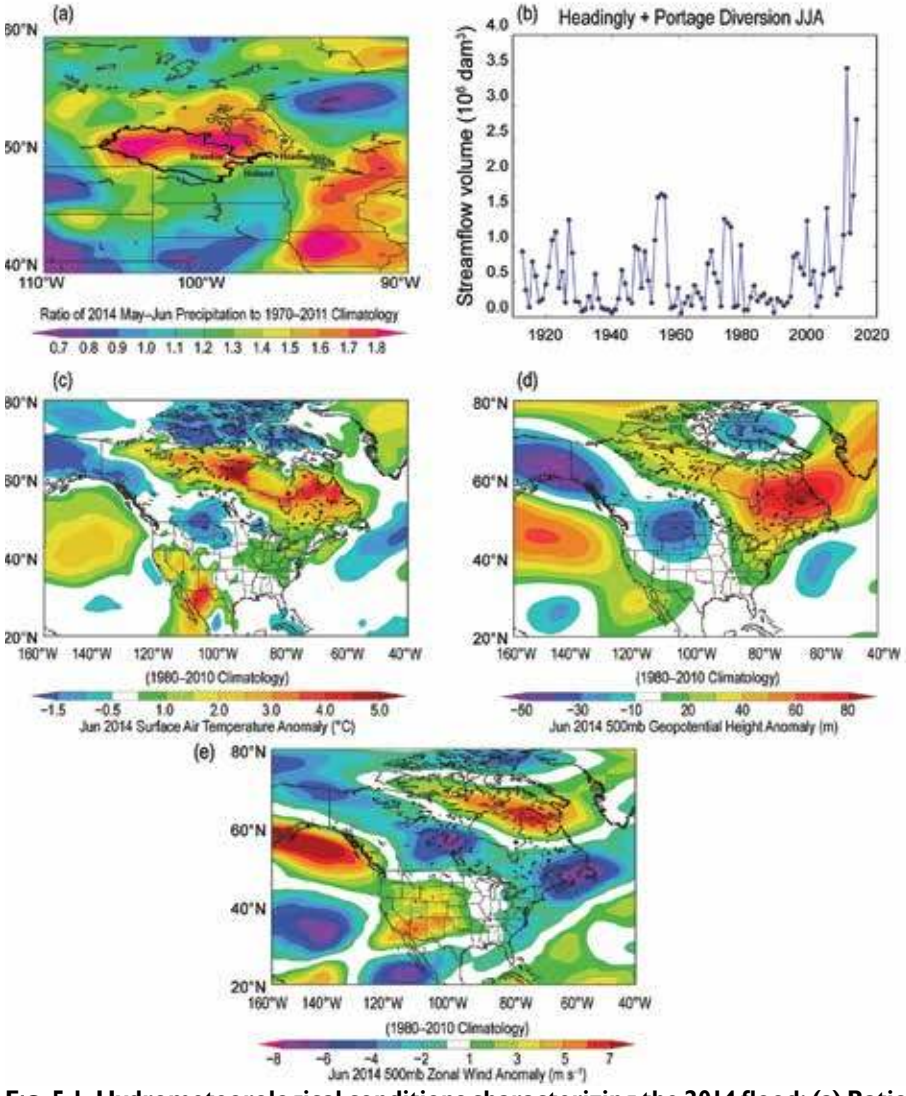

Fig. 5.1. Hydrometeorological conditions characterizing the 2014 flood: (a) Ratio of JRA-55 2014 MJ rainfall to 1970–2011 average. Also shown is the boundary for the ARB. (b) Time series of Headingley plus Portage Diversion Jun–August streamflow volume constructed from hydrometric data archived at Water Survey of Canada (http://wateroffice.ec.gc.ca/index_e.html). (c)–(e) Anomalous large-scale conditions during Jun 2014 from JRA-55: (c) surface air temperatures, (d) geopotential height at 500 hPa, and (e) zonal wind at 500 hPa.

erts the greatest impact on early summer streamflow and floods in the ARB. The discussion will thus be focused on the MJ period, which is also the period that has exhibited the most significant increase in rainfall over the past five decades (Fig. 5.2a). In addition to the mean rainfall, both the number of consecutive rain days and the rain amounts from extreme rainstorms have increased significantly since 1960 (Fig. 5.2b). The former result agrees with the Prairie-wide changes in precipitation characteristics examined in Shook and Pomeroy (2012). Also of note is that these changes were most significant after the mid-1990s.

Streamflow responses to the increasing MJ rainfall are evident in the gauge measurements. For example, before 1994 there were no years going back to 1974 at Brandon with above-average streamflows after June 1. In contrast, from 1994 onward there were 11 years when this occurred, including some years with the peak annual flow measured after June 1; this is at complete odds with the spring runoff maximum that is typical for this basin.

The observed increase in MJ rainfall in the ARB since the mid-1990s was captured by the Coupled Model Intercomparison Project Phase 5 (CMIP5) models in historical simulations with anthropogenic forcing (Fig. 5.2c). Although the relative increases were smaller (<50%) than observed (Fig. 5.2a), the increasing trend was projected to continue in the coming years with magnitudes that increase systematically from runs with low- (RCP2.6) to high-impact (RCP8.5) emissions scenarios (only RCP4.5 results are shown in Fig. 5.2c). These results suggest that anthropogenic forcing may be responsible for at least part of the observed recent increase in MJ rainfall.

Composite atmospheric conditions for the six wettest MJ periods between 1995 and 2013 were constructed to identify the large-scale features which were associated with the marked increase in MJ rainfall since the mid-1990s, and they were found to be remarkably similar to those observed in 2014. The upper-level ridging (troughing) over northeastern (central-western) North America (not shown) was associated with marked low-level warm (cool) anomalies over the respective regions of the continent (Fig. 5.2d).

Such circulation patterns also characterized the 2011 flood (Brimelow et al. 2015). These data suggest that the same large-scale forcings that preceded the extreme flood in 2014 were likely also related to the significant changes in observed precipitation characteristics in the last 20 years. The linkage between MJ ARB rainfall and atmospheric conditions over northeastern Canada is also evident in the significant (at the 98% level) contemporaneous correlations (r ~ 0.35) between the ARB MJ rainfall and 500 hPa height field over northeastern Canada between 1960 and 2013 as well as the concurrent significant increases in these variables since the mid-1990s (Figs. 5.2a, b, e).

The apparent linkage between observed changes in the MJ ARB rainfall and recent changes in northeast Canada could reflect the regional hydroclimate response to enhanced anthropogenic warming in polar regions (e.g., Francis and Vavrus 2012); and this could probably account for at least part of the increasing trend exhibited in the CMIP5 results (Fig. 5.2c). Further analysis, however, suggests that the linkage might be rooted in a common forcing originating in the tropical Pacific. Analysis shows that MJ ARB rainfall and the concurrent sea surface temperature (SST) over the eastern tropical Pacific (~130°–170°W, 10°–20°N) are negatively and even more significantly correlated (r < −0.5) than correlations with conditions in northeastern Canada. Further, Fig. 5.2f reveals a Rossby wave train pattern emanating from the same oceanic region, with action centers that correspond closely in space with the upper-level lows and highs over North America in either the composite analysis or the 2014 event (Fig. 5.1d). These results are likely related to those presented in Ding et al. (2014), who

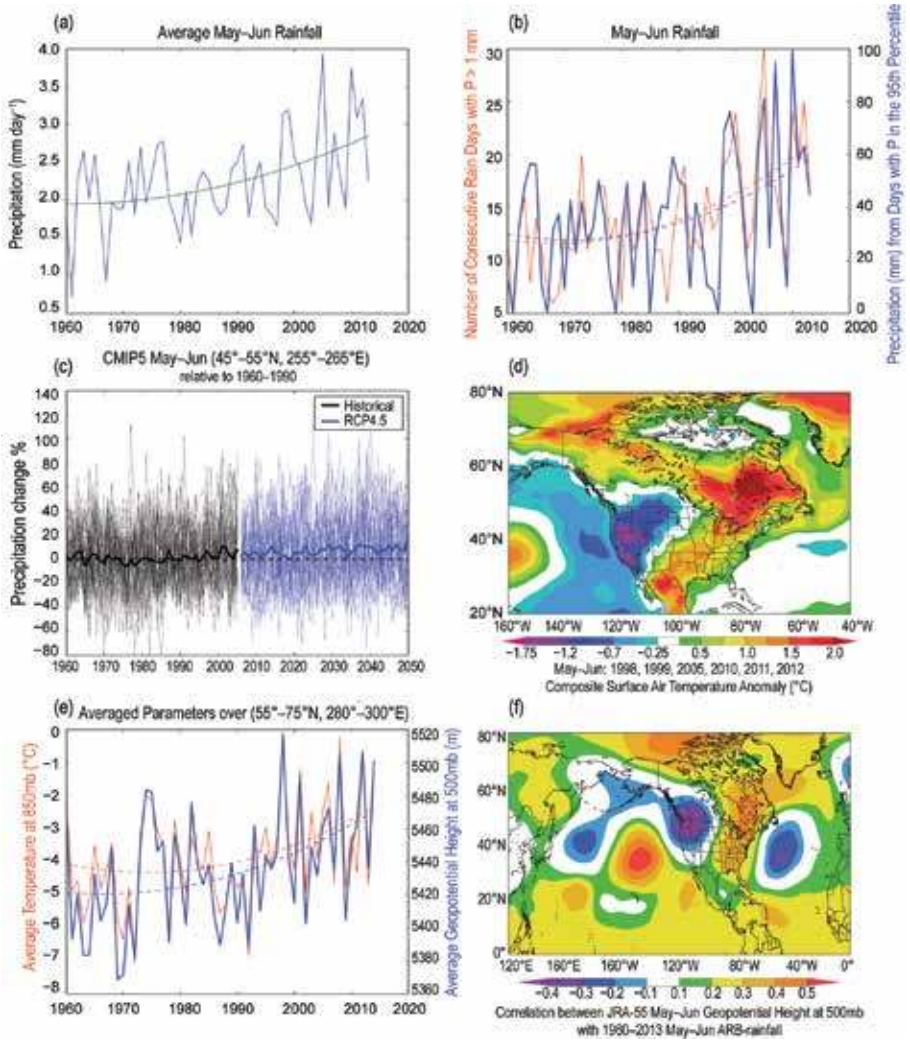

Fig. 5.2. (a) 1960–2013 time series of basin-average MJ precipitation computed from Environment Canada's CANGRD gridded monthly precipitation observation (www.ec.gc.ca/adsc-cmda/default.asp?lang=En&n=D48C5C94-1). (b) Number of consecutive days in MJ with rainfall > 1 mm (red) and MJ rainfall from days with rain rate in the 95th percentile (blue) computed from the ANUSPLIN gridded daily precipitation observation (Hutchinson et al. 2009). Observed precipitation is used to examine changes in rainfall characteristics because the precipitation in JRA-55 was not corrected with observations. (c) Time series of MJ rainfall change with respect to 1960–90 over an area encompassing the ARB from the 42-model ensemble CMIP5 AR5 RCP4.5 projections (Taylor et al. 2012) with the thick (thin) curves showing the ensemble mean (individual model spreads) for historical (black) and future (blue) periods. (d) Surface air temperature anomalies composited for the six wettest MJ within 1995–2013. (e) Time series of average MJ temperatures at 850 hPa (red) and geopotential height at 500 hPa (GZ500; blue) over NE Canada. (f) Correlation map between MJ ARB-rainfall and GZ500. Also shown in panels (a), (b), and (e) are quadratic fits to the times series.

calculated that up to half of the recent rapid warming (since the mid-1990s) over northeastern Canada (and associated upper-level circulation anomalies) may be attributed to anomalous Rossby wave activity induced by marked decreases (increases) in SSTs over eastern (western) tropical Pacific. The results presented herein suggest that the anomalous Rossby wave activity has also likely played a critical role in the recent increase in MJ ARB rainfall. It remains an open question as to whether or not the recent SST trends over tropical Pacific are related to anthropogenic effects.

Impacts of pond drainage on runoff. Historically, more than half of the total area of the ARB was covered by depressions formed during the Pleistocene epoch (Pomeroy et al. 2007). The depressions tend to form ponds or small lakes from meltwater and rainfall, and they do not always contribute to the drainage network. However, under extremely wet conditions, temporary drainage networks can connect outflow from the ponds to streams (van der Kamp and Hayashi 2009).

It has long been a concern amongst hydrologists that the conversions of ponds to agriculture and other developments via artificial drainage could have great impacts on runoff on the Prairies. Although updated systematic assessments of such conversions for the whole ARB are not yet available, earlier studies showed that at least two-thirds of the ponded area in the central Prairies has been eliminated (Environment Canada 1996). A recent study carried out at the Smith Creek watershed within the ARB (Pomeroy et al. 2014) found that more than half of the ponded area was drained between 1958 and 2008. Their simulations estimated that the annual streamflow volume for the 2011 flood would have been reduced by 29% had the ponds been restored to their 1958 levels. These results clearly illustrate the important buffering function of ponds in regulating runoff and flooding in the ARB.

One can use the bulk basin-scale water balance approach to estimate effects of pond drainage on basin-scale streamflow response to variations in atmospheric conditions. Considering the four highest flow years within two sequential 21-year periods between 1970 and 2011, the 12-month (July–June) average difference between Environment Canada's CANGRD precipitation and JRA-55 evapotranspiration ($P - E$) has increased by about 15%, whereas the corresponding January–July accumulated measured discharge has increased by a disproportionate 45%. These basin-scale estimates are consistent with those from Pomeroy et al. (2014) for the Smith Creek watershed.

Conclusions. Results from this study indicate that anthropogenic forcing may have played a role in causing the significant increase in MJ rainfall in the ARB, while the extensive removal of ponds could have amplified the runoff response to the changing climate to substantially enhance the potential for extreme floods such as those in 2011 and 2014. The increasing MJ rainfall trend is projected to continue, and the short span between the 2011 and 2014 extreme floods could be a worrying signal that recurrent devastating spring floods may be the new normal for residents in the ARB. Results from this and other studies suggest that major pond restoration in the ARB could be a viable mitigation/adaptation measure to minimize impacts of climate change in the region.

ACKNOWLEDGMENTS: We thank the two anonymous reviewers and Drs. Stephanie Herring, Monirul Mirza and Xuebin Zhang for helpful comments. This research is supported by Environment Canada and the Changing Cold Regions Network (CCRN) which is sponsored by the Natural Sciences and Engineering Research Council of Canada (NSERC).

REFERENCES

Brimelow, J., K. Szeto, B. Bonsal, J. Hanesiak, B. Kochtubajda, F. Evans, and R. E. Stewart, 2015: Hydrometeorological aspects of the 2011 Assiniboine River Basin flood. *J. Hydrometeor.*, **16**, 1250–1272, doi:10.1175/JHM-D-14-0033.1.

Ding, Q., J. M. Wallace, D. S. Battisti, E. J. Steig, A. J. E. Gallant, H. J. Kim, and L. Geng, 2014: Tropical forcing of the recent rapid Arctic warming in northeastern Canada and Greenland. *Nature*, **509**, 209–212, doi:10.1038/nature13260.

Environment Canada, 1996: *The State of Canada's Environment–1996*. Environment Canada, 808p

——, 2015: Canada's top ten weather stories for 2014. [Available online at http://ec.gc.ca/meteo-weather/default.asp?lang=En&n=C8D88613-1&offset=3&toc=show.]

Fang, X., and J. W. Pomeroy, 2008: Drought impacts on Canadian prairie wetland snow hydrology. *Hydrol. Process.*, **22**, 2858–2873.

Francis, J. A., and S. J. Vavrus, 2012: Evidence linking Arctic amplification to extreme weather in mid-latitudes. *Geophys. Res. Lett.*, **39**, L06801, doi:10.1029/2012GL051000.

Hutchinson, M. F., D. W. McKenney, K. Lawrence, J. H. Pedlar, R. F. Hopkinson, E. Milewska, and P. Papadopol, 2009: Development and testing of Canada-wide interpolated spatial models of daily minimum/maximum temperature and precipitation 1961–2003. *J. Appl. Meteor. Climatol.*, **4**, 725–741.

Kobayashi, S., and Coauthors, 2015: The JRA-55 reanalysis: General specifications and basic characteristics. *J. Meteor. Soc. Japan*, **93**, 5–48, doi:10.2151/jmsj.2015-001.

Pomeroy, J. W., D. de Boer, and L. W. Martz, 2007: Hydrology and water resources. *Saskatchewan: Geographic Perspectives*, B. Thraves et al., Eds., Canadian Plains Research Center, 63–80.

——, K. Shook, X. Fang, S. Dumanski, C. Westbrook, and T. Brown, 2014: Improving and testing the Prairie Hydrological Model at Smith Creek Research Basin. Centre for Hydrology Rep. 14, University of Saskatchewan, 102 pp. [Available online at www.usask.ca/hydrology/reports/CHRpt14_PHM_SCRB.pdf.]

Shook, K., and J. W. Pomeroy, 2012: Changes in the hydrological character of rainfall on the Canadian prairies. *Hydrol. Process.*, **26**, 1752–1766, doi:10.1002/hyp.9383.

Taylor, K. E., R. J. Stouffer, and G. A. Meehl, 2012: An overview of CMIP5 and the experiment design. *Bull. Amer. Meteor. Soc.*, **93**, 485–498, doi:10.1175/BAMS-D-11-00094.1.

van der Kamp, G., and M. Hayashi, 2009: Groundwater-wetland ecosystem interaction in the semiarid glaciated plains of North America. *Hydrogeol. J.*, **17**, 203–214.

6. EXTREME NORTH AMERICA WINTER STORM SEASON OF 2013/14: ROLES OF RADIATIVE FORCING AND THE GLOBAL WARMING HIATUS

Xiaosong Yang, G. A. Vecchi, T. L. Delworth, K. Paffendorf, R. Gudgel, L. Jia, Seth D. Underwood, and F. Zeng

The extreme 2013/14 winter storm season over much of North America was made more likely by the multiyear anomalous tropical Pacific winds associated with the recent global warming hiatus.

Introduction. Over the period December 2013–February 2014, there was a pronounced reduction of extratropical storm (ETS) activity over the North Pacific Ocean and the west coast of the United States of America (USA), and a substantial increase of ETS activity extending from central Canada down to the midwestern USA (Fig. 6.1a). The ETS activity was measured by the standard deviation of filtered 6-hourly sea level pressure in December–February (DJF) using a 24-hour-difference filter (Wallace et al. 1988). A number of large-scale climate factors could have influenced the probability of this extreme year. Natural climate variations, such as the El Niño–Southern Oscillation (ENSO) and the North Atlantic Oscillation (NAO) significantly influence ETS activity over North America (e.g., Yang et al. 2015; Grise et al. 2013). Our assessment of these factors indicates that they were not major players in the 2013/14 case (not shown). In addition, models suggest that radiative forcing changes can influence the surface storm tracks over North America, including a decrease under global warming (Chang et al. 2013). Furthermore, the recent multiyear drying over the western USA has been linked to the global warming hiatus (Delworth et al. 2015), suggesting the recent multiyear tropical Pacific wind changes that have been linked to the global warming hiatus (Kosaka and Xie 2013; England et al. 2014; Delworth et al. 2015) may impact winter ETS extremes over North America.

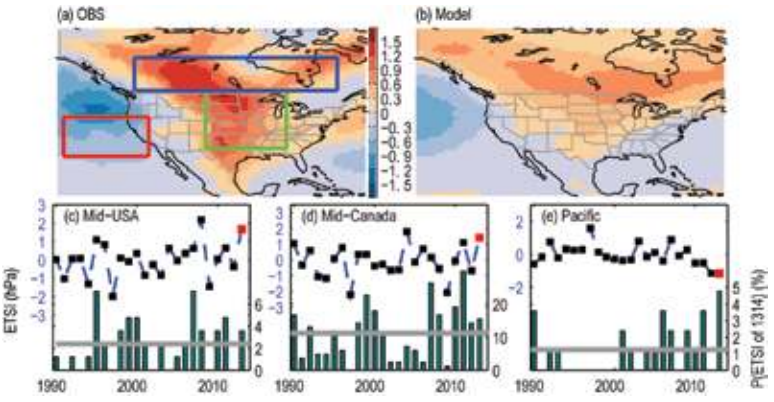

Fig. 6.1. (a) Observed (amplitudes scaled by a factor of 0.5 for displaying) and (b) forecasted ensemble mean ETS anomalies (relative to the 1980–2010 climatology) over North America during 2013/14. The ensemble mean is averaged over 84 members of all available hindcasts starting from 1 November 2013 and 1 December 2013. (c)–(e) Observed ETSI anomalies (dashed with square marker, left y-axis) and the occurrence probability (shaded bar, right y-axis) of the 2013/14 extreme ETSI estimated from the 84-member hindcasts at each year for the mid-USA [green box in (a)], the mid-Canada [blue box in (a)], and the Pacific coastal region [red box in (a)] during 1990–2013. The gray horizontal bar denotes the climatological occurrence probability of the 2013/14 extreme ETSI. Red marker highlights the 2013/14 ETSI.

The ensemble mean of initialized seasonal predictions with a high-resolution coupled model (see next section) predicted the large-scale spatial structure of the observed anomalous ETS in 2013/14 from about

AFFILIATIONS: Yang—NOAA/Geophysical Fluid Dynamics Laboratory, Princeton, New Jersey, and University Corporation for Atmospheric Research, Boulder, Colorado; Vecchi, Delworth, Paffendorf, and Jia—NOAA/Geophysical Fluid Dynamics Laboratory, Princeton, New Jersey, and Atmospheric and Oceanic Sciences Program, Princeton University, Princeton, New Jersey; Gudgel and Zeng—NOAA/Geophysical Fluid Dynamics Laboratory, Princeton, New Jersey; Underwood—Engility Corporation, Chantilly, Virginia

DOI:10.1175/BAMS-D-15-00133.1

A supplement to this article is available online (10.1175/BAMS-D-15-00133.2)

zero to one month ahead, but the predicted amplitudes are much weaker than the observations (Figs. 6.1a,b; Yang et al. 2015). Other studies show that the predicted amplitudes of surface air temperature in 2013/14 winter over North America are also weaker than the observations even given the sea surface temperature (Hartmann 2015). As discussed in Yang et al. (2015), even given climate initialization using the data assimilation, the 2013/14 winter ETS activity over North America was unlikely and thus had a large stochastic ("weather noise" and/or model errors) contribution. However, we can also see that initialization changes the probability of such extreme event from the background probability (Figs. 6.1c–e), indicating there was a climate driver that increased the probability of this extreme event in the 2013/14 season (and in the decade that preceded it). Thus, we here focus on a probabilistic assessment of the extreme ETS event and examine potential climate drivers for it, focusing on radiative forcing changes and the multiyear tropical Pacific wind changes that have been connected to the global warming hiatus. In this study, we use a suite of high-resolution climate model experiments to explore whether the extreme ETS activity over North America in the 2013/14 winter was made more likely by anthropogenic forcing or global warming hiatus.

Methodology. We used the Geophysical Fluid Dynamics Laboratory (GFDL) Forecast-Oriented Low Ocean Resolution model [FLOR; Vecchi et al. 2014; see online supplemental material (SM) Section 1] to conduct a suite of initialized and uninitialized numerical simulations. The observational ETSs were derived from the ERA-Interim reanalysis data during 1979–2014 (Dee et al. 2011). Throughout this study, we select three regions of interest in North America and the Pacific coastal ocean (Fig. 6.1a). Two regions with extremely active ETSs are the mid-USA and mid-Canada, while one region with extremely low ETS activities is California and its surrounding Pacific coastal ocean, hereafter Pacific coastal. The ETS index (ETSI) is formed by an average over each region. Following Murakami et al. (2015), we used a probabilistic rather than a deterministic approach. We will examine the probability of the ETSI of the three regions during DJF as a function of ETSI using the following equation:

$$P(x) = \frac{\textit{Number of years with ETSI} \geq x}{\textit{Total number of years}} \qquad (1)$$

where x is the ETSI value for a given region. For example, P(ETSI of 2013/14) represents the probability of occurrence of a year with ETSI values equal to or more than that of 2013/14 winter. Note that the Pacific coastal region is in the negative extreme category, so we compute 1–P(ETSI of 2013/14).

The interannual variations of the observed ETSI anomalies over the three regions are shown in Figs. 6.1c–e. The observed ETSI anomalies for 2013/14 are all in the extreme category with climatological empirical occurrence probability values of ~1.5%, ~3%, and ~10% for Pacific coastal, mid-USA, and mid-Canada, respectively. We first examined the retrospective seasonal forecasts made using FLOR for the period 1990–2014 (Vecchi et al. 2014; Jia et al. 2015). To estimate the extreme probability, we combined all available hindcasts of 0–1 month ahead to produce 84 samples for each predicted year (see SM Section 2a). The model predictions provide reliable estimates of the event probabilities (see SM Section 3).

Figures 6.1c–e show the time series of P(ETSI of 2013/14) over the three regions as predicted by FLOR. When compared with the observed ETSI, FLOR reasonably predicted the observed interannual variations, for example, higher (lower) probabilities in line with positive (negative) ETSI anomalies over the mid-USA (correlation coefficient 0.55) and Canada (correlation coefficient 0.47), and vice versa for the negative extreme over the Pacific coast (correlation coefficient −0.41), consistent with the examination of deterministic skill in ETS prediction by Yang et al. (2015). For the year 2013/14, FLOR predicted consistently higher occurrence probability than the climatological probability values over the three regions, indicating the initial conditions played roles in the extreme ETS activity of the 2013/14 winter event.

Effect of anthropogenic forcing and recent global warming hiatus. We generated multicentennial control climate simulations by prescribing radiative forcing and land-use conditions representative of the years 1860 and 1990, and 35-member ensemble simulations with prescribed time-varying historical and projected radiative forcings (see SM Sections 2b and 2c) from 1941 to 2040. The effect of anthropogenic forcing can be estimated by taking the difference of those simulations. Figures 6.2a–c show the extreme occurrence probabilities for the three regions respectively. The probabilities estimated from the 1860 and 1990 control experiments are not statistically distinguishable for any of the three regions (first column of Figs. 6.2a–c). There is no statistically significant change of the extreme occurrence probabilities over mid-USA during 1940–2040 (second column of Fig. 6.2a); the extreme occurrence probabilities over mid-Canada

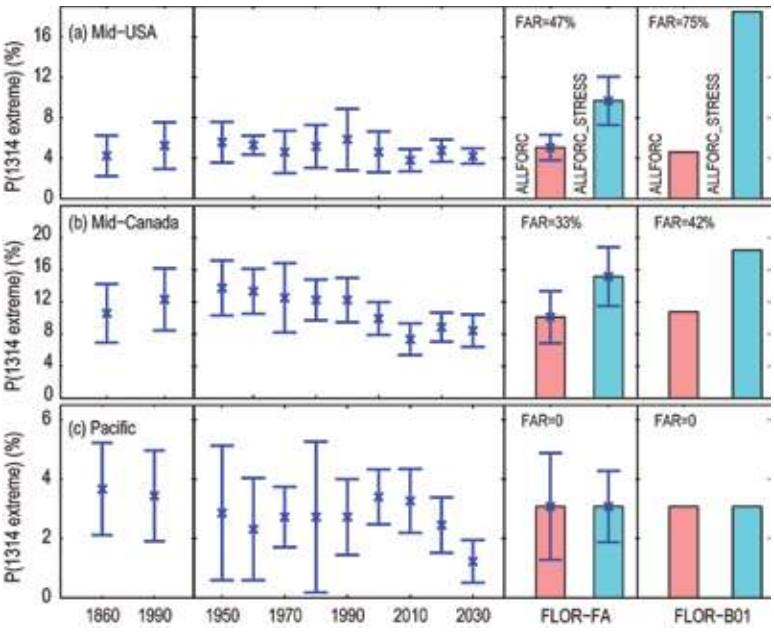

Fig. 6.2. Probability for the 2013/14 winter extreme ETSI of three regions simulated by a suite of simulations using FLOR. P(ETSI of 1314) represents the probability of occurrence of a year with ETSI more than or equal to the 2013/14 values for a given location, called the extreme probability. The error bar plots display the estimated mean P(ETSI of 1314) (cross symbols) and associated standard errors (bars). The mean and standard errors are computed from 100-year chunks from the 1990 (500 years) and 1860 (2000 years) control simulations (1st column); 100-year chunks from the 35-member historical forcing simulations every 10 years during 1941–2050 (2nd column); 91-year chunks from the 35-member ALLFORC (pink shading)/ALLFORC_STRESS (cyan shading) simulations during the hiatus period 2000–12 using FLOR_FA (3rd column). The pink (cyan) shaded bar represents the extreme probability during 2000–12 for the 5-member ALLFORC (ALLFORC_STRESS) simulations using FLOR_B01 (4th column). Fraction of attributable risk (FAR) is labelled over the shaded bars. The extreme probabilities are shown for (a) the mid-USA, (b) mid-Canada, and (c) the Pacific coastal region. The boundary of the three regions is marked in three boxes in Fig. 6.1a.

exhibit a significant decrease starting 2000 (second column of Fig. 6.2b); there is also no significant increase of the extreme occurrence over the Pacific coastal region (third column of Fig. 6.2c). Thus, the impact of anthropogenic forcing prescribed on this model did not contribute to the 2013/14 extreme ETS events over North America.

Recently, Delworth et al. (2015) found that observed multiyear changes of tropical Pacific zonal wind can drive both the global warming hiatus (consistent with Kosaka and Xie 2013; England et al. 2014) and recent multiyear western North American drying (and also an increase in precipitation in the central and eastern USA). Thus, a link may exist between the recent tropical Pacific decadal changes with the extreme ETS over North America, since the severe California drought has to be linked with reduced ETSs over California and its coastal ocean. To elucidate the possible link between the recent tropical Pacific changes and the ETS extremes over North America, we compute the extreme probabilities over the global warming hiatus period (2000–12) in an experiment with all historical radiative forcing (ALLFORC) and an experiment with radiative forcing plus observed tropical Pacific wind stress anomalies (ALLFORC_STRESS). The experiments are taken from Delworth et al. (2015), and the details can be found in SM Section 2d.

The estimated extreme probabilities from the ALLFORC_STRESS experiment during 2000–13 are significantly larger than those from the ALLFORC experiment over mid-USA and mid-Canada using FLOR_FA (third column of Figs. 6.2a and b), while the extreme probabilities are not statistically distinguishable between the two experiments over the Pacific coastal region (third column of Fig. 6.2c). The similar contrast of the extreme probability between the ALLFORC and ALLFORC_STRESS runs is reproduced using FLOR_B01 (fourth column of Fig. 6.2c). The fraction of attributable risk (FAR) of the extreme probability due to the observed zonal wind anomalies in the tropical Pacific is 47% (75%), 33% (42%) and 0% (0%) using FLOR_FA (FLOR_B01) for the mid-USA, mid-Canada, and the Pacific coast, respectively (Fig. 6.2). Thus, we conclude that the recent multiyear strengthening of the tropical Pacific easterlies increased the odds of the increase in extreme ETS occurrence probability over North America in 2013/14, but not the decrease over California.

Discussions and Conclusions. The winter of 2013/14 saw extreme ETS activity over much of North America. Based on a large ensemble of historical forcing experiments with a high-resolution coupled climate model we find no evidence to support the hypothesis that global warming contributed to this extreme ETS event. However, the recent multiyear increase in the strength of the trade winds in the tropical Pacific

Ocean that has been linked to the global warming hiatus (Kosaka and Xie 2013; England et al. 2014; Delworth et al. 2015) substantially increased the probability of the 2013/14 positive extreme ETS winter over much of North America (though it did not contribute significantly to the decrease over California). The event was unlikely even in initialized seasonal predications, highlighting the important role of stochastic forcing ("weather noise") in this event. Therefore, it is likely that the anomalous tropical Pacific Ocean state was a major climate driver of the extremely active ETSs over much of North America during the 2013/14 winter through the multiyear enhancement of the trade winds and a weak La Niña. It is likely that an enhanced probability of extreme enhanced ETS seasons like the 2013/14 winter over much of North America will continue if the anomalous easterly winds that have contributed to the global warming hiatus persist over the tropical Pacific Ocean.

ACKNOWLEDGEMENTS. This work is supported in part by NOAA's Climate Program Office. X. Yang and G. A. Vecchi are supported by NOAA/OAR under the auspices of the National Earth System Prediction Capability (National ESPC).

REFERENCES

Chang, E. K. M., 2013: CMIP5 projection of significant reduction in extratropical cyclone activity over North America. *J. Climate*, **26**, 9903–9922, doi:10.1175/JCLI-D-13-00209.1.

Dee, D. P., and Coauthors, 2011: The ERA-Interim reanalysis: Configuration and performance of the data assimilation system. *Quart. J. Roy. Meteor. Soc.*, **137**, 553–597.

Delworth, T. L., F. Zeng, A. Rosati, G. A. Vecchi, and A. T. Wittenberg, 2015: A link between the hiatus in global warming and North American drought. *J. Climate*, **28**, 3834–3845, doi:10.1175/JCLI-D-14-00616.1.

England, M. H., and Coauthors, 2014: Recent intensification of wind-driven circulation in the Pacific and the ongoing warming hiatus. *Nat. Climate Change*, **4**, 222–227, doi:10.1038/nclimate2106.

Grise, K. M., S.-W. Son, and J. R. Gyakum, 2013: Intraseasonal and interannual variability in North American storm tracks and its relationship to equatorial Pacific variability. *Mon. Wea. Rev.*, **141**, 3610–3625, doi:10.1175/MWR-D-12-00322.1.

Hartmann, D. L., 2015: Pacific sea surface temperature and the winter of 2014. *Geophys. Res. Lett.*, **42**, 1894–1902, doi:10.1002/2015GL063083.

Jia, L., and Coauthors, 2015: Improved seasonal prediction of temperature and precipitation over land in a high-resolution GFDL climate model. *J. Climate*, **28,** 2044–2062, doi:10.1175/JCLI-D-14-00112.1

Kosaka, Y., and S.-P. Xie, 2013: Recent global-warming hiatus tied to equatorial Pacific surface cooling. *Nature*, **501**, 403–407, doi:10.1038/nature12534.

Murakami, H., G. A. Vecchi, T. Delworth, K. Paffendorf, R. Gudgel, L. Jia, and F. Zeng, 2015: Investigating the influence of anthropogenic forcing and natural variability on the 2014 Hawaiian hurricane season [in "Explaining Extreme Events of 2014 from a Climate Perspective"]. *Bull. Amer. Meteor. Soc.*, **96** (12), S115-S119, doi:10.1175/BAMS-D-15-00119.1

Vecchi, G. A., and Coauthors, 2014: On the seasonal forecasting of regional tropical cyclone activity. *J. Climate*, **27**, 7994–8016, doi:10.1175/JCLI-D-14-00158.1.

Wallace, J., G. Lim, and M. Blackmon, 1988: Relationship between cyclone tracks, anticyclone tracks and baroclinic waveguides. *J. Atmos. Sci.*, **45**, 439–462.

Yang, X., and Coauthors, 2015: Seasonal predictability of extratropical storm tracks in GFDL's high-resolution climate prediction model. *J. Climate*, **28**, 3592–3611, doi:10.1175/JCLI-D-14-00517.1.

7. WAS THE EXTREME STORM SEASON IN WINTER 2013/14 OVER THE NORTH ATLANTIC AND THE UNITED KINGDOM TRIGGERED BY CHANGES IN THE WEST PACIFIC WARM POOL?

Simon Wild, Daniel J. Befort, and Gregor C. Leckebusch

The all-time record number of storms over the British Isles in winter 2013/14 cannot be linked directly to anthropogenic-induced warming of the tropical west Pacific.

Introduction. In winter 2013/14, the United Kingdom experienced exceptionally stormy and rainy weather conditions. The period from December 2013 to February 2014 was the stormiest for at least 20 years according to the Met Office (Met Office 2014). Two further studies also revealed this season to have been the stormiest in the United Kingdom since 1871. Matthews et al. (2014) found the highest value of a combined index of cyclone counts and intensity in the winter 2013/14, while a study by the Climate Research Unit at the University of East Anglia derived an unprecedented number of severe gale days with a circulation weather type analysis from mean sea level pressure fields (CRU 2014). While the United Kingdom was hit by several high-intensity storms, surface temperatures over large parts of central North America fell to near record minimum values (NCDC 2014; Environment Canada 2014). These low temperatures have been connected to warm sea surface temperatures in the North Pacific (Hartmann 2015; Lee et al. 2015). A potential driver for positive sea surface temperature anomalies in the North Pacific and cold conditions in central North America further downstream is warm surface waters in the tropical west Pacific (Palmer 2014; Hartmann 2015). It has been suggested that increasing sea surface temperatures in the tropical west Pacific could also be the cause for extreme weather over the British Isles (Huntingford et al. 2014; Slingo et al. 2014; Kendon and McCarthy 2015). In line with this hypothesis, we first quantify the interannual variability of winter windstorm frequency over the North Atlantic/European region, which can be related to very low temperatures over North America. Secondly, we test whether a mechanism originating in the tropical Pacific continues beyond the North American continent affecting storminess over the North Atlantic and Europe.

AFFILIATIONS: Wild, Befort, and Leckebusch—School of Geography and Environmental Sciences, University of Birmingham, Birmingham, United Kingdom

DOI: 10.1175/BAMS-D-15-00118.1

A supplement to this article is available online (10.1175/BAMS-D-15-00118.2)

Data and Methods. All our analyses cover the core winter months, December–February, from 1979/80 to 2013/14. (A list of all datasets used can be found in the online supplemental material.)

Strong wind events associated with extratropical cyclones are identified with an objective algorithm developed by Leckebusch et al. (2008) using exceedances of the local 98th percentile of the 10-m wind speeds. Events with a lifetime shorter than 18 hours are neglected to focus on wind fields caused by synoptic-scale extratropical cyclones. Cyclones over the North Pacific are determined by a cyclone identification and tracking algorithm (Murray and Simmonds 1991) that locates a minimum of mean sea level pressure (MSLP) in the vicinity of a maximum in the Laplacian of the MSLP. Local system track density for both types of tracks (windstorms and cyclones) are calculated in agreement with settings used in Neu et al. (2012) with a search radius of 500 km around the center of each box in a $2° \times 2°$ grid.

The stormy winter 2013/14 over the British Isles and upstream conditions. Compared to the long-term seasonal mean, we find an increase of up to 200% in the number of identified windstorm events in the eastern North Atlantic for the winter season 2013/14. This corresponds to an increase of about 10 systems per winter or to more than three times the interannual standard deviation. Considering the period from 1979 to 2014, the winter 2013/14 showed the highest storm

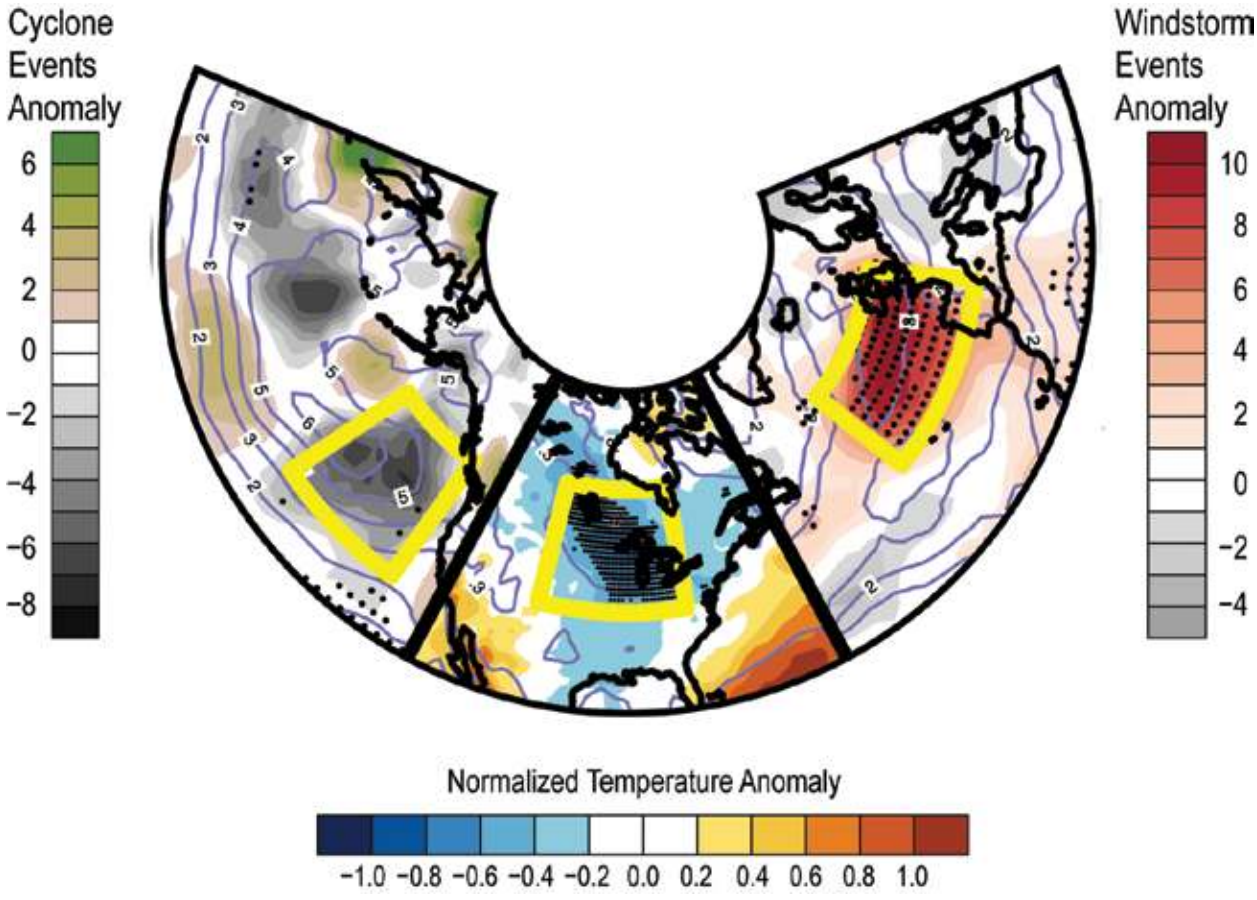

Fig. 7.1. Anomalies (ERA Interim) for Dec 2013–Feb 2014 compared to long-term climatology (1979–2014) in shadings; interannual standard deviation in contours. (right) 60°W–30°E, 25°–70°N; absolute windstorm events anomaly; black dots indicate a maximum in winter 2013/14. (center) 120°–60°W, 25°–70°N; 2-m temperature seasonal normalized anomaly mean; black dots indicate a minimum in winter 2013/14. (left) 150°E–120°W, 25°–70°N; absolute cyclone events anomaly; black dots indicate a minimum in winter 2013/14. Yellow boxes mark regions used for the calculation of correlation coefficients for Table 7.1.

frequency on record (Fig. 7.1, right panel). The main area of this positive windstorm anomaly extends from about 35°W to the Greenwich meridian along a latitudinal belt from about 40°N to 55°N, and it includes large parts of the British Isles. These results about pure windstorms corroborate findings of previous studies about cyclone counts or gale days derived from pressure data (e.g., Matthews et al. 2014; CRU 2014).

Concurrently, further upstream over the central North American continent, 2-m temperatures dropped extremely below normal conditions. The interannual standard deviation (one value per season) of the normalized temperatures (one value every six hours) shows values between 0.3 and 1.0 below the long-term seasonal mean setting the overall temperature minimum for large parts of the U.S. Midwest, the southern part of the Canadian prairies, and southwestern Ontario for the whole investigated period (Fig. 7.1, central panel).

The North American extreme cold temperatures are strongly linked to an equatorward shift of the circumpolar vortex (Ballinger et al. 2014). The circumpolar vortex accompanied by the upper tropospheric jet was deflected to the north over the eastern North Pacific (Slingo et al. 2014) allowing polar air masses to flow over North America on the trough upstream side. Associated with large amplitude Rossby waves in the mid and upper troposphere with a ridge over the North Pacific, anomalously high mean sea level pressure can decrease the number of cyclone systems and increase temperatures in the region of the climatological Aleutian Low (e.g., Lau 1988; Honda et al. 2001). In the winter 2013/14, the number of cyclones was indeed strongly reduced compared to the long-term climatology with a reduction of about 30%–60%,

equivalent to about 5–10 fewer cyclones per grid point over the eastern North Pacific (Fig. 7.1, left panel).

The Pacific–North American Pattern (PNA) can be regarded as one mode of variability that links the tropical and extratropical Pacific on a monthly to seasonal scale and is known to be strongly related to the surface temperature over North America (e.g., Leathers et al. 1991; Ning and Bradley 2014). In the winter 2013/14, the PNA was weakly positive in January and strongly negative in December and February.

Sea surface temperatures in the tropical west Pacific were exceptionally high in winter 2013/14 (Lee et al. 2015) causing enhanced convective activity, indicated by negative outgoing longwave radiation (OLR) anomalies, in this region (Supplemental Fig. S7.1).

Discussion and attribution to climate change. This study tests and quantifies a proposed mechanism linking convective activity over the tropical west Pacific and storminess over Europe. If such a link exists, the record number of storms over the British Isles in winter 2013/14 could be seen as an enhanced response of the climate system triggered by increased sea surface temperatures in the tropical west Pacific, which themselves stem from anthropogenic influences (e.g., Palmer 2014; Chan and Wu 2015). Thus, anthropogenic influences would act via a natural link leading to anomalously high storm frequency over Europe.

We diagnose that the year-to-year variability of storm frequency over the northeast Atlantic and the British Isles is significantly anticorrelated to surface temperatures in central North America (Table 7.1, regions outlined as yellow boxes in Fig. 7.1). We further confirm the link between the interannual variability of surface temperatures over North America and the PNA. The PNA is in turn significantly linked to cyclone activity in the northeast Pacific, sea surface temperatures in the North Pacific, and convective activity (OLR) over about half of the west Pacific warm pool (cf. Table 7.1, the role of the PNA in the online supplemental material, and Supplemental Fig. S7.2).

The direct relation between windstorm frequency anomalies over Europe and sea surface temperatures in the west Pacific warm pool, respectively OLR anomalies, is however weak and not significant (Table 7.1).

Thus, we find that parts of the proposed mechanism in previous studies (Huntingford et al. 2014; Slingo et al. 2014; Kendon and McCarthy 2015) linking the tropical west Pacific and European storminess show significant covariability, but we cannot find evidence for a direct relation from the beginning to the end of such a mechanism. In addition, the correlation between North American temperatures and windstorm anomalies drops to insignificant values when the winter 2013/14 is excluded from the analysis.

We thus conclude that the conditions in the Pacific and its induced anomalies over the North American continent are generally not sufficient to explain the extraordinary high winter windstorm frequency over the northeast Atlantic and the British Isles. The induced conditions were favorable to increase the number of storms in winter 2013/14, but the explained variability is too small to attribute this particular

Table 7.1. Spearman rank correlation coefficient between area-averaged detrended time series from 1979/80 to 2013/14. NAt: Northeast Atlantic/British Isles (40°–55°N, 35°W–0°); NA: North America (38°–55°N, 105°–80°W); NEP: Northeast Pacific (33°–52°N, 150°–128°W); SST NP: Sea surface temperature, North Pacific (35°–60°N, 160°E–145°W); WP: tropical west Pacific. (25°S–25°N, 90°–170°E,). For regions, see also yellow boxes in Figs. 7.1 and Supplemental Fig. S7.1. Statistically significant values in bold ($p < 0.05$).

	OLR, WP	PNA	SST, NP	Cyclone Events, NEP	Temperature, NA
Windstorms, NAt	−0.05	−0.22	−0.05	−0.21	**−0.38**
Temperature, NA	**0.41**	**0.46**	**−0.40**	**0.37**	
Cyclone Events, NEP	0.17	**0.41**	−0.12		
SST, NP	−0.14	**−0.48**			
PNA	**0.36**				

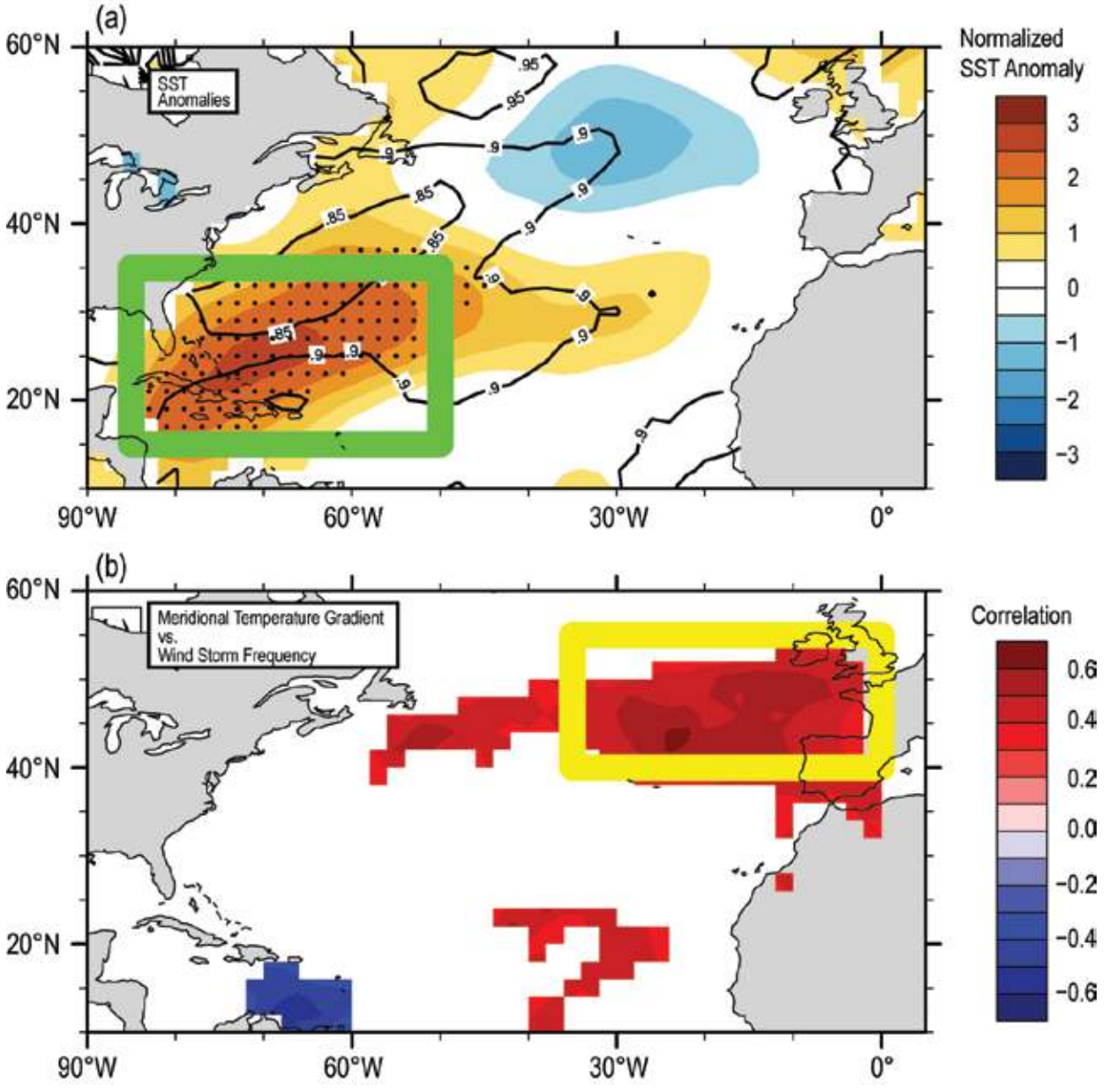

Fig. 7.2. (a) Normalized sea surface temperature (SST) anomalies (ERSSTv4) for Dec 2013–Feb 2014 compared to long-term climatology (1979–2014) in shadings; interannual standard deviation in contours. Black dots indicate a maximum in winter 2013/14 for the considered time period from 1979 to 2014. (b) Interannual correlation coefficient (Pearson) between winter windstorm frequency and meridional temperature gradient index from 1979/80 to 2013/14. The meridional temperature index is calculated by subtracting the area-averaged sea surface temperature value for the west Atlantic (15°–35°N, 85°–50°W; green box in Fig. 7.2a) minus the area-averaged 2-m temperature value for central North America (38°–55°N, 105°–80°W; yellow box in center panel of Fig. 7.1). Correlations below the 95% significance level are omitted. (For clarity: Yellow box in Fig. 7.2b corresponds to yellow box in right panel in Fig. 7.1.)

extreme mainly to conditions in the tropical Pacific and its imprinted anthropogenic signal.

One alternative potential driver partly explaining the anomalously high storm frequency in 2013/14 could have been the unprecedented anomalies of sea surface temperatures in the west Atlantic (Fig. 7.2a). High sea surface temperatures in the subtropical west Atlantic (green box, Fig. 7.2a) and low temperatures over North America (yellow box, center panel Fig. 7.1) are unrelated (the correlation equals 0.03), but when occurring concurrently, they substantially increase the meridional temperature gradient over the core genesis region of extratropical cyclones. This meridional temperature gradient is positively related

to windstorm frequency over the North Atlantic and Europe (Fig. 7.2b). Baroclinic instability in this region can be positively influenced through a strong temperature gradient, leading to enhanced cyclogenesis and potentially strong deepening of cyclones responsible for high wind speeds.

Conclusion. The anomalous high number of windstorms in winter 2013/14 over the northeast Atlantic and the British Isles cannot directly be attributed to anthropogenic-influenced factors as apparent in the tropical west Pacific. Very suitable conditions of natural internal interannual variability, including conditions over the tropical and North Pacific, North America, and the west Atlantic, favored the record number of storm counts.

ACKNOWLEDGMENTS. We would like to thank the ECMWF for providing ERA Interim data and NOAA for providing PNA, OLR, and ERSST data. We are also very grateful to three anonymous reviewers and editor Jeff Rosenfeld for their constructive criticism and helpful suggestions as well as to Stephanie Herring and Jim Kossin for their guidance throughout the drafting process of this manuscript. Research by GC Leckebusch is supported by EU FP7-MC-CIG-322208 grant.

REFERENCES

Ballinger, T. J., M. J. Allen, and R. V. Rohli, 2014: Spatiotemporal analysis of the January Northern Hemisphere circumpolar vortex over the contiguous United States. *Geophys. Res. Lett.*, **41**, 3602–3608, doi:10.1002/2014GL060285.

Chan, D., and Q. Wu, 2015: Attributing observed SST trends and subcontinental land warming to anthropogenic forcing during 1979–2005. *J. Climate*, **28**, 3152–3170, doi:10.1175/JCLI-D-14-00253.1.

CRU, 2014: Lamb weather types: UK Jenkinson gale index: Threshold counts. Climate Research Unit, University of East Anglia, 1 p. [Available online at www.cru.uea.ac.uk/cru/data/lwt/webdocs/NDJFMA_G_thresh_counts_UK.pdf.]

Environment Canada, 2014: Climate trends and variations bulletin – Winter 2013-2014. Environment Canada, 4 pp. [Available online at www.ec.gc.ca/adsc-cmda/383F5EFA-508D-45E8-89AD-4B14B53B429E/CTVB_Winter_2013_2014_E.pdf.]

Hartmann, D. L., 2015: Pacific sea surface temperature and the winter of 2014. *Geophys. Res. Lett.*, **42**, 1894–1902, doi:10.1002/2015GL063083.

Honda, M., H. Nakamura, J. Ukita, I. Kousaka, and K. Takeuchi, 2001: Interannual seesaw between the Aleutian and Icelandic lows. Part I: Seasonal dependence and life cycle. *J. Climate*, **14**, 1029–1042.

Huntingford, C., and Coauthors, 2014: Potential influences on the United Kingdom's floods of winter 2013/14. *Nat. Climate Change*, **4**, 769–777, doi:10.1038/nclimate2314.

Kendon, M., and M. McCarthy, 2015: The UK's wet and stormy winter of 2013/2014. *Weather*, **70**, 40–47, doi:10.1002/wea.2465.

Lau, N.-C., 1988: Variability of the observed midlatitude storm tracks in relation to low-frequency changes in the circulation pattern. *J. Atmos. Sci.*, **45,** 2718–2743.

Leathers, D., B. Yarnal, and M. Palecki, 1991: The Pacific/North American teleconnection pattern and United States climate. Part 1: Regional temperature and precipitation associations. *J. Climate*, **4**, 517–528.

Leckebusch, G. C., D. Renggli, and U. Ulbrich, 2008: Development and application of an objective storm severity measure for the northeast Atlantic region. *Meteor. Z.*, **17**, 575–587.

Lee, M.-Y., C.-C. Hong, and H.-H. Hsu, 2015: Compounding effects of warm sea surface temperature and reduced sea ice on the extreme circulation over the extratropical North Pacific and North America during the 2013–2014 boreal winter. *Geophys. Res. Lett.*, **42**, 1612–1618, doi:10.1002/2014GL062956.

Matthews, T., C. Murphy, R. L. Wilby, and S. Harrigan, 2014: Stormiest winter on record for Ireland and UK. *Nat. Climate Change*, **4**, 738–740, doi:10.1038/nclimte2336.

Met Office, 2014: Winter 2013/14. [Available online at www.metoffice.gov.uk/climate/uk/summaries/2014/winter.]

Murray, R., and I. Simmonds, 1991: A numerical scheme for tracking cyclone centres from digital data. Part I. Development and operation of the scheme. *Aust. Meteor. Mag.*, **39**, 155–166.

NCDC, 2014: Nov 2013 – Jan 2014 divisional ranks: Temperature. National Climatic Data Center, 1 p. [Available online at www.ncdc.noaa.gov/sotc/service/national/divisionaltavgrank/201311-201401.gif.]

Neu, U., and Coauthors, 2012: IMILAST: A community effort to intercompare extratropical cyclone detection and tracking algorithms. *Bull. Amer. Meteor. Soc.*, **94**, 529–547, doi:10.1175/BAMS-D-11-00154.1.

Ning, L., and R. S. Bradley, 2014: Winter climate extremes over the northeastern United States and southeastern Canada and teleconnections with large-scale modes of climate variability. *J. Climate*, **28**, 2475–2493, doi:10.1175/JCLI-D-13-00750.1.

Palmer, T., 2014: Record-breaking winters and global climate change. *Science*, **344**, 803–804, doi:10.1126/science.1255147.

Slingo, J., and Coauthors, 2014 The recent storms and floods in the UK. Met Office and Centre for Ecology and Hydrology, 27 pp. [Available online at www.metoffice.gov.uk/media/pdf/n/i/Recent_Storms_Briefing_Final_07023.pdf.]

8. FACTORS OTHER THAN CLIMATE CHANGE, MAIN DRIVERS OF 2014/15 WATER SHORTAGE IN SOUTHEAST BRAZIL

Friederike E. L. Otto, Caio A. S. Coelho, Andrew King, Erin Coughlan de Perez, Yoshihide Wada, Geert Jan van Oldenborgh, Rein Haarsma, Karsten Haustein, Peter Uhe, Maarten van Aalst, Jose Antonio Aravequia, Waldenio Almeida, and Heidi Cullen

Southeast Brazil experienced profound water shortages in 2014/15. Anthropogenic climate change is not found to be a major influence on the hazard, whereas increasing population and water consumption increased vulnerability.

Introduction. The southeast region of Brazil (SEB, defined as the area between 15°–25°S and 40°–48°W; Fig. 8.1a) experienced remarkably dry conditions from January 2014 to February 2015, comprising the 14-month period that includes two rainy seasons investigated here. This region includes São Paulo, Brazil´s most populated city, which suffered impacts due to water shortages, and the watersheds and reservoirs feeding the city's water supply system. The wet season occurs during austral summer and the dry season during austral winter. The South Atlantic convergence zone (SACZ) is the main mechanism responsible for the region's austral summer rainfall. During summer 2014, there was a complete absence of SACZ episodes (Coelho et al. 2015). Previous major droughts occurred in the region in 1953/54, 1962/63, 1970/71, and 2001. While droughts have very complex criteria, these were all characterized by large rainfall deficits while the effect of the SACZ needs further investigation. The 1953/54 rainfall deficit prompted construction of the largest water supply system (Cantareira) used for São Paulo (Porto et al. 2014). The 2014/15 drought had major impacts in São Paulo due partly to a four-fold population increase since 1960 (Fig. 8.1b). Although new water supply systems were constructed after Cantareira, it is still by far the largest in terms of capacity and number of people supplied (until early 2015) and hence is used as an indicator of the impacts of the SEB drought on water supply. In January 2015, Cantareira, which used to supply 8.8 million people in São Paulo, sank to a water volume of just 5% of capacity (Fig. 8.1c), and currently supplies just 5.3 million people. Other systems (Guarapiranga and Alto Tiete) started to supply the excess population, those previously supplied by Cantareira, after the water crisis was established.

In this analysis, we investigate potential changes in the hydrometeorological hazard, defined by accumulated precipitation and the difference between precipitation and evaporation ($P-E$) in the SEB region. The true impact, however, is due to a combination of a physical event with vulnerability and exposure, in this case on millions of people in the affected area (Field et al. 2012).

The current drought reflects increasing trends in exposure. São Paulo's population grew by 20% in the past 20 years. Water use has increased at an even faster rate over the same period (Fig. 8.1b). Vulnerability of water supply systems remains high. Recognizing that water governance is key to reducing vulnerability,

AFFILIATIONS: Otto, Haustein, and Uhe—Environmental Change Institute, University of Oxford, Oxford, United Kingdom; Coelho, Aravequia, and Almeida—Center for Weather Forecast and Climate Studies (CPTEC), National Institute for Space Research (INPE), Cachoeira Paulista, São Paulo, Brazil; King—ARC Centre of Excellence for Climate System Science, School of Earth Sciences, University of Melbourne, Melbourne, Victoria, Australia; Coughlan de Perez—Red Cross/Red Crescent Climate Centre, The Hague, Netherlands, and Institute for Environmental Studies (IVM), VU University Amsterdam, Amsterdam, Netherlands, and International Research Institute for Climate and Society, Palisades, New York; Wada—Department of Physical Geography, Utrecht University, Utrecht, Netherlands, and NASA Goddard Institute for Space Studies, New York, New York, and Center for Climate Systems Research, Columbia University, New York, New York; van Oldenborgh and Haarsma—Royal Netherlands Meteorological Institute (KNMI), De Bilt, Netherlands; van Aalst—Red Cross/Red Crescent Climate Centre, The Hague, Netherlands, and International Research Institute for Climate and Society, Palisades, New York; Cullen—Climate Central, Princeton, New Jersey

DOI:10.1175/BAMS-D-15-00120.1

A supplement to this article is available online (10.1175/BAMS-D-15-00120.2)

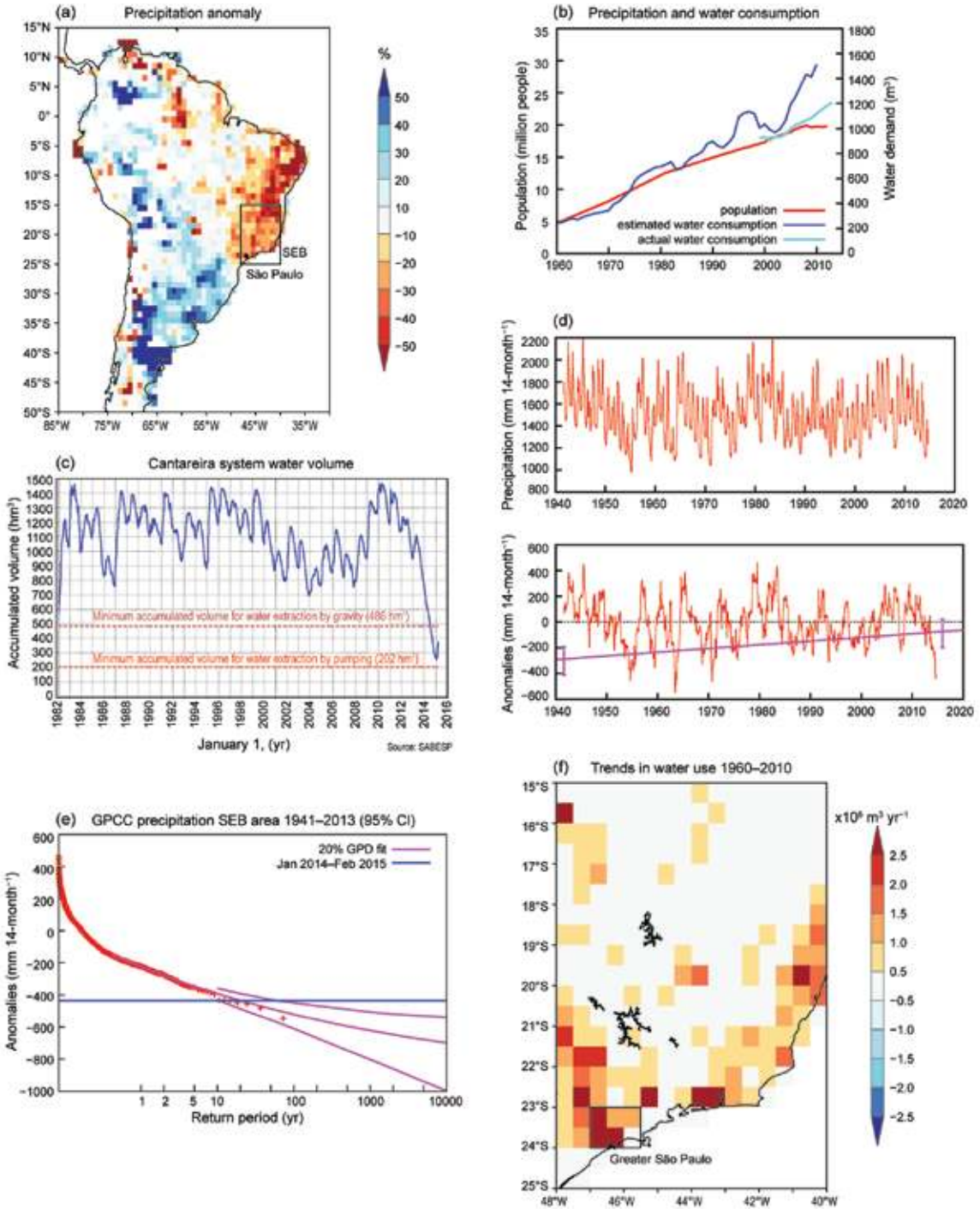

Fig. 8.1. (a) Relative precipitation anomalies in Jan 2014–Feb 2015 as a percentage of the 1941–2010 climatology. (Source: GPCC.) (b) São Paulo´s metropolitan population (red line) over the period 1960–2012 and estimated (1960–2010, blue) and actual (1999–2013, aqua) water use in Greater São Paulo (defined slightly differently) over the period 1960–2010. Actual water use was obtained from São Paulo state water/waste management company (SABESP). (c) Amount of water stored in the Cantareira water system from completion in Jan 1982 up to Mar 2015. (d, top) 14-month running mean of precipitation in SEB (95% CI: −2.3% – 1.3% 10-yr^{-1}) and (bottom) anomalies. The purple line bottom panel represents the 20th percentile increasing at 0%–4% 10-yr^{-1}. (e) Fit of the driest 20% of the 14-month running precipitation anomalies to a stationary GPD. The horizontal blue line represents the observed 2014/15 precipitation anomaly. (f) Trend in estimated water use in SEB over 1960–2010 in 10^6 m^3 yr^{-1}. (Source: Wada et al. 2014).

Brazil has advanced decentralization of water management (Engle and Lemos 2010).

Other aspects of vulnerability give a more mixed picture. This drought has not resulted in sustained power outages, a common consequence of water shortages. Similarly, no cholera outbreaks have been reported, reflecting major public health investments (Barrato et al. 2011). Dengue, however, has spiked in São Paulo, with a tripling of cases in 2015 compared with 2014, including several deaths.

Data and methods. Drought can be defined in multiple ways and have multiple drivers (Field et al. 2012). Here we employ a multimethod approach to assess whether and to what extent anthropogenic climate change contributed to the 2014/15 drought event over SEB, using both observations and general circulation model (GCM) simulations of 14-month accumulated precipitation and $P-E$. We chose these measures to robustly assess the combined thermodynamic and dynamic effect of anthropogenic climate change on the drought. Future studies will disentangle these effects and analyze the driving mechanisms (e.g., Coelho et al. 2015). Our methods include: (i) trend and return period estimation for the 2014/15 event based on historical records; (ii) an estimation of the change in return periods of this event by comparing very large ensembles of SST-driven GCM simulations of the current climate with simulations of the climate in a "world that might have been" without anthropogenic greenhouse gas emissions; and (iii) a similar procedure using state-of-the-art coupled climate model simulations (CMIP5; Taylor et al. 2012).

(i) The observational analysis is based on the GPCC-V6 analysis up to 2010 (Global Precipitation Climatology Centre; Schneider et al. 2014), GPCC monitoring analysis 2011–14, and GPCC first guess analysis Jan–Feb2015. The monitoring analysis was adjusted to GPCC-V6 using linear regression on the 1986–2010 overlap period.

Figure 8.1a shows January 2014–February 2015 precipitation anomalies relative to the 1941–2010 mean. Eastern Brazil, including SEB, shows 25% to 50% deficits. Figure 8.1d shows 14-month precipitation running means averaged over SEB. No evidence of a trend was found in the mean, whereas dry extremes showed a barely significant decrease up to 2013 (Fig. 8.1d, lower panel). The 2014/15 SEB deficit is similar to previous events, with dry episodes around 1963, 1970, and 1954 more severe than the current episode up to February 2015. Figure 8.1e shows a generalised Pareto distribution (GPD) fit to the driest 20% records assuming a stationary distribution. The January 2014–February 2015 deficit (435 mm) return period is about 20 years (95% CI: 10–60 years).

(ii) We use the distributed computing framework—weather@home—to run the Met Office Hadley Centre atmosphere-only general circulation model HADAM3P (Massey et al. 2015) to simulate precipitation and $P-E$ in two different model ensembles representing: 1) observed climate conditions of 2014/15, and 2) counterfactual conditions under pre-industrial greenhouse gas forcings and 11 different estimates of SSTs without human influence (Schaller et al. 2014). The empirical SEB total precipitation return periods (Fig. 8.2a) show that in this approach dry precipitation extremes have become less likely due to anthropogenic greenhouse gas emissions: what would have been a 1-in-20-year precipitation deficit event like the 14-month 2014/15 event has become approximately a 1-in-30-year event (95% CI: 0 to 35 years). At the same time there is no detectable change in $P-E$ due to human-induced climate change (Fig. 8.2c) because of an increase in evaporation that cancels the increase in precipitation. The decrease in extreme low precipitation seen in SEB however is not uniform (consistent with observations; see Supplementary Fig. S8.2a) across Brazil as a whole (Fig. 8.2e).

(iii) We use the same approach as described in Lewis and Karoly (2014) and King et al. (2015) to estimate the fraction of attributable risk (FAR; Allen 2003) of precipitation totals below 25%, 20%, 15%, and 10% of the 1961–90 average and $P-E$ below 170 mm (the 10th percentile) in a subset of the CMIP5 ensemble (see supplemental material). In contrast to the weather@home we find an increase in the risk of low precipitation with FARs greater than 0.167 (with 90% confidence) for the observed accumulated precipitation. However, the null result is confirmed with FARs slightly greater than zero for $P-E$.

Conclusion. While it has been speculated that anthropogenic climate change is a leading driver of the current drought (e.g., Escobar 2015) our multimethod approach finds limited support for this view. Evidence from observations shows large precipitation deficits becoming less common, albeit with large uncertainties. Likewise, large climate model ensembles show a nonsignificant effect of anthropogenic greenhouse gas emissions on the probability of low water availability ($P-E$). We therefore conclude the hydrometeorological hazard risk has likely not increased due to human-induced greenhouse gas emissions and the large impact of the 2014/15 event (particularly in the

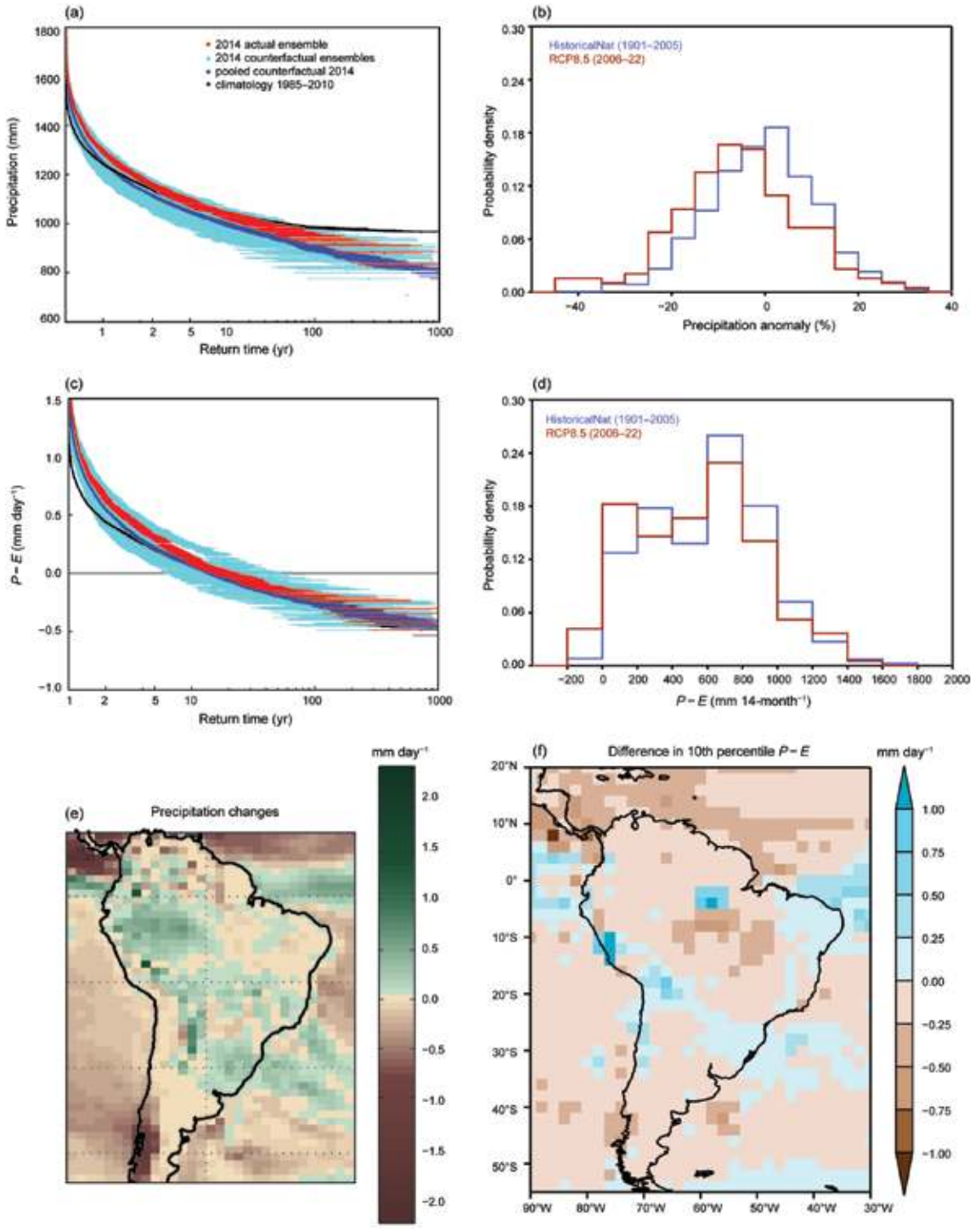

Fig. 8.2. (a) Return periods of total precipitation over SEB from Jan 2014 to Feb 2015 in HadAM3P. (b) Probability density functions (PDF) of 14-month precipitation anomalies in CMIP5 historicalNat and RCP8.5 simulations. (c) Return periods of 14-month mean *P* − *E* averaged over SEB in HadAM3P. (d) PDF of 14-month *P* − *E* in CMIP5 historicalNat and RCP8.5 simulations. (e) Mean *P* − *E* (mm day^{-1}) in the counterfactual ensemble of Jan 2014 to Feb 2015 subtracted from the actual forcing ensemble for the driest 1% of the simulations. (f) Difference in mean *P* − *E* (mm day^{-1}) for RCP8.5 (2006–22) minus historicalNat (1901–2005) for the driest 10% of the simulations. For all simulations on the left-hand side the single ensemble members have been restarted in Dec 2014 and are thus only continuous in a statistical sense.

São Paulo region) is more likely driven by water use changes and accelerated population growth.

This does not, however, mean there is no human influence on the hazard itself. We expect (and observe) evaporation to rise due to higher temperatures as a direct consequence of the Clausius–Clapeyron relationship when there is enough water availability. However, this is not the case in droughts where a precipitation deficit over an extended period of time bounds evaporation. Hence the trend in evaporation tends to cancel the trend in dry precipitation extremes, giving a null result in $P-E$ extremes. Overall, our analysis suggests changes in hydrometeorological risk are small while increasing water consumption increases the risk of profound water shortages.

The negative trend in observed dry extremes and large ensemble simulations is in contrast to a positive trend in CMIP5 dry precipitation extremes (Figs. 8.1f, 8.2b). This apparent contradiction could result from the differing physics among the CMIP5 models and weather@home, or from the different underlying assumptions of the different methodologies (e.g., climatological behavior in CMIP5 versus single year simulations using weather@home or SST-forced versus coupled). This highlights the importance of analyzing the same event using multiple methods as a means of better assessing confidence in our results.

Our analysis suggests the specific geographic location of the study area plays an important role in the results as São Paulo sits on the edge of the boundary between decreasing precipitation (to the north) and increasing precipitation (to the south) (Figs. 8.2e,f). Future projections show a continuation of this general pattern, but given the large spread between models, scenarios, and seasons, it is possible the wet–dry boundary will shift leaving São Paulo's precipitation future uncertain (van Oldenborgh et al. 2013). Hence, while the recent drought impacts were most likely not driven by an increase in hydrometeorological hazard, there is a risk that this may not hold in an even warmer world. Future analyses of the dynamical drivers of the hazard might allow this risk to be quantified.

ACKNOWLEDGEMENTS. We thank Antonio Divino Moura and David Karoly for their guidance and input on the manuscript and Dina Sperling and Roop Singh for all their help, our colleagues at the Oxford eResearch Centre and the Met Office Hadley Centre PRECIS team for their support for the application and development of weather@home and all participants in climateprediction.net. The work was supported by the EUCLEIA project funded by the European Union's Seventh Framework Programme [FP7/2007-2013].

REFERENCES

Allen, M., 2003: Liability for climate change. *Nature*, **421**, 891–892, doi:10.1038/421891a.

Barreto, M. L., M. G. Teixeira, F. I. Bastos, R. A. A. Ximenes, R. B. Barata, and L. C. Rodrigues, 2011: Successes and failures in the control of infectious diseases in Brazil: Social and environmental context, policies, interventions, and research needs. *Lancet*, **377**, 1877–1889, doi:10.1016/S0140-6736(11)60202-X.

Coelho, C. A. S., and Coauthors, 2015: The 2014 southeast Brazil austral summer drought: Regional scale mechanisms and teleconnections. *Climate Dyn.*, doi:10.1007/s00382-015-2800-1, in press.

Engle, N. L., and M. C. Lemos, 2010: Unpacking governance: Building adaptive capacity to climate change of river basins in Brazil. *Global Environ.Change*, **20**, 4–13, doi:10.1016/j.gloenvcha.2009.07.001.

Escobar, H., 2015: Drought triggers alarms in Brazil's biggest metropolis. *Science*, **347**, 812.

Field, C. B., and Coauthors, 2012: *Managing the Risks of Extreme Events and Disasters to Advance Climate Change Adaptation*. Cambridge University Press, 582 pp.

King, A. D., G. J. van Oldenborgh, D. J. Karoly, S. C. Lewis, and H. Cullen, 2015: Attribution of the record high central England temperature of 2014 to anthropogenic influences. *Environ. Res. Lett.*, **10**, 054002, doi:10.1088/1748-9326/10/5/054002.

Lewis, S. C., and D. J. Karoly, 2013: Anthropogenic contributions to Australia's record summer temperatures of 2013. *Geophys. Res. Lett.*, **40**, 3705–3709, doi:10.1002/grl.50673.

Massey, N., and Coauthors, 2015: weather@home—development and validation of a very large ensemble modelling system for probabilistic event attribution. *Quart. J. Roy. Meteor. Soc.*, **141**, 1528–1545, doi:10.1002/qj.2455.

Porto, R. L., M. F. A. Porto, and M. Palermo, 2014: A ressurreição do volume morto do Sistema Cantareira na Quaresma. *Revista DAE*, **62** (197), 18–25, doi:10.4322/dae.2014.131.

Schaller, N., F. E. L. Otto, G. J. van Oldenborgh, N. R. Massey, S. Sparrow, and M. R. Allen, 2014: The heavy precipitation event of May–June 2013 in the upper Danube and Elbe basins [in "Explaining Extreme Events of 2013 from a Climate Perspective"]. *Bull. Amer. Meteor.* Soc., **95** (9), S69–S72.

Schneider, U., A. Becker, P. Finger, A. Meyer-Christoffer, M. Ziese, and B. Rudolf, 2014: GPCC's new land surface precipitation climatology based on quality-controlled in situ data and its role in quantifying the global water cycle. *Theor. Appl. Climatol.*, **115**, 15–40, doi:10.1007/s00704-013-0860-x.

Taylor, K. E., R. J. Stouffer, and G. A. Meehl, 2012: An overview of CMIP5 and the experiment design. *Bull. Amer. Meteor. Soc.*, **93**, 485–498, doi:10.1175/BAMS-D-11-00094.1.

van Oldenborgh, G. J., M. Collins, J. Arblaster, J. H. Christensen, J. Marotzke, S. B. Power, M. Rummukainen, and T. Zhou, Eds., 2013: Annex I: Atlas of global and regional climate projections. *Climate Change 2013: The Physical Science Basis*, T. F. Stocker et al., Eds., Cambridge University Press, 1311–1393.

Wada, Y., D. Wisser, and M. F. P. Bierkens, 2014: Global modeling of withdrawal, allocation and consumptive use of surface water and groundwater resources. *Earth Syst. Dyn.*, **5**, 15–40, doi:10.5194/esd-5-15-2014.

9. CAUSAL INFLUENCE OF ANTHROPOGENIC FORCINGS ON THE ARGENTINIAN HEAT WAVE OF DECEMBER 2013

A. Hannart, C. Vera, F. E. L. Otto, and B. Cerne

The Argentinian heat wave of December 2013 was likely caused in part by anthropogenic forcings. These forcings have increased the risk of such an event occurring by a factor of five.

Introduction. A heat wave occurred 13–31 December 2013 in the Northern and central area of Argentina as well as in Northern Patagonia (Fig. 9.1a). Since the beginning of the temperature record by the Argentine National Meteorological Service (SMN), the year 2013 had the hottest month of December ever recorded over the impacted area (+2.5°C anomaly with respect to 1961–90). In the Greater Buenos Aires area, which is the second largest urban area in South America, the event stands out as the single longest heat wave that ever occurred (18 days) over the observational period. This event had significant impacts in particular on the health and energy sectors.

The analysis of the atmospheric dynamics shows that the high temperatures were primarily associated with an intensification of the South Atlantic Convergence Zone (SACZ), which jointly caused simultaneous extreme rainfall events in Southeastern Brazil (Fig. 9.1b). While particularly apparent in the case of the December 2013 heat wave, the influence of the SACZ on heat waves over this subtropical region is a mechanism that has been previously well described (Cerne et al. 2007; Cerne and Vera 2011) and can be summarized as follows: (i) intensified SACZ promotes subsidence over Argentina, favoring clear sky conditions and increasing incoming solar radiation; (ii) which in turn generates high temperatures and lack of rainfall (Fig. 9.1a,b). Furthermore, this mechanism is reinforced in general, and in particular during December 2013, by the presence of an anticyclonic circulation anomaly over central Argentina, which in turn is modulated by Rossby wave trains extended along the South Pacific (Fig. 9.1c), likely induced in part by increased tropical convection over Northern Australia and the Maritime continent (not shown).

From a long-term climate perspective, previous studies (Rusticucci 2012) documented significant trends in some temperature features in the region: while minimum temperatures clearly exhibit positive trends—particularly in Central and Eastern Argentina during the second part of the twentieth century and first decade of the twenty-first century—maximum temperatures, on the contrary, show significant negative trends. On the other hand, there is only medium confidence in the increase of warm extremes of minimum temperature in this region, and trends in maximum temperature extremes are characterized by high spatial variability. Few studies analyzed the trends related to heat waves or warm spells, which appear to have increased in some areas and decreased in others (Seneviratne et al. 2012; Perkins et al. 2012; Rusticucci et al. 2015).

While the causes of the event associated with the short-term dynamics of the atmosphere are well understood, it is not clear at present whether or not the long-term climate response to anthropogenic forcing can also be held to have causally contributed to the occurrence of the event. The present work addresses the latter causal aspects.

Data and method. A heat wave is defined to occur when the index of surface temperature averaged over the relevant area (23°–45°S, 75°–55°W; see Fig. 9.1a) and over the month of December (Z hereafter) reaches or exceeds a threshold which will be discussed further. Observed values of Z over the instrumental period were calculated from the South American gridded dataset (SAG hereafter; Tencer et al. 2011). Since this dataset only covers the period 1960–2000, the periods 1901–60 and 2001–14 were obtained from HadCRUT4 (Morice et al. 2012) anomalies added to SAG climatology. The choice to use climatology from SAG is justified by the fact that it has better spatial

AFFILIATIONS: Hannart—Institut Franco-Argentin d'études sur le climat et ses impacts (IFAECI), Centre National de la Recherche Scientifique (CNRS)/Consejo Nacional de Investigaciones Científicas y Técnicas (CONICET)/University of Buenos Aires, Argentina; Otto—Environmental Change Institute, University of Oxford, United Kingdom

DOI:10.1175/BAMS-D-15-00137.1

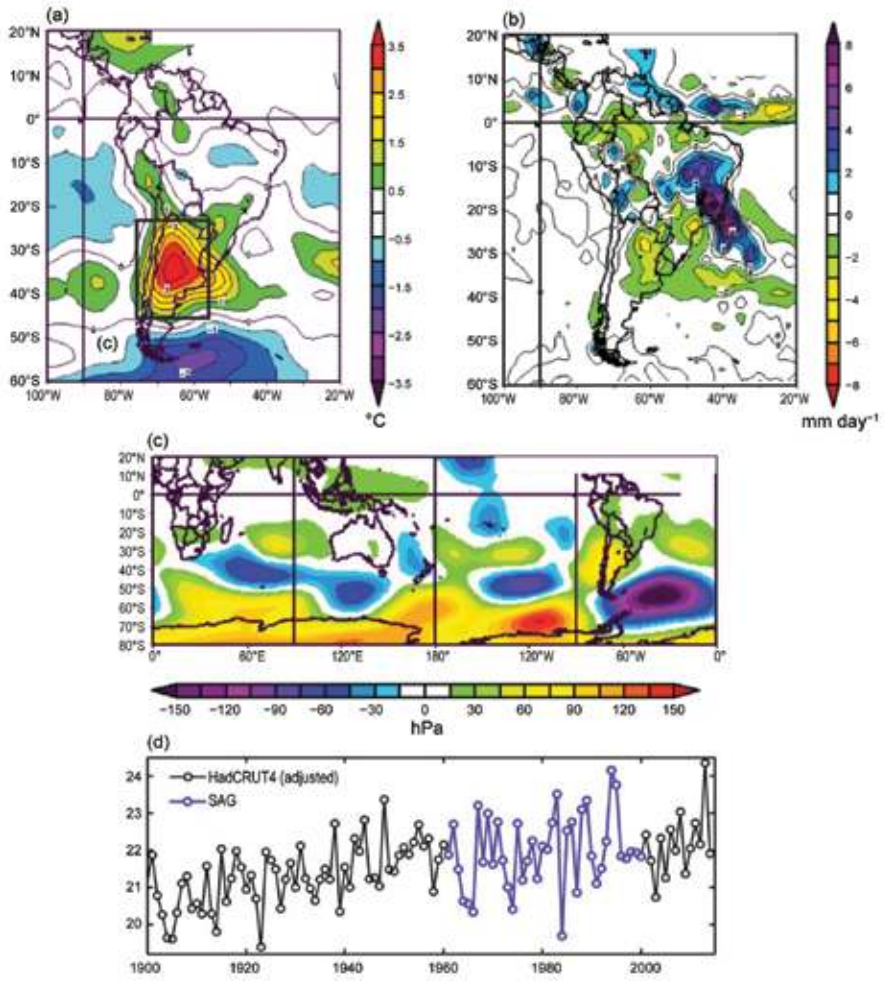

Fig. 9.1. Observations. (a,b,c) Atmospheric dynamics associated with the event: monthly anomalies with respect to 1981–2010 climatological average for Dec 2013 over South America (a,b) and Southern Hemisphere (c) obtained from NCEP–NCAR reanalysis dataset and plotted using the website esrl.noaa.gov/psd (NOAA/ESRL Physical Sciences Division, Boulder, CO, USA). (a) Surface temperature (°C). (b) Precipitation (mm day^{-1}). (c) Sea level pressure (hPa). (d) Time series of the temperature index Z (space-time average over the domain 23°–45°S, 75°–55°W, month of Dec) over the instrumental period obtained from SAG and HadCRUT4.

coverage and underwent a more detailed quality control than HadCRUT4.

Following standard practices for causal attribution (Allen 2003; Hannart et al. 2015), we analyzed whether and to what extent anthropogenic climate change changed the odds of a heat wave in central Argentina in December. We thus compared P1, the probability of occurrence of a heat wave under the observed climate conditions of 2013 (referred to as factual conditions) to P0, the same probability in the world as it might have been without anthropogenic climate change (referred to as counterfactual). For this purpose, we followed the method of Schaller et al. (2014) and we used the distributed computing framework weather@home to run the Met Office Hadley Centre atmosphere-only general circulation model HADAM3P (Massey et al. 2015), which has been shown to adequately represent some key features of atmospheric circulation over South America (Chou et al. 2012). We generated two ensembles: (i) observed climate conditions of 2013, forced with observed aerosols and greenhouse gas composition as well as SST and sea ice fraction values from 2013 obtained from the Operational Sea Surface Temperature and Sea Ice Analysis (OSTIA) dataset (Stark et al. 2007); (ii) counterfactual conditions, forced with preindustrial atmospheric gas composition, combined with the sea ice extent that corresponds to the year of maximum sea ice extent in each hemisphere of the OSTIA record, and with 11 different estimates of sea surface temperatures (SSTs) without human influence. These SSTs are obtained by subtracting 11 estimates of the human influence on SST from the 2013 OSTIA SST values. These 11 SST anomaly patterns are obtained by calculating the difference between nonindustrial and present-day simulations for available Coupled Model Intercomparison Project Phase 5 (CMIP5) models.

Two PDFs of the temperature index Z were estimated from these two ensembles, under Gaussian assumption. The so-called fraction of attributable risk (FAR = 1 – P0 / P1) was then derived; Hannart et al. (2015) have shown that in causal theory (Pearl 2000), the FAR may also be interpreted as the probability of necessary causation (PN) associated with

the causal link between the forcing and the event. A prominent feature of causal theory indeed consists of recognizing that causation corresponds to rather different situations and that three distinct facets of causality should be distinguished: (i) necessary causation, where the occurrence of the event requires that of the forcing but may also require other factors; (ii) sufficient causation, where the occurrence of the forcing drives that of the event but may not be required for the event to occur; (iii) necessary and sufficient causation, where (i) and (ii) both hold. The probability of necessary causation (PN) thus corresponds to only one of the three facets of causality, while the probability of sufficient causation PS = 1 − (1 − P1)/(1 − P0) is its second facet, and the probability of necessary and sufficient causation PNS = P1 − P0 summarizes both. With these definitions, the choice of the threshold on Z that defines occurrence has critical implications on the amount and nature of causal evidence (Fig. 9.2d). In the context of extreme event attribution, many different factors are usually necessary to trigger the occurrence of a rare event and, conversely, no single factor will ever hold as a sufficient explanation thereof: maximizing PN at the expense of PS is thus arguably a relevant approach in the present context. Here, this implies choosing the highest possible threshold for the index, that is 24.4°C (Fig. 9.2d).

Results. The observed time series over the period 1900–2014 is shown in Fig. 9.1d. The climatological mean calculated over the period 1961–90 is 21.9°C with anomalies ranging from −2.5°C in year 1923 to +2.5° C in year 2013, which is therefore the record high year over the instrumental period.

The factual and counterfactual PDFs are shown in Figs. 9.2a–c. They differ significantly, and their difference can be described quite straightforwardly: it merely consists of a ~1°C gap in their mean, while their dispersion, shape, and tails are roughly unchanged. Thereby, the intensity level of a heat wave is higher in the factual world than it would be in the counterfactual one for any return period, and the level is increased by 1°C no matter the return period. Figs. 9.2a,b emphasize this finding: one can see that the return level curves match well with each other, up to a 1°C translation. On the other hand, the tail behavior

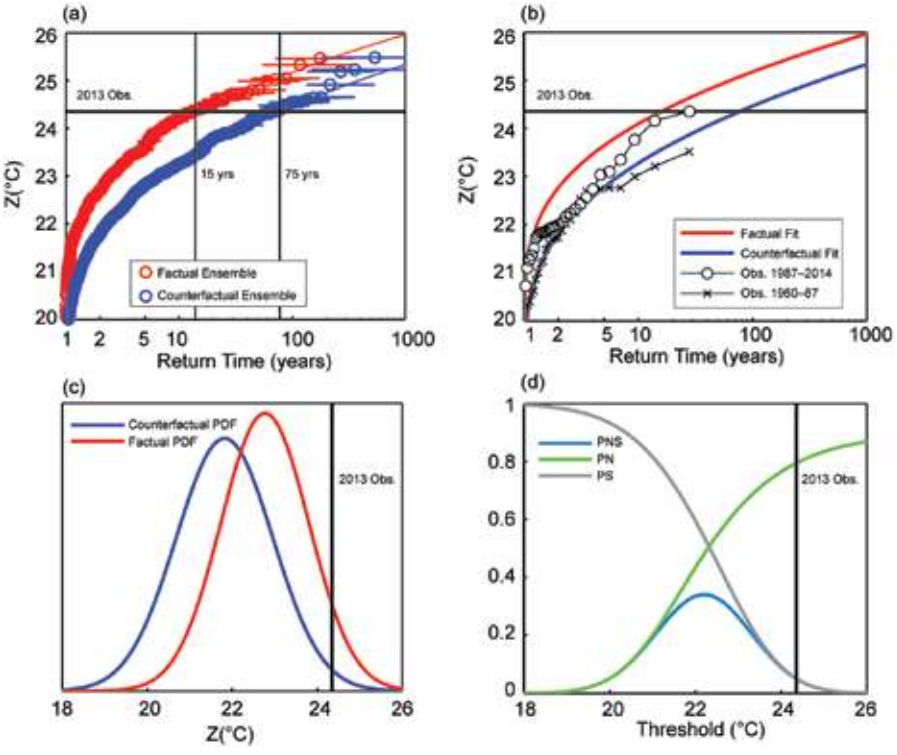

Fig. 9.2. Simulations. (a,b,c) Comparison of the factual vs counterfactual PDFs of the temperature index Z. (a) Return level curves simulated by HADAM3P: factual values (red dots) and counterfactual values (blue dots), 95% confidence interval (thin horizontal bars), Gaussian fit (red and blue lines), observed Dec 2013 value (thick horizontal black line), return periods (thin vertical black lines). (b) Same as (a) with superimposed observations over the 1960–87 (black line with crosses) and 1987–2014 (black line with circles) periods. (c) Factual and counterfactual PDFs of Z (Gaussian fit), observed Dec 2013 value (thick vertical black line). (d) PN, PS, and PNS as a function of the threshold used for event definition. Adopting a less restrictive definition (i.e., smaller threshold) decreases the level of necessity but increases that of sufficiency—which of these matters most depends on the purpose of the causal question (Hannart et al., 2015). A possible "multipurpose" approach is to balance both quantities, but this leads here to a substantially lower threshold (u = 22.3°C; 1.5 and 3.5 year return periods) which no longer reflects the extreme nature of the event and yields a well-balanced but not very stringent level of causal evidence. Maximizing PN at the expense of very low PS is arguably more relevant here, yielding PN = 0.8 and PS = 0.07.

of the two PDFs appears to be accurately described by a Gaussian distribution. The quality of the Gaussian fit is apparent in Fig. 9.2a where the empirical and the theoretical Gaussian return level curves are almost indistinguishable.

Figure 9.2b shows that simulated PDFs represent reasonably well the distribution of observed values without requiring any bias correction. Indeed, the return level curve obtained from observations over the period 1987–2014 (respectively 1960–87) appears to match decently well with the simulated return level curve in the factual (respectively counterfactual) world.

Discussion and conclusion. The value of the index reached in 2013 corresponds to a return period of 15 years in the factual world and a return period of 75 years in the counterfactual one (Fig. 9.2a): exceeding the intensity of the December 2013 heat wave thus appears to be five times more likely in the world as it was in 2013, than it was in the same world with no anthropogenic forcings.

This ratio corresponds to FAR = 80%, and it is consequently tempting to claim that 80% of the risk of the December 2013 heat wave is attributable to anthropogenic forcings. But this statement may be considered as a somewhat misleading interpretation. Indeed, the FARs associated to other causes, whether natural or anthropogenic, could be high as well. In any case, the FARs associated to the many causes of an extreme event are never bound to sum up to one, therefore the FAR can not be interpreted as a "share" of causality as the above statement suggests. It could thus be more appropriate to rename the acronym FAR into "fraction of additional risk."

Finally, the probabilistic definitions of causality recalled above offer yet a different causal interpretation and formulation. In the present case, PN = 0.8 and PS = 0.07 yields the statement that anthropogenic forcings were likely a necessary cause of the December 2013 heat wave, and yet were very likely not a sufficient cause thereof—a statement which clearly reflects the fact that other causal factors were involved in this event, and which may be shortened into "The Argentinian heat wave of December 2013 was likely caused in part by anthropogenic forcings."

ACKNOWLEDGEMENTS. We thank colleagues at the Oxford eResearch Centre and the Met Office Hadley Centre (PRECIS team) for their expertise, and the volunteers who have donated computing time to climateprediction.net. We gratefully acknowledge useful suggestions by three anonymous reviewers and an inspiring discussion with Peter Stott, which improved the manuscript. This research was supported by grant ANR-DADA (AH), and grants UBACyT 20020130100489BA and CONICET-PIP 11220120100536 (CV, BC).

REFERENCES

Allen, M. R., 2003: Liability for climate change. *Nature*, **421**, 891–892.

Cerne, B., and C. Vera, 2011: Influence of the intraseasonal variability on heat waves in subtropical South America. *Climate Dyn*., **36**, 2265–2277, doi:10.1007/s00382-010-0812-4.

——, ——, and B. Liebmann, 2007: The nature of a heat wave in eastern Argentina occurring during SALLJEX. *Mon. Wea. Rev*., **135**, 1165–1174.

Chou, S. C., and Coauthors, 2012: Downscaling of South America present climate driven by 4-member HadCM3 runs. *Climate Dyn*., **38**, 635–653, doi:10.1007/s00382-011-1002-8.

Hannart, A., J. Pearl, F. E. L. Otto, P. Naveau, and M. Ghil, 2015: Counterfactual causality theory for the attribution of weather and climate-related events. *Bull. Amer. Meteor. Soc*., doi:10.1175/BAMS-D-14-00034.1, in press.

Massey, N., and Coauthors, 2015: weather@home—development and validation of a very large ensemble modelling system for probabilistic event attribution. *Quart. J. Roy. Meteor. Soc*. **141**, 1528–1545, doi:10.1002/qj.2455.

Morice, C. P., J. J. Kennedy, N. A. Rayner, and P. D. Jones, 2012: Quantifying uncertainties in global and regional temperature change using an ensemble of observational estimates: The HadCRUT4 dataset. *J. Geophys. Res*., **117**, D08101, doi:10.1029/2011JD017187.

Pearl, J., 2000: *Causality: Models, Reasoning and Inference*. Cambridge University Press, 484 pp.

Perkins, S. E., L. V. Alexander, and J. R. Nairn, 2012: Increasing frequency, intensity and duration of observed global heatwaves and warm spells. *Geophys. Res. Lett*., **39**, L20714, doi:10.1029/2012GL053361.

Rusticucci, M., 2012: Observed and simulated variability of extreme temperature events over South America. *Atmos. Res*., **106**, 1–17, doi:10.1016/j.atmosres.2011.11.001.

——, J. Kyselý, G. Almeira, and O. Lhotka, 2015: Long-term variability of heat waves in Argentina and recurrence probability of the severe 2008 heat wave in Buenos Aires. *Theor. Appl. Climatol.*, doi:10.1007/s00704-015-1445-7, in press.

Schaller, N., F. E. L. Otto, G. J. van Oldenborgh, N. R. Massy, S. Sparrow, and M. R. Allen, 2014: The heavy precipitation event of May–June 2013 in the upper Danube and Elbe basins [in "Explaining Extreme Events of 2013 from a Climate Perspective"]. *Bull. Amer. Meteor. Soc.*, **95** (9), S69–S72.

Seneviratne, S. I., and Coauthors, 2012: Changes in climate extremes and their impacts on the natural physical environment. *Managing the Risks of Extreme Events and Disasters to Advance Climate Change Adaptation*, C. B. Field et al., Eds., Cambridge University Press, 109–230.

Stark J. D., C. J. Donlon, M. J. Martin, and M. E. McCulloch, 2007: OSTIA: An operational, high resolution, real time, global sea surface temperature analysis system. *Oceans 2007 – Europe*, Aberdeen, Scotland, IEEE, 331–334, doi:10.1109/OCEANSE.2007.4302251.

Tencer, B., M. Rusticucci, P. D. Jones, and D. Lister, 2011: A southwestern South American daily gridded data set of observed surface minimum and maximum surface temperature for 1960–2000. *Bull. Amer. Meteor. Soc.*, **92**, 1339–1346, doi:10.1175/2011BAMS3148.1.

10. EXTREME RAINFALL IN THE UNITED KINGDOM DURING WINTER 2013/14: THE ROLE OF ATMOSPHERIC CIRCULATION AND CLIMATE CHANGE

Nikolaos Christidis and Peter A. Stott

Extreme winter rainfall in the United Kingdom becomes eight times more likely when the atmospheric circulation resembles winter 2013/14, whereas anthropogenic influence is only discernible in extremes with a shorter duration.

Introduction. The winter of 2013/14 in the United Kingdom was characterized by an exceptional clustering of vigorous storms driven by the North Atlantic jet stream. The jet stream, in turn, gained momentum from this sequence of low pressure systems and was about 30% stronger than in recent decades (Slingo et al. 2014). The succession of deep depressions triggered tidal surges across coastal parts of the country, while the sustained rainfall over saturated ground culminated in widespread floodplain inundations, pronounced river flows, and record accumulated runoff totals (Huntingford et al. 2014). Coastal erosion and extended flooding led to damage in transport infrastructure and to business and residential properties and cost the U.K. government more than GBP 560 million in recovery schemes (DCLG 2014).

The positioning of a more southerly storm track increased the amount of moisture steered towards the United Kingdom over the winter season. Apart from a possible contribution from the positive phase of the North Atlantic Oscillation, possible drivers of the severe winter weather originating in the tropics have also been identified. The strengthening of the Atlantic jet stream may, for example, be linked to anomalously high precipitation in the West Pacific akin to La Niña conditions via Rossby wave interactions (Ineson and Scaife 2009) and the establishment of a pronounced temperature gradient between North America and the tropical Atlantic (Palmer and Owen 1986). The strong westerly phase of the Quasi-Biennial Oscillation during boreal winter may be another possible contributor to excessive storminess in the United Kingdom (Marshall and Scaife 2009). Although an increase in the number of deep winter depressions driven to the United Kingdom from the mid-latitude North Atlantic has not been established, new evidence suggests an increase in their intensity since the 1870s (Wang et al. 2013).

The aspect of the extreme event that we focus on in our study is rainfall. Persistent storminess throughout winter resulted in the highest rainfall amount averaged over the entire U.K. land area since 1931, as estimated with the HadUKP observational dataset (Alexander and Jones 2001). Here we consider a wider U.K. region (10°W–2°E, 48°–60°N) that is better resolved by global climate models. Rainfall data from the NCEP–NCAR reanalysis (Kalnay et al. 1996) indicate that 2013/14 was the wettest winter in the region (Fig. 10.1a) since the beginning of the record in 1948. In addition to the seasonal mean, we also employ an index for shorter events (R10x), defined as the wettest period during the year over 10 consecutive winter days. Estimates of R10x with reanalysis data also show a maximum in 2013/14 (Fig. 10.1b). The reanalysis data used here are found to be in good agreement with HadUKP. Emerging evidence suggests an increase in the frequency and intensity of extreme U.K. rainfall (Jones et al. 2013; Maraun et al. 2008), consistent with the detection of human influence on changes in extreme precipitation over larger spatial scales (Zhang et al. 2013).

Our study investigates how the interplay between anthropogenic forcings and the circulation pattern prevalent in winter 2013/14 (Fig. 10.1e) may impact the likelihood of extremely high precipitation (seasonal and R10x) in the U.K. region. We set out to answer two questions: 1) Are rainfall extremes more likely under a persistent southwesterly flow? 2) Given the characteristic winter circulation pattern, does human influence favor the occurrence of extremes? A

AFFILIATIONS: Christidis and Stott—Met Office Hadley Centre, Exeter, United Kingdom

DOI:10.1175/BAMS-D-15-00094.1

A supplement to this article is available online (10.1175/BAMS-D-15-00094.2)

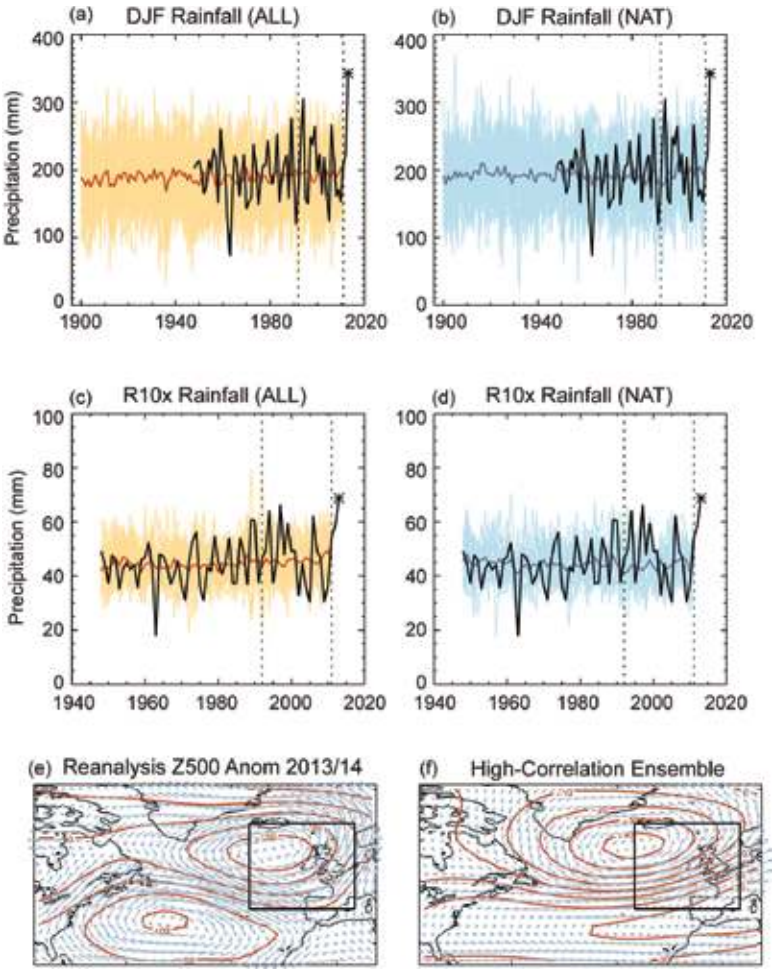

Fig. 10.1. Rainfall in the U.K. region (10°W–2°E, 48°–60°N). Panels (a)–(d) illustrate the time series of the regional DJF rainfall (a,b) and the R10x index (c,d). Time series with data from the NCEP–NCAR reanalysis are plotted in black, and 2013/14 is marked by an asterisk. Time series from model simulations with all forcings (ALL) and natural forcings (NAT) only are shown in orange (a,c) and blue (b,d) respectively. The means of the ALL and NAT simulations are represented by the red and dark blue lines respectively. The vertical dotted lines mark the last 20 years of the model simulations used in the study to represent the recent climate. Panels (e)–(f) depict the geopotential height (red lines) and wind (blue arrows) winter mean anomalies at 500 hPa relative to the climatological period 1961–90. The map shown in panel (e) is constructed with NCEP–NCAP reanalysis data for 2013/14 and the one in panel (f) with the mean of winters extracted from the last 20 years of simulations with the ALL experiment, for which the circulation pattern correlates well (coefficient greater than 0.6) with the 2013/14 reanalysis pattern over the region marked by the black box.

complementary analysis with an atmosphere-only model driven by prescribed oceanic conditions indicates that anthropogenic climate change increased the chance of getting an extremely wet winter in 2013/14 in parts of the United Kingdom (Shiermeier 2014). Following up, we employ coupled models that span the full range of possible oceanic conditions in an attempt to disentangle the possible contributions from synoptic conditions and externally forced factors.

Data and Methods. We estimate changes in the frequency of extreme rainfall based on simulations with models that contributed data to the Coupled Model Intercomparison Project Phase 5 (CMIP5). We use two multimodel ensembles of simulations, one with the effect of both natural and anthropogenic forcings and one without the anthropogenic effect. A total of seven models are employed for which both types of experiments are available (details in online supplemental material). The models provide 43 simulations with all forcings (ALL) and 33 with natural forcings only (NAT) that end in 2012. Values of R10x are estimated with fewer simulations, as two of the models did not provide the necessary daily rainfall data. As in previous work, a bias correction is applied to the data of each model to bring the simulated rainfall averaged over a climatological period (1961–90) in agreement with the reanalysis (Christidis et al. 2013). Model evaluation assessments (online supplemental material) indicate that the ALL simulations used here produce realistic rainfall distributions and return times of extreme seasonal and 10-day long events. Modeled time series of winter (December–February, or DJF) rainfall and R10x generally encompass the range of the reanalysis data (Figs. 10.1a–d), though the DJF maximum of 2013/14 is only exceeded once in a single NAT simulation. No notable long-term change is evident in the time series. However, we find that the least-square fit to the ensemble mean of the model simulations yields trends that are significantly different than zero for both DJF and

R10x, but only when human influence is accounted for.

Samples of DJF rainfall and R10x are generated by selecting the last 20 years of the simulations (marked by the dotted vertical lines in Figs. 10.1a–d), as a proxy of the near-present-day climate. Ideally, the selected period should be centered on the year of the event, but this is not possible as the NAT simulations are not extended beyond 2012. Given the small trends in rainfall, years of the recent past should represent current climatic conditions sufficiently well, as also assumed in other studies (Christidis et al. 2015). We next partition the modeled winters between those that correlate well with the 2013/14 circulation patterns over a wider U.K. region shown in Fig. 10.1e (correlation coefficients above 0.6) and those with weaker correlations. We thus create high- and low-correlation ensembles with ALL and NAT forcings, which we later use to construct rainfall distributions and obtain likelihood estimates for extreme events. Figure 10.1f shows the 500-hPa field averaged over the winter season that corresponds to the mean of the high-correlation ensemble with ALL forcings, which displays a distinct southwesterly flow into the United Kingdom similar to winter 2013/14 (Fig. 10.1e). In contrast, the mean circulation estimated from all the winters extracted from the ALL simulations displays a more zonal flow, which agrees well with the climatological pattern from reanalysis data (online supplemental material).

Results. We first compare rainfall distributions with strong and weak correlations to the 2013/14 general circulation pattern in the "real world," that is, under the influence of all climatic forcings (Figs. 10.2a,c). The characteristic flow increases the chance of heavy rainfall as the distribution shifts towards a wetter regime. A two-sided Kolmogorov–

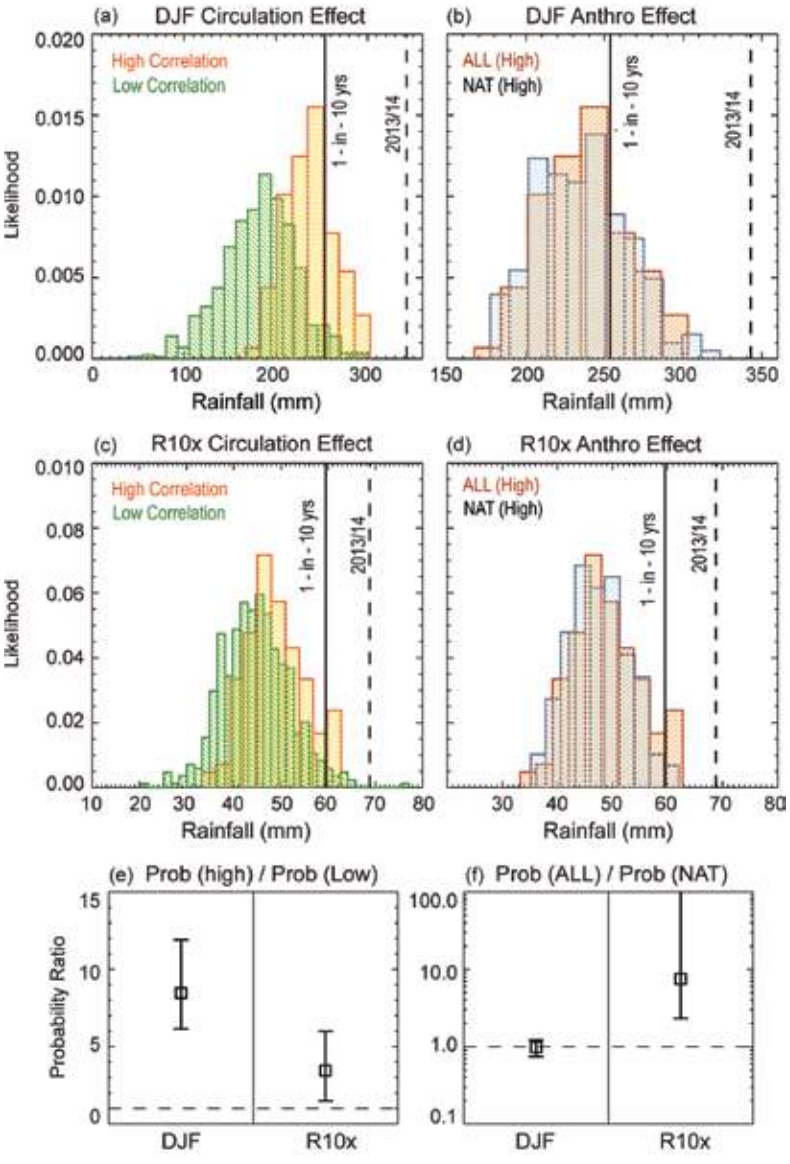

Fig. 10.2. The impact of the 2013/14 winter circulation pattern and anthropogenic forcings on DJF rainfall and R10x. Panels (a) and (c) illustrate the DJF and R10x rainfall distributions in the near-present-day climate based on simulated winters with high (orange) and low (green) correlations with the 2013/14 flow pattern. Panels (b) and (d) also illustrate the DJF and R10x rainfall distributions but for high-correlation cases only from model experiments with (red) and without (blue) anthropogenic forcings. A rainfall event is classified as extreme if the rainfall exceeds the amount associated with a 1-in-10-yr event (vertical black lines) estimated with reanalysis data since 1948. The 2013/14 rainfall amount is represented by the vertical dashed line. The distributions in panels (a)–(d) are constructed from simulated winters during the 1993–2012 period. Panel (e) shows the change in the likelihood of occurrence of extreme events under the influence of a circulation flow similar to 2013/14. Panel (f) shows the change in the likelihood due to anthropogenic forcings when the winter flow resembles the one of 2013/14. Best estimates of the change in the likelihood are marked by the square symbols and the 5%–95% uncertainty range by the vertical whiskers. The dashed horizontal line marks the ratio of 1, which suggests no likelihood change.

Smirnov test applied to the high- and low-correlation distributions confirms that they are significantly separated (near-zero p values). We next quantify how differences in the circulation may change the likelihood of an extreme event, defined as a 1-in-10-yr return level and estimated with reanalysis data since 1948/49. We compute the probabilities of exceeding the threshold using the generalised Pareto Distribution if the threshold lies at the tails. Uncertainties in the probability estimates are derived using a Monte Carlo bootstrap procedure (Christidis et al. 2013; online supplemental material). Figure 10.2e shows that in winters with circulation patterns similar to 2013/14 the chance of extreme rainfall increases by a factor of about eight for DJF and three for R10x. The effect is greater for DJF, as the persistent pattern leads to high accumulated rainfall over the whole season, whereas extreme precipitation over shorter time scales may in some years be associated with conditions not necessarily representative of the whole season.

Figures 10.2b,d,f illustrate the effect of human influence on extreme rainfall for synoptic conditions similar to 2013/14. The ALL and NAT (high-correlation) ensembles are not distinguishable for both DJF and R10x based on Kolmogorov–Smirnov tests (p values greater than 0.2). However, a minor (not statistically significant) shift to wetter conditions due to anthropogenic forcings is identified for R10x, translating to an increase in the chances of getting an extreme event by a factor of about seven. No change in the likelihood is found for DJF. Consistent with our findings, a larger ensemble of CMIP5 models shows no significant change in rainfall over the United Kingdom during cold seasons until the second half of the century, when wet winters are projected to increase in frequency (van Oldenborgh et al. 2013).

Conclusions. The prevalent southwesterly flow over the United Kingdom in winter 2013/14 provided favorable conditions for extreme rainfall. Although the atmosphere can hold more water in a warming climate (Allan and Soden 2008), associated rainfall increases are more difficult to detect on small (e.g., sub-continental, regional) scales. Here, we find some evidence for a human-induced increase in extreme winter rainfall in the United Kingdom, for events with time scales of 10 days.

ACKNOWLEDGMENTS. This work was supported by the Joint DECC/Defra Met Office Hadley Centre Climate Programme (GA01101) and the EUCLEIA project funded by the European Union's Seventh Framework Programme [FP7/2007-2013] under Grant Agreement No. 607085.

REFERENCES

Alexander, L. V., and P. D. Jones, 2001: Updated precipitation series for the U.K. and discussion of recent extremes. *Atmos. Sci. Lett.*, **1**, 142–150.

Allan, R. P., and B. J. Soden, 2008: Atmospheric warming and the amplification of precipitation extremes. *Science*, **321**, 1481–1484.

Christidis, N., P. A. Stott, A. Scaife, A. Arribas, G. S. Jones, D. Copsey, J. R. Knight, and W. J. Tennant, 2013: A new HadGEM3-A based system for attribution of weather and climate-related extreme events. *J. Climate*, **26**, 2756–2783, doi:10.1175/JCLI-D-12-00169.1.

——, ——, and F. W. Zwiers, 2015: Fast-track attribution assessments based on pre-computed estimates of changes in the odds of warm extremes. *Climate Dyn.*, doi:10.1007/s00382-014-2408-x, in press.

DCLG, 2014: Winter 2013/14 severe weather recovery report. Department for Communities and Local Government [UK], 35 pp. [Available online at www.gov.uk/government/publications/winter-2013-to-2014-severe-weather-recovery-progress-report].

Huntingford, C., and Coauthors, 2014: Potential influences on the United Kingdom's floods of winter 2013/14. *Nat. Climate Change*, **4**, 769–777, doi:10.1038/nclimate2314.

Ineson, S., and A. A. Scaife, 2009: The role of the stratosphere in the European climate response to El Niño. *Nat. Geosci.*, **2**, 32–36.

Jones, M. R., H. J. Fowler, C. G. Kilsby, and S. Blenkinsop, 2013: An assessment of changes in seasonal and annual extreme rainfall in the UK between 1961 and 2009. *Int. J. Climatol.*, **33**, 1178–1194, doi:10.1002/joc.3503.

Kalnay, E., and Coauthors, 1996: The NCEP/NCAR 40-year reanalysis project. *Bull. Amer. Meteor. Soc.*, **77**, 437–470.

Maraun, D., T. J. Osborn, and N. P. Gillett, 2008: United Kingdom daily precipitation intensity: improved early data, error estimates and an update from 2000 to 2006. *Int. J. Climatol.*, **28**, 833–842.

Marshall, A. G., and A. A. Scaife, 2009: Impact of the QBO on surface winter climate. *J. Geophys. Res.*, **114**, D18110, doi:10.1029/2009JD011737.

Palmer, T. N., and J. A. A. Owen, 1986: A possible relationship between some severe winters in North America and enhanced convective activity over the tropical west-Pacific. *Mon. Wea. Rev.*, **114**, 648–651.

Schiermeier, Q., 2014: Climate change makes extreme weather more likely to hit UK. *Nature News*, doi:10.1038/nature.2014.15141.

Slingo, J., and Coauthors, 2014: The recent storms and floods in the UK. Met Office and Centre for Ecology and Hydrology, 27 pp. [Available online at www.metoffice.gov.uk/media/pdf/1/2/Recent_Storms_Briefing_Final_SLR_20140211.pdf.]

van Oldenborgh, G. J., and Coauthors, Eds., 2103: Annex I: Atlas of global and regional climate projections. *Climate Change 2013: The Physical Basis.* T. F. Stocker et al., Eds., Cambridge University Press, 1311–1393.

Wang, X. L., Y. Feng, G. P. Compo, V. R. Swail, F. W. Zwiers, R. J. Allan, and P. D. Sardeshmukh, 2013: Trends and low frequency variability of extra-tropical cyclone activity in the ensemble of twentieth century reanalysis. *Climate Dyn.*, **40**, 2775–2800, doi:10.1007/s00382-012-1450-9.

Zhang, X., H. Wan, F. W. Zwiers, G. C. Hegerl, and S.-K. Min, 2013: Attributing intensification of precipitation extremes to human influence. *Geophys. Res. Lett.*, **40**, 5252–5257, doi:10.1002/grl.51010.

11. HURRICANE GONZALO AND ITS EXTRATROPICAL TRANSITION TO A STRONG EUROPEAN STORM

Frauke Feser, Monika Barcikowska, Susanne Haeseler, Christiana Lefebvre, Martina Schubert-Frisius, Martin Stendel, Hans von Storch, and Matthias Zahn

After transitioning from a hurricane to an extratropical storm, Gonzalo tracked unusually far, achieving exceptional strength over Europe; however, it was within the historical range of such transforming storms.

Introduction. Recent studies simulating continued anthropogenic climate change provide evidence that extratropically transitioning tropical cyclones (TCs) will become more frequent and will hit western Europe more often (Baatsen et al. 2015; Haarsma et al. 2013). Mokhov et al. (2014) asserted, "Under the tendency towards global warming, we can expect an increase in the number of intensive cyclones in the warmer and more humid troposphere." We saw Hurricane Gonzalo of 2014 as an occasion to assess if these aforementioned properties of extratropically transitioned storms—frequency, intensity, and tracks—have changed.

East of the Leeward Islands a tropical depression formed on 12 October 2014. On its way it passed through the northern Leeward Islands and intensified to a category 4 hurricane (Saffir-Simpson hurricane wind scale) on 16 October, known as "Gonzalo". After changing its direction to northeast, Gonzalo weakened and crossed Bermuda with gusts of more than 200 km h^{-1} and heavy rains of about 70 mm within 24 hours. On 19 October, the storm transitioned to an extratropical cyclone off the coast of Newfoundland (Brown 2015). While continuing its path across the North Atlantic towards northwestern Europe, the cyclone was absorbed by a cold front and strengthened again. Afterwards, it hit the northern part of the United Kingdom on 21 Octber. It crossed the North Sea and then central parts of Europe, and went down to the Balkans. On 23 October ex-Gonzalo merged with another low pressure system that led to heavy precipitation for several days in this region. Maximum wind gusts between 100 and 180 km h^{-1}, causing North Sea storm surges, were reported from several countries[1,2,3]. In addition, ex-Gonzalo triggered regional precipitation amounts of 50–100 mm in 24 hours, while the advection of cold air led to a sudden temperature drop with snowfall in some areas. Gonzalo and its remnants caused several fatalities, storm surges, structural damage, and power outages on both sides of the Atlantic[4,5]. Gonzalo attracted strong media attention as it affected many countries along its path[6].

There is no general definition of extratropical transition (ET) of TCs (Malmquist 1999). Basically, it is a gradual transformation of a TC into a system with extratropical characteristics while moving poleward into a more baroclinic environment with higher wind shear, a larger Coriolis parameter, and lower sea surface temperatures (Jones et al. 2003). The ET storm may interact with upper-level troughs or extratropical low pressure systems. Evans and Hart (2003) describe ET as the transition of a warm-core TC that interacts with a baroclinic midlatitude environment and then develops a cold core. Forty-six percent of the Atlantic TCs transitioned into extratropical cyclones between 1950 and 1996 (Hart and Evans 2001). This result was supported by Jones et al. (2003) for 1970–99 and Mokhov et al. (2014) for 1970–2012 who found 45% of North Atlantic TCs underwent ET. But only very few

AFFILIATIONS: Feser, Schubert-Frisius, Von Storch, and Zahn—Institute for Coastal Research, Helmholtz-Zentrum Geesthacht, Centre for Materials and Coastal Research, Geesthacht, Germany; Barcikowska—Princeton Environmental Institute, Princeton University, New Jersey; Haeseler, and Lefebvre—Deutscher Wetterdienst (DWD), Hamburg, Germany; Stendle— Danish Climate Centre, Danish Meteorological Institute, Copenhagen, Denmark

DOI:10.1175/BAMS-D-15-00122.1

[1]www.bsh.de/de/Meeresdaten/Vorhersagen/Sturmfluten/Berichte/Sturmflut_nordsee_22_10_2014.pdf (in German)
[2]http://blog.metoffice.gov.uk/2014/10/21/top-uk-wind-speeds-as-gonzalos-remnants-felt/
[3]www.meteofrance.fr/actualites/15846766-retour-de-la-fraicheur-sur-l-hexagone (in French)
[4]www.munichre.com/site/corporate/get/documents_E1520419191/mr/assetpool.shared/Documents/5_Touch/_Publications/302-08605_de.pdf (in German)
[5]www.deutscherueck.de/fileadmin/user_upload/Sturmdoku_2014_WEB.pdf (in German)
[6]www.gdacs.org/media.aspx?eventid=1000112&episodeid=30&eventtype=TC

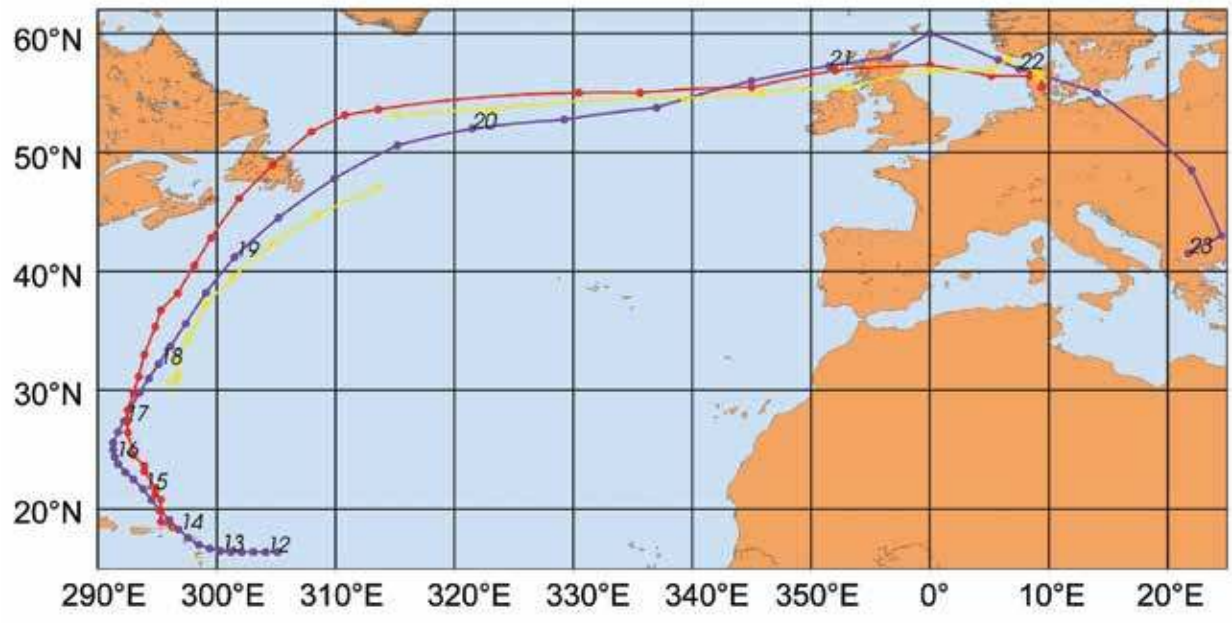

Fig. 11.1. Tracks of Hurricane Gonzalo in the GCM long-term (yellow) and short-term (red) simulations. Observed tracks of surface pressure from NOAA (Brown 2015) and the Deutscher Wetterdienst global weather forecast model assimilation fields, interpolated to a 0.25° grid (purple, numbers represent days in October 2014 at 0:00 UTC).

transitioned storms continue tracking into Europe; most extratropically transitioning cyclones decay west of 10°W over the Atlantic (Hart and Evans 2001).

Climate perspective. To answer the question whether the characteristics of ET have changed over the past decades, homogeneous datasets are necessary in order to derive long-term statistics. Mokhov et al. (2014) estimated changes of ET of TCs between 1970 and 2012 over the North Atlantic and found an increase in the number of transformed cyclones by 1 in 10 to 11 years. A climatology of ET of Atlantic TCs was given by Hart and Evans (2001). The annual frequency of transitioning TCs from 1950 to 1996 showed some year-to-year variability, but no trend was described. Hart and Evans (2001) analyzed best track data, which provide TC track location and intensity information. These are based on various meteorological measurements, aircraft reconnaissance, and satellite data in more recent decades. Since best track data often do not depict the storm after transition to an extratropical storm, reanalysis data was added to complete the climatology. But reanalysis data may contain inhomogeneities due to changes in observational density or instrumentation (Krueger et al. 2013; Landsea 2007). For instance, the addition of satellite data in November 1978 provided better observational coverage and thus improved statistics (Truchelut et al. 2013; Vecchi and Knutson 2011).

A relatively new approach applies the well-established spectral nudging method to constrain global climate models with global large-scale reanalyses to derive a global high-resolution reconstruction for the atmosphere and the land surface (Yoshimura and Kanamitsu 2008; Kim and Hong 2012). The idea is to minimize the introduction of inhomogeneities as only very few meteorological variables at larger scales and higher atmospheric layers are nudged. Here we nudge only vorticity and divergence of the general circulation model (GCM) ECHAM6 (Giorgetta et al. 2013) towards the NCEP/NCAR reanalysis (Kalnay et al. 1996) for the time period 1948–2014. Reanalysis datasets tend to underestimate TC intensity and this underestimation cannot be attributed merely to the coarse resolution of the reanalysis data (Schenkel and Hart 2012). Underestimated TC intensities are also apparent in the forcing reanalysis of this study, which lead to weaker intensities also for the GCM simulation. Even though absolute TC intensity values can therefore not be directly compared to observations, the consistency and homogeneity of this dataset allows for a climatology and analysis of the number of storms and changes in intensity and tracks during the last decades.

The ECHAM6 data (about 78-km grid distance and 95 levels) was tracked with a relatively simple algorithm, which first localizes maxima in absolute values of spatially filtered 925-hPa vorticity fields, and

then joins these locations to tracks if the distance to the maximum of the next time step is less than 250 km. Finally three further criteria are applied: wind speed needs to exceed 15 m s^{-1} at least once along the track, tracks may not exist alongside land grid points in more than 50% of their positions, and they must evolve south of 32°N in the Atlantic and decay north of 40°N. In the long-term ECHAM6 simulation, Gonzalo is represented as a TC which weakens too much during ET so that it cannot be tracked as a single storm including the extratropical phase (Fig. 11.1). Nevertheless, a three-month test simulation using the same GCM settings showed a realistic representation of Gonzalo's track (Fig. 11.1). For regional climate simulations spectral nudging leads to similar large-scale weather systems, regardless when the simulation was started (Weisse and Feser 2003; Feser and von Storch 2008). Spectral nudging has less control in this GCM run. We therefore put Gonzalo from this short simulation into a climatological context with the long-term simulation. The ET climatology was found to be comparable to the one given by Hart and Evans (2001), though the GCM gives slightly higher storm numbers (Fig. 11.2a, on average 5.4 to 4.1 storms per year). This is a result of the chosen wind speed tracking threshold of 15 m s^{-1} which we used throughout the study, a higher threshold would return smaller storm numbers. The GCM simulation shows a small increase of about one storm for the whole period of 67 years. For the entire time span 1979–93 the study of Hart and Evans (2001) shows an increase of 0.38 compared to an increase of 0.21 in ECHAM6. In the simulation, 220 ET storms are weaker than Gonzalo, 146 are stronger though. There is some year-to-year variability (between 0 and 7 storms stronger or weaker than Gonzalo) in intensity, no trend for storms weaker than Gonzalo, but a small trend (0.94 over the whole time period) for stronger ones was found (Fig. 11.2b). Baatsen et al. (2015) report that an expansion and eastward shift of the TC genesis region leads to more intense tropical cyclones and it increases their chances of reaching Europe for future climate conditions. In this study, the fixed tracking algorithm latitude constraints prevent any conclusions for a potential northward expansion of the genesis area, but an expansion towards lower latitudes was found. This

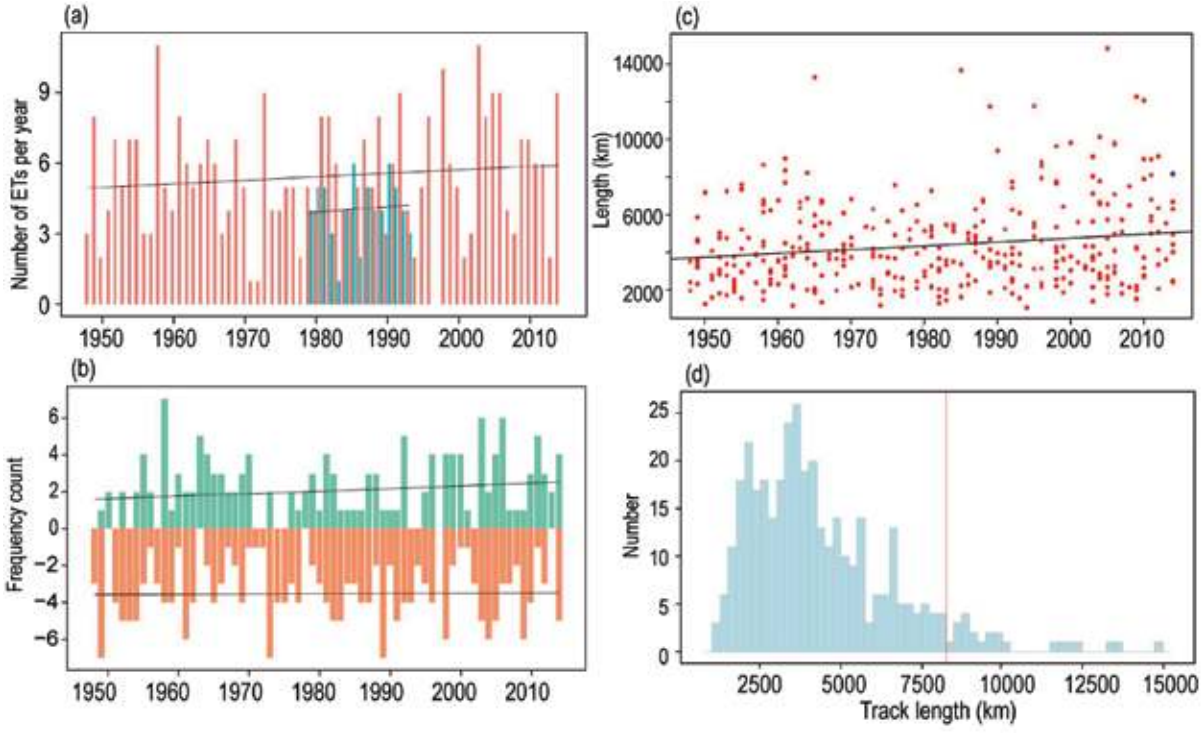

Fig. 11.2. Results from ECHAM6 multidecadal hindcast. (a) Annual numbers and trends of extratropically transitioning cyclones with a wind speed threshold of 15 m s^{-1} in the ECHAM6 simulation (red) and the study of Hart and Evans (2001) (blue); (b) numbers and trends of ET storms stronger (green) or weaker (orange) than Gonzalo (maximum simulated wind speed 22.6 m s^{-1}); (c) track lengths (km) of ET cyclones for the last decades and corresponding trend line (Gonzalo is marked as blue dot); and (d) histogram of ET cyclone track lengths in km (red line indicates Gonzalo).

change is caused by increasing numbers of cyclones which develop closer to the equator since the late 1980s. Track lengths (Fig. 11.2c) and durations (not shown) showed an increase of about 30% (1364.79 km) and of 2.4 days over the 67 years. Gonzalo ranks among the top 7% (23 out of 367 ET storms had longer tracks) in track length (Fig. 11.2d).

Conclusions. Gonzalo was a strong (category 4) hurricane in the Atlantic that underwent an ET and then headed for Europe. Within the last decades, the number of ET did increase marginally, both in the GCM simulation and the climatology of Hart and Evans (2001). The storm featured high intensities for most of its lifetime. The intensities of ET cyclones showed no trends for storms weaker than Gonzalo while a slight increase was deduced for storms that are stronger. The track of Gonzalo was also somewhat unusually long, ranking among the 7% longest-tracked of all extratropically transitioning TCs during the last 67 years. The simulated track lengths do show an increasing trend over time. For assessing if we may consider the present storm as an indication of a change, we can do two things: one is to assess if it is within the limits of what we have seen in the recent past, and the second, if certain characteristics are described in scenario simulations as more, or less, frequent than in control simulations. The latter would employ the methodology of event attribution (e.g., Stott et al. 2015, manuscript submitted to Wiley Interdiscip. Rev.: Climate Change), and the needed multiple high-resolution simulations do not exist at this time. Thus, we are attempting to answer the former "detection" question, by determining how anomalous the present event is given the cases of the past 67 years. It turns out the event is a rare event, albeit not an unprecedented one (similarly to the analysis of another European windstorm, see von Storch et al. 2014)

ACKNOWLEDGMENTS. The work was partly supported through the Cluster of Excellence "CliSAP" (EXC177), Universität Hamburg, funded through the German Research Foundation (DFG). It is a contribution to the Helmholtz Climate Initiative REKLIM (Regional Climate Change), a joint research project of the Helmholtz Association of German research centres (HGF). The German Climate Computing Center (DKRZ) provided the computer hardware for the ECHAM6 simulation in the project "global high resolution climate reconstructions" which was funded by the Federal Ministry of Education and Research (BMBF). We thank Dr. Helmut Frank from Deutscher Wetterdienst (DWD) for computing the storm track by global model forecast assimilation fields.

REFERENCES

Baatsen, M., R. J. Haarsma, A. J. Van Delden, and H. de Vries, 2015: Severe autumn storms in future western Europe with a warmer Atlantic Ocean. *Climate Dyn.*, **45**, 949–964, doi:10.1007/s00382-014-2329-8.

Brown, D. P., 2015: Hurricane Gonzalo (AL082014): 12 – 19 October 2014. National Hurricane Center tropical cyclone report, 30 pp. [Available online at www.nhc.noaa.gov/data/tcr/AL082014_Gonzalo.pdf.]

Evans, J. L., and R. E. Hart, 2003: Objective indicators of the life cycle evolution of extratropical transition for Atlantic tropical cyclones. *Mon. Wea. Rev.*, **131**, 909–925.

Feser, F., and H. von Storch, 2008: A dynamical downscaling case study for typhoons in SE Asia using a regional climate model. *Mon. Wea. Rev.*, **136**, 1806–1815.

Giorgetta, M. A., and Coauthors, 2013: The atmospheric general circulation model ECHAM6: Model description. Berichte zur Erdsystemforschung (Reports on Earth system science) 135, Max Planck Institute for Meteorology, 172 pp. [Available online at www.mpimet.mpg.de/fileadmin/publikationen/Reports/WEB_BzE_135.pdf.]

Haarsma, R. J., W. Hazeleger, C. Severijns, H. de Vries, A. Sterl, R. Bintanja, G. J. van Oldenborgh, and H. W. van den Brink, 2013: More hurricanes to hit western Europe due to global warming. *Geophys. Res. Lett.*, **40**, 1783–1788, doi:10.1002/grl.50360.

Hart, R. E., and J. L. Evans, 2001: A climatology of the extratropical transition of Atlantic tropical cyclones. *J. Climate*, **14**, 546–564.

Jones, S. C., and Coauthors, 2003: The extratropical transition of tropical cyclones: Forecast challenges, current understanding, and future directions. *Wea. Forecasting*, **18**, 1052–1092.

Kalnay, E., and Coauthors, 1996: The NCEP/NCAR 40-year reanalysis project. *Bull. Amer. Meteor. Soc.*, **77**, 437–471.

Kim, J.-E., and S.-Y. Hong, 2012: A global atmospheric analysis dataset downscaled from the NCEP–DOE reanalysis. *J. Climate*, **25**, 2527–2534, doi:10.1175/JCLI-D-11-00534.1.

Krueger, O., F. Schenk, F. Feser, and R. Weisse, 2013: Inconsistencies between long-term trends in storminess derived from the 20CR reanalysis and observations. *J. Climate*, **26**, 868–874, doi:10.1175/JCLI-D-12-00309.1.

Landsea, C. W., 2007: Counting Atlantic tropical cyclones back to 1900. *Eos, Trans. Amer. Geophys. Union*, **88**, 197–208.

Malmquist, D. L., 1999: Meteorologists and insurers explore extratropical transition of tropical cyclones. *Eos, Trans. Amer. Geophys. Union*, **80**, 79–80, doi:10.1029/99EO00055.

Mokhov, I. I., E. M. Dobryshman, and M. E. Makarova, 2014: Transformation of tropical cyclones into extratropical: The tendencies of 1970–2012. *Dokl. Earth Sci.*, **454**, 59–63, doi:10.1134/S1028334X14010127.

Schenkel, B. A., and R. A. Hart, 2012: An examination of tropical cyclone position, intensity, and intensity life cycle within atmospheric reanalysis datasets. *J. Climate*, **25**, 3453–3475, doi:10.1175/2011JCLI4208.1.

Truchelut, R. E., R. E. Hart, and B. Luthman, 2013: Global identification of previously undetected pre-satellite-era tropical cyclone candidates in NOAA/CIRES twentieth-century reanalysis data. *J. Appl. Meteor. Climatol.*, **52**, 2243–2259, doi:10.1175/JAMC-D-12-0276.1.

Vecchi, G. A., and T. R. Knutson, 2011: Estimating annual numbers of Atlantic hurricanes missing from the HURDAT database (1878–1965) using ship track density. *J. Climate*, **24**, 1736–1746, doi:10.1175/2010JCLI3810.1.

Von Storch, H., F. Feser, S. Haeseler, C. Lefebvre, and M. Stendel, 2014: A violent midlatitude storm in Northern Germany and Denmark, 28 October 2013 [in "Explaining Extremes of 2013 from a Climate Perspective"]. *Bull. Amer. Meteor. Soc.*, **95** (9), S76–S78.

Weisse, R., and F. Feser, 2003: Evaluation of a method to reduce uncertainty in wind hindcasts performed with regional atmosphere models. *Coastal Eng.*, **48**, 211–225.

Yoshimura, K., and M. Kanamitsu, 2008: Dynamical global downscaling of global reanalysis. *Mon. Wea. Rev.*, **136**, 2983–2998, doi:10.1175/2008MWR2281.1.

12. EXTREME FALL 2014 PRECIPITATION IN THE CÉVENNES MOUNTAINS

R. Vautard, G.-J. van Oldenborgh, S. Thao, B. Dubuisson, G. Lenderink, A. Ribes, S. Planton, J.-M. Soubeyroux, and P. Yiou

Extreme daily fall precipitation in the Cévennes mountains has very likely intensified. The probability of amounts witnessed in 2014 is estimated to have tripled since 1950, with large uncertainties.

Introduction. Fall thunderstorms along the northern Mediterranean coast can produce a few hundred millimeters of precipitation within one day (Ducrocq et al. 2014). Such extremes, also called "Mediterranean events", occurred repeatedly during the fall (September–November, SON) of 2014, triggering 12 severe weather warnings from Météo-France, and inducing floods and casualties in several places during the season. The yearly number of events with precipitation exceeding 100mm in a day does not exhibit a significant long-term trend, and furthermore it has been difficult to establish a significant trend in the most extreme cases of each year (Soubeyroux et al. 2015). Here we investigate trends in the fall seasonal maximum of daily precipitation, using a homogenized and quality-controlled dataset. We focus on a specific area, the Cévennes mountain range, where the highest daily precipitation amount is found in France in the fall (Fig. 12.1a). These phenomena are triggered by moist air advected from the warm Mediterranean Sea, hitting the mountain range with convection possibly amplified by colder continental air aloft.

Data. Recently, a homogenized dataset of monthly temperature and precipitation covering continental France was constructed (Gibelin et al. 2014) using the HOMER software (Mestre et al. 2013). A few statistical methods exist to help homogenize daily climate data for temperature and precipitation but generally require specific conditions (close well-correlated neighbor series, e.g., SPLIDHOM, Mestre et al. 2011). For the analysis, we used a set of 27 quality controlled daily series of rain gauge measurements from Météo-France daily reference series (DRS) datasets. The DRS are not corrected, but selected using quality information from monthly homogenization (little amplitude and adjustments of inhomogeneities), low daily values missing rate and few successive relocations (Moisselin and Dubuisson 2006). The daily records of DRS are then used without any adjustment.

Most daily series start between 1950 and 1953. The fall precipitation events are small-scale, a few kilometers across but more coherent along the direction of motion, inducing a large spatial variability of seasonal maxima. This creates an observational difficulty as a loose network of rain gauges may miss some events. In order to improve independence among stations, and to have a sample of sites with comparable climatology, we selected a subsample of the rain gauges with the following conditions: (i) the long-term mean of the highest daily precipitation in fall was in the range 70–110 mm day^{-1}, (ii) the correlation of any two series was below 0.70 ($r^2 < 0.5$); in this set the highest 10 precipitation events occur on different days. This leaves 14 rain gauge series (see list in Fig. 12.1b) with 926 station years that we can assume to be identically distributed because of this selection criterion, allowing us to better estimate long return times with extreme value theory. However, the season maxima observed the same year are statistically dependent among locations, which has to be taken into account for statistical inference. We verified that fall maxima are uncorrelated from year to year.

Analysis of fall maxima and their trends. Figure 12.1b shows the time series of each of the 14 stations' fall maxima of daily precipitation amounts. The figure

AFFILIATIONS: Vautard and Yiou—Laboratoire des Sciences du Climat et de l'Environnement–Institut Pierre-Simon Laplace (LSCE-IPSL), Commissariat for Atomic Energy and Alternative Energies (CEA)/National Centre for Scientific Research (CNRS)/ University of Versailles Saint-Quentin (UVSQ), Gif sur Yvette, France; van Oldenborgh and Lenderink—Royal Netherlands Meteorological Institute (KNMI), De Bilt, Netherlands; Thao, Ribes, and Planton—National Centre for Meteorological Research–Research Group of Atmospheric Meteorology (CNRM-GAME), Toulouse, France; Dubuisson and Soubeyroux—Météo-France, Toulouse, France

DOI:10.1175/BAMS-D-15-00088.1

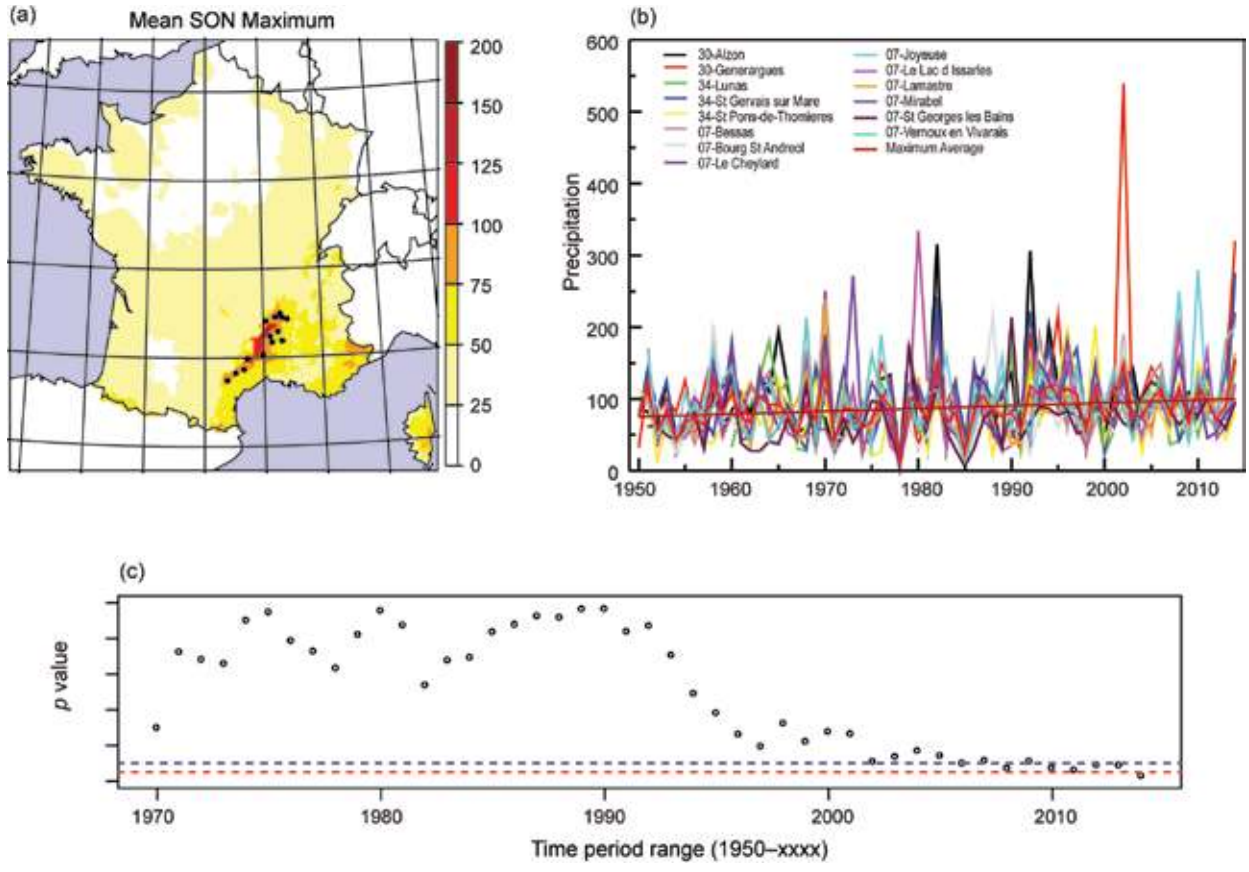

Fig. 12.1. (a) Mean SON maxima of daily precipitation amounts (mm day^{-1}) as obtained from the SAFRAN (Système d'Analyze Fournissant des Renseignements Atmosphériques à la Neige) reanalysis (Quintana-Segui et al. 2008), together with the locations of the stations used in the analysis; (b) Individual time series of SON seasonal maxima of daily amounts for each selected site, together with the series of average of these maxima. (c) Two-sided *p* values obtained for the trend in the SON maximum averaged over the 14 stations, using a time period ranging from 1950 to the value in abscissa.

also shows the yearly average and maximum value found in this subset. The maximum rainfall amount found in the rain gauge set in 2014 is 320 mm day^{-1}. This value was exceeded only in 2002 and 1980, with total values of 539 mm day^{-1} and 334 mm day^{-1} (see Fig. 12.1b). The highest seasonal mean of the 14 station maxima is observed in 2014 with 156 mm day^{-1}.

Average seasonal maxima have a trend of about 4% decade^{-1}, with a two-sided significance of p~5% using all years, but p has a more robust value of 10% when excluding 2014 (see Fig. 12.1c). Individual series trends, calculated using all available years, vary between 0 and 10% decade^{-1}, with median values around 4%–5% decade^{-1}, and none of them is negative. However, only two stations have trends with p less than 5% (Fig. 12.2a). To compare all stations over a common 50-year period we also calculated trends over the period 1965–2014 and found similar, and in fact more often larger than smaller positive trends than in the full data series (Fig. 12.2a).

Pooled time-dependent return period analysis. To estimate changes in return periods, we pooled all 14 station years and fitted an extreme value function to the resulting dataset that depends on a time-varying covariate. We modeled the time series with a Gumbel distribution after transforming the precipitation with a power 2/3 to compensate the expected power 3/2 scaling that results from three factors that each contribute a scaling 1/2 to extreme precipitation in the Gaussian approximation: the mass flux, specific humidity and precipitation efficiency (Wilson and Toumi 2005; van den Brink and Können 2011). The shape and scale parameters are assumed to vary together with the global mean temperature, as a covariate to simulate climate change. Uncertainties are

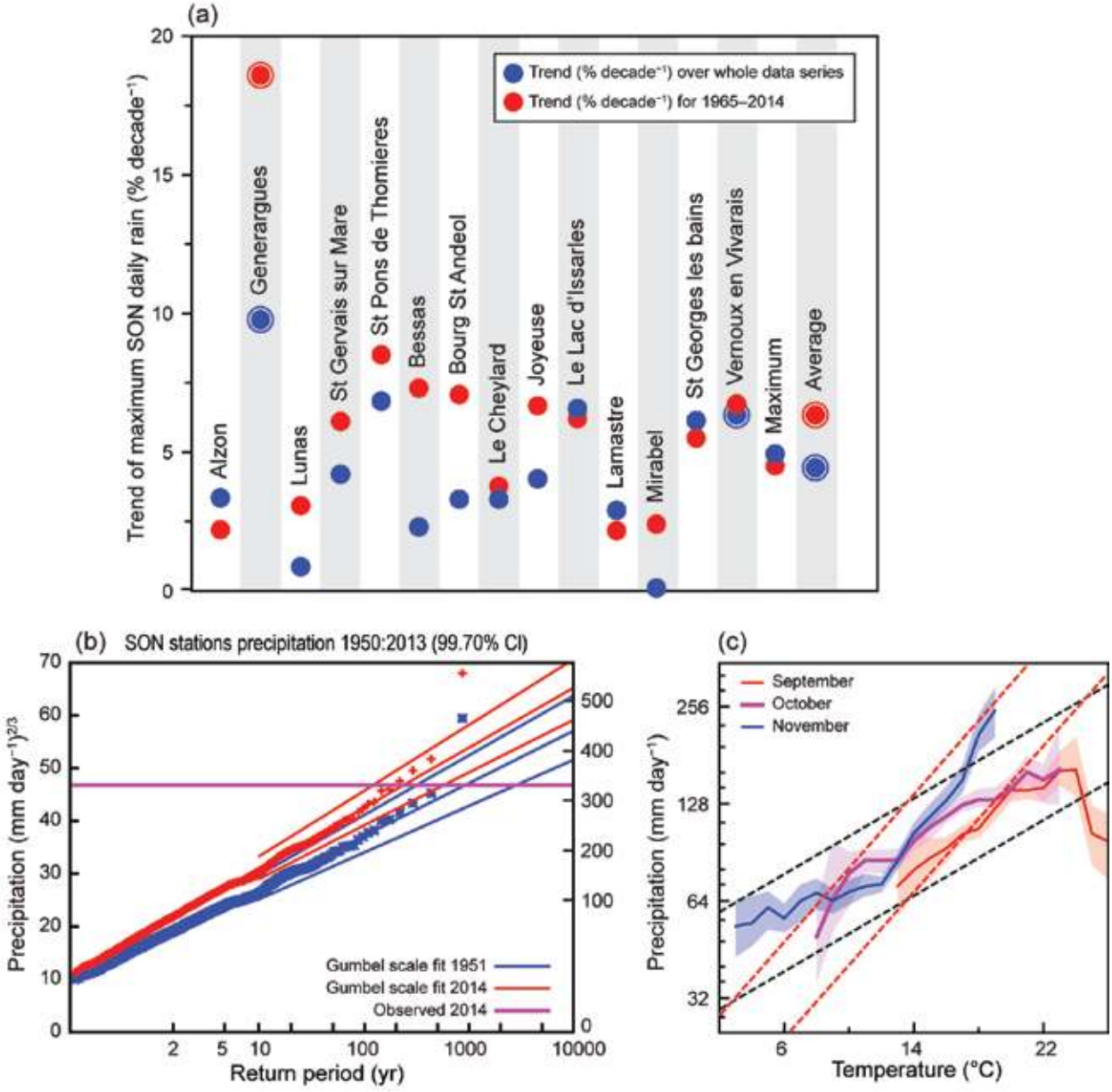

Fig. 12.2. (a) Trend values (% decade^{-1}) for each rain gauge SON maximum, the average (calculated from 1950 on; circled point). Red points show the values obtained from the same analysis but over the 50-year 1965–2014 period. Circled points are those having a two-sided *p* value exceeding 5%. (b) Fit of a time-dependent Gumbel distribution to the fall maximum of precipitation of the 865 station years to the power 2/3. The position and scale parameters of the Gumbel distribution are assumed to scale with the smoothed global mean temperature. The red lines indicate the fit for the climate of 2014 with one-sided 95% confidence interval, taking spatial dependencies into account to first order, the blue lines the same for 1950. The observations are also plotted twice: once shifted up with the fitted trends to 2014, once shifted down to 1950. The horizontal line denotes the value observed in 2014. (c) Dependency of the 99th percentile of daily precipitation on wet-days (and 5% to 95% uncertainty range) on daily mean (43.5°–45°N, 2.5°–5°E average) temperature (°C) from E-OBS (Haylock et al. 2008) for stations below 611 m, dotted black (red) lines denote Clausius–Clapeyron (two times CC) scaling. The method is described in Lenderink et al. (2011).

estimated by a non-parametric bootstrap. To account for stations dependence, we used, in the calculation of significance, an equivalent number of degrees of freedom N* = 3.2 (instead of 14 for the number of sites), derived from the analysis of pooled trends, and consistent with the range of values suggested in Bretherton et al. (1999). This has been implemented in the bootstrap by scaling the p-value. From this

analysis, the fitted return time of the value of fall 2014 in the current climate is about 250 years (Fig. 12.2a, with uncertainty range 120–600 years) at a given location. This translates to an event like the 2014 amounts every 10–40 years at any of the 14 stations. We estimate that around 1950 the return time would have been a factor three higher, with a lower bound of the 90% confidence interval of 1.15.

Attribution. The increase found in intensities of extreme daily precipitation can, in principle, be caused by a variety of mechanisms (natural variability, changes in climate forcings). Anthropogenic climate change is an obvious candidate, but low-frequency natural variability and changing aerosol loads can also have played a role. This can only be investigated using a climate model able to reproduce precipitation extremes. However, hydrostatic global and regional climate models have problems representing the tail of the distribution well in particular for precipitation of convective origin (Chan et al 2014) and long simulations of non-hydrostatic models are not yet available. We therefore resort to a statistical model relating extreme daily convective precipitation to the local temperature in areas with ample moisture availability (Lenderink and van Meijgaard 2008; Lenderink et al 2011). The wet-day 99th percentile of daily precipitation for the individual months, September to November, shows a robust increase with temperature, except for the highest temperatures in September (Fig. 12.2b). Excepting these, this increase follows a dependency of 7%–14% of precipitation amount per degree, in correspondence to one to two times the Clausius–Clapeyron (CC) relation—a behavior also obtained for the 99.9th percentile (Fig. 12.2c). The observed increase of precipitation extremes with temperature can be understood by the moisture increase. The enhanced scaling compared to the Clausius–Clapeyron relation can be explained by convective cloud feedbacks to increasing moisture levels (see Westra et al. 2014 for a review on scaling). Lenderink and van Meijgaard (2008) also found an enhancement of short-term precipitation extremes with sea surface temperature of 14% per degree in The Netherlands.

September temperatures in this region have increased about 50% faster than the global mean temperature over 1950–2014 (not shown), so temperatures are about 1.1°C higher now than they were around 1950. This agrees very well with results from the CMIP5 ensemble in Mediterranean areas (Stocker et al. 2013). Using the scaling found above the warming trend translates into an increase in intensity of extreme daily precipitation of roughly 7%–14%. This indicates that at least part of the observed increase of precipitation extremes is attributable to the increase in temperature in the region, which in turn has been attributed to anthropogenic modification of the atmospheric composition (e.g., Stocker et al. 2013). However, given the large uncertainties and the unknown influences of other factors such aerosol changes that may have influenced precipitation extremes we cannot directly attribute trends to atmospheric composition changes.

Conclusion. Extreme precipitation in the Cévennes mountains in the fall of 2014 reached more than 300mm in a day and induced a record (since 1950) maximal intensity when averaged over an ensemble of rain gauges. Our analysis shows a strong increase of the fall maxima in this area of about 30% since the middle of the 20th century, with trends of about 4% decade^{-1} (p~10%). The return period of events such as those found in 2014 is estimated to having been reduced by a factor of about three, with a 90% confidence lower bound of 1.15. In this area heavy precipitation increases as a function of regional temperature, with a rate exceeding 7% °C^{-1}, indicating that at least part of the trend is due to warming. While suggesting a human influence, a formal attribution of these trends, using non-hydrostatic models, would be required for establishing and quantifying the fraction of attributable risk, since other factors may have entered into play in this area such as changes in aerosol loads, radiation, and natural variability.

ACKNOWLEDGEMENTS. This study was supported by the French Ministry of Ecology, Sustainable Development and Energy, through the national climate change adaptation plan project EXTREMOSCOPE, and by the FP7 EUCLEIA project under Grant # 607085.

REFERENCES

Bretherton, C. S., M. Widmann, V. P. Dymnikov, J. M. Wallace, and I. Bladé, 1999: The effective number of spatial degrees of freedom of a time-varying field. *J. Climate*, **12**, 1990–2009.

Chan, S. C., E. J. Kendon, H. J. Fowler, S. Blenkinsop, N. M. Roberts, and C. A. T. Ferro, 2014: The value of high-resolution Met Office regional climate models in the simulation of multihourly precipitation extremes. *J. Climate*, **27**, 6155–6174, doi:10.1175/JCLI-D-13-00723.1.

Ducrocq, V., and Coauthors, 2014: HyMeX-SOP1: The field campaign dedicated to heavy precipitation and flash flooding in the northwestern Mediterranean. *Bull. Amer. Meteor. Soc.*, **95**, 1083–1100, doi:10.1175/BAMS-D-12-00244.1.

Gibelin, A. L., and Coauthors, 2014: Evolution de la température en France depuis les années 1950: Constitution d'un nouveau jeu de séries homogénéisées de référence (Evolution of temperature in France since the 1950s: Constitution of a new reference dataset of homogenized time series). *La Météorologie*, **87**, 45–53, doi:10.4267/2042/54336.

Haylock, M. R., N. Hofstra, A. M. G. Klein Tank, E. J. Klok, P. D. Jones, and M. New. 2008: A European daily high-resolution gridded dataset of surface temperature and precipitation. *J. Geophys. Res.*, **113**, D20119, doi:10.1029/2008JD10201.

Lenderink, G., and E. van Meijgaard, 2008: Increase in hourly precipitation extremes beyond expectations from temperature changes. *Nat. Geosci.*, **1**, 511–514, doi:10.1038/ngeo262.

——, H. Y. Mok, T. C. Lee, and G. J. van Oldenborgh, 2011: Scaling and trends of hourly precipitation extremes in two different climate zones – Hong Kong and the Netherlands. *Hydrol. Earth Syst. Sci.*, **15**, 3033–3041, doi:10.5194/hess-15-3033-2011.

Mestre, O., C. Gruber, C. Prieur, H. Caussinus, and S. Jourdain, 2011: SPLIDHOM: A method for homogenization of daily temperature observations. *J. Appl. Meteor. Climatol.*, **50**, 2343–2358, doi:10.1175/2011JAMC2641.1.

——, and Coauthors, 2013: HOMER: A homogenization software – methods and applications. *Időjárás, Quart. J. Hung. Meteor. Serv.*, **117**, 47–67.

Moisselin, J.-M., and B. Dubuisson, 2006: Évolution des valeurs extrêmes de température et de précipitations au cours du XXe siècle en France (Evolution of extremes of temperature and precipitations during the 20th century in France). *La Météorologie*, **54**, 33–42, doi:10.4267/2042/20099.

Quintana-Seguí, P., and Coauthors, 2008: Analysis of near-surface atmospheric variables: Validation of the SAFRAN analysis over France. *J. Appl. Meteor. Climatol.*, **47**, 92–107, doi:10.1175/2007JAMC1636.1.

Soubeyroux, J.-M., L. Neppel, J.-M. Veysseire, Y. Tramblay, J. Carreau, and V. Couget, 2015: Evolution des précipitations extrêmes en France en contexte de changement climatique (Evolution of extreme rainfall in France with a changing climate). *La Houille Blanche*, **1**, 27–33, doi:10.1051/lhb/2015004.

Stocker, T. F., and Coauthors, Eds., 2013: *Climate Change 2013: The Physical Science Basis*. Cambridge University Press, 1535 pp. [Available online at www.climatechange2013.org/images/report/WG1AR5_ALL_FINAL.pdf.]

van den Brink, H. W., and G. P. Können, 2011: Estimating 10000-year return values from short time series. *Int. J. Climatol.*, **31**, 115–126, doi:10.1002/joc.2047.

Westra, S., and Coauthors, 2014: Future changes to the intensity and frequency of short-duration extreme rainfall. *Rev. Geophys.*, **52**, 522–555, doi:10.1002/2014RG000464.

Wilson, P. S., and R. Toumi, 2005: A fundamental probability distribution for heavy rainfall. *Geophys. Res. Lett.*, **32**, L14812, doi:10.1029/2005GL022465.

13. RECORD ANNUAL MEAN WARMTH OVER EUROPE, THE NORTHEAST PACIFIC, AND THE NORTHWEST ATLANTIC DURING 2014: ASSESSMENT OF ANTHROPOGENIC INFLUENCE

Jonghun Kam, Thomas R. Knutson, Fanrong Zeng, and Andrew T. Wittenberg

According to CMIP5 models, the risk of record annual mean warmth in European, northeast Pacific, and northwest Atlantic regions—as occurred in 2014—has been greatly increased by anthropogenic climate change.

Introduction. HadCRUT4v3 observed surface temperature data (Morice et al. 2012) indicate that during 2014, record annual mean warm anomalies occurred in regions of Europe, the eastern North Pacific region (EPac), and the western North Atlantic (WAtl) (Fig. 13.1b). Considering the 5° × 5° grid cells with at least 100 years of coverage, 12% of this area globally set a new warm record during 2014, and *none* set a cold record (Fig. 13.1b). Globally since 1990, there have been almost no cold annual mean records observed at this spatial scale (Knutson et al. 2013). The unprecedented warm surface temperature anomalies in 2014 were accompanied by anomalous atmospheric circulations, changes in seasonal weather, and adverse effects on regional ecosystems (Bond et al. 2015). To explore the possible contributions of anthropogenic radiative forcings to these unprecedented regional warm anomalies, we use a 25-model set of historical all-forcing (anthropogenic + natural) and control (unforced) climate model runs, along with a 10-model set of natural-forcing-only ensemble historical runs from the Coupled Model Inter-comparison Project Phase 5 (CMIP5-All and CMIP5–Nat; Taylor et al. 2012). Many of our methods follow Knutson et al. (2013, 2014), and some descriptive text is derived from these reports with minor modification.

Model-based detection of long-term regional anthropogenic warming. Annual mean temperature anomaly time series extending back to the mid-to-late 1800s for the three regions (Figs. 13.1f–h) are shown in Figs. 13.1c–e. Europe shows a pronounced recent observed warming, particularly since the 1980s, which is well captured by the CMIP5-All ensemble but not the CMIP5-Nat ensemble. The observed trends (black curve in Fig. 13.1g) are generally outside the 5th–95th percentile range of natural-forced trends-to-2012 (blue/purple envelope) that begin before the early 1980s (except for those beginning around 1930 or 1940). The observed trends are generally consistent with CMIP5-All runs (pink/purple envelope) for all trends-to-2012 that start prior to 2000 (Fig. 13.1g).

Observed time series for the EPac and WAtl regions show a mixture of multi-decadal variability and warming trend. The "sliding trend" analyses (Figs. 13.1f and h) indicate that the warming trends over the EPac and WAtl regions are generally indistinguishable from intrinsic variability, except for trends beginning prior to about 1920 for the EPac region and beginning around 1910 for the WAtl region. The observed time series show that the EPac and WAtl regions have relatively strong multidecadal SST variability compared to the long-term trend, and were particularly warm during 1930–60. Including the highly anomalous year 2014 in the observed trends (Figs. 13.1f–h, white dashed) does not change the main conclusions, except that EPac trends beginning around 1950 become marginally detectable, according to the models.

Thus according to CMIP5 models, the long-term warming over Europe is likely attributable in part to anthropogenic forcing, as it is consistent with the CMIP5-All runs but generally inconsistent with CMIP5-Nat, with some dependence on the start year for the trend. Meanwhile, due to strong intrinsic variability, the long-term warming over the EPac and

AFFILIATIONS: Kam—NOAA/Geophysical Fluid Dynamics Laboratory, and Program in Atmospheric and Oceanic Sciences, Princeton University, Princeton, New Jersey; Knutson, Zeng, and Wittenberg—NOAA/Geophysical Fluid Dynamics Laboratory, Princeton, New Jersey

DOI:10.1175/BAMS-D-15-00101.1

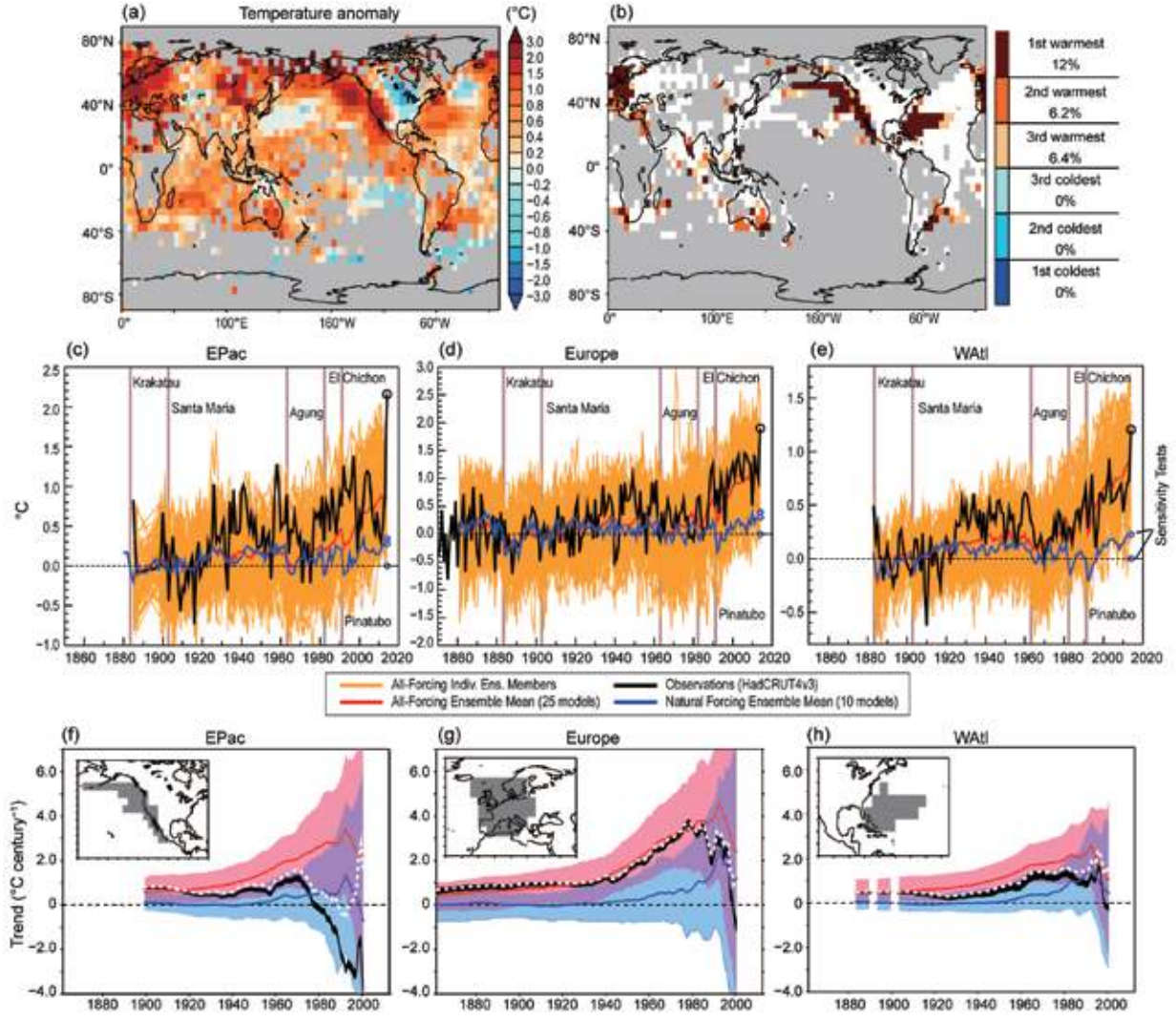

Fig. 13.1. (a) Annual mean surface air temperature anomalies (°C) for 2014 (1961–90 base period) from the HadCRUT4 dataset. (b) Colors identify grid boxes with annual mean anomalies that rank 1st (dark red), 2nd (orange-red), or 3rd (yellow-orange) warmest in the available observed record. Gray areas did not have sufficiently long records, defined here as containing at least 100 available annual means, which require at least four available months. (c)–(e) Annual mean surface temperature anomalies (°C) for the eastern Pacific, Europe, and western Atlantic regions. Black curves: observed (HadCRUT4) anomalies; dark red (dark blue) curves: ensemble anomalies for CMIP5-All (CMIP5-Nat) runs, with each available model weighted equally; orange curves: individual CMIP5-All ensemble members. Blue circles labelled N_{low} (zero), N_{mid} (the modeled temperature anomaly for 2012), and N_{high} (the maximum over the full period) depict three estimates of the CMIP5-Nat response for 2014. CMIP5-All time series are extended as needed with data from RCP4.5 runs. All time series adjusted to have zero mean over the period 1881–1920. (f)–(h) Trends to 2012 [°C (100 yr^{-1})] in the regional series in (c–e) as a function of starting year. Black, red, and blue curves depict observations, the CMIP5-All ensemble mean, and the CMIP5-Nat ensemble mean, respectively. Pink envelope (blue-region) depicts the 5th–95th percentile range of trends from the CMIP5-All (CMIP5-Nat) runs. Purple shading indicates pink- and blue-region overlap. White dashed curves depict observed trends ending in 2014, rather than 2012. Maps indicating the three regions are shown in (f–h).

WAtl regions is generally not clearly attributable to anthropogenic forcing.

Model-based attribution of the 2014 regional annual mean extreme warm anomalies. To assess the contribution of anthropogenic forcing to the 2014 extreme temperature anomalies, we first constructed histograms (Figs. 13.2a–c) of HadCRUT4v3 observed anomalies (black distributions) and "observed residuals" (solid green distributions). The observed

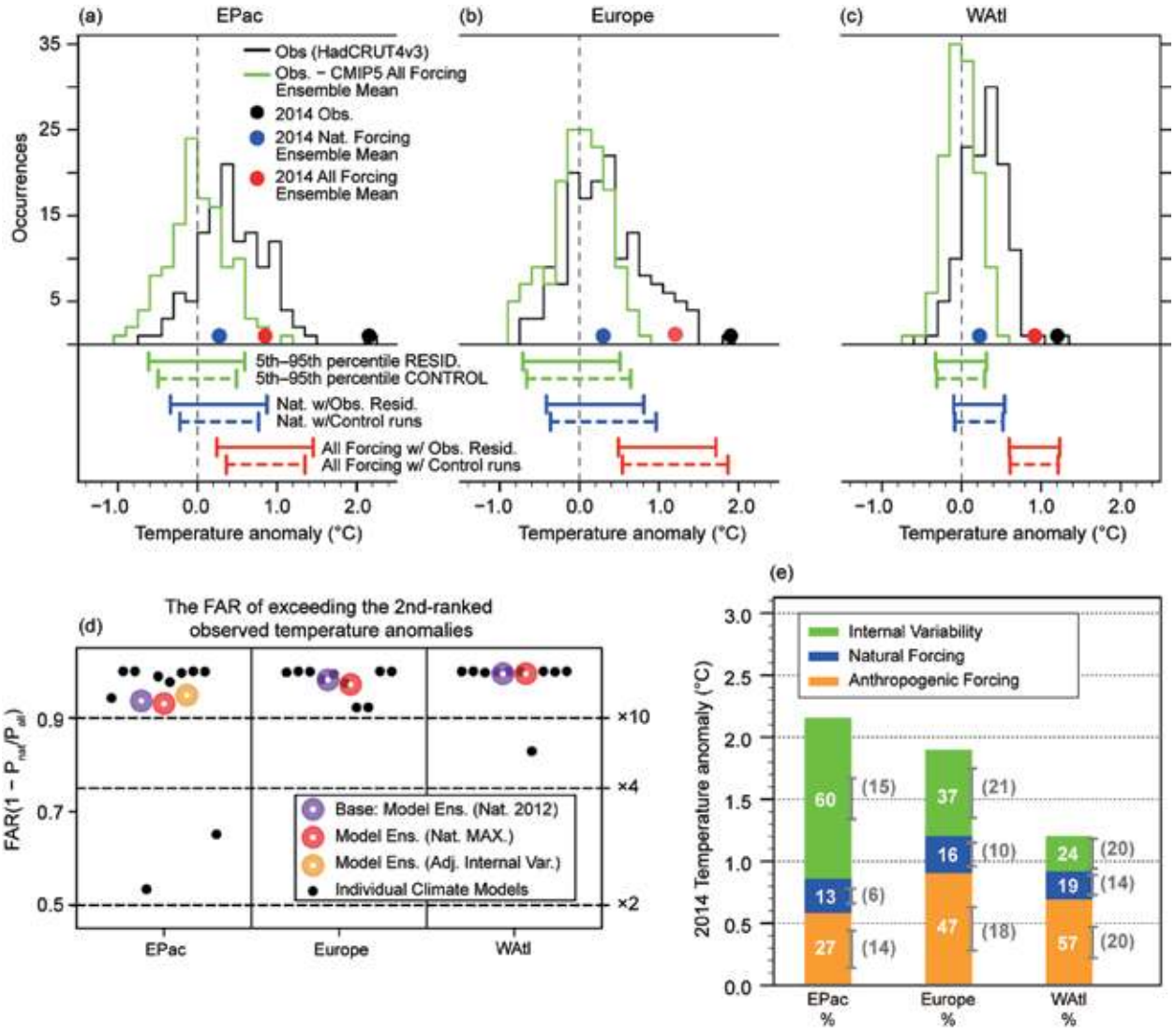

Fig. 13.2. (a)–(c): Histograms of "observed residuals" (solid green lines) and observed annual mean temperature anomalies (black lines) over the three regions. Observed residuals obtained by subtracting CMIP5-All forcing ensemble means from observations and then subtracting any remaining long-term mean. The 5th to 95th percentile ranges of observed residuals and control run variations are depicted by green solid and dashed error bars. Blue (red) error bars depict the 5th–95th percentiles of observed residuals and CMIP5-Control runs, respectively, offset by ensemble means for 2014 from CMIP5-Nat (CMIP5–All) simulations. Black, red, and blue dots in (a)–(c) depict observed, CMIP5-All, and CMIP5-Nat anomalies for 2014. (d) Estimates of the FAR of exceeding the second-ranked observed temperature anomalies from the CMIP5 multimodel ensemble (large purple circle) and its uncertainty (black solid circles) as estimated from the 10 paired CMIP5-All and CMIP5-Nat runs from individual CMIP5 models. Large red circles depict FAR sensitivity tests using—for the 2014 CMIP5-Nat value—the maximum temperature anomalies in any one year from the CMIP5-Nat multimodel ensemble means (online supplemental material); large yellow circle shows a test using adjusted (+22%) internal variability over the EPac region. Dashed lines labeled "×10", "×4", and "×2" indicate risk ratios (probability of occurrence in the CMIP5-All vs. CMIP5-Nat distributions). (e) Stack bars show the estimated contributions of anthropogenic forcing (CMIP5-All – CMIP5-Nat; orange), natural forcing (CMIP5-Nat; blue), and internal variability (Obs. – CMIP5-All; green) to 2014 anomalies (relative to 1881–1920) over the three regions. Standard errors of the various contribution estimates are given in parentheses with ±1 standard error ranges depicted by gray error bars (online supplemental material).

residuals, obtained by subtracting the CMIP5-All multimodel mean from observations, are an estimate of "observed" unforced climate variability which can be compared to the model control runs. Figure 13.2a–c compares the 5th–95th percentiles of the observed residuals (green solid bars) and the CMIP5

Control runs (green dashed bars). Fig. 13.2a–c also shows these ranges shifted by the magnitude of 2014 annual mean forced anomalies as derived from either CMIP5-Nat (blue bars) or CMIP5-All (red bars) ensemble means (see online supplemental material). The observed 2014 anomalies (black solid circles) for all three regions are far beyond the 95th percentile of the observed residuals, or the CMIP5 Control or CMIP5-Nat. distributions; for the EPac and Europe regions they are even beyond those from the CMIP5–All distributions. The 2014 observed anomaly over the WAtl region is near the 95th percentile of the CMIP5-All distribution. These results indicate that the 2014 annual mean anomalies over all three regions are extremely unusual compared to model-simulated natural variability, and over the EPac and Europe regions are even unusual compared to CMIP5-All runs (though the latter runs including anthropogenic forcing are closer to the observations). Modeled internal variability compares fairly well to the observed residual variability, though Fig. 13.2a suggests a ~20% underestimate of internal variability of annual means by the control runs in the EPac region. This possible underestimate does not markedly affect our conclusions about the 2014 extremes, as discussed below.

To assess the contribution of anthropogenic forcing to the risk of extremes like 2014, we estimated the fraction of attributable risk (FAR) for extreme anomalies in each region, using annual mean temperature anomaly distributions derived from the CMIP5-All, CMIP5-Nat, and control runs. The FAR compares the event probability (P) between the CMIP5-Nat and CMIP5-All runs ($FAR = 1 - P_{nat}/P_{all}$). Our FAR estimates address the question of attribution specifically for the three regions with highly anomalous warmth in 2014, and are not intended to be representative of global behavior or of other regions or years in general.

Observed annual mean anomalies for 2014 and an alternative (second-ranked) year are used as alternative extreme-event thresholds in our FAR analysis. The simulated probabilities of exceeding the observed 2014 anomalies over the EPac, Europe, and WAtl regions are 0.2% (0.1%), 4% (0.1%), and 5% (0.2%) based on distributions derived from the CMIP5-All (CMIP-Nat) runs, respectively, and using control-run-estimated internal variability. Therefore, the initial FAR estimates for anthropogenic forcing are 0.42, 0.97, and 0.96 for the EPac, Europe, and WAtl regions, respectively. However, the record 2014 events are far out in the tails of the modeled distributions. The EPac has a particularly long "warm tail" in the modeled internal variability distribution (not shown) which causes some instability in the FAR estimates for high thresholds like 2014. Therefore, we also examined the occurrence rates and FAR of the observed temperature anomalies using the second-ranked anomalies (1997, 2006, and 2003 over the EPac, Europe, and WAtl regions); the probabilities are 4% (0.2%), 26% (0.4%), and 46% (0.2%) for the CMIP5-All (CMIP-Nat.) runs, respectively. Using these thresholds, the FAR estimates are 0.94, 0.98, and 0.99, for the EPac, Europe, and WAtl regions. Sensitivity tests (Fig. 13.2d) were done using alternative estimates of the Natural Forcing 2014 contribution (N_{mid} and N_{high}) from CMIP5-Nat runs (large red circles), or adjusting (increasing) the simulated internal variability over the EPac region by the factor 1.22 (large orange circle); these confirm that our FAR estimates for the second-ranked-year thresholds are robust to these assumptions. Uncertainties in the FAR estimates were also explored by computing the spread of results across individual CMIP5 models (Fig. 13.2d; methods described in online supplemental material). These sensitivity tests show that, using the second-ranked-year threshold values, the estimated FAR is above 0.9 for all 10 individual models for Europe. For the WAtl and EPac, nine and eight of the 10 models have FAR above 0.9, respectively.

We evaluate, using CMIP5 models, the contributions of different factors to the observed annual mean temperature anomalies for 2014 (Fig. 13.2e). The 2014 annual mean anomalies (relative to 1881–1920) for the EPac, Europe, and WAtl regions are 2.2°, 1.9°, and 1.2°C, respectively. For the three regions, the model-derived central estimates of external forcing (anthropogenic + natural) contributions to these observed anomalies are: 0.85°, 1.2°, and 0.9°C; for natural forcing only: 0.28°, 0.3°, and 0.22°C; and for internal variability: 1.35°, 0.7°, and 0.3°C. Thus the portion of extreme 2014 annual mean anomalies attributable to internal variability is about 60%, 37%, and 24% for the EPac, Europe, and WAtl regions, respectively. Also, according to the CMIP5 multimodel ensemble, about 40%, 63%, and 76% of the 2014 annual mean anomalies over the EPac, Europe, and WAtl regions are attributable to natural and anthropogenic forcing combined. Finally, About 27%, 47%, and 57% (13%, 16%, 19%) of the anomaly magnitudes are attributable to anthropogenic forcing (natural forcing) alone. The standard errors of these estimates due to intermodel differences (Fig. 13.2e, gray/parenthesis; see online supplemental material) suggest that the

anthropogenic contribution estimates are relatively robust across the models.

Conclusions. According to the CMIP5 models, the *risk* of events surpassing the extreme (second-ranked) thresholds set in 1997, 2006, and 2003 over the EPac, Europe, and WAtl regions is almost entirely attributable to anthropogenic forcing, with FAR above 0.9 for the ensemble model and almost all of the 10 individual models examined. The strongest model-based evidence for detectable long-term anthropogenic warming was found for the European region, while the case is not as compelling for the WAtl and EPac regions. In the EPac region, there is some indication that internal variability may be at least modestly underestimated by the model control runs. Nonetheless, interannual variability in this region is estimated to have made a larger percentage contribution to the 2014 anomalies than anthropogenic forcing. Thus, the overall evidence for an anthropogenic contribution to the anomalous 2014 temperatures and long-term trend is stronger for Europe than the other two regions. Uncertainties in the models' estimated forced response and the influence of intrinsic variability remain, due to limitations of climate models, uncertainties in the forcings, and (probably to a much lesser extent) uncertainties in the observed temperatures.

ACKNOWLEDGEMENTS. We thank the WCRP's Working Group on Coupled Modeling, participating CMIP5 modeling groups, PCMDI, the Met. Office Hadley Centre, and the Climatic Research Unit, University of East Anglia for making available the CMIP5 and HadCRUT4 datasets. We also thank two anonymous reviewers for helpful comments on the manuscript.

REFERENCES

Bond, N. A., M. F. Cronin, H. Freeland, and N. Mantua, 2015: Causes and impacts of the 2014 warm anomaly in the NE Pacific. *Geophys. Res. Lett.*, **42**, 3414–3420, doi:10.1002/2015GL063306.

Knutson, T. R., F. Zeng, and A. T. Wittenberg, 2013: Multimodel assessment of regional surface temperature trends: CMIP3 and CMIP5 twentieth-century simulations. *J. Climate*, **26**, 8709–8743, doi:10.1175/JCLI-D-12-00567.1.

——, ——, and ——, 2014: Multimodel assessment of extreme annual-mean warm anomalies during 2013 over regions of Australia and the western tropical Pacific. [in "Explaining Extreme Events of 2013 from a Climate Perspective"]. *Bull. Amer. Meteor. Soc.*, **95** (9), S26–S30.

Morice, C. P., J. J. Kennedy, N. A. Rayner, and P. D. Jones, 2012: Quantifying uncertainties in global and regional temperature change using an ensemble of observational estimates: The HadCRUT4 data set. *J. Geophys. Res.*, **117**, D08101, doi:10.1029/2011JD017187.

Taylor, K. E., R. J. Stouffer, and G. A. Meehl, 2012: An overview of CMIP5 and the experimental design. *Bull. Amer. Meteor. Soc.*, **93**, 485–498, doi:10.1175/BAMS-D-00094.1.

14. THE CONTRIBUTION OF HUMAN-INDUCED CLIMATE CHANGE TO THE DROUGHT OF 2014 IN THE SOUTHERN LEVANT REGION

K. Bergaoui, D. Mitchell, R. Zaaboul, R. McDonnell, F. Otto, and M. Allen

A combined modeling and observational study suggests that the persistent rainfall deficit during the 2014 rainy season in southern Levant was made more likely due to anthropogenic climate change.

Introduction. While the extent to which the 2007/08 drought in the Levant region destabilized the Syrian government continues to be debated, there is no questioning the enormous toll this extreme event took on the region's population. The movement of refugees from both the drought and war affected regions into Jordan and Lebanon ensured that the anomalously low precipitation in the winter of 2013/14 amplified impacts on already complex water and food provisions.

It is hypothesized that droughts over the Levant region can be linked to three types of synoptic regimes (Saaroni et al. 2014). The regimes include 1) an expansion of the subtropical high over the majority of the Mediterranean Basin, 2) a pronounced stagnant ridge/block, and 3) an intrusion of lower-level continental polar air. The 2014 drought, affecting parts of Jordan, Lebanon, Palestine, and Israel, was characterized by extremes in low rainfall, the extent of the long dry periods, and three exceptional rainfall events that interspersed these. The drought itself was thought to be due to a large-scale winter blocking event that prevented weather systems from reaching the region (Udasin 2014).

The motivation for this study is twofold: 1) due to the instability in the Levant region, stresses such as meteorological extremes can often lead to enhanced public and political tensions. 2) There is a clear bias in the literature for looking at extreme events over industrialized countries (e.g., Herring et al. 2014)—this study provides an example in an alternative geographic region.

Data and Methods. In studying the 2014 drought, one of the challenges to overcome is accessing data in this extremely politically charged region. As such, we only concentrate on precipitation changes here and discuss their relevance for wider impacts.

A spatially and temporally coherent set of station precipitation data is available from the Israeli Meteorological Service (http://data.gov.il/ims), and it follows the World Meteorological Organization quality control guidelines. The data span the period 1980–2014. Additional data for the Levant region was obtained from the Jordanian Ministry of Water and Irrigation and the Palestinian Water Authority. All station locations are plotted on Fig. 14.1a, and these stations provide the longest reliable record available for this region. In addition, we use the gridded E-OBS dataset (Haylock et al. 2008) to put the analysis in the context of longer-term climate variability.

Often direct observational inferences of extreme events are highly uncertain due to small sample sizes (e.g., Sipple et al. 2015). This is especially true in the Levant region. One well-established technique to circumvent this issue is using climate models to run many thousands of simulations of "possible" climate, thereby sampling internal climate variability. Here, we make use of the weather@home project (Massey et al. 2015), which allows us to run many thousands of simulations for 2014 over the region of interest. We use the atmosphere-only model, HadAM3P, to drive a regional model (HadRM3P) that simulates climate for mid-northern Africa and the southern Levant

AFFILIATIONS: Bergaoui—International Centre for Biosaline Agriculture, Dubai, United Arab Emirates, and Institut National de la Météorologie, Tunis, Tunisia; Mitchell, Otto, and Allen—Environmental Change Institute, Oxford University, Oxford, United Kingdom; Zaaboul—International Centre for Biosaline Agriculture, Dubai, United Arab Emirates; McDonnell—International Centre for Biosaline Agriculture, Dubai, United Arab Emirates, and Environmental Change Institute, Oxford University, Oxford, United Kingdom

DOI:10.1175/BAMS-D-15-00129.1

A supplement to this article is available online (10.1175/BAMS-D-15-00129.2)

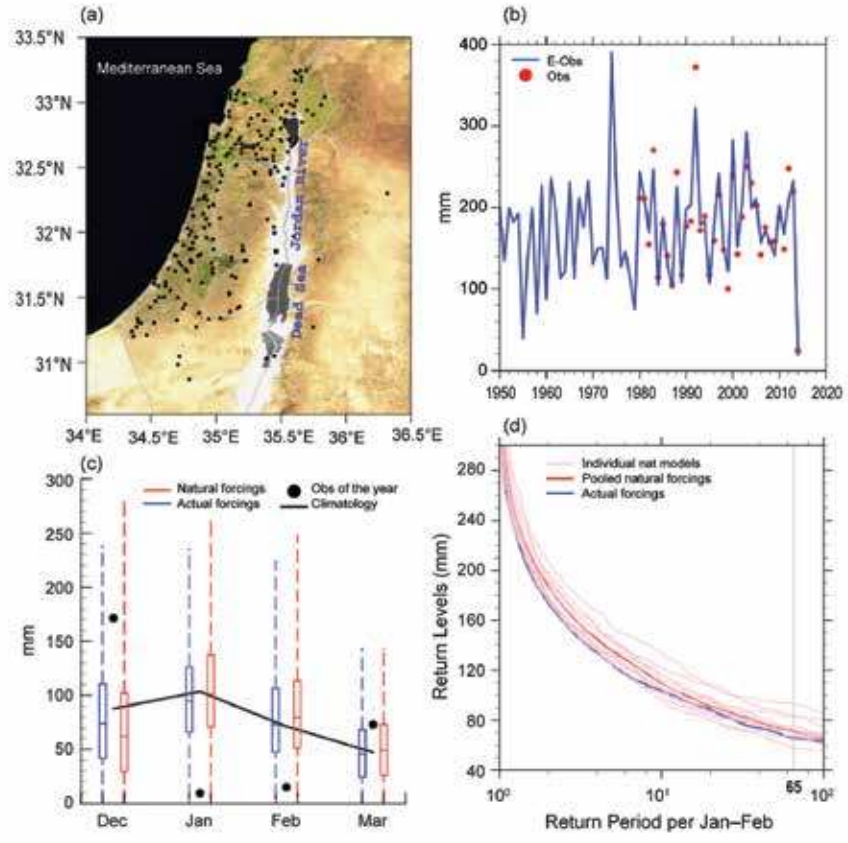

Fig. 14.1. (a) A map of the southern Levant region, showing the topography, political boundaries, and station locations. The region is bounded by 46°N–14°S and 25°W–63°E. (b) The cumulative rainy season (JF) precipitation totals for each year of the observational record averaged over the whole domain. The dots show stations, and the blue line shows E-OBS. The correlation coefficient between these datasets is ~0.94. (c) The monthly observed climatology (black line) of domain-averaged precipitation from 1980 to 2014. The 2013/14 values are plotted as black circles. Box-and-whisker plots show the median, interquartile range, and range for the biased corrected model data for actual conditions (blue) and natural conditions (red). (d) Return level plots of cumulative precipitation for Jan and Feb during the rainy season for natural conditions (red) and actual conditions (blue). Gray line shows the 65-year return level. Individual natural SST patterns are shown with thin pink lines, and the pooled SST pattern is shown with a thick orange line.

at 50-km resolution. The details are the same as the European model described in Massey et al. 2015.

To perform the 2014 event attribution, we simulate two possible climates under 2014 conditions: 1) an experiment with all known natural and anthropogenic climate forcings ("actual conditions") and 2) an experiment with only natural climate forcings ("natural conditions"). All anthropogenic and natural conditions follow the recommendations outlined by the Intergovernmental Panel on Climate Change (IPCC; Solomon et al. 2007). For the actual conditions experiment, the sea surface temperatures (SSTs) are taken from Operational Sea Surface Temperature and Sea Ice Analysis (OSTIA) observations (Stark et al. 2007). For the natural conditions experiment, the anthropogenic signal is taken out of the OSTIA SST patterns to leave only the naturalized SST pattern. The anthropogenic fingerprint is calculated by differencing the Coupled Model Intercomparison Project Phase 5 (CMIP5) "historical" and "historicalNat" simulations from 11 GCMs that performed these experiments and then subtracting this change in SST pattern from the OSTIA SSTs (see Schaller et al. 2014 for details). The use of 11 different models gives us 1 potential naturalized SST pattern.

The observed perspective. Figure 14.1b shows the extreme persistence of this two-month precipitation deficit event is unprecedented in the observational record. The cumulative JF precipitation for 2014 is clearly an outlier over the 1950–present period. Figure 14.1c shows the monthly climatology of observed precipitation along with the specific 2013/14 observed values. In December, the precipitation was in the upper quartile of the observed range, and most of that was due to a 10-day extreme downpour midway into the month (not shown). Following that wet extreme event, both January and February had the lowest rainfall since observations began. While the wet and dry events balance out in the seasonal average, the extreme persistence of this two-month precipitation deficit event is unprecedented.

The modeled perspective. To understand how anthropogenic climate change increased the likelihood of such a persistent drought, we use climate simulations to sample the internal climate variability during the rainy season of 2013/14. A well-known issue

is the large dry bias in precipitation over this region, which may be due to any combination of 1) the varied land cover/topography and relationship to convection in the region, 2) the representation of Mediterranean storm tracks in models (Anagnostopoulou et al. 2006), or 3) capturing upslope flow of moist air masses (Black 2009). In general, models have trouble capturing all the complex factors contributing to precipitation in this region. Here, we make the plausible assumption that the statistics of observed precipitation are quasi stationary over the 30-year period, and we use this as a climatology to evaluate the regional model. Comparing the cumulative distribution functions (CDFs) of the observations and the model simulations, it is also found that there is a dry bias in the model. In Supplementary Fig. S14.1, we show the CDFs for grid boxes with the lowest and highest biases, respectively. The bias was found to be linearly changing, with no significant difference between the "actual" and "natural" simulations, suggesting that it was not a result of misrepresentation of large-scale climate modes. To correct the bias, we use a nonparametric quantile mapping technique, matching estimated empirical quantiles between the observations and the "actual conditions" model scenario (Boe et al. 2007). The same bias correction is then applied to the natural model scenario. Figure 14.1c shows the bias corrected actual conditions and natural conditions model data plotted as box-and-whisker plots. There is a tendency for the actual conditions scenario to have less extreme precipitation with a persistently drier mean state (at least for January–March). Return level plots of these data averaged over the whole domain are shown in Fig. 14.1d, and the natural forcings scenario shows wetter conditions than the actual conditions throughout.

Figure 14.2a expands on this by showing the region averaged, January–February averaged, and 65-year return levels for the actual scenario and natural scenarios based on the individual estimates of naturalized SSTs. In general, meteorological drought conditions are more frequent in the actual conditions scenario, and this holds true for 9 out of 11 of the estimated naturalized experiments. For instance, the average return level in the natural scenarios is estimated to have around ~10 mm more precipitation than the actual conditions scenario.

To understand these differences in more detail, we calculate the Fraction of Attributable Risk (FAR; Allen 2003), defined as FAR = 1 – (p_{nat} / p_{act}), where p_{nat} is the probability of a rainfall deficit as low as or lower than the observed 2014 January–February

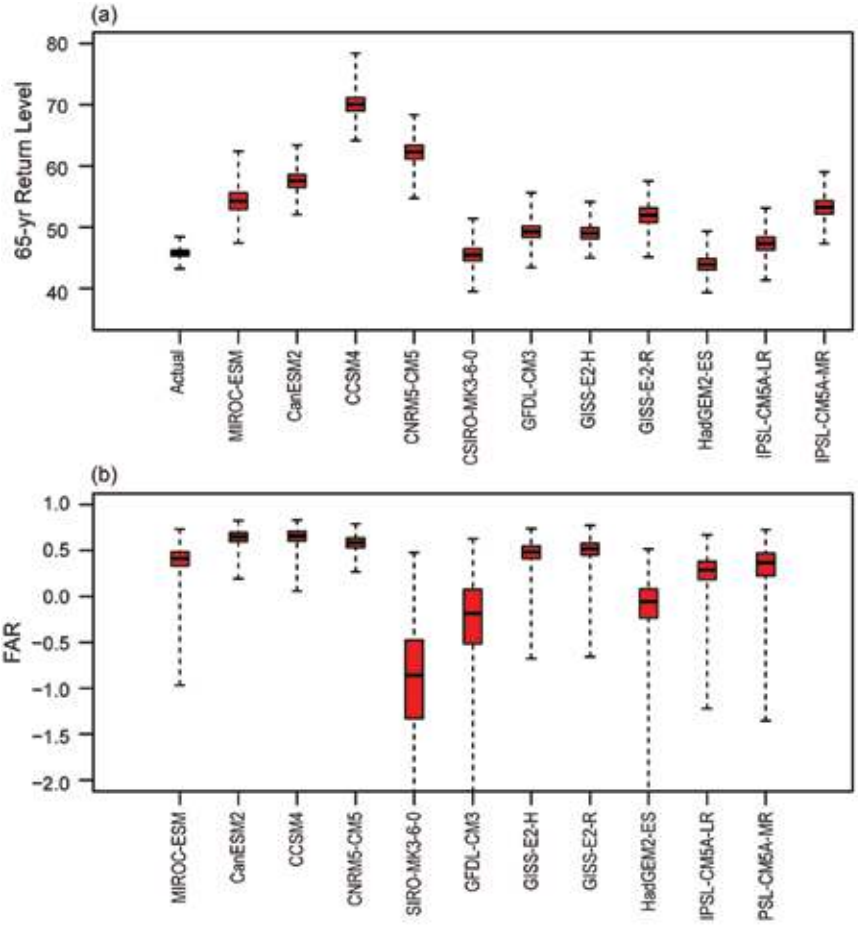

Fig. 14.2. (a) 65-year return levels over the entire region for the actual conditions (blue) and the individual estimates of natural conditions (red). (b) As in (a), but for estimates of the FAR. The uncertainty estimates are calculated by randomly resampling (with replacement) the underlying distribution 10 000 times. The bars show the median, interquartile range, and range of uncertainty.

average in the individual natural conditions scenarios, and p_{act} is the same but for the actual conditions. From Fig. 14.2b, it is shown that the persistent drought of 2014 was made more likely because of the anthropogenic climate change signal, indicating that patterns of precipitation are shifting to a drier state in this region. The mean FAR is ~0.45, indicating that anthropogenic climate change made the event ~45% more likely. This is consistent with the predicted weakening of the Mediterranean storm tracks in a warming climate (Hatzaki et al. 2009), a response that is captured in our model (Anagnostopoulou et al. 2006). The increased SSTs between our actual and natural simulations are relatively uniform across the globe (e.g., Schaller et al. 2015, manuscript submitted to *Nat. Climate Change*, their Fig. S3), and Hoerling et al. 2012 showed that this would induce an Eastern Mediterranean drying through circulation changes, also consistent with our detected response.

Discussion. In this study, we have used local station data to understand the uniquely persistent drought that occurred in the southern Levant rainy season of 2014. We show that the event was unprecedented for the critical January–February period in the observational record, and through modeling the event, we showed that anthropogenic climate change made it ~45% more likely. However, our model is dry-biased in the region of interest, most likely due to a lack of very intense cyclones in the Mediterranean region (Anagnostopoulou et al. 2006). If changes in these processes are nonlinear under human-induced emissions, our model is unlikely to capture them fully. This wet season is when reservoirs and groundwater systems are recharged and snow pack accumulates to support summer streamflows. The consequent external stresses that came with this drought, such as crop failures, degraded grazing land, and overpumping of nonrenewable groundwater, suggest that water and agriculture authorities in the southern Levant region should have additional fail-safes in place going into the future.

ACKNOWLEDGMENTS. This project was funded by NERC ACE Africa, and by USAID Office of the Middle East Programme's MAWRED project. We would like to thank the Met Office Hadley Centre PRECIS team and our colleagues at the Oxford eResearch Centre for their technical and scientific support for the development and application of Weather@Home. Finally, we thank all of the volunteers who have donated their computing time to Weather@Home.

REFERENCES

Allen, M., 2003: Liability for climate change. *Nature*, **421**, 891–892.

Anagnostopoulou, Chr., K. Tolika, H. Flocas, and P. Maheras, 2006: Cyclones in the Mediterranean region: present and future climate scenarios derived from a general circulation model (HadAM3P). *Adv. Geosci.*, **7**, 9–14.

Black, E., 2009: The impact of climate change on daily precipitation statistics for Jordan and Israel.*Atmos. Sci. Lett.*, **10**, 192–200, doi:10.1002/asl.233.

Boe, J., L. Terray, F. Habets, and E. Martin, 2007: Statistical and dynamical downscaling of the Seine basin climate for hydro-meteorological studies. *Int. J. Climatol.*, **27**, 1643–1655, doi:10.1002/joc.1602.

Hatzaki, M., H. A. Flocas, C. Giannakopoulos, and P. Maheras, 2009: The impact of the eastern Mediterranean teleconnection pattern on the Mediterranean climate. *J. Climate*, **22**, 977–992.

Haylock, M. R., N. Hofstra, A. M. G. Klein Tank, E. J. Klok, P. D. Jones, and M. New, 2008: A European daily high-resolution gridded dataset of surface temperature and precipitation. *J. Geophys. Res.*, **113**, D20119, doi:10.1029/2008JD10201.

Herring, S. C., M. P. Hoerlin, T. C. Peterson, and P. A. Stott, Eds., 2014: Explaining extreme events of 2013 from a climate perspective. *Bull. Amer. Meteor. Soc.*, **95** (9), S1–S104.

Hoerling, M., J. Eischeid, J. Perlwitz, X. Quan, T. Zhang, and P. Pegion, 2012: On the increased frequency of Mediterranean drought. *J. Climate*, **25**, 2146–2161, doi:10.1175/JCLI-D-11-00296.1.

Massey, N., and Coauthors, 2015: weather@ home—development and validation of a very large ensemble modelling system for probabilistic event attribution. *Quart. J. Roy. Meteor. Soc.*, **141,** 1528-1545, doi:10.1002/qj.2455.

Saaroni, H., B. Ziv, J. Lempert, Y. Gazit, and E. Morin, 2014: Prolonged dry spells in the Levant region: Climatologic-synoptic analysis. *Int. J. Climatol.*, **35**, 2223–2236, doi:10.1002/joc.4143.

Schaller, N., F. E. L. Otto, G. J. van Oldenborgh, N. R. Massy, S. Sparrow, and M. R. Allen, 2014: The heavy precipitation event of May–June 2013 in the upper Danube and Elbe basins [in "Explaining Extreme Events of 2013 from a Climate Perspective"]. *Bull. Amer. Meteor. Soc.*, **95** (9), S69–S7.

Sipple, S., D. Mitchell, M. T. Black, A. J. Dittus, L. Harrington, N. Schaller, and F. E. L. Otto, 2015: Combining large model ensembles with extreme value statistics to improve attribution statements of rare events. *Wea. Climate Extremes*, **9**, 25-35, doi:10.1016/j.wace.2015.06.004.

Solomon, S., D. Qin, M. Manning, Z. Chen, M. Marquis, K. Averyt, M. Tignor, and H. L. Miller Jr., Eds., 2007: *Climate Change 2007: The Physical Science Basis*. Cambridge University Press, 996 pp.

Stark, J. D., C. J. Donlon, M. J. Martin, and M. E. McCulloch, 2007: OSTIA: An operational, high resolution, real time, global sea surface temperature analysis system. *Proc., Oceans 2007, Marine Challenges: Coastline to Deep Sea*, Aberdeen, Scotland, IEEE/OES, 1–4, doi:10.1109/OCEANSE.2007.4302251.

Udasin, S., 2014: Israel experiencing unprecedented drought conditions. *Jerusalem Post*, 10 February 2014. [Available online at www.jpost.com/Enviro-Tech/Israel-experiencing-unprecedented-drought-conditions-341003.]

15. DROUGHT IN THE MIDDLE EAST AND CENTRAL–SOUTHWEST ASIA DURING WINTER 2013/14

Mathew Barlow and Andrew Hoell

Of three identified proximate drought factors, climate change does not appear important for two. The third factor, western Pacific SSTs, exhibits a strong warming trend but attribution is an open question.

Introduction. During November 2013–April 2014, drought occurred over an area extending from the Mediterranean coastal Middle East, northward through Turkey and eastward through Kazakhstan, Uzbekistan, and Kyrgyzstan. An estimate of precipitation deficits during the drought is shown in Fig. 15.1a. Data issues mandate caution (e.g., Hoell et al. 2015; Barlow et al. 2015) but reports from throughout the region are consistent with the general area of drought, including for Syria (UNICEF 2014; WFP 2014), Turkey (Gokoluk 2014), Israel (Ackerman 2014), Kazakhstan (Kazinform 2014; Thomson Reuters 2014), and Kyrgyzstan (FAO 2014). Notably, the eastern (main) basin of the Aral Sea dried up for the first time in modern history (NASA 2014; Howard 2014). Although the long-term draining of the Aral Sea is due to agricultural withdrawals (Micklin 1988; Micklin and Aladin 2008), the current state of minimal storage may represent a new regime where yearly fluctuations are strongly affected by climate.

A time series of November–April precipitation anomalies averaged over the main drought region (black box in Fig. 15.1a) is shown in Fig. 15.1b. A statistically-significant downward trend is observed over the 1950–2014 period, with the post-1999 rainfall declines playing an important role and 2013/14 having the lowest value in the period, although data scarcity and continuity issues make confident trend analysis difficult in this region.

The goal of this analysis is to identify important factors in the drought, considered in the next section, and to examine those factors in the context of global warming, considered in the third section.

AFFILIATIONS: Barlow—Department of Environmental, Earth, and Atmospheric Sciences, University of Massachusetts Lowell, Lowell, Massachusetts; Hoell—NOAA Earth System Research Laboratory, Physical Sciences Division, Boulder, Colorado

DOI:10.1175/BAMS-D-15-00127.1

A supplement to this rticle is available online (10.1175/BAMS-D-15-00127.2)

Proximate drought factors. Three factors were active during the season that have been previously identified as important for drought in the region, based on both observational and modeling analyses as noted below: the North Atlantic Oscillation (NAO), a cold central Pacific, and a warm western Pacific. Here we consider whether each factor had a magnitude consistent with an important influence on drought based on previous events.

The NAO has been shown to influence precipitation in the western part of the region by Cullen and Demenocal (2000), Aizen et al. (2001), Cullen et al. (2002), Mann (2002), Krichak et al. (2002), Syed et al. (2006), and Black (2011). Based on the SST-derived NAO index of Cullen et al., the NAO was at its sixth-largest value in the last 65 years during the 2013/14 drought, with its overall pattern evident in the large-scale circulation anomalies, including a ridge extending into the western part of the domain (Supplemental Fig. S15.1).

The cold central Pacific SSTs associated with La Niña have also been shown to influence precipitation in the region by Price et al. (1998), Barlow et al. (2002), Nazemosadat and Ghasemi (2004), Mariotti et al. (2002, 2005), Syed et al. (2006), Mariotti (2007), Hoell et al. (2014a, 2014b), Yin et al. (2014), and Krichak et al. (2014). The values during the 2013/14 drought were similar to previous droughts, although of roughly two-thirds the magnitude (Supplemental Fig. S15.2).

Finally, warm anomalies in the western Pacific have been linked to drought in the region, generally in association with central Pacific cold anomalies (Agrawala et al. 2001; Barlow et al. 2002, 2015; Hoerling and Kumar 2003; Trigo et al. 2010; Hoell et al. 2012, 2014a,b). During the 2013/14 season, large positive SST anomalies were observed in the western Pacific (Fig. 15.1c), as part of a notable positive trend

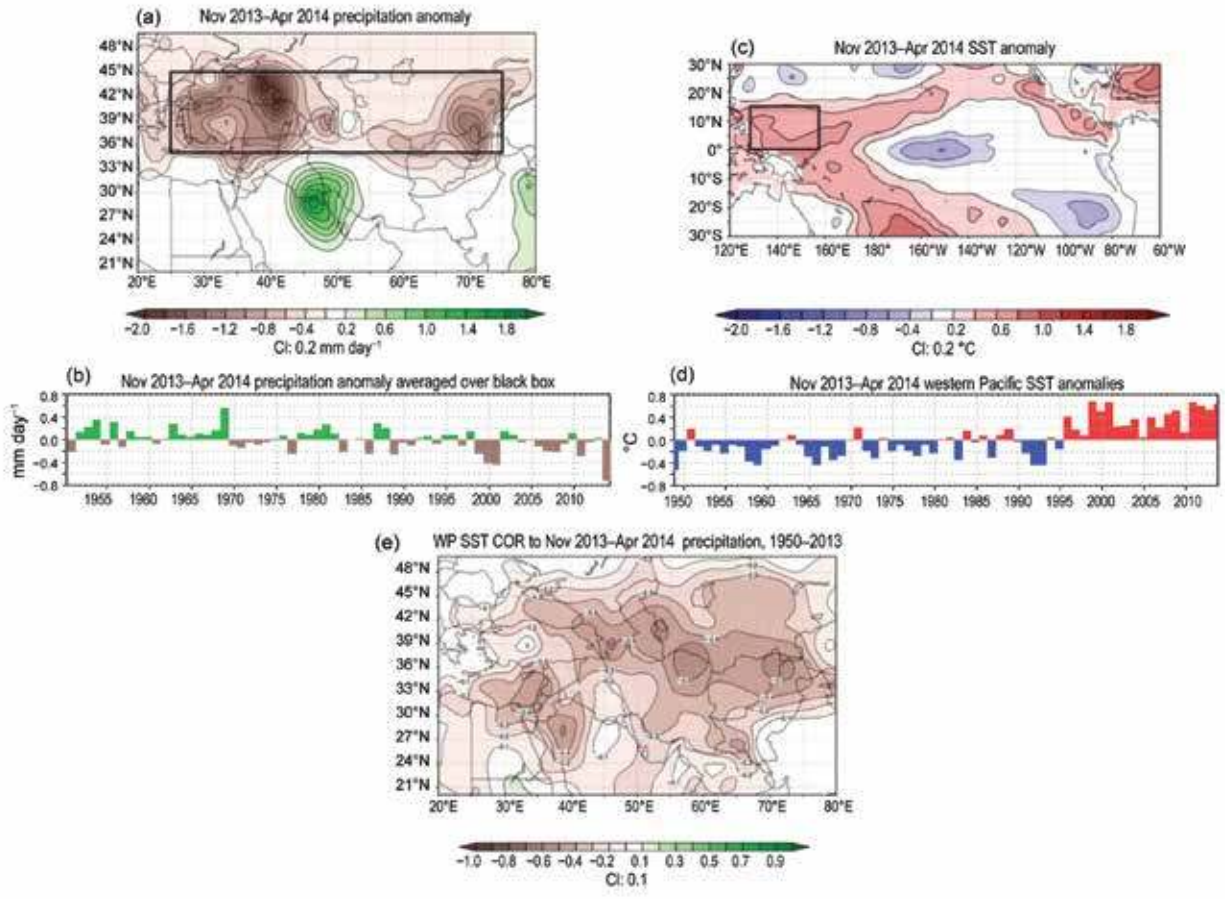

Fig. 15.1. Observational analysis: (a) Precipitation anomalies for Nov 2013–Apr 2014, contoured at 0.2 mm day^{-1}; (b) time series of Nov–Apr precipitation anomalies (mm day^{-1}) over the main drought region [black box in (a)]; (c) tropical Pacific SST anomalies for Nov 2013–Apr 2014, with a contour interval of 0.2°C; (d) time series of Nov–Apr SST anomalies (°C) over the western Pacific [black box in (c)], and (e) correlation of western Pacific SST anomalies to precipitation for 1950–2013, with a contour interval of 0.1. Precipitation is from the PREC dataset (Chen et al. 2002) and SST is from the ERSST dataset (Smith et al. 2008).

in the region (Fig. 15.1d; cf. Cravatte et al. 2009). To focus on the western Pacific–precipitation link, Fig. 15.1e shows the correlation between western Pacific SSTs and regional precipitation for 1950–2014. The largest correlation is −0.57 for this 65-year period.

Examination of the role of global warming in drought factors. Of the three factors, neither the NAO index nor the central Pacific SSTs exhibit a clear trend over the past 65 years, which strongly suggests that global warming has not played a direct role in these factors over that period.

The western Pacific SST, however, does exhibit a strong increase during this period. To further investigate this we have examined CAM4 model output for three sets of experiments: an ensemble of SST-forced runs of the 2013/14 season compared to climatology, a set of runs that isolate the influence of the western Pacific over the last 34 years, and a set of runs that isolate the influence of increased greenhouse gases (GHGs).

The SST-forced realization of the 2013/14 seasonal anomalies (Fig. 15.2a) shows considerable similarity to the observed anomalies, with dry over much of the observed drought region and some wet anomalies to the south. The modeled drought has a strong wet anomaly in the westernmost part of the domain, in distinction from observations, which may be related to the likely role of the NAO in the observed drought. Overall, the CAM4 provides further support for the influence of SST in the drought episode.

To isolate the effect of the western Pacific Ocean warming on Southwest Asia climate, a set of experiments was considered where a warm western Pacific Ocean SST (Supplemental Fig. S15.3a) was added to the monthly time-varying 1979–2013 SST trend (Supplemental Fig. S15.3b). The SST pattern added to the monthly climatology was used to force the

CAM4 model for 50 years. This model simulation was compared with a similar 50-year run of CAM5 that was forced only by the monthly time-varying 1979–2013 SST trend added to the monthly climatology. The difference between the two runs shows the forcing of Southwest Asia climate by the western Pacific. The result, shown in Fig. 15.2b, shows that the western Pacific itself is a strong drought forcing for the region, consistent with previous modeling and observational work, as well as the analysis shown in Fig. 15.1e. Since the western Pacific precipitation anomalies (Fig. 15.2b) are considerably stronger than the all-SST precipitation anomalies (Fig. 15.2a), it appears that some aspects of the global SSTs played a counteracting role, which would be a useful topic for future research.

Finally, model runs were analyzed to compare the behavior of precipitation in the current climate to the behavior of precipitation in the climate of the 1880s. In this experiment, precipitation from an SST-forced simulation of the observed climate was compared with precipitation from an SST-forced experiment where the SSTs were detrended to the equivalent 1880s mean conditions while GHG and ozone were adjusted to their 1880s values. (Please see NOAA ESRL's FACTS for further information: www.esrl.noaa.gov/psd/repository/alias/facts.) The net effect in the CAM4 model is shown in Fig. 15.2c. The effect of the current climate produces drying throughout Southwest Asia relative to the 1880s climate during November–April 1979–2012 (the years of the run), with a match in sign and magni-

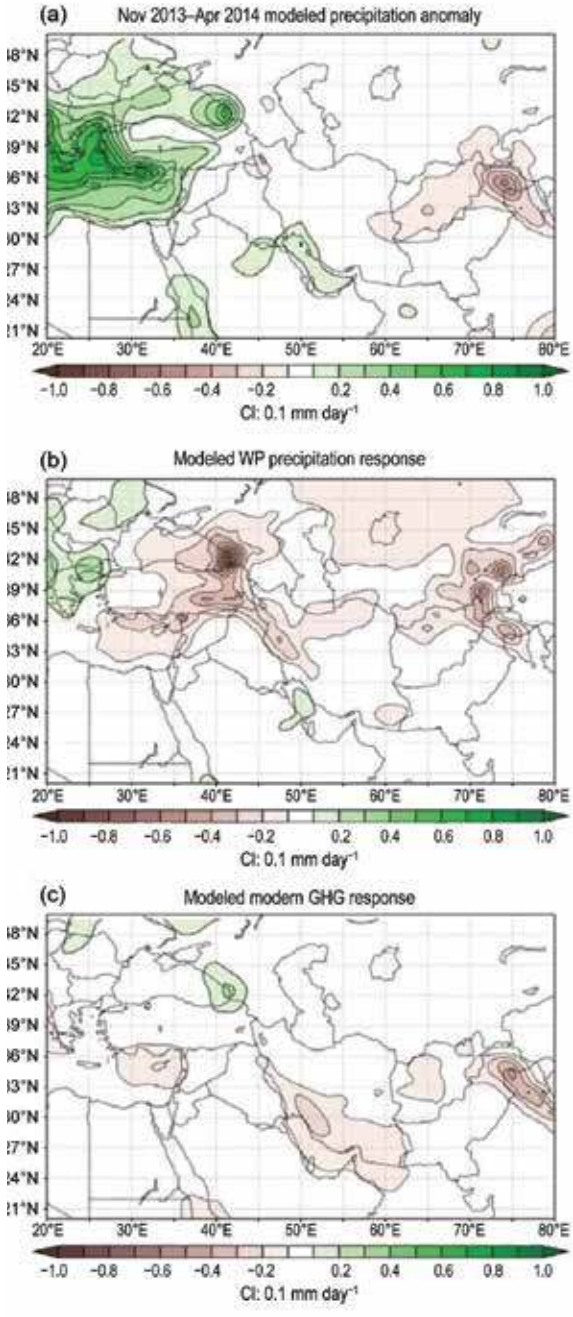

Fig. 15.2. Modeling analysis: (a) *CAM4 simulation of 2013–14 drought:* Precipitation anomaly for Nov 2013–Apr 2014 simulated by the average of 30-ensemble simulations of the CAM4 model driven by observed SST; (b) *Western Pacific forcing:* Precipitation difference for Nov–Apr between a 50-yr SST simulation of western Pacific SST added to the 1999–2012 SST trend superimposed on the monthly climatology and a 50-yr SST simulation of the 1999–2012 SST trend superimposed on the monthly climatology simulated by the CAM4 model. Stippling denotes significant differences at $p < 0.10$; and (c) *Climate change*: Precipitation difference for Nov–Apr 1979–2012 between the average of 30-ensemble simulations of the CAM4 model driven by observed SST and 30-ensemble simulations of the CAM4 model driven by detrended SSTs meant to simulate the 1880s climate. All precipitation anomalies are contoured and shaded at 0.1 mm day^{-1}.

tude over Afghanistan for the 2013/14 drought. This can be taken as an indication that climate change may have an effect on Southwest Asia precipitation, though further research is needed.

Discussion. Three factors previously identified as important for drought in the region were active during the 2013/14 season: the NAO, a cold central Pacific, and a warm western Pacific. Based on historical relationships, all three factors were of a magnitude consistent with an important role in the drought. The NAO and the central Pacific did not exhibit clear trends over that period and so do not appear to have been directly affected by climate change. The western Pacific, however, did experience a notable warming trend from 1950–2013, in conjunction with a statistically significant downward trend in precipitation over the drought region. Model experiments also show an important influence of the western Pacific on regional drought.

Consensus climate model projections, however, do not indicate increased drying over most of the region or preferential warming over the western Pacific (Stocker et al. 2014). If the models are correctly reproducing the relevant dynamics, then the observed warming trend in the western Pacific and associated influence on drought in the region is likely due to multidecadal variability. Unfortunately, there are several reasons to withhold full confidence in the model projections: there are problems with the models' regional seasonal cycle of precipitation (Stocker et al. 2014, chapter 9), the models' ability to reproduce the basic variability for the region hasn't been fully validated (Stocker et al. 2014, chapter 14), and the models' limitations in reproducing observed SST trends (e.g., Jha et al. 2014) call into question their predilection for projecting uniform warming of SSTs. Thus, it is not clear how closely the observed regional trend in western Pacific SSTs and associated regional drought is related to global warming: this is a critical problem for the field.

In summary: Of the three identified proximate factors in the drought—the NAO, the central Pacific, and the western Pacific—climate change does not appear to have played a strong role in the first two. The third factor, western Pacific SSTs, exhibits a strong warming trend but whether this trend is an expression of multidecadal variability or a signature of climate change is an important open question. Additionally, in model experiments, the increased GHG forcing during the last 34 years dries the region.

ACKNOWLEDGMENTS. We gratefully acknowledge the Facility for Climate Assessments (FACTS) database provided online by the Physical Sciences Division of NOAA's Earth System Research Laboratory.

REFERENCES

Ackerman, G., 2014: Israel suffering from unprecedented drought: Water agency. Bloomberg. [Available online at www.bloomberg.com/news/articles/2014-03-04/israel-suffering-from-unprecedented-drought-water-agency.]

Agrawala, S., M. Barlow, H. Cullen, and B. Lyon, 2001: The drought and humanitarian crisis in central and Southwest Asia: A climate perspective. IRI Special Rep., 01-11, 20 pp. [Available online at http://reliefweb.int/sites/reliefweb.int/files/resources/F5881844EEA93151C1256B1F005B3F62-iri-asiadrought-30nov.pdf.]

Aizen, E. M., V. B. Aizen, J. M. Melack, T. Nakamura, and T. Ohta, 2001: Precipitation and atmospheric circulation patterns at mid-latitudes of Asia. *Int. J. Climatol.*, **21**, 535–556.

Barlow, M., H. Cullen, and B. Lyon, 2002: Drought in central and southwest Asia: La Niña, the warm pool, and Indian Ocean precipitation. *J. Climate*, **15**, 697–700.

——, B. Zaitchik, S. Paz, E. Black, J. Evans, and A. Hoell, 2015: A review of drought in the Middle East and Southwest Asia. *J. Climate*, in press, doi:10.1175/JCLI-D-13-00692.1.

Black, E., 2011: The influence of the North Atlantic Oscillation and European circulation regimes on the daily to interannual variability of winter precipitation in Israel. *Int. J. Climatol.*, **32**, 1654–1664, doi:10.1002/joc.2383.

Chen, M., P. Xie, J. E. Janowiak, and P. A. Arkin, 2002: Global land precipitation: A 50-yr monthly analysis based on gauge observations. *J. Hydrometeor.*, **3**, 249–266.

Cravatte, S., T. Delcroix, D. Zhang, M. McPhaden, and J. Leloup, 2009: Observed freshening and warming of the western Pacific warm pool. *Climate Dyn.*, **33**, 565–589.

Cullen, H. M., and P. B. Demenocal, 2000: North Atlantic influence on Trigris–Euphrates streamflow. *Int. J. Climatol.*, **20**, 853–863.

Cullen, H. M., A. Kaplan, and P. A. Arkin, 2002: Impact of the North Atlantic Oscillation on Middle Eastern climate and streamflow. *Climatic Change*, **55**, 315–338.

FAO, 2014: GIEWS Update Kyrgyzstan: Severe drought in northern parts affects 2014 wheat production. [Available online at http://reliefweb.int/report/kyrgyzstan/giews-update-kyrgyzstan-severe-drought-northern-parts-affects-2014-wheat.]

Gokoluk, S., 2014: Turkey's lira drops most in two weeks as drought spurs inflation. Bloomberg. [Available online at www.bloomberg.com/news/articles/2014-09-02/lira-set-for-biggest-drop-in-2-weeks-as-drought-spurs-inflation.]

Hoell, A., M. Barlow, and R. Saini, 2012: The leading pattern of intraseasonal and interannual Indian Ocean precipitation variability and its relationship with Asian circulation during the boreal cold season. *J. Climate*, **25**, 7509–7526, doi:10.1175/JCLI-D-11-00572.1.

——, C. Funk, and M. Barlow, 2014a: The regional forcing of Northern Hemisphere drought during recent warm tropical west Pacific Ocean La Niña events. *Climate Dyn.*, **42**, 3289–3311, doi:10.1007/s00382-013-1799-4.

——, ——, and ——, 2014b: La Niña diversity and northwest Indian Ocean rim teleconnections. *Climate Dyn.*, **43**, 2707–2724, doi:10.1007/s00382-014-2083-y.

——, ——, and ——, 2015: The forcing southwest Asia teleconnections by low frequency Indo-Pacific sea surface temperature variability during boreal winter. *J. Climate*, **28**, 1511–1526, doi:10.1175/JCLI-D-14-00344.1.

Hoerling, M., and A. Kumar, 2003: The perfect ocean for drought. *Science*, **299**, 691–694.

Howard, B. C., 2014: Aral Sea's eastern basin dry for the first time in 600 years. National Geographic. [Available online at http://news.nationalgeographic.com/news/2014/10/141001-aral-sea-shrinking-drought-water-environment/.]

Jha, B., Z. Z. Hu, and A. Kumar, 2014: SST and ENSO variability and change simulated in historical experiments of CMIP5 models. *Climate Dyn.*, **42**, 2113–2124, doi:10.1007/s00382-013-1803-z.

Kazinform, 2014: Drought causes low wheat yields in S Kazakhstan – Agriculture Ministry. [Available online at www.inform.kz/eng/article/2685521.]

Krichak, S. O., P. Kishcha, and P. Alpert, 2002: Decadal trends of main Eurasian oscillations and the Eastern Mediterranean precipitation. *Theor. Appl. Climatol.*, **72**, 209–220.

——, J. S. Breitgand, S. Gualdi, and S. B. Feldstein, 2014: Teleconnection—extreme precipitation relationships over the Mediterranean region. *Theor. Appl. Climatol.*, **117**, 679–692, doi:10.1007/s00704-013-1036-4.

Mann, M. E., 2002: Large-scale climate variability and connections with the Middle East in past centuries. *Climatic Change*, **55**, 287–314.

Mariotti, A., 2007: How ENSO impacts precipitation in southwest central Asia. *Geophys. Res. Lett.*, **34**, L16706, doi:10.1029/2007GL030078.

——, N. Zeng, and K. M. Lau, 2002: Euro-Mediterranean rainfall and ENSO—a seasonally varying relationship. *Geophys. Res. Lett.*, **29** (12), doi:10.1029/2001GL014248.

——, J. Ballabrera-Poy, and N. Zeng, 2005: Tropical influence on Euro–Asian autumn rainfall variability. *Climate Dyn.*, **24**, 511–521, doi:10.1007/s00382-004-0498-6.

Micklin, P. P., 1988: Dessication of the Aral Sea: A water management disaster in the Soviet Union. *Science*, **241**, 1170–1176.

——, and N. V. Aladin, 2008: Reclaiming the Aral Sea. *Sci. Amer.*, **48** (4), 64–71.

NASA, 2014: The Aral Sea loses its eastern lobe. NASA Earth Observatory. [Available online at http://earthobservatory.nasa.gov/IOTD/view.php?id=84437.]

Nazemosadat, M. J., and A. R. Ghasemi, 2004: Quantifying the ENSO-related shifts in the intensity and probability of drought and wet periods in Iran. *J. Climate*, **17**, 4005–4018.

Price, C., L. Stone, A. Huppert, B. Rajagopalan, and P. Alpert, 1998: A possible link between El Niño and precipitation in Israel. *Geophys. Res. Lett.*, **25**, 3963–3966, doi:10.1029/1998GL900098.

Smith, T. M., R. W. Reynolds, T. C. Peterson, and J. Lawrimore, 2008: Improvements to NOAA's historical merged land–ocean temperature analysis (1880–2006). *J. Climate*, **21**, 2283–2296, doi:10.1175/2007JCLI2100.1.

Stocker, T. F., and Coauthors, Eds., 2014: *Climate Change 2013: The Physical Science Basis*. Cambridge University Press, 1535 pp., doi:10.1017/CBO9781107415324.

Syed, F. S., F. Giorgi, J. S. Pal, and M. P. King, 2006: Effect of remote forcings on the winter precipitation of central southwest Asia part 1: Observations. *Theor. Appl. Climatol.*, **86**, 147–160, doi:10.1007/s00704-005-0217-1.

Thomson Reuters, 2014: Thomson Reuters Commodities Research & Forecast analysts report forecasted rain critical for wheat crop in key regions. [Available online at http://blog.financial.thomsonreuters.com/dry-weather-threat-wheat-crop-key-regions/.]

Trigo, R. M., C. M. Gouveia, and D. Barriopedro, 2010: The intense 2007–2009 drought in the Fertile Crescent: Impacts and associated atmospheric circulation. *Agric. For. Meteor.*, **150**, 1245–1257.

UNICEF, 2014: Drying up: The growing water crises facing Syria and the region. UNICEF, 6 pp. [Available online at http://childrenofsyria.info/wp-content/uploads/2014/06/UNICEF-Syria-Region-water-alert-FINAL-En.pdf.]

WFP, 2014: Special focus: Syria—Will drought worsen the impact of conflict on food insecurity? World Food Programme, 8 pp. [Available online at www.wfp.org/content/syria-special-focus-will-drought-worsen-impact-conflict-food-insecurity]

Yin, Z. Y., H. Wang, and X. Liu, 2014: A comparative study on precipitation climatology and interannual variability in the lower midlatitude East Asia and central Asia. *J. Climate*, **27**, 7830–7848, doi:10.1175/JCLI-D-14-00052.1.

16. ASSESSING THE CONTRIBUTIONS OF EAST AFRICAN AND WEST PACIFIC WARMING TO THE 2014 BOREAL SPRING EAST AFRICAN DROUGHT

Chris Funk, Shraddhanand Shukla, Andy Hoell, and Ben Livneh

Anthropogenic warming contributed to the 2014 East African drought by increasing East African and west Pacific temperatures, and increasing the gradient between standardized western and central Pacific SST causing reduced rainfall, evapotranspiration, and soil moisture.

Introduction. During April–June of 2014 some areas of East Africa (EA) experienced substantial rainfall deficits (Funk et al. 2014) and warm land surface temperatures (Supplemental Fig. S16.1). Here, using the Variable Infiltration Capacity model (VIC; Liang et al. 1994; Nijssen et al. 1997), we evaluate and contrast the potential influence of (i) warm East African air temperatures and (ii) rainfall reductions associated with a more intense West Pacific Index (WPI; Funk et al. 2014). The WPI is a standardized version of the West Pacific Gradient (Hoell and Funk 2013a); here defined as the standardized difference between the Niño 4 and West Pacific (WP; 10°S–10°N, 110°–150°E) SST (Funk et al. 2014): WPI = Z(Z(Niño 4) − Z(WP)), where Z() denotes standardization.

The April–June 2014 drought, like many droughts over the past 20 years, occurred in conjunction with an enhanced WP SST gradient (Funk et al. 2014; Liebmann et al. 2014; Lyon and DeWitt 2012; Shukla et al. 2014a). Interagency research by Famine Early Warning Systems Networks (FEWS NET) scientists has been focusing on using SST gradients to predict some of these spring droughts (Funk et al. 2014; Shukla et al. 2014a; Shukla et al. 2014b). Climate model ensembles reveal strong 3-month lagged WPI–EA spring rainfall relationships (Funk et al. 2014), and these simulation results help justify successful forecasts based on empirical relationships (Funk et al. 2014) or hybrid statistical–dynamic forecasts (Shukla et al. 2014a). Diagnostic analyses of simulations from the ECHAM5 (Liebmann et al. 2014) and GFSv2 (Hoell and Funk 2013b) models help confirm these relationships, and WP SST gradients were used to predict the 2014 boreal spring drought (Funk et al. 2014). Extreme WPI conditions represent a combination of warming west Pacific SST (Funk and Hoell 2015) and La Niña-like cool central Pacific SST, which enhances rainfall and moisture convergence over the Indo-Pacific warm pool while decreasing it over eastern East Africa (Hoell and Funk 2013b; Hoell et al. 2014; Liebmann et al. 2014; Williams and Funk 2011).

Methods and Results. While 2014 EA air temperatures and WP SST anomalies were extremely warm, Niño 4 SST anomalies were not. Figures 16.1a–c compare the observed EA air temperatures, WP and Niño 4 SST to 1900–50 probability density functions (PDFs) based on observations, and an ensemble of historical (Taylor et al. 2011) simulations based on all forcings (natural and anthropogenic) from the Coupled Model Intercomparison Project Phase 5 (CMIP5; Supplemental Table 16.1). The selected EA region (Supplemental Fig. S16.1) was chosen because it was hot and dry in 2014, and reasonably homogeneous (Funk et al. 2014). The +1°C NASA Goddard Institute for Space Studies (GISS) air temperature anomaly (Hansen et al. 2010) far exceeds the 1900–50 PDFs based on historical observations or the CMIP5 historical simulations. The 1900–50 period was used to represent near preindustrial conditions. When bias corrected using the ratio of the observed (0.53°C) and simulated (0.42°C) temperatures, the smoothed (15-yr average) CMIP5 ensemble mean tracks very closely with observations (r = 0.97; Fig. 16.1d), and the observed +1°C anomaly is very similar to the center of the 2014 CMIP5 PDF (Fig. 16.1a) and the mean of the CMIP5 ensemble (0.99°C). Thus, we find that (i) the CMIP5 models do a very good job of recreating

Affiliations: Funk—U.S. Geological Survey, and University of California, Santa Barbara, Santa Barbara, California; Shukla—University of California, Santa Barbara, Santa Barbara, California; Hoell—NOAA, Earth System Research Laboratory Physical Sciences Division, Boulder, Colorado; Livneh—Department of Civil, Environmental, and Architectural Engineering & Cooperative Institute for Research in Environmental Sciences, University of Colorado, Boulder, Colorado

DOI: 10.1175/BAMS-D-15-00106.1

A supplement to this article is available online (10.1175/BAMS-D-15-00106.2)

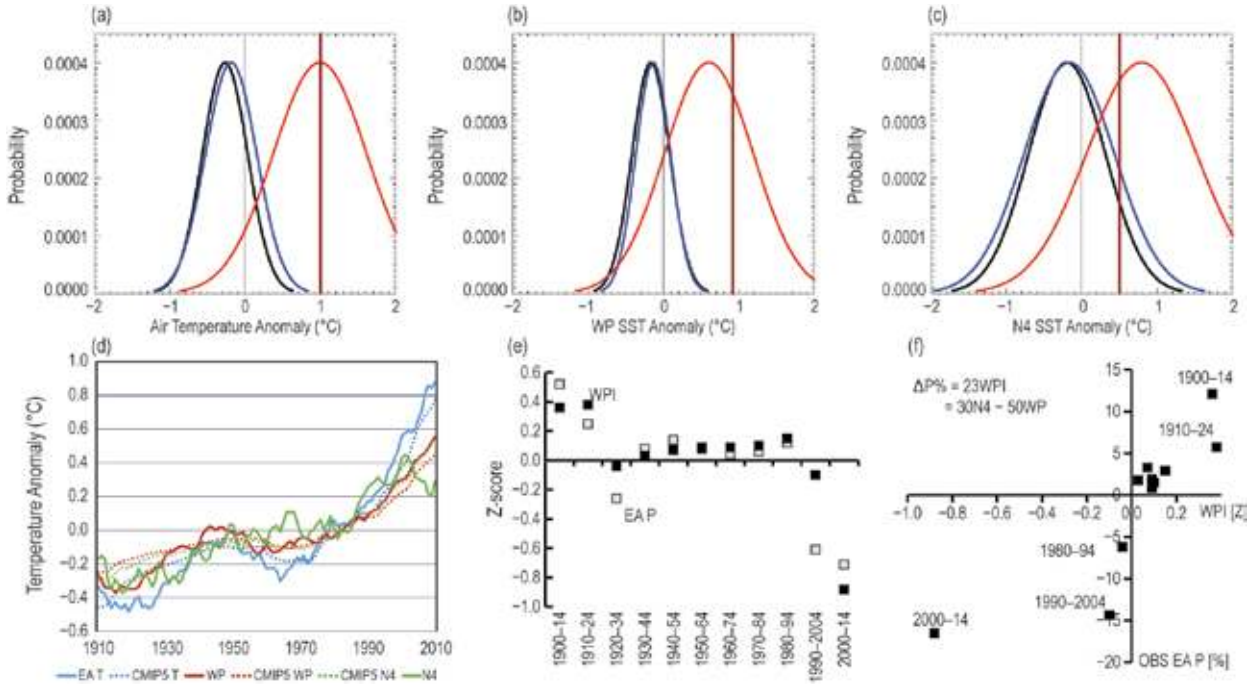

Fig. 16.1. (a) East African air temperature anomalies PDFs based on 1900–50 observations (black), 1900–50 CMIP5 simulations (blue), and 2014 CMIP5 all forcings (natural and anthropogenic) simulations (red); observed 2014 air temperatures shown with a vertical line. (b) As in (a) but for WP SSTs. (c) As in (a) but for Niño 4 SSTs. (d) Observed and CMIP5 time series, smoothed with 15-yr running means. (e) 15-yr averages of the WPI and standardized EA precipitation. (f) Same data as a scatterplot. All data are expressed as anomalies from a 1900–2014 reference period.

the observed pattern of warming (Fig. 16.1d), (ii) the observed +1°C anomaly appears extremely unlikely without recent anthropogenic warming, and (iii) the observed +1°C warming was very likely to be due in part to anthropogenic influences.

We find similar results when examining WP SSTs (Fig. 16.1b). The large +0.9 WP SST anomaly—the warmest in the extended reconstruction dataset (Smith et al. 2008)—sits far beyond the observed and historical CMIP5 1900–50 PDFs. WP SST is heavily influenced by radiative forcing (Funk and Hoell 2015) and tracks closely with the CMIP5 ensemble mean (r = 0.96; Fig. 16.1d). The observed +0.9°C anomaly is substantially more than the CMIP5 prediction (+0.6°C). Here again, we find that (i) the CMIP5 models do a very good job of recreating the observed pattern of warming (Fig. 16.1d), (ii) the observed +0.9°C anomaly appears extremely unlikely without recent anthropogenic warming, and (iii) the observed +0.9°C warming was very likely to be due in part to anthropogenic influences.

Niño 4 SSTs have high interannual variance, and the chances of an anomaly as warm as or warmer than the observed +0.5°C anomaly occurring were therefore likely (Fig. 16.1c) given the variance in both the observed and CMIP5 1900–50 PDFs (8% and 13%, respectively; Table 16.1). Between 1900 and 1990, the observed Niño 4 time series tended to follow the CMIP5 mean (Fig. 16.1d), but since about 1990, warming in the Niño 4 region has been limited (Funk et al. 2014). This relative cooling may be due to Pacific Decadal Variability (PDV; Lyon et al. 2013; Meehl et al. 2013) or perhaps a poorly understood and poorly forced response, which might potentially be related to increased warm pool SSTs, precipitation, and more rapid central Pacific trade winds (Funk and Hoell 2015). The observed 2000–14 Niño 4 average (0.28°C) was substantially below the +0.5°C warming predicted by the CMIP5 simulations (Fig. 16.1d).

Figures 16.1e and f show 1900–2014 EA Centennial Trends (CenTrends; Funk et al. 2015) precipitation as a function of the WPI. These data are from the new FEWS NET CenTrends archive (Funk et al. 2015). CenTrends incorporate numerous stations from the Nicholson database (Nicholson et al. 2012) and observations acquired from the Tanzanian, Kenyan, and Ethiopian Meteorological Agencies (Funk et al. 2015). Decadal CenTrends (Funk et al. 2015) and the Global Precipitation Climatology Centre dataset (Funk et al. 2014) EA spring rainfall vary with WP/Niño SST

Table 16.1. Observed and modeled anomalies. Probabilities with and without climate change were based, respectively, on the 2014 and the 1900–50 values from the CMIP5 ensemble (Supplemental Table S16.1).

Observation	Observation anomaly	1900–2014 Percentile Observation (CMIP5)	Probability 1900–1950 PDF Observation (CMIP5)	Probability 2014 PDF	Estimated anthropogenic contribution
AMJ air temperatures	+1.0°C†	96.5% (97.9%)	0% (0%)	(50%)	+1.0°C
WP SST	+0.9°C†	100% (99.6%)	0% (0%)	(30%)	+0.6°C
Niño 4 SST	+0.5°C	82% (78%)	8% (13%)	(66%)	+0.6°C
Z(N4) - Z(WP)	−1.9°C	16% (0%)	8% (0%)	(1%)	−0.6°C
AMJ CenTrends P	−0.8σ†				−0.4σ*
AMJ ET	−1σ‡				−0.σ** 0.0σ ***
AMJ soil moisture	−0.5σ‡				−0.3σ** 0.0σ***

† Based on 1900–2014 baseline

‡ Based on 1982–2014 baseline

* Based on estimated anthropogenic contribution to WP warming and the WPI regression results shown in Fig.16.1f.

** Based on assumed 11% WP-related rainfall reduction and +1°C anthropogenic warming.

*** Based on an assumed +1°C anthropogenic warming.

gradients (Fig. 16.1e), falling markedly during the 1990s and 2000s as the WP warmed and the Niño 4 did not (Fig. 16.1d). ECHAM5 (Liebmann et al. 2014) and GFSv2 (Funk et al. 2014) and CESM (Funk et al. 2014) models help confirm the WPI–EA relationship (Supplemental Fig. S16.2).

The data shown in Fig. 16.1f imply a quasi-linear relation with the percent change EA April–June rainfall equal to 23 times the WPI. By inverting the WPI standardization: Z(Z(N4) − Z(WP)), we can estimate changes based on SST anomalies: ΔP% = 30Niño 4 − 49WP. While the observed WP warming has been substantially greater than Niño 4 warming (Fig. 16.1d) and the 2014 WP values the warmest on record (+0.9°C; Fig. 16.1b), here we simply test the impact associated with an identical +0.6°C "bathtub" anthropogenic warming in each region. Under this assumption, rainfall would decrease by 11%; ΔP% = 30 • 0.6 − 49WP • 0.6 = −11%.

We next assess the possible hydrologic impacts associated with an assumed +1°C increase in EA air temperatures, based on the CMIP5 ensemble mean, and an 11% rainfall decrease using the VIC model (Liang et al. 1994; Nijssen et al. 1997), which has been used to analyze recent EA drought (Sheffield et al. 2014; Shukla et al. 2014b). We evaluate these impacts by contrasting VIC simulations forced with the observed 2014 precipitation and temperatures (Supplemental Fig. S16.3) with (i) simulations forced with 11% more precipitation and 1°C cooler air temperatures and (ii) simulations forced with observed precipitation and 1°C cooler air temperatures (Figs. 16.2b,c).

We begin by showing recent changes in April–June hydrology (Fig. 16.2a). The well-documented post-1999 decline (Funk and Hoell 2015; Funk et al. 2014; Hoell and Funk 2013b; Liebmann et al. 2014; Lyon 2014; Lyon and DeWitt 2012; Yang et al. 2014) has resulted in a 10 to 30% reduction in rainfall. Dry and warm conditions have been much more likely since 1998 across the eastern portions of EA. The associated evapotranspiration (ET) reductions follow rainfall deficits closely, and southeastern Kenya, south-central

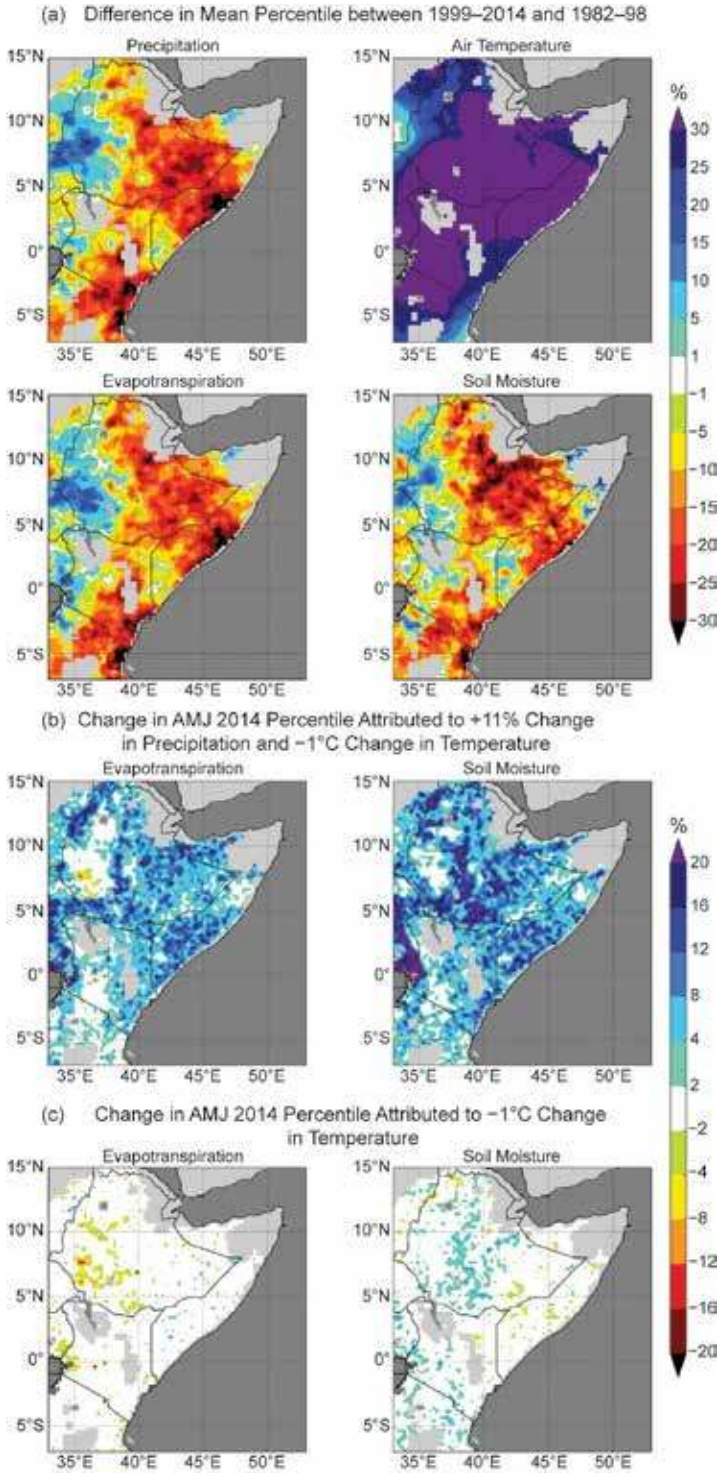

Fig. 16.2. (a) Changes in Apr–Jun precipitation, air temperature, ET, and soil moisture between 1999–2014 and 1982–98, expressed as differences in the 1981–2014 percentiles. (b) Change in Apr–Jun 2014 ET and soil moisture percentiles, based on an 11% rainfall increase and a 1°C cooling of air temperatures. (c) As in (b) but based on just a 1°C cooling of air temperatures. Areas receiving, on average, less than 75 mm of rainfall have been masked.

Somalia, and eastern Ethiopia appear to be the most affected.

We next compare the impact of (i) less rainfall and warmer air temperatures, and (ii) only warmer air temperatures, by using counterfactual experiments. In the first experiment (i), we increased the April–June precipitation by 11% (+0.4 standardized deviations) and reduced the air temperature by 1°C. Supplemental Fig. S16.3 compares 2014 to 2011, 2012, and 2013. While not as dry as 2011, the VIC simulations (Fig. 16.2b) indicate that much of Kenya, Somalia, and Ethiopia experienced low ET and soil moisture, with percentile values of less than 30%. The combination of increased precipitation and reduced air temperatures increased the simulated percentiles by about 4%–25% (Fig. 16.2b). In western Kenya, however, large changes in soil moisture are found in key crop producing areas of the Rift Valley. This is true as well in central Ethiopia, between 7°–10°N at about 38°E.

Figure 16.2c shows results for our experiment (ii), where we changed only the air temperatures. These results imply that, given the observed precipitation conditions, warmer air temperatures acting alone had little influence on ET and soil moisture. This may indicate that the evaporative demand, even in the −1°C scenario, was more than the available moisture supply in most places.

We can compare the 2014 anomalies to the empirical 1982–2014 distributions of ET and soil moisture, averaged over the study site (Supplemental Fig. 4). The 2014 ET anomaly was low compared to the historical distribution (a −1 standardized anomaly). Cooling the air temperatures changed this value very little. Increasing rainfall and cooling air temperatures moderated the drought, resulting in a −0.7 standardized anomaly. The 2014 soil moisture anomaly was mild (a −0.5 standardized anomaly); increasing rainfall and cooling air temperatures moderated soil moisture deficits, resulting in a −0.2 standardized anomaly. Averaging these soil moisture results across the entire domain may mask important localized impacts (Fig. 16.2b).

Conclusion. In summary, we found that the CMIP5 models predicted very well ($r \approx 0.96$) low frequency EA and WP temperature variations, and the very warm ~+1°C WP and EA anomalies appear extremely unlikely without anthropogenic warming. WP SSTs track closely with climate change projections (Supplemental Fig. S16.5a), climate change simulations indicate an increase in the standardized west Pacific SST gradient (Supplemental Figs. S16.5b; Fig. S16.6a), and 1900–2014 15-yr running averages of March–June Greater Horn of Africa rainfall follow closely changes in the WPI (Funk et al. 2014; Supplemental Fig. S16.5d). The Pacific SST gradient is amplified when the ENSO-related SST component is removed (Supplemental Fig. S16.6b), suggesting that stronger gradient events may occur when ENSO conditions are neutral or La Niña-like. Our hydrologic modeling results suggest that a 1°C temperature increase combined with an 11% WPI-related precipitation decrease, associated with a ~+0.6°C warming in both the WP and Niño 4 regions, would have appreciably increased the 2014 April–June drought intensity, enhancing ET and soil moisture anomalies from −0.7 and −0.2 standardized deviations to −1 and −0.5 in areas experiencing some isolated food security crises (Supplemental Fig. S16.7). Air temperature changes alone were found to have little effect.

ACKNOWLEDGEMENTS. This work was supported by US Geological Survey (USGS) cooperative agreement #G09AC000001), NOAA Award NA11OAR4310151, the USGS Climate and Land Use Change program, NASA SERVIR, and NASA grants NNH12ZDA001N-IDS and NNX14AD30G. We would like to thank our editor (Stephanie Herring), our anonymous reviewers, and Colin Kelley whose suggestions substantially improved this manuscript.

REFERENCES

Funk, C., and A. Hoell, 2015: The leading mode of observed and CMIP5 ENSO-residual sea surface temperatures and associated changes in Indo-Pacific climate. *J. Climate*, **28**, 4309–4329, doi:10.1175/JCLI-D-14-00334.1.

——,——, S. Shukla, I. Bladé, B. Liebmann, J. B. Roberts, and G. Husak, 2014: Predicting East African spring droughts using Pacific and Indian Ocean sea surface temperature indices. *Hydrol. Earth Syst. Sci.*, **18**, 4965–4978, doi:10.5194/hess-18-4965-2014.

——, S. Nicholson, M. Landsfeld, D. L. Klotter, M., P. Peterson, and L. Harrison, 2015: The Centennial Trends Greater Horn of Africa precipitation dataset. *Nat. Scientific Data*, **2**, Article 150050, doi:10.1038/sdata.2015.50.

Hansen, J., R. Ruedy, M. Sato, and K. Lo, 2010: Global surface temperature change. *Rev. Geophys.*, **48**, RG4004, doi:10.1029/2010RG000345.

Hoell, A., and C. Funk, 2013a: The ENSO-related west Pacific sea surface temperature gradient. *J. Climate*, **26**, 9545–9562, doi:10.1175/JCLI-D-12-00344.1.

——, and ——, 2013b: Indo-Pacific sea surface temperature influences on failed consecutive rainy seasons over eastern Africa. *Climate Dyn.*, **43**, 1645–1660, doi:10.1007/s00382-013-1991-6.

——, ——, and M. Barlow, 2014: La Niña diversity and northwest Indian Ocean rim teleconnections. *Climate Dyn.*, **43**, 2707–2724, doi:10.1007/s00382-014-2083-y.

Liang, X., D. P. Lettenmaier, E. F. Wood, and S. J. Burges, 1994: A simple hydrologically based model of land surface water and energy fluxes for general circulation models. *J. Geophys. Res.*, **99**, 14415–14428, doi:10.1029/94JD00483.

Liebmann, B., and Coauthors, 2014: Understanding recent eastern Horn of Africa rainfall variability and change. *J. Climate*, **27**, 8630–8645, doi:10.1175/JCLI-D-13-00714.1.

Lyon, B., 2014: Seasonal drought in the Greater Horn of Africa and its recent increase during the March–May long rains. *J. Climate*, **27**, 7953–7975, doi:10.1175/JCLI-D-13-00459.1.

——, and D. G. DeWitt, 2012: A recent and abrupt decline in the East African long rains. *Geophys. Res. Lett.*, **39**, L02702, doi:10.1029/2011GL050337.

——, A. G. Barnston, and D. G. DeWitt, 2013: Tropical pacific forcing of a 1998–1999 climate shift: Observational analysis and climate model results for the boreal spring season. *Climate Dyn.*, **43**, 893–909, doi:10.1007/s00382-013-1891-9.

Meehl, G. A., A. Hu, J. M. Arblaster, J. Fasullo, and K. E. Trenberth, 2013: Externally forced and internally generated decadal climate variability associated with the interdecadal Pacific oscillation. *J. Climate*, **26**, 7298–7310, doi:10.1175/JCLI-D-12-00548.1.

Nicholson, S. E., A. K. Dezfuli, and D. Klotter, 2012: A two-century precipitation dataset for the continent of Africa. *Bull. Amer. Meteor. Soc.*, **93**, 1219–1231, doi:10.1175/BAMS-D-11-00212.1.

Nijssen, B., D. P. Lettenmaier, X. Liang, S. W. Wetzel, and E. F. Wood, 1997: Streamflow simulation for continental-scale river basins. *Water Resour. Res.*, **33**, 711–724.

Sheffield, J., and Coauthors, 2014: A drought monitoring and forecasting system for sub-Sahara African water resources and food security. *Bull. Amer. Meteor. Soc.*, **95**, 861–882, doi:10.1175/BAMS-D-12-00124.1.

Shukla, S., C. Funk, and A. Hoell, 2014a: Using constructed analogs to improve the skill of National Multi-Model Ensemble March–April–May precipitation forecasts in equatorial East Africa. *Environ. Res. Lett.*, **9**, 094009, doi:10.1088/1748-9326/9/9/094009.

——, A. McNally, G. Husak, and C. Funk, 2014b: A seasonal agricultural drought forecast system for food-insecure regions of East Africa. *Hydrol. Earth Syst. Sci.*, **18**, 3907–3921, doi:10.5194/hess-18-3907-2014.

Smith, T. M., R. W. Reynolds, T. C. Peterson, and J. Lawrimore, 2008: Improvements to NOAA's Historical Merged Land–Ocean Surface Temperature Analysis (1880–2006). *J. Climate*, **21**, 2283–2296.

Taylor, K. E., R. J. Stouffer, and G. A. Meehl, 2011: An overview of CMIP5 and the experiment design. *Bull. Amer. Meteor. Soc.*, **93**, 485–498, doi:10.1175/BAMS-D-11-00094.1.

Williams, P., and C. Funk, 2011: A westward extension of the warm pool leads to a westward extension of the Walker circulation, drying eastern Africa. *Climate Dyn.*, **37**, 2417–2435.

Yang, W., R. Seager, M. A. Cane, and B. Lyon, 2014: The East African long rains in observations and models. *J. Climate*, **27**, 7185–7202, doi:10.1175/JCLI-D-13-00447.1.

17. THE 2014 DROUGHT IN THE HORN OF AFRICA: ATTRIBUTION OF METEOROLOGICAL DRIVERS

T. R. Marthews, F. E. L. Otto, D. Mitchell, S. J. Dadson, and R. G. Jones

Ensemble modelling of the East African 2014 long rains season suggests no anthropogenic influence on the likelihood of low rainfall but clear signals in other drivers of drought.

Introduction. Drought has always been a natural part of climatic variability in Africa (Masih et al. 2014), but the Greater Horn of Africa region (GHoA; taken as the area east of the Nile River between Khartoum, Sudan, and Mombasa, Kenya, see Fig. 17.1) is especially vulnerable to the impacts of drought because of a unique combination of several adverse factors. Despite favorable soils, the GHoA has long experienced widespread poverty and high levels of food insecurity (Global Hunger Index 2013; FEWS NET 2015). Political instability and the high dependence of GHoA's population on rain-fed agriculture exacerbate the impacts of droughts (Love 2009; Masih et al. 2014).

Most areas of the GHoA experience two rainy seasons: the "long rains" during March–June as the intertropical convergence zone (ITCZ) crosses the equator from south to north and the "short rains" during October–December as the ITCZ returns to the south (Yang et al. 2015). The long rains have received much recent attention, first, because identifying their large-scale climate drivers has proved challenging (Lyon and DeWitt 2012; Funk et al. 2014; Yang et al. 2014) and second, because since 1999 the long rains have been decreasing across the region (Lyon and DeWitt 2012; Lyon 2014), with disastrous consequences for local populations (Boulter et al. 2013; Masih et al. 2014).

The focus of this study is the 2014 drought in GHoA. In late 2013, the short rains failed almost completely in Kenya, Somalia, and southern Ethiopia, leading to an abnormally-dry growing season from January to March 2014, followed by a widespread drought in many agricultural areas of the GHoA because of much-reduced long rains during March to June (FAO 2014; ECHO 2014; see also Hoell and Funk 2014). A similar failure of both rainy seasons occurred in 2010–11, causing widespread crop failures in 2011 and led, as a result of political instability, to famine in Somalia (UNOCHA 2011; Lott et al. 2013; Coghlan et al. 2014; Nicholson 2014). Because climate-related extremes have been the dominant trigger of natural disasters in the GHoA (Omondi et al. 2014), understanding these extreme climatic events and their impacts is critically important.

The decrease of the long rains during March to June has been the dominant driver of the increased frequency and severity of droughts in the GHoA in recent years (Yang et al. 2015), but how much of this decrease is part of natural variability and how much is attributable to anthropogenic climate change? Events such as drought usually occur as a result of a combination of factors (Trenberth 2012), only some of which may be related to recent human activities. Therefore, attribution studies of extreme climatic events are important, but such studies remain rare for Africa partly because of shorter instrumental records that limit our ability to assign causation with certainty (Tierney et al. 2013; Stott et al. 2014). The attribution issue gains added urgency because extreme weather events such as heatwaves, floods, and droughts can be associated with high levels of loss and damage to human society (James et al. 2014; Stott et al. 2014). In this study we ask whether human-induced climate change played a role in the meteorology of the 2014 East African long rains season that could have contributed to the 2014 drought in the GHoA.

Methods. We use probabilistic event attribution (PEA) techniques (e.g., Allen 2003; Stott et al. 2014), which

AFFILIATIONS: Marthews—School of Geography and the Environment, University of Oxford, Oxford, United Kingdom; Otto—Environmental Change Institute, University of Oxford, Oxford, United Kingdom; Dadson—School of Geography and the Environment, University of Oxford, Oxford, United Kingdom; Jones—School of Geography and the Environment, University of Oxford, Oxford, United Kingdom and Met Office Hadley Centre, Exeter, United Kingdom

DOI:10.1175/BAMS-D-15-00115.1

A supplement to this article is available online (10.1175/BAMS-D-15-00115.2)

involve taking an ensemble approach to the problem of estimating the response of the climate system to external forcing (Massey et al. 2015). Two sets of simulations are employed: one factual set generated from multiple realizations of the event in question using observed climate forcings and one counterfactual set based on the "world that might have been without higher greenhouse gas emissions". These counterfactual simulations are the result of running the same climate model but with anthropogenic greenhouse gas forcings removed (Otto et al. 2015). Comparisons between these two ensembles allow us to quantify the change in extreme event probability that is attributable to anthropogenic as opposed to natural drivers (Pall et al. 2011).

Large ensembles of model simulations are necessary for PEA to understand extreme or rare events (Allen 2003). Our ensemble sets are simulated using HadRM3P, a regional climate model, embedded in the Hadley Centre atmosphere-only general circulation model (HadAM3P) with perturbed initial conditions and observed sea surface temperatures (SSTs), derived from the operational sea surface temperature and sea ice analysis (OSTIA; Stark et al. 2007). These simulations were run using the volunteer computing framework weather@home (Massey et al. 2015).

We used a 0.44° resolution simulation domain (~50 km at midlatitudes) covering Africa from 14.3°S to 46.0°N and from 25.0°W to 62.6°E: a much greater area than the GHoA (Fig. 17.1) to ensure that edge effects were negligible during these simulations. Data from factual and counterfactual simulations form the basis of the subsequent analysis. Statistics are calculated for an area comprising south Ethiopia, north Kenya, and south-west Somalia, the areas where precipitation deficit, hydrological drought, and food insecurity overlapped during the 2014 Horn of Africa drought event (FAO 2014; hereafter the "center of drought impact", CDI; Fig. 17.1).

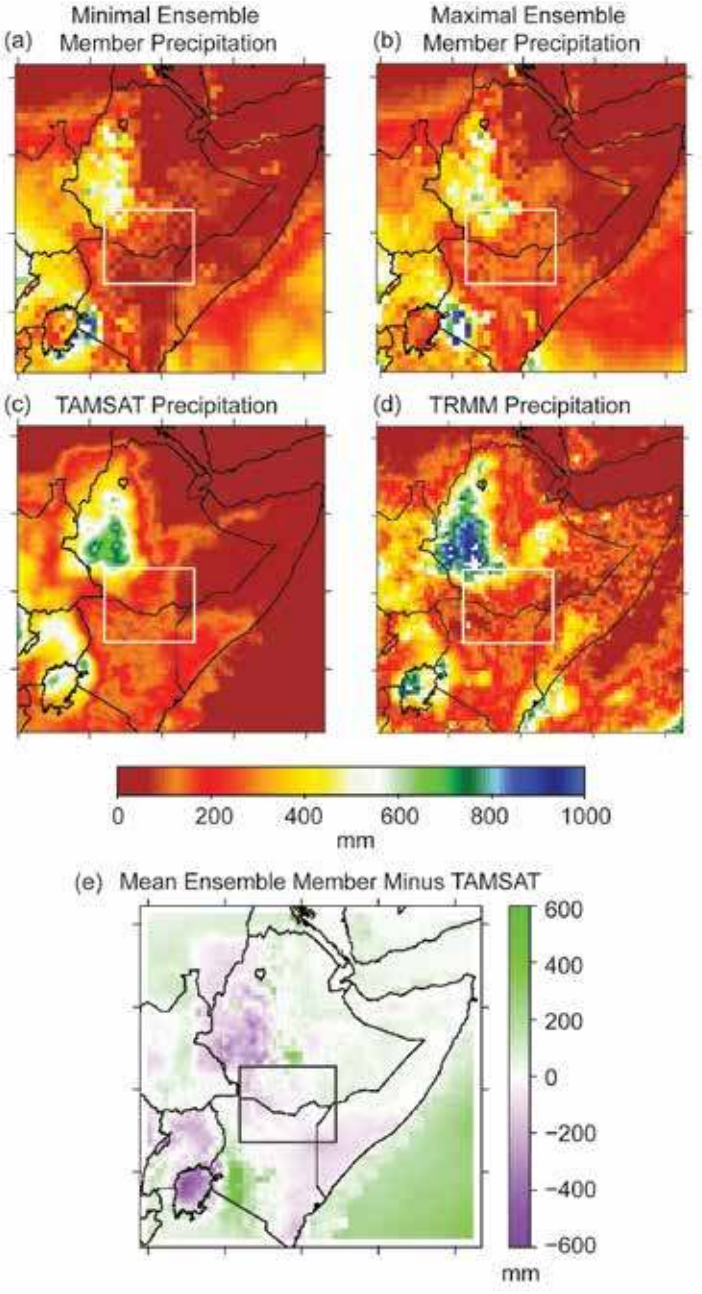

Fig. 17.1. Long rains (Mar–Jun) total precipitation (mm) for 2014 as simulated from the weather@home factual experiment, showing the two ensemble members that presented the (a) driest and (b) wettest seasonal means over the CDI. For comparison, estimates of the observed precipitation for the same season are shown from (c) the TAMSAT (e.g., Tarnavsky et al. 2014; n.b. Yemen and oceanic points are not included in TAMSAT) and (d) TRMM datasets (e.g., Dinku et al. 2007) and (e) the anomaly between the mean factual ensemble and TAMSAT (green shows areas where the model overestimates precipitation, purple underestimations). The CDI during 2014 is boxed [Lake Turkana, Kenya (36.00°E), to the Juba River, Somalia (42.28°E), and from Wajir, Kenya (1.75°N), to Imi, Ethiopia (6.46°N)], coinciding approximately with the Turkana Basin/Southeastern Horn region of Liebmann et al. (2014).

Results. With the focus of our study on simulations of the 2014 East African long rains season (Fig. 17.1), we compared the weather@home simulations of the seasonal average rainfall in representative members of the factual ensemble with two estimates of the observed rainfall. Initially we examined the distribution of simulated average March to June precipitation over the CDI (Fig. 17.1) and divided this into 20 bins, from each of which an equal number of representative members was chosen (20 bins was an optimal number in order to allow adequate sampling of the tail of low-precipitation simulations). The general spatial pattern of observed rainfall estimates for the 2014 March to June season is correctly returned by the model simulations (Fig. 17.1). Specifically, the spatial mean long rains total precipitation for the CDI averaged across the ensemble was 155 mm (ranging from 94 mm to 195 mm for the minimal and maximal ensembles shown in Fig. 17.1) compared with TAMSAT (e.g., Tarnavsky et al. 2014) and TRMM (e.g., Dinku et al. 2007) data averages for 2014 of 169 mm and 201 mm, respectively. In relation to available data, 2014 was in the driest 33% of years recorded since 1983 (TAMSAT data, Supplemental Fig. S17.1) and its importance as an extreme drought event is not in question.

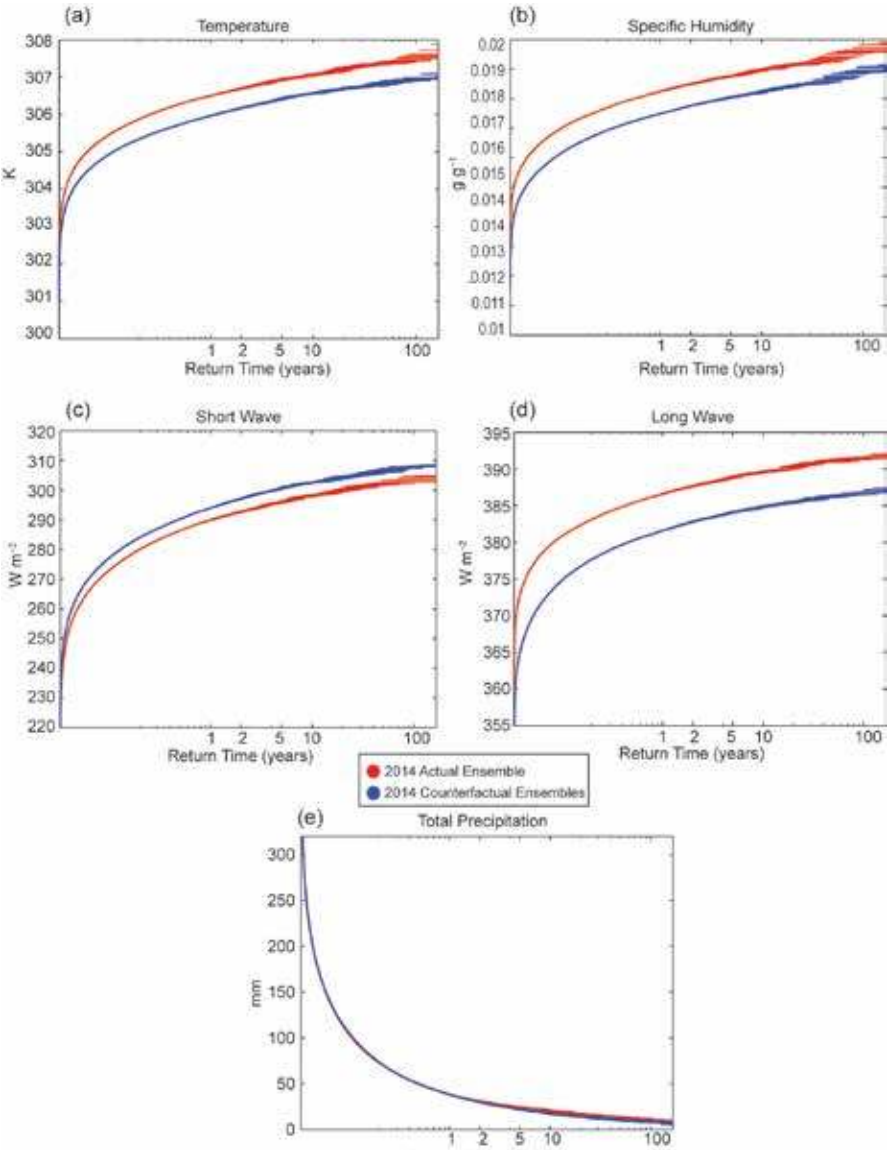

Fig. 17.2. Return-time periods (years) from the regional model (HadRM3P) showing the change in occurrence frequency between simulations of the factual (red) and counterfactual (blue) ensembles for extreme values of a selection of climate model outputs (a) surface temperature (K), (b) specific humidity (g g^{-1}), (c) downward shortwave radiation received at the surface (W m^{-2}), (d) downward longwave radiation (W m^{-2}) and (e) total precipitation (mm). Means and 5%–95% confidence intervals are calculated from bootstrapping for each threshold value across all ensembles in the set (for details see Otto et al. 2015).

We focus on surface (1.5-m) meteorological variables that are relevant to the vegetation and soil moisture state of the land surface and therefore to indicators of drought. These are precipitation, which directly influences soil moisture, along with temperature, downward shortwave and longwave radiation, and specific humidity, which in turn affect potential evapotranspiration and other variables relevant to vegetation productivity. In Fig. 17.2 we compare simulations of these variables in the factual climate with the corresponding counterfactual simulations averaged over the CDI. These results show clear increases in the occurrence frequency of higher temperature and humidity at the surface (Figs. 17.2a,b), along with a slightly lower shortwave input but a higher longwave flux at the surface (Figs. 17.2c,d). These differences

are attributable to human-induced changes in greenhouse gas concentrations. Nonetheless, there is no corresponding change in precipitation (Fig. 17.2e).

Discussion. As large-scale teleconnections play a significant role in the climate of the GHoA, for example, robust correlations have been found linking the East African long rains with SST oscillations such as the Indian Ocean dipole and the El Niño southern oscillation (ENSO; e.g., Funk et al. 2014; Lanckriet et al. 2014; Lyon 2014; Liebmann et al. 2014; Yang et al. 2014, 2015), it is important to note that both our factual and counterfactual simulation ensembles use SSTs with essentially the same oscillations and hence the same large-scale teleconnections. With the SSTs used in the counterfactual simulation being formed from observed values with estimated large-scale anthropogenic SST signals subtracted, the SST gradients, and their temporal evolution, are very similar to the observed values. Thus the same teleconnection signature will be present in both sets of simulations and by comparing these we are able to assess the additional effect of the anthropogenic influences (Otto et al. 2015).

Our results suggest that while anthropogenic increases in greenhouse gas concentrations and associated warming of sea surface temperatures did not increase the likelihood of reduced precipitation in the 2014 East African long rains season, human influences did result in higher temperatures and increased net incoming radiation at the surface over the region most affected by the drought. Conversely, Lott et al. (2013) did find that the failure of the 2011 long rains was more probable following anthropogenic climate change, indicating that climatic conditions for the 2014 drought were not identical to the 2011 drought in the same area. The drivers of the East African long rains are not yet sufficiently understood (Nicholson 2014; Yang et al. 2014, 2015) so there are many possible reasons why anthropogenic change was less significant in terms of climatological drought in 2014 than 2011: for example, 2014 was globally a warmer year than 2011 which perhaps overwhelmed a relatively small anthropogenic signal.

These findings do not constitute a clear attribution of the 2014 climatological drought to human influences. However, simulating the causal chain from precipitation deficit to hydrological or agricultural drought and other impacts is nontrivial and involves many processes that are themselves poorly known at high resolution (Prudhomme et al. 2014). Increased temperature and net incoming radiation at the surface both enhance evaporation and, therefore, the conditions for either or both hydrological or agricultural drought so we suggest that the occurrence of climatological drought and drought impacts may be decoupled in this region. Our results show that anthropogenic influence could well have contributed to drought conditions during the East African long rains but also that more comprehensive studies are required before more definitive statements can be made.

ACKNOWLEDGMENTS. This work was conducted as part of the ACE-Africa project, University of Oxford (www.eci.ox.ac.uk/research/climate/ACEAfrica.php). We would like to thank the Met Office Hadley Centre PRECIS team and our colleagues at the Oxford eResearch Centre for their technical and scientific support for the development and application of Weather@Home. Finally, we would like to thank all of the volunteers who have donated their computing time to Weather@Home.

REFERENCES

Allen, M., 2003: Liability for climate change. *Nature,* **421**, 891–892.

Boulter, S., J. Palutikof, D. J. Karoly, and D. Guitart, 2013: *Natural Disasters and Adaptation to Climate Change*. Cambridge University Press, 273 pp.

Coghlan, C., M. Muzammil, J. Ingram, J. Vervoort, F. Otto, and R. James, 2014: A sign of things to come? Examining four major climate-related disasters, 2010-2013, and their impacts on food security. Oxfam Res. Rep., Oxfam International, 43 pp. [Available online at http://go.oxfam.ca/docs/sign-of-things-to-come-2014-09.pdf.]

Dinku, T., P. Ceccato, E. Grover-Kopec, M. Lemma, S. J. Connor, and C. F. Ropelewski, 2007: Validation of satellite rainfall products over East Africa's complex topography. *Int. J. Remote Sens.,* **28**, 1503–1526.

ECHO, 2014: Humanitarian implementation plan (HIP), 2015: Horn of Africa. ECHO/-HF/BUD/2015/91000, European Commission Humanitarian Aid Department, 17 pp. [Available online at http://reliefweb.int/sites/reliefweb.int/files/resources/hoa_en_4.pdf.]

FEWS NET, 2015: East Africa. Famine Early Warning Systems Network, accessed 9 June 2015. [Available online at www.fews.net/east-africa/.]

FAO, 2014: Greater Horn of Africa: Late and erratic rains raise serious concern for crop and livestock production. GIEWS update, Food and Agricultural Organization, accessed 9 June 2015. [Available online at www.fao.org/giews/english/shortnews/hof03062014.pdf.]

Funk, C., A. Hoell, S. Shukla, I. Bladé, B. Liebmann, J. B. Roberts, F. R. Robertson, and G. Husak, 2014: Predicting East African spring droughts using Pacific and Indian Ocean sea surface temperature indices. *Hydrol. Earth Syst. Sci.,* **18**, 4965–4978, doi:10.5194/hess-18-4965-2014.

Global Hunger Index, 2013: GHI map. Accessed 9 June 2015. [Available online at www.ifpri.org/tools/2013-ghi-map.]

Hoell, A., and C. Funk, 2014: Indo-Pacific sea surface temperature influences on failed consecutive rainy seasons over eastern Africa. *Climate Dyn.* **43**, 1645–1660, doi:10.1007/s00382-013-1991-6.

James, R., F. Otto, H. Parker, E. Boyd, R. Cornforth, D. Mitchell, and M. Allen, 2014: Characterizing loss and damage from climate change. *Nat. Climate Change,* **4**, 938–939, doi:10.1038/nclimate2411; Correction (2015), **5**, 92, doi:10.1038/nclimate2499.

Lanckriet, S., A. Frankl, E. Adgo, P. Termonia, and J. Nyssen, 2014: Droughts related to quasi-global oscillations: a diagnostic teleconnection analysis in North Ethiopia. *Int. J. Climatol.,* **35**, 1534–1542, doi:10.1002/joc.4074.

Liebmann, B., and Coauthors, 2014: Understanding recent eastern Horn of Africa rainfall variability and change. *J. Climate,* **27**, 8630–8645, doi:10.1175/JCLI-D-13-00714.1.

Lott, F. C., N. Christidis, and P. A. Stott, 2013: Can the 2011 East African drought be attributed to human-induced climate change? *Geophys. Res. Lett.,* **40**, 1177–1181, doi:10.1002/grl.50235.

Love, R., 2009: Economic drivers of conflict and cooperation in the Horn of Africa. ARP BP 2009/01, Chatham House, 16 pp. [Available online at www.chathamhouse.org/publications/papers/view/109208.]

Lyon, B., 2014: Seasonal drought in the Greater Horn of Africa and its recent increase during the March–May long rains. *J. Climate,* **27**, 7953–7975, doi:10.1175/JCLI-D-13-00459.1.

——, and D. G. DeWitt, 2012: A recent and abrupt decline in the East African long rains. *Geophys. Res. Lett.,* **39**, L02702, doi:10.1029/2011GL050337.

Masih, I., S. Maskey, F. E. F. Mussá, and P. Trambauer, 2014: A review of droughts on the African continent: A geospatial and long-term perspective. *Hydrol. Earth Syst. Sci.,* **18**, 3635–3649, doi:10.5194/hess-18-3635-2014.

Massey, N., and Coauthors, 2015: weather@home—development and validation of a very large ensemble modelling system for probabilistic event attribution. *Quart. J. Roy. Meteor. Soc.,***141**, 1528–1545, doi:10.1002/qj.2455.

Nicholson, S. E., 2014: A detailed look at the recent drought situation in the Greater Horn of Africa. *J. Arid Environ.*, **103**, 71–79, doi:10.1016/j.jaridenv.2013.12.003.

Omondi, P. A., and Coauthors, 2014: Changes in temperature and precipitation extremes over the Greater Horn of Africa region from 1961 to 2010. *Int. J. Climatol.,* **34**, 1262–1277, doi:10.1002/joc.3763.

Otto, F. E. L., E. Boyd, R. G. Jones, R. J. Cornforth, R. James, H. R. , Parker, and M. R. Allen, 2015: Attribution of extreme weather events in Africa: a preliminary exploration of the science and policy implications. *Climatic Change*, doi:10.1007/s10584-015-1432-0, Open Access.

Pall, P., T. Aina, D. A. Stone, P. A. Stott, T. Nozawa, A. G. J. Hilberts, D. Lohmann, and M. R. Allen, 2011: Anthropogenic greenhouse gas contribution to flood risk in England and Wales in autumn 2000. *Nature,* **470**, 382–385.

Prudhomme, C., and Coauthors, 2014: Hydrological droughts in the 21st century, hotspots and uncertainties from a global multimodel ensemble experiment. *Proc. Natl. Acad. Sci. USA,* **111**, 3262–3267, doi:10.1073/pnas.1222473110.

Stark, J. D., C. J. Donlon, M. J. Martin, and M. E. McCulloch, 2007: OSTIA: An operational, high resolution, real time, global sea surface temperature analysis system. *Proc. IEEE Oceans 2007 Europe Int. Conf.*, Aberdeen, UK, Institute of Electrical and Electronics Engineers, 331–334.

Stott, P. A., G. C. Hegerl, S. C. Herring, M. P. Hoerling, T. C. Peterson, X. Zhang, and F. W. Zwiers, 2014: Introduction to explaining extreme events of 2013 from a climate perspective. *Bull. Amer. Meteor. Soc.*, **95** (9), S1–S3.

Tarnavsky, E., D. Grimes, R. Maidment, E. Black, R. P. Allan, and M. Stringer, 2014: Extension of the TAMSAT Satellite-Based Rainfall Monitoring over Africa and from 1983 to Present. *J. Appl. Meteor. Climatol.,* **53**, 2805–2822, doi:10.1175/JAMC-D-14-0016.1.

Tierney, J. E., J. E. Smerdon, K. J. Anchukaitis, and R. Seager, 2013: Multidecadal variability in East African hydroclimate controlled by the Indian Ocean. *Nature*, **493**, 389–392, doi:10.1038/nature11785.

Trenberth, K. E., 2012: Framing the way to relate climate extremes to climate change. *Climatic Change,* **115**, 283–290, doi:10.1007/s10584-012-0441-5.

UNOCHA, 2011: Eastern Africa drought. Humanitarian Rep. 4, UN Office for the Coordination of Humanitarian Affairs, 10 pp. [Available online at http://reliefweb.int/sites/reliefweb.int/files/resources/Full_Report_1717.pdf.]

Yang, W., R. Seager, M. A. Cane, and B. Lyon, 2014: The East African long rains in observations and models. *J. Climate,* **27**, 7185–7202, doi:10.1175/JCLI-D-13-00447.1.

——, ——, ——, and ——, 2015: The annual cycle of East African precipitation. *J. Climate,* **28**, 2385–2404, doi:10.1175/JCLI-D-14-00484.1.

18. THE DEADLY HIMALAYAN SNOWSTORM OF OCTOBER 2014: SYNOPTIC CONDITIONS AND ASSOCIATED TRENDS

S.-Y. Simon Wang, Boniface Fosu, Robert R. Gillies, and Pratibha M. Singh

The Himalayan snowstorm of October 2014 resulted from the unusual merger of a tropical cyclone with an upper trough, and their collective changes under climate warming have increased the odds for similar events.

The event. October 14, 2014, was a particularly dark day in the history of the Nepal Himalayas. An unanticipated blizzard initiated avalanches that killed 43 people, including 21 trekkers on the popular trekking routes of Mount Annapurna. The blizzard was connected with Cyclone Hudhud, a category 4 tropical cyclone (TC) that developed in the Bay of Bengal (BoB). After making landfall in eastern India, Hudhud proceeded northward towards Nepal. The synoptic evolution leading up to 14 October is illustrated in Fig. 18.1a, with daily 250-hPa winds and precipitation overlaid with Hudhud's location. During 12–13 October, a short-wave trough was moving eastward across the Himalayas. This trough deepened and subsequently collided with a weakening TC Hudhud on 13 October, forming a classic tropical-extratropical interaction (e.g., Kim et al. 2012; Riemer et al. 2014) that combined the abundant moisture supply associated with the remnants of Hudhud and the upstream upper-level trough, enhancing cross-mountain moisture fluxes. This interaction provided a dynamical mechanism for tropospheric ascent and caused stationarity of the weather systems, further compounding the orographic enhancement of precipitation in the Himalayas on October 14 (Fig. 18.1a).

Nepal is ranked the fourth most climate-vulnerable country in the world and it is prone to a wide variety of weather-related hazards that encompass droughts, floods, and landslides (Wang et al. 2013a; Gillies et al. 2013). Because Nepal has not yet established a warning system linked to weather forecasting, authorities did not issue an alert for the hazardous weather conditions that eventually led to the October 2014 disaster (Nair and Sharma 2014). However, BoB TCs of Hudhud's magnitude are not unprecedented, and neither are snowstorms in the Himalayas. Tropical-extratropical interactions in this area are rare but not unique, yet one associated with so much moisture is extraordinary. Hence, it is imperative to investigate the specific meteorological processes that trigger such extreme events, as well as the climatic processes that tend to enhance them, with a goal of improving future predictability.

Data and methodology. Two global reanalyses were used: the NCEP–NCAR Reanalysis (R1; Kalnay 1996) that covers the 1948–2014 period and the satellite-era NCEP–DoE Reanalysis II (R2; Kanamitsu et al. 2002) beginning in 1979. Tropical cyclone tracks were obtained from the Joint Typhoon Warning Center (JTWC) best track records (www.usno.navy.mil). For the depiction of the event precipitation in October 2014, we used the NOAA Climate Prediction Center (CPC) morphing technique (CMORPH) global precipitation analyses derived from low-orbiter satellite microwave observations (Joyce et al. 2004). For the purposes of attribution, we analyzed the Coupled Model Intercomparison Project (CMIP5) historical single-forcing experiments (Taylor et al. 2012) that were driven by (i) anthropogenic aerosol forcing only (AERO), (ii) anthropogenic greenhouse gas forcing only (GHG), and (iii) natural only, including solar and volcanic forcings (NAT)—these were initialized from long stable preindustrial (1850) control settings and simulated up to 2005. We adopted seven models as listed in Supplemental Table S18.1. In this paper, the season analyzed covers the two-month period from September 15 to November 15.

A few variables were derived from the reanalyses: (i) transient eddies associated with synoptic-scale dis-

AFFILIATIONS: Wang and Gillies—Utah Climate Center, and Department of Plants, Soils, and Climate, Utah State University, Logan, Utah; Fosu—Department of Plants, Soils, and Climate, Utah State University, Logan, Utah; Singh—Department of Hydrology and Meteorology, Kathmandu, Nepal, and Utah Climate Center, Utah State University, Logan, Utah

DOI: 10.1175/BAMS-D-15-00113.1

A supplement to this article is available online (10.1175/BAMS-D-15-00113.2)

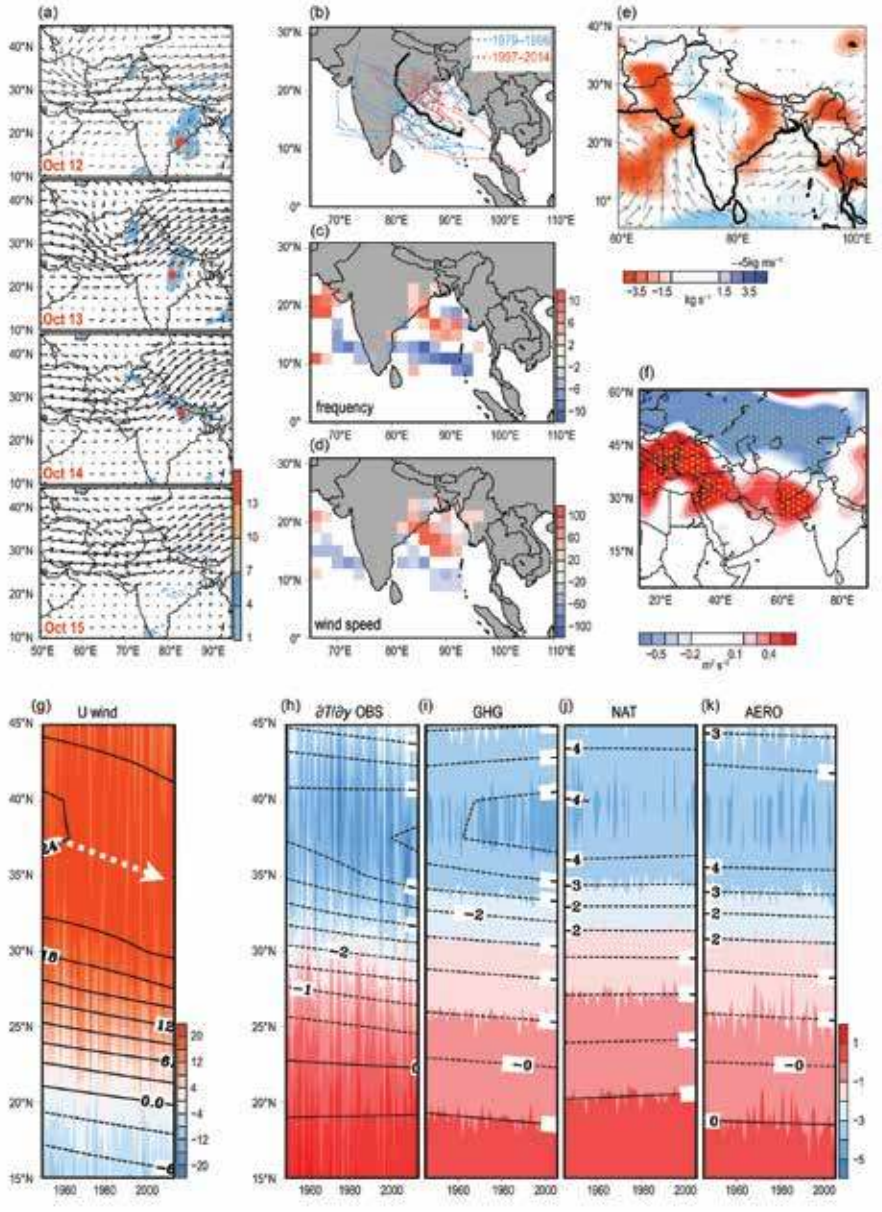

Fig. 18.1. (a) Daily evolution of the 250-hPa wind vectors and CMORPH precipitation (shadings) from 12–15 Oct 2014, overlaid with the location of TC Hudhud and its remnants as hurricane symbol. (b) Post-monsoon (Sep–Oct) TC tracks in the BoB over the period of 1979–2014, with the dotted lines showing the JTWC best tracks and solid lines depicting the residual lows defined through manual tracking. The track of TC Hudhud is shown by thick black line. (c),(d) Areal frequency differences of TC occurrences and maximum sustained wind speed, respectively, between the pre- and post-1997 periods after 1979; only values significant at $p < 0.05$ are plotted. (e) Total changes in Q (vectors), and mean $\nabla \cdot Q$ computed by the linear trend (slope) multiplied by the number of years from 1979 to 2014, using R2. (f) As in (e), but for the 250-hPa transient activity $\overline{v'}$ with the significant values ($p < 0.05$) represented by dots. (g) Latitude-time section of 250-hPa zonal wind (u) across 68°–78°E overlaid with the linear trends of u computed at each latitude over the 1948–2014 period (contours), using R1. The white arrow indicates southward shift of the jet. (h) As in (g), but for the 250-hPa meridional temperature gradient. (i)–(k) As in (h), but using the CMIP5 ensembles from the GHG, NAT, and AERO experiments (see text).

turbances that were computed from the variance of daily meridional winds at 250-hPa bandpass-filtered with 2–9 days, denoted as $\overline{v'}$ (e.g., Lau and Nash 1991). To depict TC remnants after making landfall, which are not included in the JTWC best tracks, we utilized 850-hPa streamline and vorticity analyses to track from each TC's last best-track position onwards until the center relative vorticity became smaller than 3×10^{-5} s^{-1}, following the tracking method of Chen et al. (2005) and using R2. We also projected the 6-h TC positions onto a 2 × 2 grid mesh, producing a gridded frequency (by count) and intensity (by maximum sustained wind speed) of BoB TCs. To understand the moisture budget, we computed the column water vapor flux (Q) by integrating up to 300 hPa and the moisture flux convergence ($\nabla \cdot Q$).

Results. a. Lower-level changes. Figure 18.1b shows the post-monsoon TC tracks since 1979, with TC Hudhud highlighted and the tracks before/after 1997 marked as blue/red. Unlike most BoB storms that dissipate quickly over land, Hudhud has been the only TC whose remnant ever reached as far north as the Himalayas. Moreover, post-1997 cyclones appear more concentrated in the northern BoB than before, suggesting an increase in the TC

threat to northern India. To verify this observation, we computed the areal frequency differences in TC occurrence (Fig. 18.1c) and maximum sustained wind speed (Fig. 18.1d) between the post- and pre-1997 periods. The result shows a significant increase in TC occurrence over the northern part of BoB, especially the stronger ones, but with a decrease over the southern bay. The impact of the changing TCs on the regional water budget is illustrated in Fig. 18.1e, which shows total changes in the seasonal-mean Q and $\nabla \cdot Q$ computed from their respective linear trend/slope multiplied by 36 years (1979–2014). A cyclonic anomaly of Q appears at BoB's northwestern shore accompanied by increased convergence of water vapor fluxes extended from the cyclonic center to Nepal, maximized along the foothill of the Nepalese Himalayas. The transient activity of moisture convergence (not shown) also is increased within the cyclonic anomaly of Q, and this corresponds with the change in TC tracks (Figs. 18.1b–d). Together, these results suggest an overall increase in the moisture transport associated with tropical disturbances in BoB, resulting in enhanced moisture pooling towards the Himalayas.

Previous research has noted an intensification in BoB TCs that supports our results. Recent studies (Wang et al. 2013b; Sahoo and Bhaskaran 2015) found that post-monsoon TCs have tended to grow more intense even though their number has decreased, and such intensification was a response to increased sea surface temperature (SST). Moreover, because the sustained increase in the Indian Ocean SST is linked to anthropogenic global warming (Rao et al. 2012), the observed intensification of post-monsoon BoB TCs is expected to continue in the future (Balaguru et al. 2014; Sarthi et al. 2015).

b. Upper-level changes. To examine whether and how the upper-level circulations conducive to short waves similar to the October 2014 case have changed, we examined the linear trend of the synoptic transient activity ($\overline{v}'$) at 250 hPa, which is shown in Fig. 18.1f. There is a universal increase in $\overline{v}'$ all the way from northern India to the Mediterranean Sea. Given the prevailing westerly flow, this band of increased $\overline{v}'$ implies a shift of the storm track diverting more and/or stronger short waves towards Nepal. This notion was validated from the latitude-time section of the 250-hPa zonal winds (u) across 68°E and 78°E, which is upstream of Nepal; this is shown in Fig. 18.1g from 1948 onwards using the R1 data. A southward migration of the jet is discernable, and this is further illustrated by the linear trend of u computed at each latitude (in y-axis) over the 1948–2014 period (in x-axis). Based on the contours around 30°N, the southward migration of the jet stream was estimated to be around 300 km since 1948, and this explains the increased $\overline{v}'$ in the southern flank of the jet stream.

So what affected the South Asian jet? To answer this question, we further analyzed the change in the meridional temperature gradients ($\partial T/\partial y$) at 250 hPa. Figure 18.1h depicts a clear equatorward shift in ($\partial T/\partial y$) which appears to have accelerated after 1990, corresponding to the zonal wind shift. This result suggests that the tropospheric warming that prevailed after the 1980s has modulated the jet maintenance related to thermal wind balance. To understand the role of external climate forcing in such a change, we derived ($\partial T/\partial y$) from the CMIP5 ensembles of GHG, NAT, and AERO-forcing experiments; these are shown in Figs. 18.1i–k. By visual comparison, the equatorward shift of ($\partial T/\partial y$) results primarily from GHG, which depicts a gradual equatorward migration (south of 35°N) with an expansion of the jet core (between 35°N and 40°N). The NAT forcing produced a slight poleward shift of ($\partial T/\partial y$), opposite to the observation. A possible secondary cause comes from AERO producing a southward shift that only occurred after 1990. This AERO-induced shift in the jet stream maintenance is likely linked to the recent increase in anthropogenic aerosols along the Gangetic Plains, which act to warm the mid-troposphere (Lodhi et al. 2013; Wang et al. 2013b; Kastaoutis et al. 2014). Interdecadal climate variations due to natural causes do exist and can affect Nepal (e.g., Guhathakurta et al. 2014; Wang et al. 2013a) and these cannot be ruled out, but, the CMIP5 analysis does paint a probable scenario whereby increasing anthropogenic GHGs and aerosols are envisaged to contribute to change in regional storm tracks. Future work will focus on examining the full archive of CMIP5 model outputs in order to validate and quantify the impact of individual climate forcings.

c. Implication to weather patterns. The collective changes in the upper and lower circulations suggest that the chance for synoptic short waves crossing northern India to interact with BoB TCs intruding into the Gangetic Plains has increased. To clarify this supposition, we derived the daily eddy geopotential height (Z_E) on 13–14 October 2015 and compared it with Z_E of any given day during the September 15–November 15 period in order to identify past synoptic settings similar to October 2014. The comparison was made within the domains of 55°–85°E, 20°–45°N for 250 hPa and 65°–95°E, 5°–35°N for 850 hPa, based

upon the dimension of the upper trough and TC Hudhud. Supplemental Fig. S18.1a shows these domains overlaid with the observed Z_E. Next, the spatial correlation coefficient (ρ) of daily Z_E was computed between 13–14 October 2014 for each day from 1950 to 2014, for both pressure levels. Fifteen criteria of ρ were defined ranging from 0.6 to 0.9 with an increment of 0.02. At either level, each ρ criterion has to be satisfied for two consecutive days in order to depict the evolution of the October 2014 case. We show in Supplemental Fig. S18.1 the case composites produced from three criteria: 0.9 (b), 0.8 (c), and 0.7 (d), with the number of cases indicated for visual comparison. Naturally, higher ρ results in a lower case number and a more compatible weather pattern in both location and magnitude. It is worth noting that, at ρ=0.9, there was not a single case at 850 hPa that matches the 14 October 2015 situation; this coincides with the earlier observation in Fig. 18.1b that Hudhud was the only TC on record whose residual low ever reached Nepal.

The statistics of the identified cases at both pressure levels are displayed in Fig. 18.2: the occurrence of cases identified by each ρ-criterion is plotted as thin color lines while the mean of the 15 ρ-criteria is given as thick black line. To illustrate the long-term change, the 20-year moving average of the mean occurrence is also plotted as thick red line (one-sided). There appears to be a steady and significant increase that doubles the occurrence of upper troughs since the mid-1990s (Fig. 18.2a). The increase

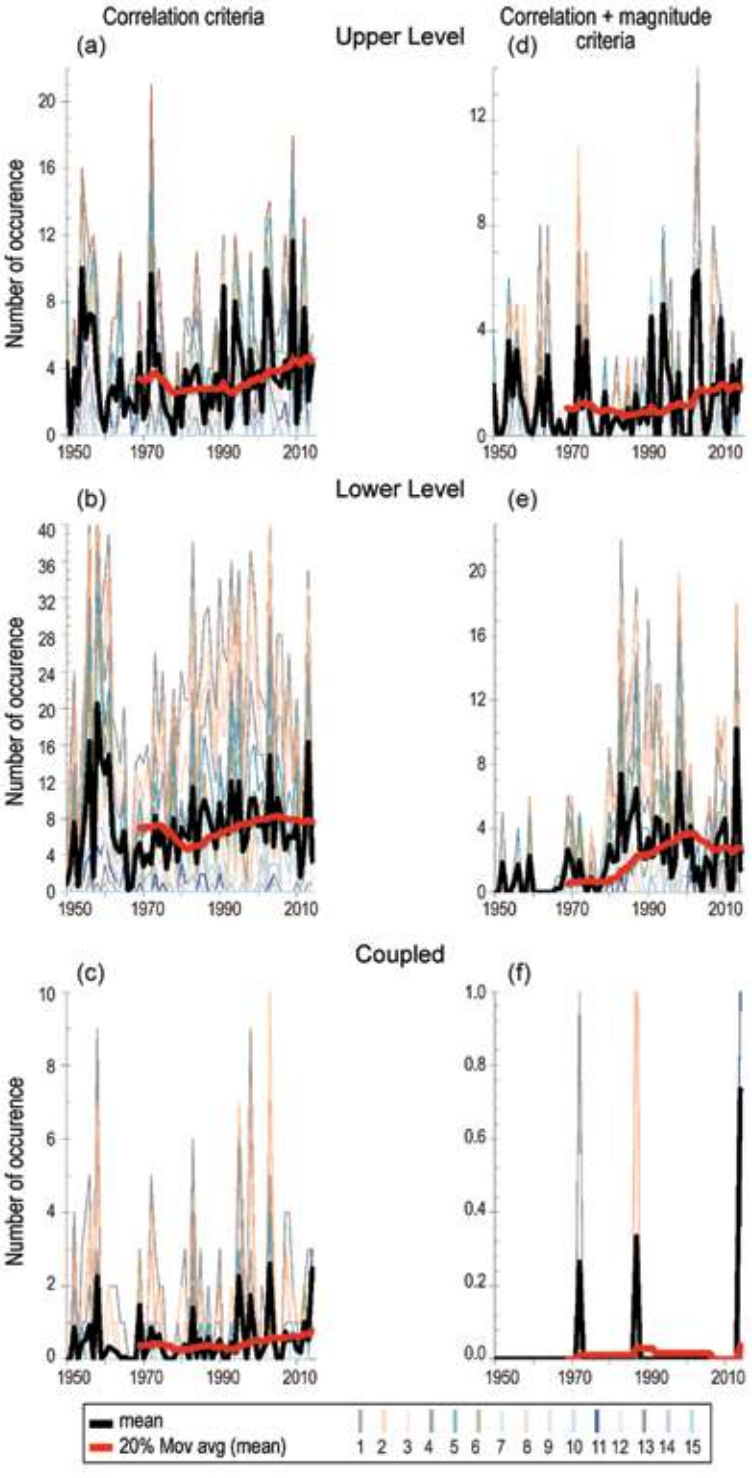

Fig. 18.2. (a) Occurrence of cases identified using the criteria of spatial correlation coefficient (ρ) derived from 250 hPa Z_E, overlaid with the 20-year moving averages (one-sided) . (b) As in (a), but for the 850 hPa level. (c) Same as (a) but for the coupled cases determined by the criteria being met at both levels on the same day. (d)–(f) Similar to (a)–(c) but for the result after the inclusion of RMS on top of the ρ criteria. Notice that some numbers of 2014 exceed the y-axis range.

in the low-level disturbances is also substantial (Fig. 18.2b), though it did not exceed the 1970s high point by much. Next, we introduced an additional criterion for magnitude as determined by the root-mean-square (RMS) of Z_E, which was computed within the domain outlined in Supplemental Fig. S18.1. The RMS has to be at least 80% of that of 13–14 October 2014 at either level. The addition of this magnitude criterion resulted in a reduction in the overall case number, as expected, and it shows a similar range of increase in the upper troughs (Fig. 18.2d). What is more, the magnitude criterion led to a more robust growth of the low-level disturbances after the mid-1980s (Fig. 18.2e), reflecting the intensification of post-monsoon BoB TCs as was discussed earlier.

More importantly, the *concurrence* of the two types of weather systems has indeed increased, as is shown in Fig. 18.2c, determined when the criteria of both levels were met on the same day. The case number of the concurrent weather systems that featured a compatible strength declined substantially (Fig. 18.2f; when taking into account the magnitude criterion), leaving only three years of possible cases including the October 2014 ones. The implication of these results is that, although weather systems similar to that of 13–14 October 2014 did occur in the past, there is a tendency for both types of weather systems to interact more frequently. The potential for heavy precipitation in Nepal as a result of this interaction has increased as well, given the strengthened moisture convergence accompanied by the intensification and northward shift of BoB TCs.

Conclusion. The unusual coupling of a deepened upper trough with the remnants of TC Hudhud over the Nepalese Himalayas enhanced lifting and moisture pooling, causing a blizzard concomitant with heavy snowfall and subsequent avalanches on 14 October 2014. Climate diagnostics point to a tendency for more and/or stronger upper troughs propagating from the Mediterranean region that could coincide with increasingly stronger tropical disturbances coming from BoB. For the lower level, previous studies have linked the intensification of post-monsoon BoB TCs with increased SST and anthropogenic global warming. For the upper level, attribution analyses using an ensemble of 7 CMIP5 models indicate that increased anthropogenic GHG and aerosols both have contributed to the equatorward shift of the jet stream, a feature that arguably diverts more synoptic short waves towards Nepal. By combining these findings, one can conclude that the changing synoptic regimes over both northern India and Nepal would signal an increased possibility of similar events occurring in the future.

ACKNOWLEDGMENT: This study was partly supported by the United States Agency for International Development (USAID) Grant EEM-A-00-10-00001. Comments provided by three anonymous reviewers are highly appreciated.

REFERENCES

Balaguru, K., S. Taraphdar, L. R. Leung, and G. R. Foltz, 2014: Increase in the intensity of postmonsoon Bay of Bengal tropical cyclones. *Geophys. Res. Lett.*, **41**, 3594–3601, doi:10.1002/2014GL060197.

Chen, T.-C., J.-H. Yoon, and S.-Y. Wang, 2005: Westward propagation of the Indian monsoon depression. *Tellus*, **57A**, 758–769.

Gillies, R. R., S.-H. Wang, Y. Sun, and O. Y. Chung, 2013: Supportive empirical modelling for the forecast of monsoon precipitation in Nepal. *Int. J. Climatol.*, **33**, 3047–3054, doi:10.1002/joc.3649.

Guhathakurta, P., M. Rajeevan, D. R. Sikka, and A. Tyagi, 2014: Observed changes in southwest monsoon rainfall over India during 1901–2011. *Int. J. Climatol.*, **35**, 1881–1898, doi:10.1002/joc.4095.

Joyce, R. J., J. E. Janowiak, P. A. Arkin, and P. Xie, 2004: CMORPH: A method that produces global precipitation estimates from passive microwave and infrared data at high spatial and temporal resolution. *J. Hydrometeor.*, **5**, 487–503.

Kalnay, E., and Coauthors, 1996: The NCEP/NCAR 40-year reanalysis project. *Bull. Amer. Meteor. Soc.*, **77**, 437–471.

Kanamitsu, M., W. Ebisuzaki, J. Woollen, S.-K. Yang, J. J. Hnilo, M. Fiorino, and G. L. Potter, 2002: NCEP-DOE AMIP-II Reanalysis (R-2). *Bull. Amer. Meteor. Soc.*, **83**, 1631–1643.

Kaskaoutis, D. G., and Coauthors, 2014: Synoptic weather conditions and aerosol episodes over Indo-Gangetic Plains, India. *Climate Dyn.*, **43**, 2313–2331, doi:10.1007/s00382-014-2055-2.

Kim, J.-S., R. C.-Y. Li, and W. Zhou, 2012: Effects of the Pacific–Japan teleconnection pattern on tropical cyclone activity and extreme precipitation events over the Korean peninsula. *J. Geophys. Res.*, **117**, D18109, doi:10.1029/2012JD017677.

Lau, N.-C., and M. J. Nath, 1991: Variability of the baroclinic and barotropic transient eddy forcing associated with monthly changes in the midlatitude storm tracks. *J. Atmos. Sci.*, **48**, 2589–2613.

Lodhi, N. K., S. N. Beegum, S. Singh, and K. Kumar, 2013: Aerosol climatology at Delhi in the western Indo-Gangetic Plain: Microphysics, long-term trends, and source strengths. *J. Geophys. Res. Atmos.*, **118**, 1361–1375, doi:10.1002/jgrd.50165.

Nair, R. J., and G. Sharma, 2014: Nepal blames poor forecasts, lax rules for trek disaster. Reuters, 17 October, 1:47 p.m. EDT. [Available online at www.reuters.com/article/2014/10/17/uk-nepal-hikers-idUSKCN0I622720141017.]

Rao, S. A., A. R. Dhakate, S. K. Saha, S. Mahapatra, H. S. Chaudhari, S. Pokhrel, and S. K. Sahu, 2012: Why is Indian Ocean warming consistently? *Climatic Change*, **110**, 709–719, doi:10.1007/s10584-011-0121-x.

Riemer, M., and S. C. Jones, 2014: Interaction of a tropical cyclone with a high-amplitude, midlatitude wave pattern: Waviness analysis, trough deformation and track bifurcation. *Quart. J. Roy. Meteor. Soc.*, **140**, 1362–1376, doi:10.1002/qj.2221.

Sahoo, B., and P. K. Bhaskaran, 2015: Assessment on historical cyclone tracks in the Bay of Bengal, east coast of India. *Int. J. Climatol.*, doi:10.1002/joc.4331, in press.

Sarthi, P. P., A. Agrawal, and A. Rana, 2015: Possible future changes in cyclonic storms in the Bay of Bengal, India under warmer climate. *Int. J. Climatol.*, **35**, 1267–1277, doi:10.1002/joc.4053.

Taylor, K. E., R. J. Stouffer, and G. A. Meehl, 2012: An overview of CMIP5 and the experiment design. *Bull. Amer. Meteor. Soc.*, **93**, 485–498, doi:10.1175/BAMS-D-11-00094.1.

Wang, S.-Y., R. E. Davies, W. R. Huang, and R. R. Gillies, 2011: Pakistan's two-stage monsoon and links with the recent climate change. *J. Geophys. Res.*, **116**, D16114, doi:10.1029/2011JD015760.

——, J.-H. Yoon, R. R. Gillies, and C. Cho, 2013a: What caused the winter drought in western Nepal during recent years? *J. Climate*, **26**, 8241–8256, doi:10.1175/JCLI-D-12-00800.1.

——, B. M. Buckley, J. H. Yoon, and B. O. Fosu, 2013b: Intensification of premonsoon tropical cyclones in the Bay of Bengal and its impacts on Myanmar. *J. Geophys. Res. Atmos.*, **118**, 4373–4384, doi:10.1002/jgrd.50396.

19. ANTHROPOGENIC INFLUENCE ON THE 2014 RECORD-HOT SPRING IN KOREA

Seung-Ki Min, Yeon-Hee Kim, Seungmok Paik, Maeng-Ki Kim, and Kyung-On Boo

A comparison of observations and multiple global climate models indicates human influence has increased the chance of extreme hot springs in Korea such as the 2014 event by two to three times.

Introduction. During March–May (MAM) 2014 South Korea experienced the hottest spring days on record for the past 61 years. The observed 2014 MAM average daily maximum temperature (Tmax) reached 19.2°C, exceeding the 1971–2000 climatology by 1.7°C (Fig. 19.1a). This warming was evident at all weather stations across South Korea (Supplemental Fig. S19.1). Average minimum temperature (Tmin) was 9.1°C, the second highest on record, 1.6°C warmer than climatology. Average daily mean temperature (Tmean) was also the second warmest (13.8°C) behind only 1998. Due to the unusually warm spring weather, many spring flower festivals ran earlier than scheduled, indicating the dominant influence of temperature on plant phenology (Kim et al. 2015). Further, tropical nights (daily minimum temperature >25°C; e.g., Choi et al. 2009) appeared in May for the first time over South Korea (Jeju and Gangneung stations) since meteorological observations began in the early 20th century.

Along with the 2014 extreme events, spring temperatures have been consistently increasing over the past 61 years with statistically significant trends in Tmax (Fig. 19.1b). For most of 2014 MAM, Tmean exceeded the climatology, especially in the late March and late May (Fig. 19.1c). It is not surprising that the 2014 spring heat was in accord with the earliest start of summer on record (Fig. 19.1b), which was 22 May, 10 days earlier than climatology, 1 June. [Summer onset day is defined as a calendar date with over 20°C in Tmean and 25°C in Tmax, obtained through applying a Butterworth low-pass filter to raw daily data with a cutoff period of 90-days (Kwon et al. 2007)]. Interestingly, the correlation between Korean Tmax and the summer onset day is very strong ($r = -0.71$), indicating that a hot spring leads to an earlier onset of summer. The spatial correlation map (Fig. 19.1d) indicates that Korean spring temperature is closely related to spring temperatures over northeastern China, which also observed a warmer spring in 2014 (Supplemental Fig. S19.2).

A question might be raised whether, and how much, such warmer spring is due to human-induced greenhouse warming. Here, we conduct a quantitative attribution analysis of 2014 spring heat over Korea in the context of climate change. Anthropogenic contribution to extreme spring temperature is assessed by comparing the probability of the observed temperature and its long-term trend to those from coupled climate model simulations with and without human influences.

Data and Methods. We use Tmax, Tmin, and Tmean observations from 12 Korean weather stations for 1954–2014. We also use monthly surface air temperature (SAT) data from HadCRUT4 (Morice et al. 2012) to find a large-scale indicator of the Korean spring heat, utilizing an upscaling approach (Min et al. 2014). Global climate model outputs usually cannot capture spatial details of Korean climate due to relatively coarse resolution, so we use this large-scale indicator instead.

We use multimodel datasets available from the Coupled Model Intercomparison Project Phase 5 (CMIP5; Taylor et al. 2012) experiments (see Supplemental Table S19.1) in order to assess the contribution of human influence to the observed spring heat. We use data from the "historical" experiment integrated with natural (due to changes in solar and volcanic activities) and anthropogenic forcings (due mainly

AFFILIATIONS: Min, Y.-H. Kim, and Paik—School of Environmental Science and Engineering, Pohang University of Science and Technology, Pohang, Gyeongbuk, South Korea; M.-K. Kim—Department of Atmospheric Science, Kongju National University, Gongju, Chungnam, South Korea; Boo—Climate Research Laboratory, National Institute of Meteorological Research, Jeju, South Korea

DOI:10.1175/BAMS-D-15-00079.1

A supplement to this article is available online (10.1175/BAMS-D-15-00079.2)

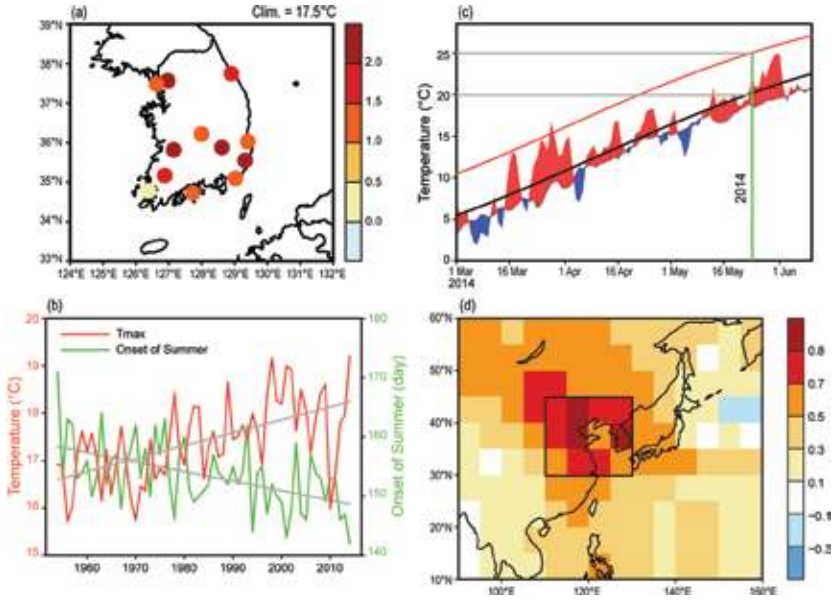

Fig. 19.1. (a) Distribution of MAM mean Tmax anomalies (°C) observed at 12 stations over South Korea in 2014. Anomalies are with respect to 1971–2000 mean. (b) Time series of MAM mean Tmax (red, °C) and summer onset day (green) averaged over 12 stations for 1954–2014. Warming trends (gray straight lines) in Tmax (0.27°C decade^{-1}) and onset of summer (−1.6 day decade^{-1}) are statistically significant at 1% significance level based on the Mann-Kendall test. (c) Time series of Tmean in the spring of 2014. Red and blue shading indicate above normal and below normal, respectively. The black and red lines represent the Butterworth low-pass filtered Tmean and Tmax in 2014. The vertical green line represents the onset of summer in 2014. The horizontal gray lines indicate the 20°C (Tmean) and 25°C (Tmax) thresholds for summer onset date. (d) Spatial distribution of correlation coefficients between Korean Tmax and SAT calculated for 1954–2014. Box indicates an area selected as an indicator of Korean spring heat.

to increases in greenhouse gases and aerosols) for 1860–2005 and extend them to 2014 using data from RCP (Representative Concentration Pathway) 4.5 scenario simulations for 2006–14. We chose RCP4.5 scenario runs that provide the largest number of model samples because difference between RCP scenarios is very small until the near-term future (Moss et al. 2010). Subsequently, two 61-year periods are selected as 1860–1920 (ALL_P0), which is assumed to close to the pre-industrial period with negligible anthropogenic influence, and 1954–2014 (ALL_P1), which represents climate conditions with human influence. We also use datasets from the "historical-GHG" (greenhouse-gas only forcing) and "historical-Nat" (natural forcing only) experiments to examine contribution of the individual factors (note that the analysis period of these experiments is 1954–2012 because they end in 2012). Anomalies from all model runs are calculated relative to each 1971–2000 mean of ALL_P1 in order to consider climate response to different forcings.

Next, in order to identify a large-scale SAT indicator for Korean spring temperature in general, we obtain a correlation map (Fig. 19.1d) between Korean Tmax and observed East Asian SAT for 1954–2014, both of which are MAM averages. We then choose a latitude–longitude box (30°–45°N and 110°–130°E) with strong correlation ($r > 0.7$) and calculate area-averaged SAT anomalies from observations and all CMIP5 simulations (referred to as "observed SAT anomaly" and "modeled SAT anomaly", respectively). A similar local Tmax and large-scale SAT relationship is simulated by the models (Supplementary Fig. S19.3).

Using the fraction of attributable risk (FAR; Stott et al. 2004) approach, we evaluate the risk of long-term warming trends and 2014 spring heat wave in terms of anthropogenic forcing. The FAR approach compares the probability of extreme events occurring between a real world (with human influence) and a counterfactual world (without human influence), so as to quantitatively estimate anthropogenic influence. Here, FAR is calculated as $FAR = 1 - (P_N/P_A)$, where P_N denotes the probability of exceeding the observed event (trends in SAT anomaly or 2014 SAT anomaly) occurring in natural unforced conditions (ALL_P0 or NAT_P1), and P_A represents the same probability estimated in anthropogenic forced conditions (ALL_P1 or GHG_P1). FAR uncertainty (5th–95th percentile) is estimated through bootstrap resampling.

Results. The observed SAT anomaly represents striking long-term warming (Fig. 19.2a) with a record high in 2014 (+1.8°C), tied with 1998. This SAT acts as a good predictor for the Korean spring Tmax with a correlation coefficient of 0.88. Modeled SAT anomalies are illustrated together in Fig. 19.2 for ALL_P0 (blue), ALL_P1 (green), GHG_P1 (red), and NAT_P1 (purple). Trends in ALL_P0 and NAT_P1 are very weak while GHG_P1 possesses stronger positive trends than observation (Fig. 19.2a). This

suggests a dominant contribution of the greenhouse warming to the ALL_P1 trend considering that other anthropogenic forcing (mainly aerosols) will induce long-term cooling. The interannual variability of SAT anomaly is found to be reasonably well simulated by CMIP5 models with slight overestimation (Standard deviation of observed detrended SAT is 0.64°C. Multimodel mean of standard deviations of detrended SAT from ALL_P1 is 0.80°C with a 5th–95th percentile range of 0.60°–1.03°C).

We first compare the trends of observed and modeled SAT anomaly using probability density functions (PDF) in Fig. 19.2b. The trend PDFs are constructed from linear trends from all ensemble members for each experiment (thin lines in Fig. 19.2a). While the observed trend (1.64°C per 61 years) exceeds the trends PDF of ALL_P0 and NAT_P1, it is positioned inside the trends PDF of ALL_P1 and located near the center of GHG_P1 distributions. Thus, fraction of risk of the observed SAT trend attributable to anthropogenic forcing is 100% (FAR = 1; Table 19.1) considering a negligible influence of natural forcing. According to various trend periods (all ending in 2014), a FAR value of 1 is obtained for a trend period longer than 40 years (Supplementary Fig. S19.4a). For the recent 30-year period (1985–2014), the trends in SAT anomaly exceeding the observed trend (1°C per 30 years) is simulated in ALL_P0 (5.59% probability), ALL_P1 (37.19%), and GHG_P1 (33.33%) (Fig. 19.2c; Table 19.1). The corresponding FAR values of ALL_P1 and GHG_P1 relative to ALL_P0 are 0.85 and 0.83, respectively (about a six- to seven-time increase in risk). The slightly larger FAR in ALL_P1 than in GHG_P1 for the recent 30-year trends seems partly due to the NAT_P1 contribution to the ALL_P1 warming trend (i.e., recovery after volcanic cooling in the early decades; Supplementary Fig. S19.5).

We also compare the 2014 spring heat wave event using a similar method. The PDF distributions for the modeled SAT anomaly are displayed in Fig. 19.2d. The PDF distribution consists of all values of SAT anomalies during 61 years from all ensemble members for each experiment. SAT anomalies stronger than the observed 2014 event are extremely rare in ALL_P0 (0.91%) and NAT_P1 (0.73%). The chance of 2014-like extreme events increases to 2.49% and 17.74% in ALL_P1 and GHG_P1, respectively (Table 19.1). The corresponding FAR values with respect to ALL_P0 are 0.64 (5th–95th percentile range of 0.57–0.69) and 0.95 (5th–95th percentile range of 0.94–0.96), indicating a 2- to 3- and 20-time increase in risk due to human influence, respectively. The record extreme 2014 (+1.8°C) SAT anomalies were greater than +2σ above

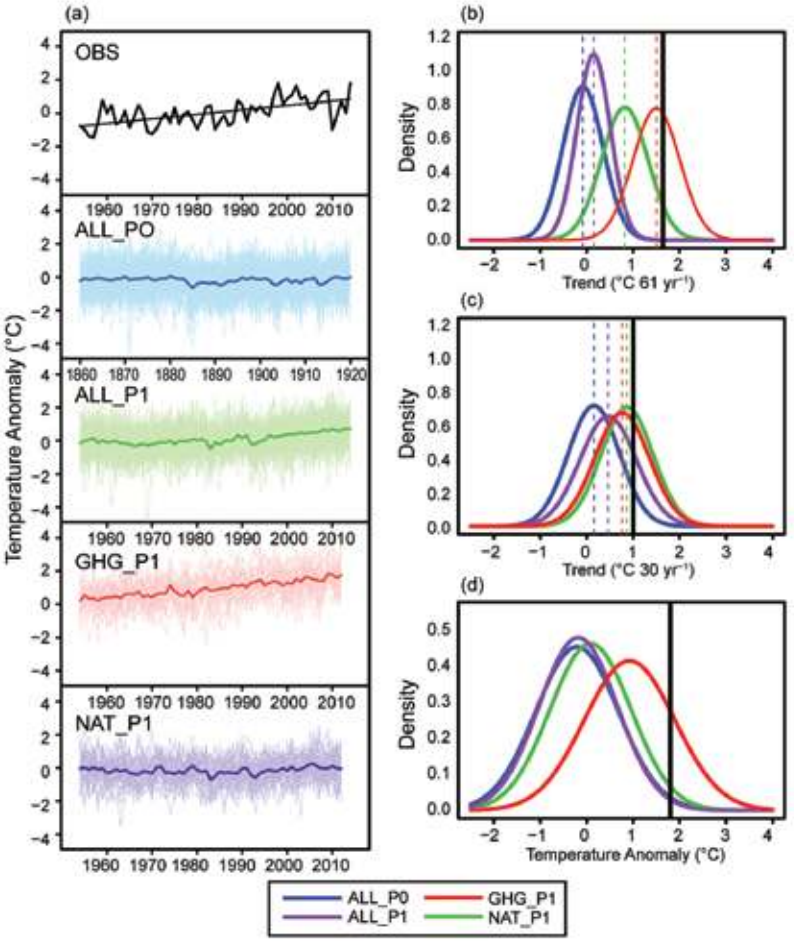

Fig. 19.2. (a) Time series of SAT anomaly (°C) from observation, ALL_P0, ALL_P1, GHG_P1, and NAT_P1. Black straight line represents the observed linear trend; thick colored lines indicate ensemble mean of each experiment. (b) Normalized PDF for trend in SAT anomaly (°C 61 yr−1) from ALL_P0 (blue), ALL_P1 (green), GHG_P1 (red), and NAT_P1 (purple) in comparison with the observed trend (vertical black line) for the past 61 years (1954–2014). Colored vertical dotted lines indicates ensemble mean trends. (c) As in (b), but for the recent 30 years (1985–2014). (d) As in (b), but for SAT anomaly from models (all years) and the observed SAT anomaly in 2014 (°C).

Table 19.1. Probability of occurrence exceeding the observed trend in SAT anomaly and the observed 2014 SAT anomaly. The fraction of attributable risk is calculated as $FAR_{ALL\_PI} = 1 - P_{ALL\_P0}/P_{ALL\_PI}$ and $FAR_{GHG\_PI} = 1 - P_{ALL\_P0}/P_{GHG\_PI}$

	Observations	ALL_P0	ALL_PI	GHG_PI
SAT anomaly Trend (61 years)	1.64 (°C 61 yr^{-1})	0%	3.31% FAR = 1	43.33% FAR = 1
SAT anomaly Trend (30 years)	1.00 (°C 30 yr^{-1})	5.59%	37.19% FAR = 0.85	33.33% FAR = 0.83
2014 spring SAT anomaly	1.8 (°C)	0.91%	2.49% FAR = 0.64 (0.57–0.69)	17.74% FAR = 0.95 (0.94–0.96)

the climatological mean. A relationship between hypothetical SAT anomaly and FAR (Supplementary Fig. S19.4b; Christidis et al. 2014) suggests more than a 10-time increase in risk when an SAT anomaly stronger than +3σ is observed, for example.

We have also tested the sensitivity of FAR to the use of different model samples (Supplementary Fig. S19.6). The models are divided into two groups which have warm and cold biases relative to observed climatology (see Supplementary Table S19.1 for model lists). FAR values are similar between the two model groups (0.66 and 0.67, respectively), indicating that the FAR results are largely insensitive to the use of different model samples.

Conclusions. South Korea experienced the hottest spring and the earliest summer onset in 2014, and spring temperatures have been consistently increasing during the past 61 years. This study examines the possible impact of anthropogenic influence on the observed spring heat and warming trends by comparing CMIP5 multimodel experiments with and without human influences utilizing a large-scale SAT indicator of the Korean spring temperature. It is found that the observed SAT long-term trend is outside of the PDF of modeled natural and near-preindustrial simulations indicating that risk due to anthropogenic influence is 100% and that extreme hot springs like the 2014 event have increased two to three times due to human influence. Overall, our results show that greenhouse warming has contributed to warming trends in Korea spring temperature and an increasing risk of spring temperature extremes.

ACKNOWLEDGEMENTS. This research is supported by a project NIMR-2012-B-2 (Development and Application of Methodology for Climate Change Prediction). We acknowledge the World Climate Research Programme's Working Group on Coupled Modelling, which is responsible for CMIP, and we thank the climate modeling groups for producing and making available their model output.

REFERENCES

Choi, G., and Coauthors, 2009: Changes in means and extreme events of temperature and precipitation in the Asia–Pacific Network region, 1955–2007. *Int. J. Climatol.*, **29**, 1906–1925.

Christidis, N., P. A. Stott, and F. W. Zwiers, 2014: Fast-track attribution assessments based on precomputed estimates of changes in the odds of warm extremes. *Climate Dyn.*, doi:10.1007/s00382-014-2408-x, in press.

Kim, K.-S., S. O. Kim, D. J. Kim, K. H. Moon, and J. I. Yun, 2015: Using daily temperature to predict phenology trends in spring flowers. *Asia-Pac. J. Atmos. Sci.*, **51**, 167–172.

Kwon, Y.-A., W.-T. Kwon, and K.-O. Boo, 2007: Future projections on the change of onset date and duration of natural seasons using SRES A1B data in South Korea. *J. Korean Geogr. Soc.*, **42**, 835–850. (In Korean with English abstract.)

Min, S.-K., Y.-H. Kim, M.-K. Kim, and C. Park, 2014: Assessing human contribution to the summer 2013 Korean heat wave [in "Explaining Extreme Events of 2013 from a Climate Perspective"]. *Bull. Amer. Meteor. Soc.*, **95** (9), S48–S51.

Morice, C. P., J. J. Kennedy, N. A. Rayner, and P. D. Jones, 2012: Quantifying uncertainties in global and regional temperature change using an ensemble of observational estimates: The HadCRUT4 dataset. *J. Geophys. Res.*, **117**, D08101, doi:10.1029/2011JD017187.

Moss, R. H., and Coauthors, 2010: The next generation of scenarios for climate change research and assessment. *Nature*, **463**, 747–756.

Stott, P. A., D. A. Stone, and M. R. Allen, 2004: Human contribution to the European heatwave of 2003. *Nature*, **432**, 610–614, doi:10.1038/nature03089.

Taylor, K. E., R. J. Stouffer, and G. A. Meehl, 2012: An overview of CMIP5 and the experiment design. *Bull. Amer. Meteor. Soc.*, **93**, 485–498, doi:10.1175/BAMS-D-11-00094.1.

20. HUMAN CONTRIBUTION TO THE 2014 RECORD HIGH SEA SURFACE TEMPERATURES OVER THE WESTERN TROPICAL AND NORTHEAST PACIFIC OCEAN

Evan Weller, Seung-Ki Min, Donghyun Lee, Wenju Cai, Sang-Wook Yeh, and Jong-Seong Kug

CMIP5 models suggest that human influence has increased the probability of regional high SST extremes over the western tropical and northeast Pacific Ocean during the 2014 calendar year and summer.

Introduction. Global mean sea surface temperature (SST) during 2014 was the highest over observational records, with distinct patterns of regional and seasonal extremes (Figs. 20.1a,b). This surpassed the previous record high in 1998, which followed an extreme El Niño event (Cai et al. 2014). However, the 2014 record-breaking SST is of great importance as it occurred without the influence of a strong El Niño event and follows a long-term pause, or hiatus, in global warming since the late 1990s (e.g., Watanabe et al. 2014). Thus, this event provides evidence of long-term warming trends due to anthropogenic forcing and/or possible shifts in multidecadal variability. Maps of 2014 annual and boreal summer (June–August, JJA) SST anomalies (Figs. 20.1a,b) reveal that the unprecedented global warmth was primarily due to anomalously high temperatures in the western tropical Pacific, northeast Pacific, southern Indian, and Atlantic Oceans. Overall, the fraction of global ocean with record positive anomalies in 2014 was less than half of that observed in 1998, but the 2014 warming over these regions was indeed an extreme event (Supplementary Fig. S20.1). The western tropical Pacific was the largest region for record-breaking SSTs (Figs. 20.1a–d), whilst in the northeast Pacific, although less widespread, prominent SST anomalies exceeded the 1971–2000 climatology by up to 1.76°C (Figs. 20.1e,f). Interestingly, both regions exhibited the highest seasonal mean during JJA (Supplementary Fig. S20.2). Here, we examine the observed 2014 SST extremes in these two key regions in the context of anthropogenic climate change.

AFFILIATIONS: Weller, Min, Lee, and Kug—School of Environmental Science and Engineering, Pohang University of Science and Techonology, Pohang, Gyeongbuk, Korea; Cai—CSIRO Marine and Atmospheric Research, Aspendale, Victoria, Australia, and Physical Oceanography Laboratory, Qingdao Collaborative Innovation Center of Marine Science and Technology, Ocean University of China, Qingdao, China; Yeh—Hanyang University, Seoul, Korea

DOI:10.1175/BAMS-D-15-00055.1

A supplement to this article is available online (10.1175/BAMS-D-15-00055.2)

Data and Methods. We assess SST changes in the western tropical Pacific (hereinafter WTP) and the northeast Pacific (hereinafter NEP) regions. Observations are monthly SST data from Extended Reconstruction Sea Surface Temperature (ERSST) version 3 (Smith et al. 2008). We use multimodel data available from the Coupled Model Intercomparison Project Phase 5 (CMIP5; Taylor et al. 2012). We consider the "historical" experiment (anthropogenic and natural forcings) from 1953 to 2005, extended to 2014 utilizing the "RCP4.5" (Representative Concentration Pathway 4.5) experiment, resulting in a 62-year-long all-forcing experiment period, referred to as ALL_P1. We also utilize "historicalGHG" (greenhouse gas only forcing, GHG_P1) and "historicalNat" (natural only forcing, NAT_P1) experiments to examine relative contributions by individual forcing factors, and preindustrial control (CTL_P0) experiments to provide a measure and test of the unforced internal climate variability. Anomalies are calculated relative to the 1971–2000 climatology. Refer to the online supplemental material for full details on CMIP5 data processing.

An attribution analysis of the 2014 record-breaking SSTs is carried out by comparing observed trends (calculated using the least squares method) and anomalies with those from the models. We employ the fraction of attributable risk (FAR; Stott et al. 2004) approach in which the probability of extreme events occurring is compared between worlds without and with human influences to quantitatively estimate anthropogenic influence. Here, FAR is calculated as $FAR = 1 - (P_0 / P_1)$, with P_0 being the probability of extremes exceeding the observed strength in CTL_P0,

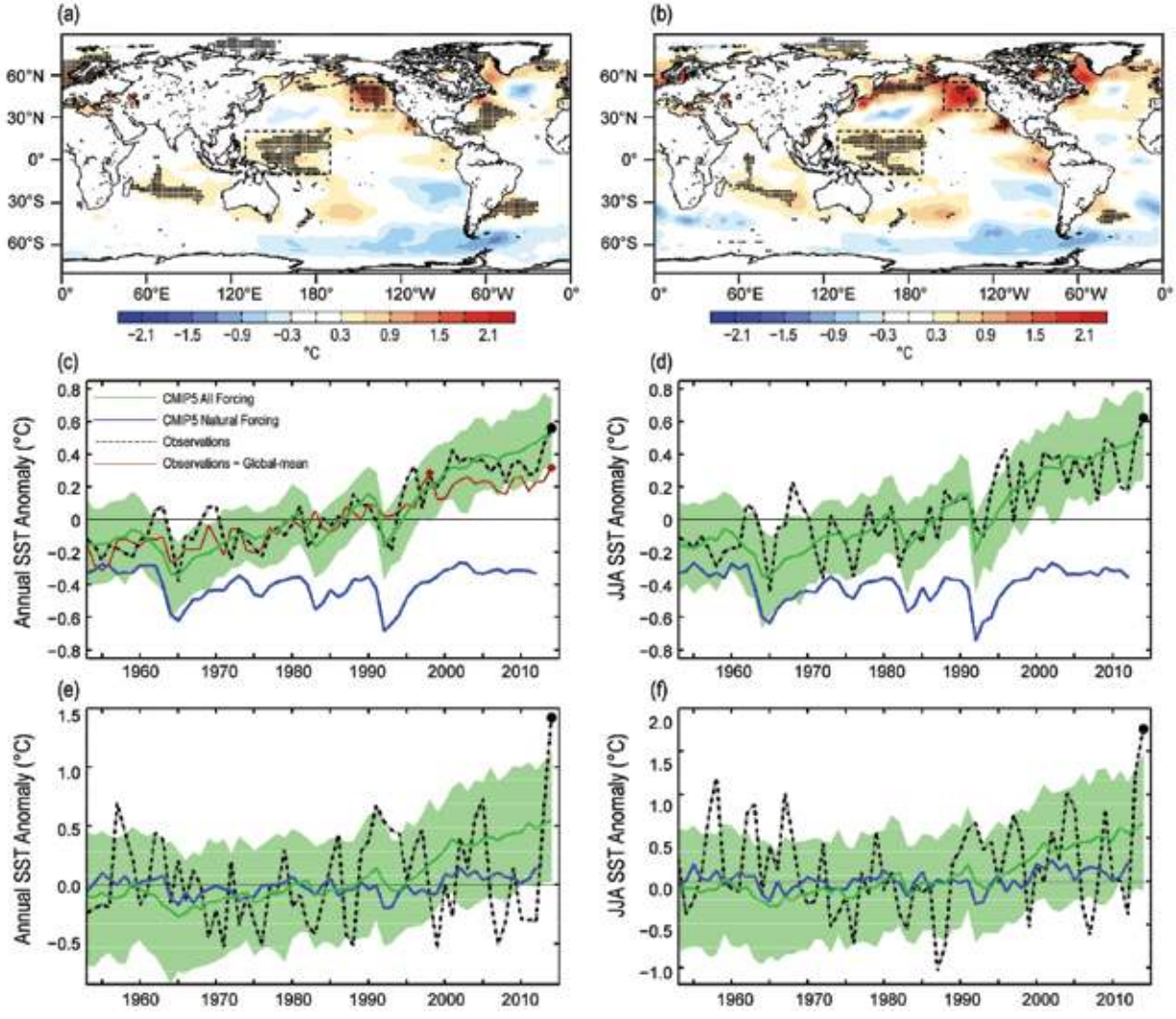

Fig. 20.1. (a,b) Observed (a) annual and (b) boreal summer (JJA) SST anomalies (°C) during 2014, relative to the 1971–2000 mean. Stippling indicates regions where 2014 was the highest on record since 1900. (c,d) Time series of (c) annual and (d) summer SST anomalies (°C), respectively, averaged over the western tropical Pacific Ocean [see dashed box in (a)], relative to the 1971–2000 climatology. (e,f) As in (c,d), but for the northeast Pacific Ocean [see dashed box in (a)]. In (c)–(f), green lines and shading indicate the all-forcing (historical and RCP4.5, ALL_P1) ensemble mean and 10%–90% range across ensemble members, blue indicates the natural-forcing (historicalNat, NAT_P1) ensemble means, and the dashed black indicates the observed SSTs (ERSST v3), with the 2014 record-breaking values represented by black circles. In (c), the observed global mean SST anomaly is also indicated by the brown line, with the record high 2014 and the previous record high 1998 values represented by brown circles. Note that SST anomalies in individual ensemble natural-forcing time series are obtained relative to each 1971–2000 mean of ALL_P1 to account for varying climatology responses to different forcing factors.

and P_1 the probability in ALL_P1 or GHG_P1. FAR values of 0.5 and 0.67, for example, indicate doubled and tripled risk of extreme events due to human influences, respectively.

Results. The observed annual SST anomalies in the WTP reveal the 2014 record high has occurred in conjunction with long-term warming since the 1950s, at a faster rate than the global mean (Fig. 20.1c). The ALL_P1 ensemble mean and range are consistent with the observed changes with similar trends (Figs. 20.1c and 20.2a). Trends in CTL_P0 and NAT_P1 are centered on zero and weak, whereas GHG_P1 has stronger positive trends than the observations (Fig. 20.2a) because it does not include offsetting forcing, such as anthropogenic aerosols. Results for summer trends are similar (Fig. 20.1d and Supplementary Fig. S20.3a). The histograms of modeled trends show none

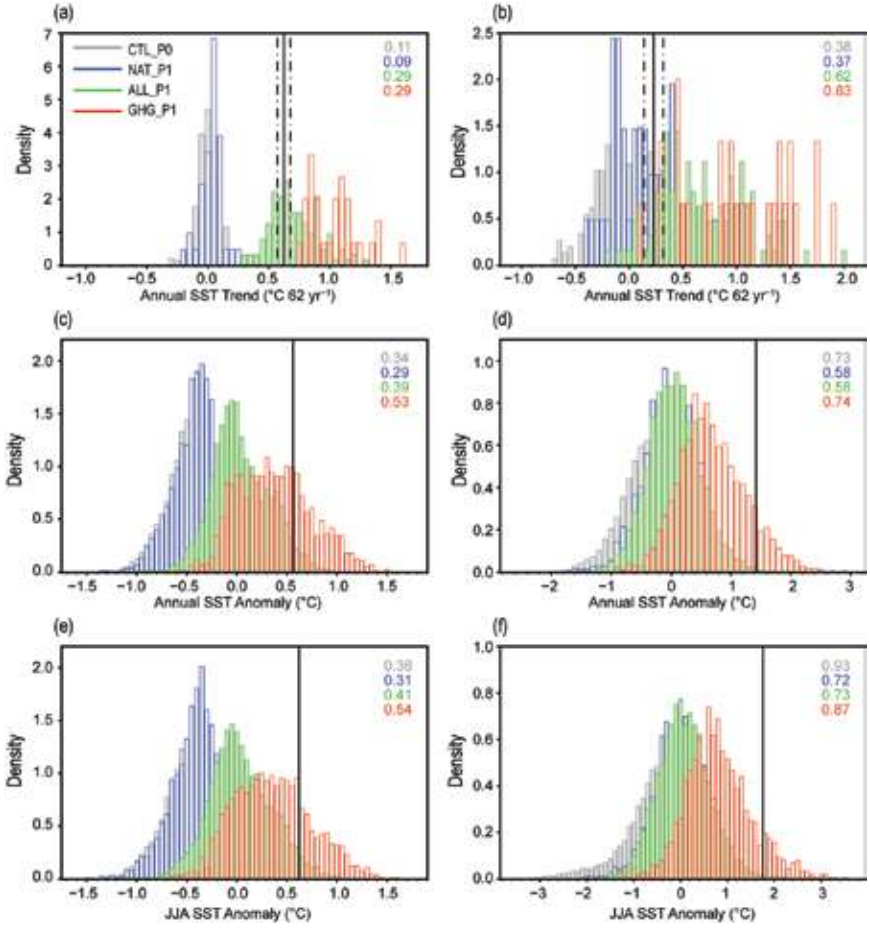

Fig. 20.2. (a,b) Histogram of the annual SST trends (1953–2014) in the (a) western tropical Pacific Ocean and (b) northeast Pacific Ocean, from preindustrial (CTL_P0, gray), historicalNat only (NAT_P1, blue), all (ALL_P1, green), and greenhouse-gas-only (GHG_P1, red) forcing experiments, compared with the observed trend and its 90% confidence interval (ERSST v3, vertical solid and dashed black lines). (c,d) As in (a,b), but for annual SST anomalies from models and the observed extreme 2014 anomaly. (e,f) As in (c,d), but for boreal summer (JJA) SST anomalies. In all panels, the interquartile range for each distribution is shown where differences between forced experiments (NAT_P1, ALL_P1, and GHG_P1) and unforced experiments (CTL_P0) indicate estimates of the uncertainty due to intermodel spread of climate sensitivity.

of CTL_P0 and NAT_P1 trends exceed the observed trend (0.62°C 62 yr^{-1}), whereas it is positioned near the center (49.21 percentile) of ALL_P1 and 100% exceeded in GHG_P1. Thus, the modeled fraction of risk of the SST trend in the WTP that is attributable to anthropogenic forcing is 100% (FAR = 1, Table 20.1), with a negligible influence of natural forcing.

In contrast, Figs. 20.1e,f show little to no significant long-term observed trend of SST anomalies in the NEP. Probability of occurrence exceeding the observed annual trend in ALL_P1 is 84.92%, and also increases, compared to the WTP, for CTL_P0 (16.67%) and NAT_P1 (21.95%; Fig. 20.2b). Similar results are found for summer (Supplementary Fig. S20.3b). FAR values for NEP SST trends range from 0.80 to 0.84 (Table 20.1), providing evidence that there is about a five times increase in risk due to anthropogenic forcings. However, multidecadal variability is clearly evident in the observations, as is stronger warming in ALL_P1 since the early-to-mid 1990s compared to the observations (Figs. 20.1e,f). This indicates that there is a likely role for natural variability in the NEP. Varying the trend period (all ending in 2014), the impact of multidecadal variability on NEP SST trends is evident when compared to the WTP (Supplementary Figs. S20.4a–d). For the WTP, a FAR value of one is obtained for a trend period longer than 25 years. For the NEP, a maximum FAR value (0.90–0.98, a 10–50-fold increase in risk) coincides with a trend from the early 1970s, and smaller values for shorter and longer periods.

We next conduct a similar attribution analysis of extreme 2014 annual SST anomalies. Distributions of all modeled SST anomalies are compared in Figs. 20.2c and d, together with the observed record 2014 anomaly value for the WTP and NEP, respectively. Similar to SST trend distributions, there is an increase in the probability of extreme annual SST anomalies in the WTP when anthropogenic forcings are included (Fig. 20.2c). SST anomalies exceeding the 2014 anomaly (0.56°C) do not occur in CTL_P0 or NAT_P1. Probability increases to 2.79% (1 in 35 years) and 24.72% (1 in 4 years) in ALL_P1 and GHG_P1, respectively. Thus, the modeled fraction of risk of the extreme 2014 WTP SST anomaly is 100% attributable to anthropogenic forcing (FAR = 1, Table 20.1), which appears to be exacerbated by

Table 20.1. Probability of occurrence exceeding the observed 2014 annual and boreal summer (JJA) mean long-term trend and extreme SST anomalies in the western tropical Pacific (WTP) and northeast Pacific (NEP) Ocean regions. The fraction of attributable risk is calculated as $FAR_{ALL\_P1} = 1 - P_{CTL\_P0} / P_{ALL\_P1}$ and $FAR_{GHG\_P1} = 1 - P_{CTL\_P0} / P_{GHG\_P1}$.

	Observations	CTL_P0	ALL_P1	GHG_P1
Trend in WTP Ann/JJA SST	0.62°/0.62°C 62 yr^{-1}	0%/0%	50.79%/55.56% FAR = 1	100%/100% FAR = 1
Trend in NEP Ann/JJA SST	0.23°/0.24°C 62 yr^{-1}	16.67%/15.31%	84.92%/83.33% FAR = 0.80/0.82	96.67%/96.67% FAR = 0.83/0.84
2014 WTP Ann/JJA SST anomaly	0.56°/0.62°C	0%/0%	2.79%/2.51% FAR = 1	24.72%/20.28% FAR = 1
2014 NEP Ann/JJA SST anomaly	1.42°/1.76°C	0.03%/0.03%	0.17%/0.49% FAR = 0.82/0.94	9.22%/8.89% FAR ≈ 1

internal variability given the small percentage of such anomalies occurring in ALL_P1. During summer, the corresponding FAR value is also one (Fig. 20.2e and Table 20.1). Even a threshold equal to the 1971–2000 climatological mean is greater than 10 times more likely due to human influence, highlighting the large shift of the mean state in the WTP from preindustrial levels (Supplementary Figs. S20.4e,h).

For the NEP, the record extreme 2014 annual (1.42°C) and summer (1.76°C) SST anomalies were greater than +3.5σ above the climatological mean (Figs. 20.2d,f). Modeled SST anomalies in CTL_P0, NAT_P1, and ALL_P1 are centered on zero, with only a warm shift in GHG_P1. SST anomalies stronger than the 2014 event are extremely rare in CTL_P0, NAT_P1, and ALL_P1 (Table 20.1). Corresponding FAR values with ALL_P1 are 0.82 and 0.94 for annual and summer, respectively, representing 5–10 times more likely due to human influence. Probabilities increase to 9.22% and 8.89% in GHG_P1 for annual and summer anomalies, with a FAR value essentially equal to one. However, there appears to be a likely role for natural variability on such SST anomalies in the NEP. Unlike the WTP, larger interannual variability in this region results in the FAR value varying considerably for different thresholds above the climatological mean (Supplementary Figs. 20.4f,i).

Sensitivity tests (see online supplemental material for full details) were conducted to assess robustness of the overall conclusions. These included model biases in natural internal variability, observed trend and anomaly uncertainty, and selection bias using the 2014 event for attribution. Conclusions for the WTP do not change despite models exhibiting slightly larger internal variability (Supplementary Figs. S20.5a,c and 20.6a), or if more conservative thresholds (previous record or trends ending in 2013) are used (Supplementary Figs. S20.4a,c and e,h). For the NEP, scaling modeled variability up to better match observed variability reduces the FAR by no more than 0.1 (Supplementary Figs. S20.5b,d and S20.6b). Using a conservative threshold or trends ending in 2013 also reduces our confidence in the NEP conclusions (Supplementary Figs. S20.4b,d and f,i), but the 2014 anomalies are still significantly attributable to anthropogenic forcing. Additionally, choice of RCP experiments used for 2006–14 when constructing ALL_P1 should not affect the main conclusions, as they do not diverge appreciably until the near-term future (Moss et al. 2010). It is also reported that solar irradiance is overestimated to a small degree in CMIP5 simulations (Schmidt et al. 2014); however, this will be only a small fraction of total forcings. Uncertainty arising from intermodel differences in climate sensitivity is also found to be small (Supplementary Fig. S20.7). The use of another observational SST dataset or extending the analysis period to cover the entire twentieth century do not change the main results (Supplementary Fig. S20.8).

Conclusions. Possible impacts of greenhouse gas increases on long-term changes and extreme 2014 record-breaking SSTs in the WTP and NEP are assessed based on the CMIP5 multimodel simulations, representing climate conditions with and without human influences. In the WTP, a strong long-term warming in SST can be explained only when greenhouse gas forcing is included, consistent with Funk and Hoell (2015). Modeled results suggest the record extreme 2014 annual and summer SST anomalies in this region are essentially attributable to anthropogenic forcing. For the NEP, the probability of SST

anomalies such as those observed during 2014 has become about five times as likely with human influences. However, owing to large variability on interannual to multidecadal time scales, there is evidence for the likely role of natural internal variability.

Regional extremes can be due to compounding effects of long-term warming coinciding with natural climate variability. The NEP provides an example of such concurrence. Spatial patterns of 2014 SST anomalies in the North Pacific resemble those observed during a warm phase of the Pacific decadal oscillation (PDO; Mantua et al. 1997) and/or negative phase of the North Pacific Gyre Oscillation (NPGO; Di Lorenzo et al. 2008; Chhak et al. 2009) (Supplementary Figs. S20.9a,b). Indeed, the PDO displayed an intense switch to positive in 2014, partly owing to the anomalously high SST anomalies in the NEP, and the NPGO was observed to be negative (Supplementary Figs. S20.9c,d). Both climate phenomena are associated with large anomalies in the NEP but not particularly associated with anomalies in the WTP. When such natural climate fluctuations act in conjunction with a warming background mean state, annual or seasonal regional extremes are highly likely to continue, resulting in extreme patterns similar to natural climate variability.

ACKNOWLEDGMENTS. This work was supported by the Brain Pool Program through the Korean Federation of Science and Technology Societies (KOFST) funded by the Ministry of Science, ICT and Future Planning (141S-1-3-0023), and the Korea Meteorological Administration Research and Development Program under grant CATER 2013-3180.

REFERENCES

Cai, W., and Coauthors, 2014: Increasing frequency of extreme El Niño events due to greenhouse warming. *Nat. Climate Change*, **4**, 111–116, doi:10.1038/nclimate2100.

Chhak, K., E. Di Lorenzo, N. Schneider, and P. Cummins, 2009: Forcing of low-frequency ocean variability in the northeast Pacific. *J. Climate*, **22**, 1255–1276.

Di Lorenzo, E., and Coauthors, 2008: North Pacific gyre oscillation links ocean climate and ecosystem change. *Geophys. Res. Lett.*, **35**, L08607, doi:10.1029/2007GL032838.

Funk, C. C., and A. Hoell, 2015: The leading mode of observed and CMIP5 ENSO-residual sea surface temperatures and associated changes in Indo-Pacific climate. *J. Climate*, **28**, 4309–4329, doi:10.1175/JCLI-D-14-00334.1.

Mantua, N. J., S. R. Hare, Y. Zhang, J. M. Wallace, and R. C. Francis, 1997: A Pacific interdecadal oscillation with impacts on salmon production. *Bull. Amer. Meteor. Soc.*, **78**, 1069–1079.

Moss, R. H., and Coauthors, 2010: The next generation of scenarios for climate change research and assessment. *Nature*, **463**, 747–756, doi:10.1038/nature 08823.

Schmidt, G. A., D. T. Shindell, and K, Tsigaridis, 2014: Reconciling warming trends. *Nat. Geosci.*, **7**, 158–160, doi:10.1038/ngeo 2105.

Smith, T. M., R. W. Reynolds, T. C. Peterson, and J. Lawrimore, 2008: Improvements to NOAA's historical merged land-ocean surface temperature analysis (1880–2006). *J. Climate*, **21**, 2283–2296.

Stott, P. A., D. A. Stone, and M. R. Allen, 2004: Human contribution to the European heatwave of 2003. *Nature*, **432**, 610–614, doi:10.1038/nature03089.

Taylor, K. E., R. J. Stouffer, and G. A. Meehl, 2012: An overview of CMIP5 and the experiment design. *Bull. Amer. Meteor. Soc.*, **93**, 485–498, doi:10.1175/BAMS-D-1100094.1.

Watanabe, M., H. Shiogama, H. Tatebe, M. Hayashi, M. Ishii, and M. Kimoto, 2014: Contribution of natural decadal variability to global warming acceleration and hiatus. *Nat. Climate Change*, **4**, 893–897, doi:10.1038/nclimate2355.

21. THE 2014 HOT, DRY SUMMER IN NORTHEAST ASIA

L. J. Wilcox, B. Dong, R. T. Sutton, and E. J. Highwood

Northeast Asia experienced a severe drought in summer 2014. Sea surface temperature forcing may have increased the risk of low precipitation, but model biases preclude reliable attribution to anthropogenic forcing.

Observational evidence. Northeast Asia (including a large part of north and northeast China, North Korea, and South Korea) experienced a severe drought in the summer (June to August, JJA) of 2014 (Fig. 21.1a). Seasonal mean rain rates were 1 mm day^{-1} less than the 1964–93 mean; a deficit of 30%. It was the fourth driest year recorded by the Global Precipitation Climatology Centre (GPCC) since 1901 (after 1901, 1902, and 1943), and the third driest year recorded by the Global Precipitation Climatology Project (GPCP) since 1979 (after 1997 and 1999). The 2014 drought occurred in the context of over a decade of summer drought in the region, with an apparent phase shift in precipitation amounts taking place in the late 1990s (Fig. 21.1a). In addition to persistent summer droughts, northeast Asia has experienced steadily increasing temperatures in recent decades (Fig. 21.1b), and indeed most of Asia was warmer in JJA 2014 compared to the 1964–93 mean (Fig. 21.1c).

Summer drought in northeast Asia is part of a larger pattern of southern flooding and northern drought. This pattern is clear when JJA 2014 precipitation is compared to the 1964–93 mean (Fig. 21.1d). Comparing these anomalies to those relative to the more recent period since 1997 (Supplemental Fig. S21.1) shows that the summer of 2014 is an extreme example of the pattern of recent decades, and is therefore likely to be the result of similar underlying mechanisms.

The pattern of summer precipitation in east Asia is related to the meridional propagation of the Mei-Yu front. This is typically located over the south coast in May, propagates north to reach the Yangtze basin by June and northern China by July, and retreats in August with the end of the East Asian monsoon (e.g., Chang et al. 2000). Drought occurs in northern China when the southerly flow over east China is weak, and the propagation of the Mei-Yu front stagnates in the Yangtze River valley (e.g., Zhu et al. 2011).

Summer drought in northern China has been observed to have significant quasi-50-year periodicity (Tan et al. 2014). The main factor controlling this decadal variability in precipitation is thought to be the southerly water vapor transport associated with the monsoon (e.g., Zhao et al. 2010; Tan et al. 2014). However, drought has also been attributed more widely to other factors, such as the positive phase of the Pacific decadal oscillation (PDO; e.g., Zhu et al. 2011), warming tropical Pacific and Indian Oceans (e.g., Zhao et al. 2010), anthropogenic aerosols (Xu 2001; Menon et al. 2002), and the positive phase of the Atlantic multidecadal oscillation (AMO; Qian et al. 2014).

The 850-hPa wind anomalies for 2014 relative to 1964–93 (Fig. 21.1e), and to 1997 to 2014 (Supplemental Fig. S21.1f), show weakened southwesterly flow over China in 2014, consistent with slower northward propagation of the Mei-Yu front. They also show a weaker Indian monsoon circulation, which is again consistent with a more southerly location of the Mei-Yu front.

Sea surface temperature (SST) anomalies for 2014 relative to 1964–93 (Fig. 21.1f), and to 1997 to 2014 (Supplemental Fig. S21.1c), show very warm SSTs along the northern edge of the North Pacific and into the Bering Sea, extending along the western coast of North America. A tongue of cool SSTs extends from the south of Japan into the central North Pacific. Such anomalies are characteristic of the warm phase of the PDO, which has previously been associated with drought in northern China (e.g., Zhu et al. 2011). The similarity of the SST anomalies relative to 1964–93 and 1997 to 2014 suggest that 2014 is a particularly extreme case of the recent decadal pattern.

Indications from CMIP5. Historical experiments for the Coupled Model Intercomparison Project Phase

AFFILIATIONS: Wilcox, Dong, and Sutton—National Centre for Atmospheric Science, Department of Meteorology, University of Reading, Reading, United Kingdom; Highwood—Department of Meteorology, University of Reading, Reading, United Kingdom

DOI:10.1175/BAMS-D-15-00123.1

A supplement to this article is available online (10.1175/BAMS-D-15-00123.2)

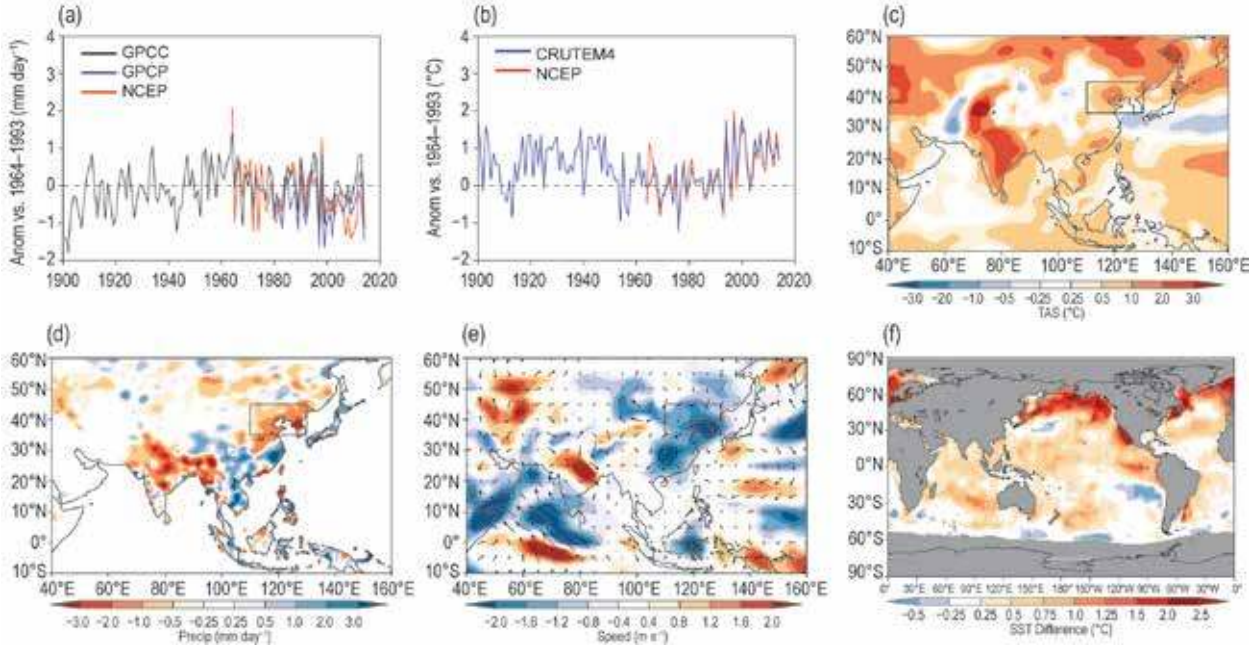

Fig. 21.1. (a) Seasonal mean precipitation anomalies over northeast Asia from GPCC (Schneider et al. 2011, 2013), GPCP (Adler 2003), and the NCEP–NCAR reanalysis (Kalnay et al. 1996). The northeast Asia region is indicated by the boxes in panels (c)–(e). Anomalies are relative to 1964–93. GPCP is shown relative to the GPCC mean. (b) Seasonal mean temperature anomalies (relative to 1964–93) over northeast Asia from CRUTEM4 (Jones et al. 2012) and the NCEP–NCAR reanalysis. (c) Near-surface temperature anomalies (2014 vs. 1964–93) from the NCEP–NCAR reanalysis. (d) Precipitation anomalies (2014 vs. 1964–93) from GPCC. (e) 850-hPa wind anomalies (2014 vs. 1964–93) from NCEP–NCAR. (f) SST anomalies (2014 vs. 1964–93) from HadISST.

5 (CMIP5) subset listed in Table 21.1 were compared for scenarios with all forcings, greenhouse gas (GHG) changes only, and anthropogenic aerosol (AA) changes only. The all-forcing simulations indicate a positive trend in multimodel mean JJA near-surface temperature in northeast Asia, in good agreement with HadCRUT4. This is driven primarily by GHG increases, mitigated in part by AA increases. However, the AA influence on temperature trends is small in recent decades (Supplemental Fig. 21.2).

The multi-model mean trend in precipitation in northeast Asia is small. GHG simulations show a small positive trend. AA forces a larger, bit still small, negative trend from around 1950 to around 1980, and little change in recent decades (Supplemental Fig. S21.2). CMIP5 mean precipitation does not show the

Table 21.1. CMIP5 models, and the number of ensemble members for each experiment, used in this study.

Center	Model	Historical Members	GHG-only Members	AA-only Members	Reference
CCCma	CanESM2	5	5	5	Von Salzen et al. (2013)
CSIRO-QCCCE	CSIRO-Mk3.6.0	10	10	10	Rotstayn et al. (2012)
NOAA-GFDL	GFDL-CM3	3	3	2	Donner et al. (2011), Levy et al. (2013)
IPSL	IPSL-CM5A-LR	6	3	1	Dufresne et al. (2013)
MOHC	HadGEM2-ES	4	4	4	Bellouin et al. (2007), Collins et al. (2011)
NCC	NorESM1-M	3	1	1	Iversen et al. (2013)

pattern of decreases in the north and increases in the south seen in the NCEP–NCAR reanalysis. However, the consistent responses to forcing across the models suggests a degree of understanding of the forced response that is useful in quantifying the relative influence of AA and GHG on the sign and magnitude of the regional response.

Attribution using HadGEM3-A. We use the atmospheric component of the Hadley Centre Global Environment Model version 3 (HadGEM3-A; Hewitt et al. 2011), with prescribed SST and sea ice extent (SIE) from the Hadley Centre Sea Ice and Sea Surface Temperature dataset (HadISST; Rayner et al. 2003) to attempt to quantify the role of SST and SIE, GHG, and AA changes in causing the 2014 drought.

We use a set of four specially designed experiments for attribution of the 2014 drought (Table 21.2), analyzing the last 25 years of each 27-year experiment. Assuming responses to individual forcings can be linearly combined, we can examine the influence of each individual forcing component on the summer of 2014: GHG only (SSTGHG2014–SST2014), AA only (ALL2014–SSTGHG2014), SST only (SST2014–CONTROL), and all-forcing (ALL2014–CONTROL).

The HadGEM3-A experiments show a reduction of precipitation over most of China, and in excess of 3mm day^{-1} in the south, in response to all forcings, associated with a weakening of the East Asian summer monsoon. SST changes account for the majority of the spatial structure and magnitude of the anomalies seen in the all-forcing case (Fig. 21.2). This is consistent with Zhu et al. (2011) who found that SST explained a large part of the weakening of the East Asian summer monsoon. AA and GHG changes cause an increase in precipitation (in HadGEM3-A) in northeast Asia (Fig. 21.2). This offsets the decrease in precipitation driven by SST changes, resulting in the small response seen in the all-forcing case.

Although AA and GHG appear only to make a small contribution to the HadGEM3-A all-forcing response compared to SST changes, this does not preclude an anthropogenic role in the severe drought of 2014. The HadGEM3-A response to SST may be exaggerated by a lack of air–sea coupling in the model (e.g., Zhu and Shukla 2013), and the SST changes themselves may have an anthropogenically driven component. In particular, drought in northern China has previously been linked to PDO and AMO variability, which are potentially driven, at least in part, by AA changes (Booth et al. 2012; Zhang et al. 2013; Allen et al. 2014; Boo et al. 2015).

The precipitation pattern in the mean of the 25 HadGEM3-A realizations of JJA 2014 does not agree with observations. Additionally, no single one of the 25 realizations correctly reproduces the precipitation pattern seen in observations (Supplemental Fig. S21.3). Thus no reliable attribution statement can be made. Christidis et al. (2013) found that HADGEM3-A was unable to provide reliable results for the 2010 flooding in Pakistan, and suggested that biases in the Asian region may be the cause. All CMIP5 generation models have biases in this region, which need to be addressed for successful attribution (e.g., Sperber et al. 2013; Supplemental Fig. S21.2).

When forced with 1964–93 mean SST and SIE, HadGEM3-A has a zonal band of heavy precipitation over the Indian Ocean, a line of heavy precipitation following the Himalayas, and a line following the Burmese coast (Supplemental Fig. S21.4). Precipitation rates are too high over south China and too low over India in HadGEM3-A compared to the NCEP–NCAR reanalysis, which shows a more uniform precipitation distribution, with maxima off the Indian west coast and in the Bay of Bengal (Supplemental Fig. S21.4). The HadGEM3-

Table 21.2. Summary of attribution experiments performed with HadGEM3-A.

Experiment	Boundary Conditions
CONTROL	Monthly climatological sea surface temperature (SST) and sea ice extent (SIE) averaged over the period 1964–93, with greenhouse gas (GHG) concentrations set at their mean values over the same period, and anthropogenic aerosol (AA) precursor emissions (Lamarque et al. 2010) at mean values over the period 1970–93.
ALL2014	Forced with monthly mean SST and SIE from October 2013 to September 2014 using HadISST data, with GHG concentrations from 2013 (WMO 2014) and AA precursor emissions for 2010 (Lamarque et al. 2010), which is the most recent year for which emissions data were available, and is not expected to be substantially different to actual 2014 emissions.
SST-GHG2014	As ALL2014, but with AA precursor emissions the same as in CONTROL.
SST2014	As ALL2014, but with GHG concentrations and AA precursor emissions the same as in CONTROL.

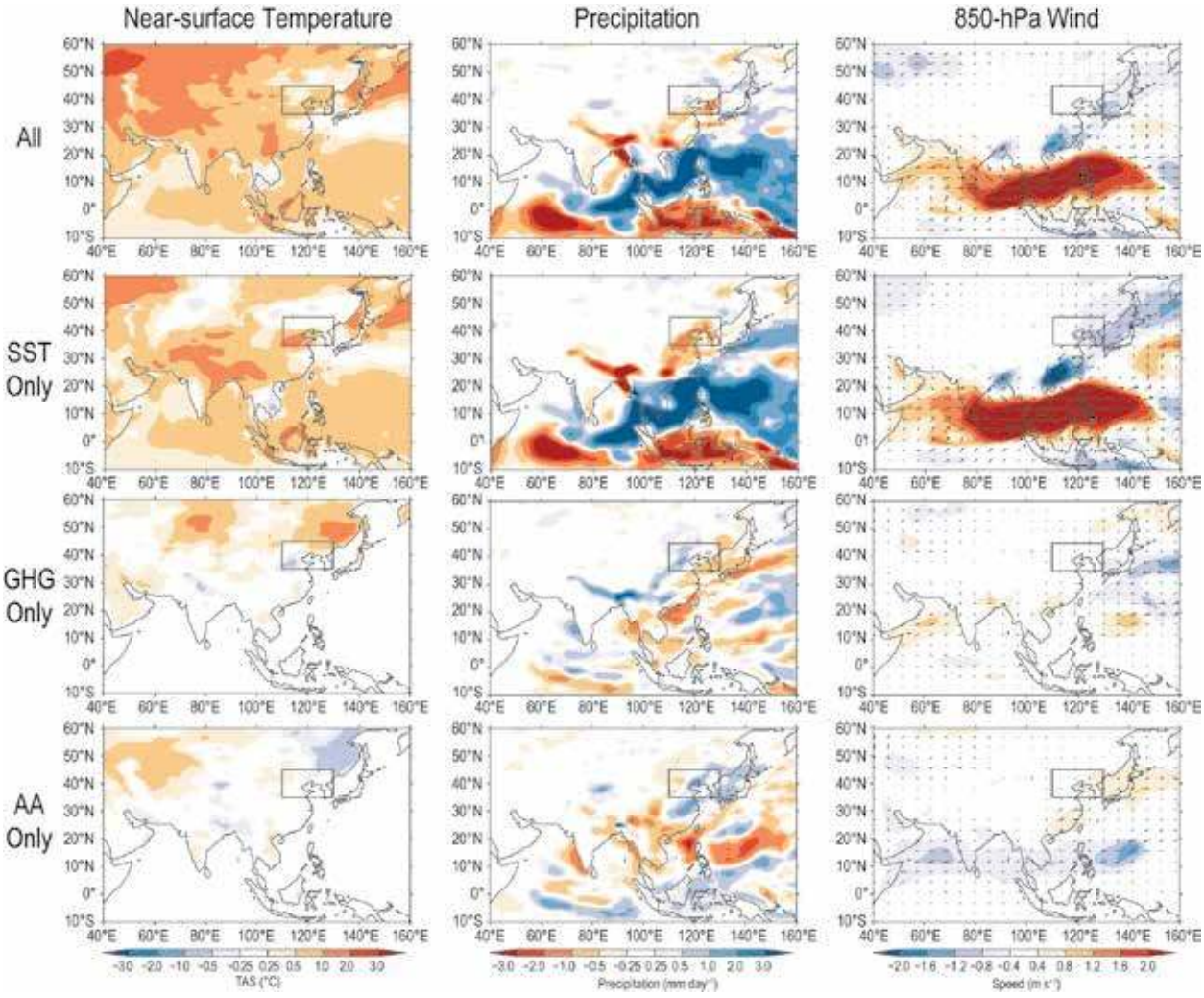

Fig. 21.2. HadGEM3-A responses to summer 2014 forcings, relative to the 1964–93 mean.

A Indian monsoon circulation is comparable to the reanalysis over the Arabian Sea, but weaker and more meridionally diffuse over India and the Bay of Bengal, with weaker flow into southern China. HadGEM3-A near-surface temperatures are generally too warm over Asia (Supplemental Fig. S21.4).

Conclusions. Northeast Asia experienced a severe drought in summer 2014. This was not an isolated event, occurring in the context of two decades of dry summers. The spatial pattern of precipitation in these years is for there to be flooding in southern China and drought in the north, linked to a stagnation of the northward propagation of the Mei-Yu front (e.g., Zhu et al. 2011).

Analysis of an ensemble of CMIP5 models suggests that it is likely that greenhouse gas emissions have caused increased summer temperatures in northeast Asia, partially offset by increasing anthropogenic aerosols. Precipitation responses to forcing are small. HadGEM3-A experiments designed to simulate summer 2014 show reductions in precipitation over China in response to recent changes in SST, but do not capture the observed pattern of precipitation anomalies, thus precluding definitive attribution.

Sperber et al. (2013) show that all climate models have biases in the Asian summer monsoon. Our results, and those of Christidis et al. (2013), suggest that these biases need to be reduced to enable successful attribution of extreme precipitation events in Asia.

ACKNOWLEDGEMENTS. This work was supported by the UK-China Research & Innovation Partnership Fund through the Met Office Climate Science for Service Partnership (CSSP) China as part of the Newton Fund.

Data for the HadGEM2-ES anthropogenic aerosol only experiment was provided by Liang Guo. GPCC

and GPCP precipitation data, and NCEP/NCAR reanalysis data were provided by the NOAA/OAR/ESRL PSD, Boulder, Colorado, via their website at www.esrl.noaa.gov/psd/. CRUTEM4.3 temperature data was provided by CRU, via their website at www.cru.uea.ac.uk/cru/data/temperature/. HadISST temperature data was provided by the UK Met Office, via their website at www.metoffice.gov.uk/hadobs/hadisst/data/download.html.

We acknowledge the World Climate Research Programme's Working Group on Coupled Modelling, which is responsible for CMIP, and we thank the climate modelling groups for producing and making available the model output listed in Table 21.1. For CMIP the U.S. Department of Energy's Program for Climate Model Diagnosis and Intercomparison provides coordinating support and led development of software infrastructure in partnership with the Global Organization for Earth System Science Portals. We also thank the British Atmospheric Data Centre (BADC) for providing access to their CMIP5 data archive.

REFERENCES

Adler, R. F., and Coauthors, 2003: The version 2 Global Precipitation Climatology Project (GPCP) monthly precipitation analysis (1979–Present). *J. Hydrometeor.*, **4**, 1147–1167.

Allen, R. J., J. R. Norris, and M. Kovilakam, 2014: Influence of anthropogenic aerosols and the Pacific decadal oscillation on tropical belt width. *Nat. Geosci.*, **7**, 270–274, doi:10.1038/ngeo2091.

Bellouin, N., O. Boucher, J. Haywood, C. Johnson, A. Jones, J. Rae, and S. Woodward, 2007: Improved representation of aerosols for HadGEM2. Hadley Centre Tech. Note 73, 42 pp. [Available online at www.metoffice.gov.uk/media/pdf/8/f/HCTN_73.pdf.]

Boo, K.-O., B. B. B. Booth, Y.-H. Byun, J. Lee, C. H. Cho, S. Shim, and K.-T. Kim, 2015: Influence of aerosols in multidecadal SST variability simulations over the North Pacific. *J. Geophys. Res. Atmos.*, **120**, 517–531, doi:10.1002/2014JD021933.

Booth, B. B. B., N. J. Dunstone, P. R. Halloran, T. Andrews, and N. Bellouin, 2012: Aerosols implicated as a prime driver of twentieth-century North Atlantic climate variability. *Nature*, **484**, 228–232.

Chang, C., Y. Zhang, and T. Li, 2000: Interannual and interdecadal variations of the East Asian summer monsoon and tropical Pacific SSTs. Part I: Roles of the subtropical ridge. *J. Climate*, **13**, 4310–4325.

Christidis, N., P. A. Stott, A. A. Scaife, A. Arribas, G. S. Jones, D. Copsey, J. R. Knight, and W. J. Tennant, 2013: A new HadGEM3-A-based system for attribution of weather- and climate-related extreme events. *J. Climate*, **26**, 2756–2783, doi:10.1175/JCLI-D-12-00169.1.

Collins, W., and Coauthors, 2011: Development and evaluation of an Earth-system model – HadGEM2. *Geosci. Model Dev.*, **4**, 1051–1075, doi:10.5194/gmd-4-1051-2011.

Donner, L., and Coauthors, 2011: The dynamical core, physical parameterizations, and basic simulation characteristics of the atmospheric component AM3 of the GFDL global coupled model CM3. *J. Climate*, **24**, 3484–3519, doi:10.1175/2011JCLI3955.1.

Dufresne, J.-L., and Coauthors, 2013: Climate change projections using the IPSL-CM5 Earth System Model: From CMIP3 to CMIP5. *Climate Dyn.*, **40**, 2123–2165, doi:10.1007/s00382-012-1636-1.

Hewitt, H. T., D. Copsey, I. D. Culverwell, C. M. Harris, R. S. R. Hill, A. B. Keen, A. J. McLaren, and E. C. Hunke, 2011: Design and implementation of the infrastructure of HadGEM3: The next-generation Met Office climate modelling system. *Geosci. Model Dev.*, **4**, 223–253, doi:10.5194/gmd-4-223-2011.

Iversen, T., and Coauthors, 2013: The Norwegian Earth System Model, NorESM1-M – Part 2: Climate response and scenario projections. *Geosci. Model Dev.*, **6**, 389–415, doi:10.5194/gmd-6-389-2013.

Jones, P. D., D. H. Lister, T. J. Osborn, C. Harpham, M. Salmon, and C. P. Morice, 2012: Hemispheric and large-scale land surface air temperature variations: An extensive revision and an update to 2010. *J. Geophys. Res.*, **117**, D05127, doi:10.1029/2011JD017139.

Kalnay, E., and Coauthors, 1996: The NCEP/NCAR 40-year reanalysis project. *Bull. Amer. Meteor. Soc.*, **77**, 437–470.

Lamarque, J.-F., and Coauthors, 2010: Historical (1850–2000) gridded anthropogenic and biomass burning emissions of reactive gases and aerosols: Methodology and application. *Atmos. Chem. Phys.*, **10**, 7017–7039, doi:10.5194/acp-10-7017-2010.

Levy, H., L. W. Horowitz, M. D. Schwarzkopf, Y. Ming, J.-C. Golaz, V. Naik, and V. Ramaswamy, 2013: The roles of aerosol direct and indirect effects in past and future climate change. *J. Geophys. Res. Atmos.*, **118**, 4521–4532, doi:10.1002/jgrd.50192.

Menon, S., J. Hansen, L. Nazarenko, and Y. Luo, 2002: Climate effects of black carbon aerosols in China and India. *Science*, **297**, 2250–2253.

Qian, C., J.-Y. Yu, and G. Chen, 2014: Decadal summer drought frequency in China: The increasing influence of the Atlantic Multi-decadal Oscillation. *Environ. Res. Lett.*, **9**, 124004, doi:10.1088/1748-9326/9/12/124004.

Rayner, N. A., D. E. Parker, E. B. Horton, C. K. Folland, L. V. Alexander, D. P. Rowell, E. C. Kent, and A. Kaplan, 2003: Global analyses of sea surface temperature, sea ice, and night marine air temperature since the late nineteenth century. *J. Geophys. Res.*, **108**, 4407, doi:10.1029/2002JD002670.

Rotstayn, L., S. Jeffrey, M. Collier, S. Dravitzki, A. Hirst, J. Syktus, and K. Wong, 2012: Aerosol- and greenhouse gas-induced changes in summer rainfall and circulation in the Australasian region: A study using single-forcing climate simulations. *Atmos. Chem. Phys.*, **12**, 6377–6404, doi:10.5194/acp-12-6377-2012.

Schneider, U., A. Becker, P. Finger, A. Meyer-Christoffer, B. Rudolf, and M. Ziese, 2011: GPCC full data reanalysis version 6.0 at 1.0 degree: Monthly land-surface precipitation from rain-gauges built on GTS-based and historic data. Deutscher, Wetterdienst, Offenbach, Germany, digital media, doi:10.5676/DWD_GPCC/FD_M_V6_100.

——, ——, ——, ——, M. Ziese, and B. Rudolf, 2013: GPCC's new land surface precipitation climatology based on quality-controlled in situ data and its role in quantifying the global water cycle. *Theor. Appl. Climatol.*, **115**, 15–40, doi:10.1007/s00704-013-0860-x.

Sperber, K. R., H. Annamalai, I.-S. Kang, A. Kitoh, A. Moise, A. Turner, B. Wang, and T. Zhou, 2013: The Asian summer monsoon: An intercomparison of CMIP5 vs. CMIP3 simulations of the late 20th century. *Climate Dyn.*, **41**, 2711–2744, doi:10.1007/s00382-012-1607-6.

Tan, L., and Coauthors, 2014: Cyclic precipitation variation on the western Loess Plateau of China during the past four centuries. *Sci. Rep.*, **4**, 6381, doi:10.1038/srep06381.

von Salzen, K., and Coauthors, 2013: The Canadian fourth generation atmospheric global climate model (CanAM4). Part I: Representation of physical processes. *Atmos.–Ocean*, **51**, 104–125, doi:10.1080/07055900.2012.755610.

WMO, 2014: The state of greenhouse gases in the atmosphere based on global observations through 2013. *WMO Greenhouse Gas Bulletin*, No. 10, 8 pp. [Available online at www.wmo.int/pages/prog/arep/gaw/ghg/GHGbulletin.html.]

Xu, Q., 2001: Abrupt change of the mid-summer climate in central east China by the influence of atmospheric pollution. *Atmos. Environ.*, **35**, 5029–5040.

Zhang, R., and Coauthors, 2013: Have aerosols caused the observed Atlantic multidecadal variability? *J. Atmos. Sci.*, **70**, 1135–1144, doi:10.1175/JAS-D-12-0331.1.

Zhao, P., S. Yang, and R. Yu, 2010: Long-term changes in rainfall over eastern china and large-scale atmospheric circulation associated with recent global warming. *J. Climate*, **23**, 1544–1562, doi:10.1175/2009JCLI2660.1.

Zhu, J., and J. Shukla, 2013: The role of air–sea coupling in seasonal prediction of Asia–Pacific summer monsoon rainfall. *J. Climate*, **26**, 5689–5697, doi:10.1175/JCLI-D-13-00190.1.

Zhu, Y., H. Wang, W. Zhou, and J. Ma, 2011: Recent changes in the summer precipitation pattern in East China and the background circulation. *Climate Dyn.*, **36**, 1463–1473, doi:10.1007/s00382-010-0852-9.

22. ROLE OF ANTHROPOGENIC FORCING IN 2014 HOT SPRING IN NORTHERN CHINA

Lianchun Song, Ying Sun, Siyan Dong, Botao Zhou, Peter A. Stott, and Guoyu Ren

Anthropogenic forcing may have contributed to an 11-fold increase in the chance of the 2014 hot spring in northern China.

Introduction. The spring of 2014 was the third warmest spring in northern China since reliable observations were established in the late 1950s. The spring mean temperature was 2.2°C higher than the 1961–90 average (Fig. 22.1). In late May, daily maximum temperatures broke their historical records at 12 stations and exceeded 40°C in many regions (CMA 2015). The number of hot spring days in northern China also ranked third highest in the observational record (Fig. 22.1b). The drought and hot winds related to this high-temperature event resulted in serious impacts to agriculture and other important sectors (CMA 2015). Therefore, there is considerable societal interest in whether anthropogenic influence has contributed to the occurrence of such an unusually hot spring.

Here, we investigate the relative contribution from natural and human-caused forcings to the 2014 hot spring with high mean temperatures in northern China. We closely follow the method developed by Sun et al. (2014). First, we establish that there is a high correlation between spring mean temperature and the number of hot spring days. Second, we show that both spring mean temperature and the number of hot spring days have been increasing. We then establish that the increased likelihood of such hot spring mean temperatures in northern China increased 11-fold due to human influence on the climate system. Based on this, we can conclude that human influence may have contributed to the high number of hot days in the spring of 2014. Since the natural forcing field used in the Coupled Model Intercomparison Project Phase 5 (CMIP5) simulations (Taylor et al. 2012) for the 21st century underestimates volcanic aerosols, the model-simulated NAT (natural forcings) response during this period could become too warm (Santer et al. 2014), which would make our estimate of the attributable human influence conservative.

Data. Homogenized daily temperatures at 2419 stations in China for the period 1951–2014 are available for this study (Xu et al. 2013). We compute monthly

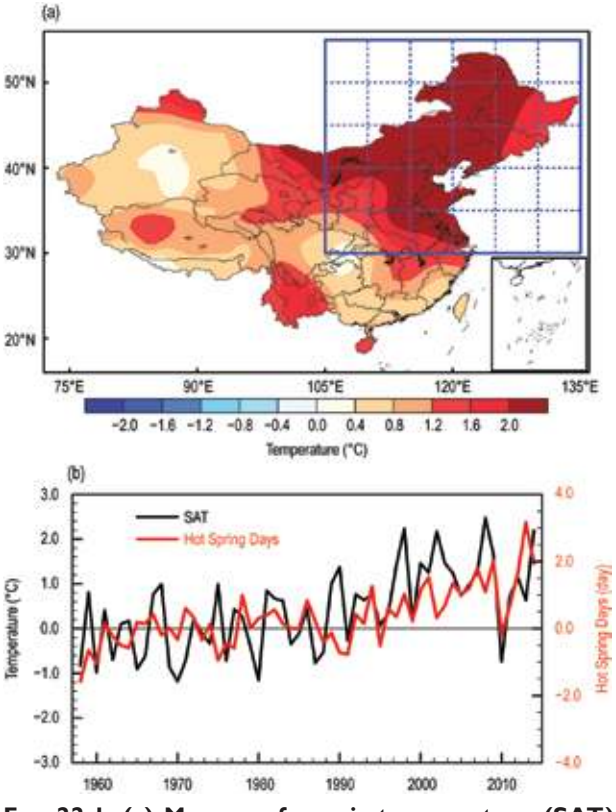

Fig. 22.1. (a) Mean surface air temperature (SAT) anomalies (relative to the 1961–90 average) in spring 2014, Mar–May (MAM), in China. The key study region of northern China is shown as a 5° × 5° grid box. (b) Anomalies (relative to the 1961–90 average) of hot spring days (maximum temperature greater than 25°C) and mean SAT during the period of 1958–2014.

AFFILIATIONS: Song and Dong—National Climate Center, China Meteorological Administration, Beijing, China; Sun and Ren—National Climate Center, China Meteorological Administration, Beijing, and Joint Center for Global Change Studies, Beijing; Zhou—National Climate Center, China Meteorological Administration, Beijing, and Collaborative Innovation Center on Forecast and Evaluation of Meteorological Disasters, Nanjing University of Information Science and Technology, Nanjing, China; Stott—Met Office Hadley Centre, Exeter, United Kingdom

DOI: 10.1175/BAMS-D-15-00111.1

mean temperature anomalies relative to their 1961–90 average at each station and then average available station data within 5° × 5° grid boxes to produce gridded temperature anomalies. The hot spring days are counted as the number of days with daily maximum temperatures exceeding 25°C. The regional mean temperature anomalies for the spring season (March–May, MAM) in northern China, covering a rectangular box at 30°–55°N, 105°–135°E (Fig. 22.1), are then computed based on the gridded data.

Since the urbanization effect is not accounted for in climate model simulations (Sun et al. 2014), we attempt to remove this effect prior to the detection and attribution analysis. We use monthly data at 143 rural stations identified by Ren et al. (2015) and produce gridded monthly temperature anomalies in northern China following the same procedure as used for the full dataset. We consider the difference in the trends of regional mean temperatures computed from the full dataset and from the rural dataset as the effect of urbanization and distribute this effect to the years when urbanization is strong. We produce an annual series representing the urbanization effect with the consideration of different urbanization development prior to 1970 (little urbanization) and after the 1990s (most stations become urban stations). We set the urbanization effect zero prior to 1970 and stabilize after 2000, with a linear temperature increase between the two years where the total increase equals the identified total urbanization effect (Fig. 22.2a, brown line). This annual series is removed from the regional mean series.

Temperature responses to external forcings are estimated based on model-simulated responses to historical all forcing (ALL) and natural forcing (NAT) by CMIP5 climate models. Two independent estimates of internal climate variability are based on climate model simulations including interensemble differences of forced simulations as well as preindustrial control (CTL) simulations. We use the model simulations listed in Supplemental Table 1 in Sun et al. (2014) and follow the same procedure when processing the model data. All the model data are interpolated onto a 5° × 5° grid box to obtain the regional temperature average for MAM. Prior to regional averaging, model data are masked with the observations to mimic the availability of observed data.

Results. Spring 2014 has positive temperature anomalies relative to the 1961–90 mean over almost the whole country, with the strong positive anomalies being more than 2.5°C in northern China (Fig. 22.1a). The number of hot spring days shows a large positive anomaly in the same region (not shown). Both the mean temperature and the number of hot spring days increase in a manner consistent with the rising seasonal mean temperatures (Fig. 22.1b), with a correlation coefficient of 0.53 between the two regional mean series. The correlation coefficient between the two series, after a linear trend is removed from both of the series, is 0.19. This is a positive correlation though not statistically significant. Thus, in northern China the increase in spring mean temperature is indicative of an increase in the number of hot spring days.

Figure 22.2a shows temperature anomalies in the observations and in model simulations under the combined effect of anthropogenic and natural (ALL) forcings and under natural forcings alone (NAT) from 1958 to 2012. There is a large overlap in the range of model-simulated responses to ALL and NAT forcing, indicating that it is difficult to separate responses to natural and anthropogenic forcing. There is a strong upward trend in the observations especially after 1970. In contrast, the trend in NAT is very weak (0.03°C $10yr^{-1}$). The positive trend in the ALL simulations (0.16°C $10yr^{-1}$) is also weaker than that observed (0.33°C $10yr^{-1}$ for 1958–2012 and 0.43°C $10yr^{-1}$ for 1970–2012). However, the large positive temperature anomalies in the observations after the late 1990s are more consistent with the ALL simulations. Given that urbanization has resulted in positive temperature trends (Ren et al. 2008), the effect of urbanization should not be neglected. As a result, we conduct detection and attribution analysis on the temperature series (OBS) after the removal of the estimated urbanization effect (URB), i.e., that is on OBS − URB.

We regress nonoverlapping five-year means of regional average spring OBS − URB temperatures to model-simulated responses to ALL and NAT forcings based on the optimal fingerprinting method (Hegerl et al. 1997; Allen and Stott 2003; Ribes et al. 2013), first with separate regressions for each signal (one-signal analyses) and then jointly in a regression involving both signals (two-signal analysis). The one-signal analysis yields a scaling factor of 1.53 (90% confidence interval: 0.87–2.21) for ALL, but the scaling factor for NAT is not significantly detected. This indicates that the effects of anthropogenic (ANT) forcings on observed changes in the northern China spring temperature can be detected, but the effects of NAT forcings cannot. In the two-signal analysis, the ANT signal and the NAT signal are regressed jointly. The scaling factor for the ANT signal is 1.78 (90% confi-

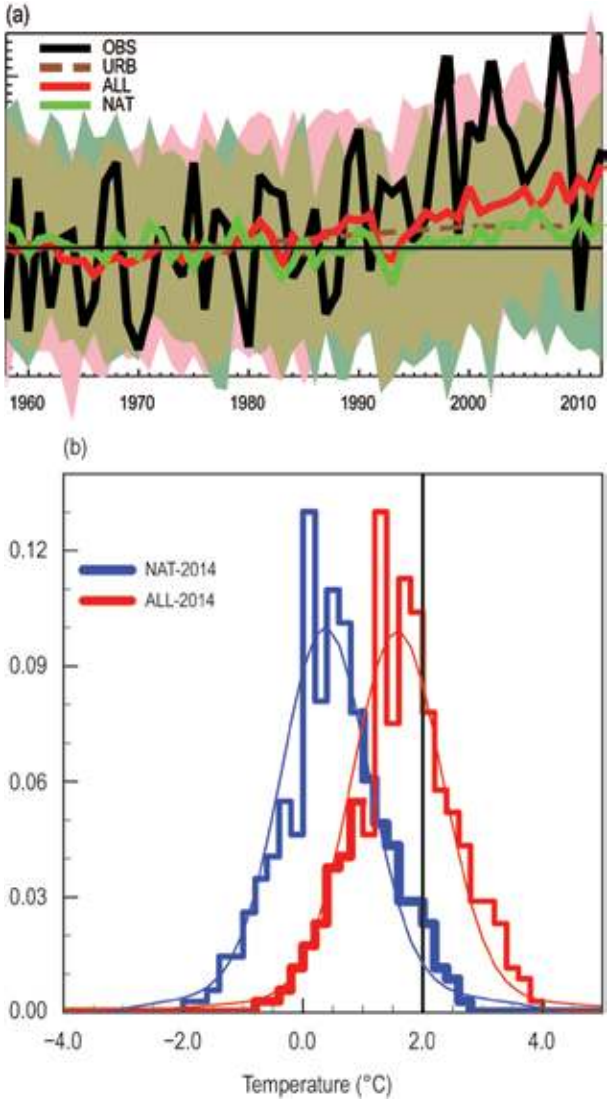

Fig. 22.2. (a) Observed and simulated mean spring temperature anomalies (relative to the 1961–90 average) in northern China (box in Fig. 22.1a). Black, brown, red, and green lines show the observed temperature anomalies (OBS), the annual series representing the urbanization effect (URB), and multimodel response to anthropogenic and natural (ALL) and natural (NAT) forcing, respectively. The pink and green shadings show the 5%–95% ranges of the ALL and NAT responses in individual simulations, respectively. The overlap in the range is shown as dark khaki. Data for the response to ALL forcing for 2006–12 are extended using RCP4.5 simulations. (b) Normalized histogram for the mean spring temperature anomalies from the best estimates of NAT (green) and ALL (red) forcing simulations in comparison with the OBS – URB (vertical black line) in 2014.

dence interval: 0.94–2.68), indicating that the ANT signal is detected. The NAT signal is not detected. This means that the observed spring temperature increase is mainly attributable to ANT forcing, and NAT forcing does not have a discernible influence. The residual consistency tests for the above analyses do not suggest inconsistency between the regression residuals and the model-simulated variability.

The standard deviations of the observed temperature with and without external influence, computed using a method described in Sun et al. (2014), are 0.91°C and 0.77°C, respectively. For the models, the median values of the standard deviations computed from preindustrial control simulations and from reconstructed observations are 0.79°C (with a 90% range of 0.56°–1.03°C) and 0.98°C (with a 90% range of 0.74°–1.22°C), respectively. These indicate that interannual variability of the model-simulated natural climate system is consistent with the observations.

The observed 2014 spring temperature is 2.2°C above the 1961–90 mean. With the urbanization effects removed, the anomaly is about 2.0°C. The best estimate of response to ALL forcing by 2014 is 1.5°C above the 1961–90 climatology. Therefore, the hot 2014 spring is only about 0.5°C above the mean of the current state of the climate. The percentage of years with temperature anomalies at or above 2.0°C in the reconstructed simulations with ALL forcings and with only NAT forcings are 25.7% (90% confidence interval: 12.7%–51.7%) and 2.31%, respectively. We estimate therefore that the observed high spring mean temperature for 2014 would be roughly a once-in-43.3-year event in the NAT world, and that it became a once-in-3.9-year event in ALL due to anthropogenic forcing. This translates to an 11-fold (90% confidence interval: 5-fold to 23-fold) increase in the probability of occurrence (Fig. 22.2b) or, alternatively, a fraction of attributable risk (FAR; Stott et al. 2004) of 0.91 (90% confidence interval: 0.81–0.96) for the event.

Conclusions. We find a close relationship between the number of hot spring days (with maximum temperatures above 25°C) and the mean spring temperature in northern China. Using a two-step attribution procedure we find that the spring temperature increase is explained by the combined effects of anthropogenic and natural forcings with human influence dominating. The 2014 spring temperature is 2.2°C above the 1961–90 mean of which 0.2°C of the increase may be due to the urbanization effect and 1.5°C of the increase may be due to external influence on climate. This translates to about an 11-fold increase in the probability of an event such as the extreme 2014 hot spring occurring.

We also find that urbanization plays an identifiable role in this hot spring event. However, after removing the urbanization effects, the climate models still underestimate the observed increasing trend in the spring temperature. Further analyses are needed to understand the mechanisms behind this underestimation.

ACKNOWLEDGEMENTS: We thank Xuebin Zhang for helpful comments and discussions. L.S., Y.S., B.Z. and G.R. are supported by China funding agencies through multiple grants: 2012CB955900, GYHY201406020, 2012CB417205, GYHY201206012. PAS was supported by the UK-China Research & Innovation Partnership Fund through the Met Office Climate Science for Service Partnership (CSSP) China as part of the Newton Fund, the EUCLEIA project funded by the European Union's Seventh Framework Programme [FP7/2007–13] under Grant Agreement No. 607085 and by the Joint UK DECC/Defra Met Office Hadley Centre Climate Programme (GA01101).

REFERENCES

Allen, M., and P. Stott, 2003: Estimating signal amplitudes in optimal fingerprinting. Part I: Theory. *Climate Dyn.*, **21**, 477–491.

CMA, 2015: *China Climate Bulletin 2014*. China Meteorological Administration, 50 pp.

Hegerl, G. C., and Coauthors, 1997: Multi-fingerprint detection and attribution of greenhouse-gas and aerosol-forced climate change. *Climate Dyn.*, **13**, 613–634.

Ren, G. Y., and Coauthors, 2008: Urbanization effect on observed surface air temperature trend in North China. *J. Climate*, **21**, 1333–1348.

——, and Coauthors, 2015: An integrated procedure to determine reference station network for evaluating and adjusting urban bias in surface air temperature data. *J. Appl. Meteor. Climatol.*, **54**, 1248–1266, doi:10.1175/JAMC-D-14-0295.1.

Ribes, A., S. Planton, and L. Terray, 2013: Application of regularised optimal fingerprinting to attribution. Part I: Method, properties and idealised analysis. *Climate Dyn.*, **41**, 2817–2836, doi:10.1007/s00382-013-1735-7.

Santer, B. D., and Coauthors, 2014: Volcanic contribution to decadal changes in tropospheric temperature. *Nat. Geosci.*, **2**, 185–189, doi:10.1038/ngeo2098.

Stott, P., D. A. Stone, and M. R. Allen, 2004: Human contribution to the European heatwave of 2003. *Nature*, **432**, 610–613.

Sun, Y., X. Zhang, F. W. Zwiers, L. Song, H. Wan, T. Hu, H. Yin, and G. Ren, 2014: Rapid increase in the risk of extreme summer heat in Eastern China. *Nat. Climate Change*, **4**, 1082–1085, doi:10.1038/nclimate2410.

Taylor, K. E., R. J. Stouffer, and G. A. Meehl, 2012: An overview of CMIP5 and the experiment design. *Bull. Amer. Meteor. Soc.*, **93**, 485–498, doi:10.1175/BAMS-D-11-00094.1.

Xu, W.-H., Q. Li, X. L. Wang, S. Yang, L. Cao, and Y. Feng, 2013: Homogenization of Chinese daily surface air temperatures and analysis of trends in the extreme temperature indices. *J. Geophys. Res. Atmos.*, **118**, doi:10.1002/jgrd.50791.

23. INVESTIGATING THE INFLUENCE OF ANTHROPOGENIC FORCING AND NATURAL VARIABILITY ON THE 2014 HAWAIIAN HURRICANE SEASON

Hiroyuki Murakami, Gabriel A. Vecchi, Thomas L. Delworth, Karen Paffendorf, Richard Gudgel, Liwei Jia, and Fanrong Zeng

New climate simulations suggest that the extremely active 2014 Hawaiian hurricane season was made substantially more likely by anthropogenic forcing, but that natural variability of El Niño was also partially involved.

Introduction. Three hurricanes approached the Hawaiian Islands during the 2014 hurricane season (Fig. 23.1a), which is the third largest number since 1949 (black bars in Fig. 23.1b). Previous studies suggest that the frequency of tropical cyclones (TCs) around Hawaii will increase under global warming (Li et al. 2010; Murakami et al. 2013). The projected increase is primarily associated with a northwestward shifting of TC tracks in the open ocean southeast of the islands, where climate models robustly predict greater warming than the other open oceans. Natural variability, such as that associated with the El Niño–Southern Oscillation (ENSO), also has a significant influence on TC activity near Hawaii (Chu and Wang 1997; Jin et al. 2014). In fact, moderate El Niño conditions were observed during the 2014 hurricane season that might have been favorable for TC activity near Hawaii. In this study, we use a suite of climate experiments to explore whether the unusually large number of Hawaiian TCs in 2014 was made more likely by anthropogenic forcing or natural variability.

Methodology. We explore a suite of simulations using the Geophysical Fluid Dynamics Laboratory (GFDL) Forecast-oriented Low Ocean Resolution model (FLOR; Vecchi et al. 2014; see Supplementary Material). Simulated TCs were detected using an automated tracking algorithm as proposed by Murakami et al. (2015; see online supplemental material). For the observational dataset, we used "best-track" data obtained from the International Best Track Archive for Climate Stewardship (IBTrACS; Knapp et al. 2010) and the Unisys Corporation website (Unisys 2015) for the period 1949–2014. We focus on TCs with tropical storm strength or stronger. For the observed sea surface temperature (SST), we used the Hadley Center Global Sea Ice and Sea Surface Temperature dataset (HadISST1; Rayner et al. 2003). We define simulated/observed TCs near Hawaii as those TCs propagating within the coastal region of the Hawaiian Islands; that is, the zone extending 500 km from the coastline (see blue domain in Fig. 23.1a). We performed a preliminary investigation of the dependence of distance on the effect of anthropogenic forcing and natural variability on TC frequency near Hawaii, which revealed that the dependence is small qualitatively.

To assess the ability of FLOR to predict the TCs near Hawaii, we first analyzed a retrospective seasonal forecast made using FLOR initialized on 1 July for each year of 1980–2014 (Vecchi et al. 2014; Jia et al. 2015; see online supplemental material). Figure 23.2a shows the time series of TC number predicted by FLOR, which reasonably predicts the interannual variations of observed TC frequency ($r = 0.59$). Moreover, FLOR predicted marked multidecadal variations in the probability of TC occurrence (for example, higher during the period 1980–94 relative to 1995–2014), which is consistent with the observed variability. However, FLOR underestimates TC number in the abnormal years of 1982, 2009, and 2014, although FLOR predicts relatively larger numbers in 2009 and 2014 compared to the mean of the last two decades (1995–2014). The deficiency in predicting the abnormal years indicates that there may be another forcing that is missing in the experimental setting (for example, atmospheric initialization; aerosols). Or

AFFILIATIONS: Murakami, Vecchi, Delworth, Paffendorf, and Jia—NOAA/Geophysical Fluid Dynamics Laboratory, and Atmospheric and Oceanic Sciences Program, Princeton University, Princeton, New Jersey; Gudgel and Zeng—NOAA/Geophysical Fluid Dynamics Laboratory. Princeton, New Jersey

DOI:10.1175/BAMS-D-15-00119.1

A supplement to this article is available online (10.1175/BAMS-D-15-00119.2)

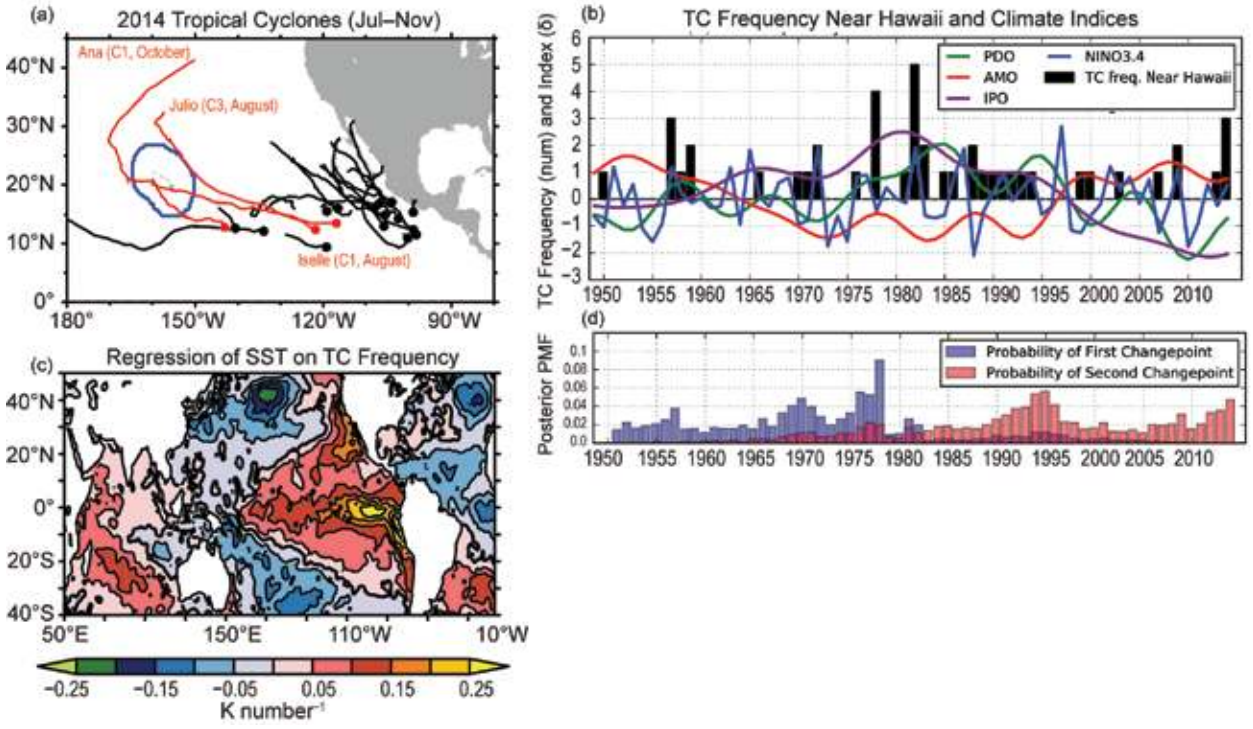

Fig. 23.1. Observed TCs near Hawaii and indices of natural variability. (a) TCs in 2014. Three TCs (red: Iselle, Julio, and Ana) approached the coastal region of Hawaii (blue). Dots denote TC genesis locations. C1 and C3 indicate category 1 and 3 TCs by the Saffir–Simpson hurricane wind scale, respectively. (b) Yearly variability in the number of TCs near Hawaii during the peak season of Jul–Nov for the period 1949–2014 (black bars, number). Colored lines denote climate indices for the PDO (green), AMO (red), IPO (purple), and Niño-3.4 (blue). Units for the indices are one standard deviation. For details of the climate indices and methods used to detect them, see the online supplemental material. (c) Regression of seasonal mean sea surface temperature (SST) onto the number of TCs near Hawaii. Units: K number^{-1}. (d) Results of change-point analysis applied to TC frequency near Hawaii showing the posterior probability mass function (PMF) for the year of the first change point (blue) and second change point (red) under the hypothesis of two change points.

these abnormal events may be unpredictable because of random noise emerging in nature.

Hereafter, we will examine the empirical probability of exceedance for the frequency of TCs near Hawaii during July–November as a function of TC number using the following equation:

$$P(x) = \frac{Number\ of\ years\ with\ TC\ number \geq x}{Total\ number\ of\ years} \qquad (1)$$

where x is the annual number of TCs near Hawaii. For example, *P(3)* represents the probability of occurrence of a year with three or more TCs near Hawaii.

Effect of Anthropogenic Forcing on TCs near Hawaii. Here we form a preliminary estimate of the impact of anthropogenic forcing on Hawaiian TCs, comparing a pair of control climate simulations using FLOR, which were run for 2000-yr (500-yr) intervals by prescribing radiative forcing and land-use conditions representative of the year 1860 (1990) (see online supplemental material). The probability of exceedance for seasonal Hawaiian TC frequency in the 1990 control experiment compares much more reasonably with the observed probability than does the 1860 control experiment (Fig. 23.2b), although the 1990 control experiment still slightly underestimates the observed values. The 1860 control experiment shows substantially reduced probability relative to the 1990 control experiment. The *P(2)* and *P(3)* from the 1990 control experiment are about 5 and 17 times, respectively, larger than those from the 1860 control experiment, or a fraction of attributable risk (FAR; Jaeger et al. 2008) of 80% and 94%, respectively. These experiments suggest that anthropogenic forcing has substantially changed the odds of TC seasons like 2014 near Hawaii relative to natural variability alone.

Effect of Natural Variability on TCs near Hawaii. The black bars in Fig. 23.1b reveal substantial interannual and decadal variations—including a relatively inactive era for Hawaiian TCs for the decade prior to 2014.

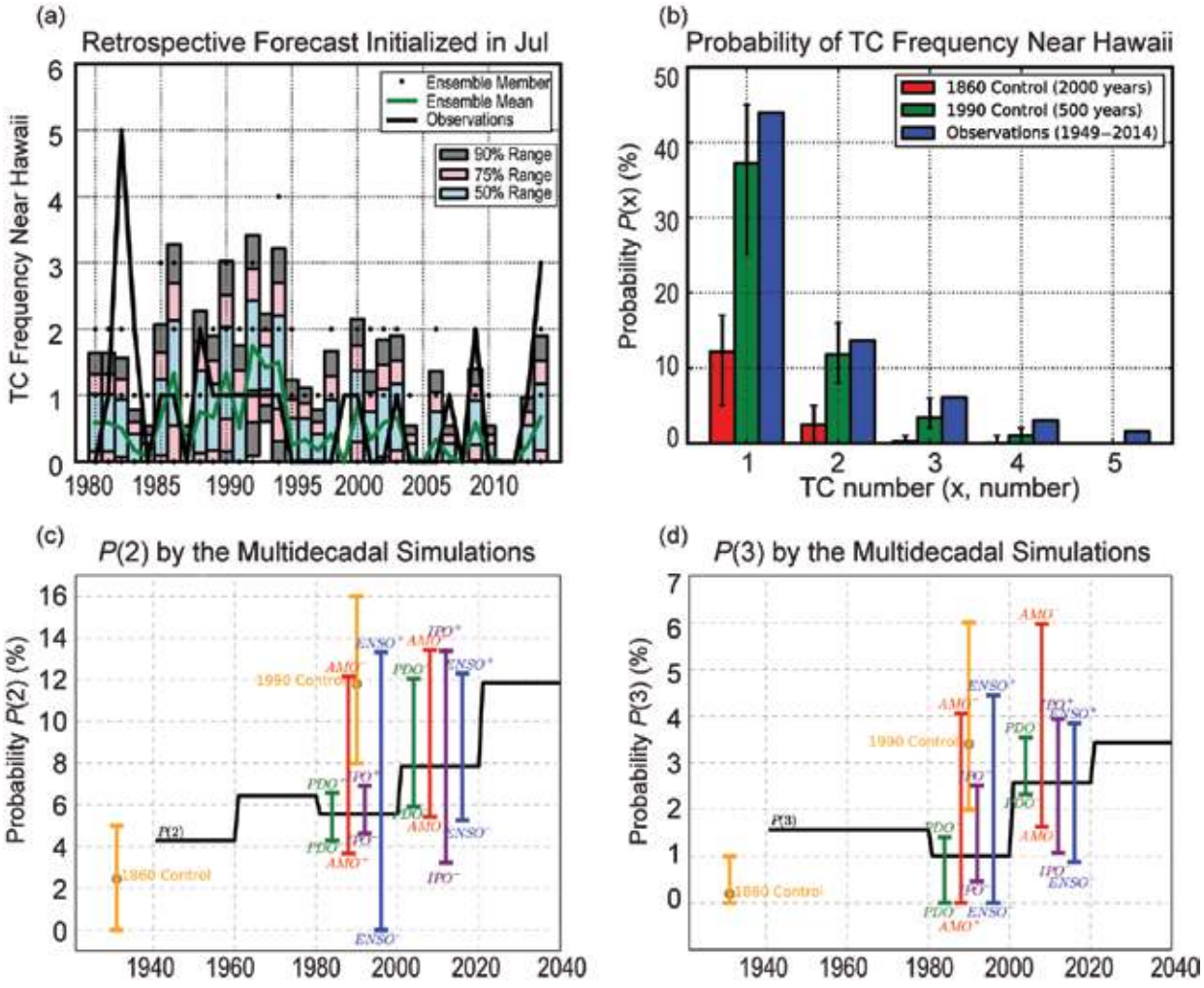

Fig. 23.2. Probability for the frequency of TCs near Hawaii between Jul and Nov simulated by a suite of simulations using FLOR. *P(2)* represents the probability of occurrence of a year with TC number more than or equal to near Hawaii. (a) Retrospective forecasts for TC frequency near Hawaii initialized in Jul. The black line indicates observed TC frequency, green line indicates the mean forecast value, shading indicates the confidence intervals, dots indicate values simulated by one or more ensembles. (b) Results of *P(x)* from the control simulations and observations. Blue bars are probability obtained by observations (1949–2014). Green bars are the results from the 1990 control simulation (500 years), whereas red bars are the results from the 1860 control simulation (2000 years). Error bars in the control simulations denote the range of minimum and maximum values of *P(x)*, computed from each 100-year period. (c) Results of *P*(2) from the multi-decadal simulation. For each 20-year period, *P(2)* (black line) was calculated from 700 samples. Colored bars show the range of conditional *P(2)* induced by natural variability. For example, red bars cover *P*(2|AMO$_+$) and *P*(2|AMO$_-$), namely, the range of *P(2)* under the conditions between positive AMO and negative AMO phases. Likewise, *P(2)* under the condition of positive and negative phases of PDO (green), ENSO (blue), and IPO (purple) are shown. Orange circles denote results of *P(2)* from the control simulations. The orange error bars show the range of minimum and maximum when *P(2)* is computed for each 100-year period. (d) As (c), but for *P(3)*.

Figure 23.1c shows the seasonal mean SST regressed onto TC frequency near Hawaii, and reveals an El Niño-like spatial pattern. This reflects the tendency for an increase in Hawaiian TC activity during El Niño: the Niño3.4 index (blue line, Supplemental Fig. S23.2) is moderately correlated with TC frequency (Chu and Wang 1997). Moreover, Fig. 23.1b reveals marked multidecadal variations in the TC frequency near Hawaii. There appear to be abrupt shifts in Hawaiian TC frequency in the mid-1970s and 1990s. We applied a change-point analysis developed by Zhao and Chu (2010) to the TC frequency time series, which indicated that the most likely first (second) change point was 1978 (1995) (Fig. 23.1d). The spatial pattern

shown in Fig. 23.1c is also similar to the low-frequency variations of the Pacific Decadal Oscillation (PDO; Mantua et al. 1997; green line, Supplementary Fig. S23.3) or Interdecadal Pacific Oscillation (IPO; Power et al. 1999; Folland et al. 2002; purple line, Supplementary Fig. S23.4). Both indices changed sign around 1997 (Fig. 23.1b), which may contribute to the multidecadal variations in TC frequency (Wang et al. 2010). Moreover, Fig. 23.1c shows marked negative SSTs in the tropical Atlantic, indicating reduced TC frequency near Hawaii when the tropical Atlantic is warmer. A recent study by Kucharski et al. (2011) reported that the Atlantic warming in the late twentieth century could have led to a reduction in Pacific warming via the Walker circulation. The Atlantic multidecadal oscillation (AMO; Delworth and Mann 2000; red line, Supplementary Fig. S23.5) index also changed sign around 1997 (Fig. 23.1b), and this could have caused the abrupt shift in TC frequency.

To elucidate the potential influence of the natural variability outlined above on TC frequency near Hawaii, we conducted 35-member ensemble multidecadal simulations (see online supplemental material) from 1941 to 2040. For each 20-year period from 1941, 700 (20×35) samples were available to calculate *P(x)*. In contrast to the seasonal forecasts, because the simulated internal variability is out of phase among the ensemble members (even with the observations), we can estimate the conditional probability of *P(x)* under any phase of natural variability. In other words, we can estimate potential probability under any phase of natural variability in a specific range of decades. Here, we define a simulated/observed positive (or negative) phase of ENSO, PDO, IPO, and AMO as these indices exceeding one standard deviation and estimate the amplitude of *P(x)* between the two phases. For details of the climate indices and methods used to detect them, see the online supplemental material.

Figures 23.2c and d summarize the results for *P(2)* and *P(3)*. Similar results were obtained for *P(1)* (figure not shown). The black lines show *P(2)* and *P(3)* , and reveal a gradual increase from 1940 to 2040, indicating that global warming generates more TCs near Hawaii, which is consistent with the control simulations. The colored bars denote the range of conditional probability induced by natural variability, revealing that natural variability has considerable potential to influence the probability of TC frequency. The amplitude of the bars is similar to the amplitude of the global warming effect (that is, the difference in orange circles in Figs. 23.2c and d), implying that internal variations could act to either temporarily mask or substantially amplify the impact of anthropogenic forcing on the number of TCs near Hawaii.

Discussions and Conclusions. As shown in Fig. 23.1b, the observed TC frequency was greater during the period 1980–94 than 1995–2014. Moreover, the observations show positive PDO and IPO indices, as well as a negative AMO index between 1980 and 1994, whereas these indices reversed sign between 1995 and 2014. From Figs. 23.2c and d, it is possible that the earlier decades (1981–2000) could have had a higher probability of TC occurrence than more recent decades (2001–20), provided that the PDO, IPO, and AMO indices were more favorable for TC activity during the previous decades. Therefore, it can be concluded that the observed multidecadal difference between 1980–94 and 1995–2014 was mainly caused by natural variability. However, the extremely large number of TCs during the 2014 hurricane season occurred despite the unfavorable IPO (–2.0), AMO (+0.7), and PDO (–0.7), and moderate El Niño (+0.5). The FLOR suggests that historical global warming could have contributed to a substantial increase in probability of active Hawaiian TC seasons. The evidence for this can be shown by the composites of the years in which the phase of natural variability is similar to 2014 case in the control experiments. We found that *P(1)* from the 1990 control experiment under the condition of negative IPO, positive AMO, negative PDO, and moderate El Niño is about 3.4 times larger than that from the 1860 control experiment (FAR = 71%). Therefore, it is possible that global warming increased the odds of the extremely large number of Hawaiian TCs in 2014, in combination with the moderately favorable condition of El Niño. The ensemble experiments with FLOR indicate a continued increasing probability of active seasons around Hawaii over the next few decades [consistent with Murakami et al. (2013)]—although there will be substantial modulation on interannual and decadal time scales from internal variability.

ACKNOWLEDGMENT. This report was prepared by Hiroyuki Murakami under award NA14OAR4830101 from the National Oceanic and Atmospheric Administration, U.S. Department of Commerce. The statements, findings, conclusions, and recommendations are those of the authors and do not necessarily reflect the views of the National

Oceanic and Atmospheric Administration, or the U.S. Department of Commerce.

REFERENCES

Chu, P.-S., and J. Wang, 1997: Tropical cyclone occurrences in the vicinity of Hawaii: Are the difference between El Niño and non-El Niño years significant? *J. Climate*, **10**, 2683–2689.

Delworth, T. L., and M. E. Mann, 2000: Observed and simulated multidecadal variability in the Northern Hemisphere. *Climate Dyn.*, **16**, 661–676.

Folland, C. K., J. A. Renwick, M. J. Salinger, and A. B. Mullan, 2002: Relative influences of the Interdecadal Pacific Oscillation and ENSO on the South Pacific Convergence Zone. *Geophys. Res. Lett.*, **29** (13), doi:10.1029/2001GL014201.

Jaeger, C. C., J. Krause, A. Haas, R. Klein, and K. Hasselmann, 2008: A method for computing the fraction of attributable risk related to climate damages. *Risk Anal.*, **28**, 815–823.

Jia, L., and Coauthors, 2015: Improved seasonal prediction of temperature and precipitation over land in a high-resolution GFDL climate model. *J. Climate*, **28**, 2044–2062,doi:10.1175/JCLI-D-14-00112.1.

Jin, F.-F., J. Boucharel, and I-I Lin, 2014: Eastern Pacific tropical cyclone intensified by El Niño delivery of subsurface ocean heat. *Nature*, **516**, 82–85, doi:10.1038/nature13958.

Knapp, K. R., M. C. Kruk, D. H. Levinson, H. J. Diamond, and C. J. Neuman, 2010: The international best track archive for climate stewardship (IBTrACS): Unifying tropical cyclone best track data. *Bull. Amer. Meteor. Soc.*, **91**, 363–376, doi:10.1175/2009BAMS2755.1.

Kucharski, K., I.-S. Kang, R. Farneti, and L. Feudale, 2011: Tropical Pacific response to 20th century Atlantic warming. *Geophys. Res. Lett.*, **38**, L03702, doi:10.1029/2010GL046248.

Li, T., M. Kwon, M. Zhao, J.-S. Kug, J.-J Luo, and W. Yu, 2010: Global warming shifts Pacific tropical cyclone location. *Geophys. Res. Lett.*, **37**, L21804, doi:10.1029/2010GL045124.

Mantua, N. J., S. R. Hare, Y. Zhang, J. M. Wallace, and R. C. Francis, 1997: A Pacific interdecadal climate oscillation with impacts on salmon production. *Bull. Amer. Meteor. Soc.*, **78**, 1069–1079.

Murakami, H., B. Wang, T. Li, and A. Kitoh, 2013: Projected increase in tropical cyclones near Hawaii. *Nat. Climate Change*, **3**, 749–754, doi:10.1038/nclimate1890.

——, and Coauthors, 2015: Simulation and prediction of category 4 and 5 hurricanes in the high-resolution GFDL HiFLOR coupled climate model. *J. Climate*, doi:10.1175/JCLI-D-15-0216.1, in press.

Power, S., T. Casey, C. Folland, A. Colman, and V. Mehta, 1999: Interdecadal modulation of the impact of ENSO on Australia. *Climate Dyn.*, **15**, 319–324.

Rayner, N. A., D. E. Parker, E. B. Horton, C. K. Folland, L. V. Alexander, and D. P. Rowell, 2003: Global analysis of sea surface temperature, sea ice, and night marine air temperature since the late nineteenth century. *J. Geophys. Res.*, **108**, 4407, doi:10.1029/2002JD002670.

Unisys, 2015: Unisys Weather Hurricane/tropical data. [Available online at http://weather.unisys.com/hurricane/.]

Vecchi, G. A., and Coauthors, 2014: On the seasonal forecasting of regional tropical cyclone activity. *J. Climate*, **27**, 7994–8016, doi:10.1175/JCLI-D-14-00158.1.

Wang, B., Y. Yang, Q.-H. Ding, H. Murakami, and F. Huang, 2010: Climate control of the global tropical storm days (1965-2008). *Geophys. Res. Lett.*, **37**, L07704, doi:10.1029/2010GL042487.

Zhao, X., and P.-S. Chu, 2010: Bayesian changepoint analysis for extreme events (typhoons, heavy rainfall, and heat waves): An RJMCMC approach. *J. Climate*, **23**, 1034–1046. doi:10.1175/2009JCL,I2597.1.

24. ANOMALOUS TROPICAL CYCLONE ACTIVITY IN THE WESTERN NORTH PACIFIC IN AUGUST 2014

Lei Yang, Xin Wang, Ke Huang, Dongxiao Wang

The absence of western North Pacific tropical cyclone activity during August 2014 was apparently related to strong easterly wind anomalies induced by combined negative intraseasonal and Pacific decadal oscillation phases.

Introduction. During the boreal summer of 2014, the western North Pacific (WNP; 0°–25°N, 105°E–180°) experienced highly anomalous tropical cyclone (TC) activity: no TC formed from early August through early September, when maximum TC genesis occurs climatologically (Figs. 24.1a,b). Of the five TCs that developed during July, three became super typhoons, making 2014 the year with the highest percentage of super typhoons since 1949 (Supplemental Fig. S24.1). Tropical cyclones are significant sources of summer rainfall in the WNP and its surrounding regions. Such low TC activity in August has directly contributed to the anomalous low precipitation in south Asia and the entire WNP (Lin et al. 2015; Supplemental Fig. S24.2). The three super typhoons in July together caused at least 210 deaths, and severe damage to housing and electrical and agricultural infrastructure, amounting to a total of 7.3 billion U.S. dollars (International Disaster Database, www.emdat.be/database).

The TC data used here are from the best-track dataset produced by the Joint Typhoon Warning Center (JTWC), which has TC records from 1949 through 2014. In this study, a TC is defined as a storm with enclosed cyclonic circulation and sustained winds of 25 knots (kt; 1 kt = 0.51 m s^{-1}) or above. A TC with maximum wind greater than 135 kt is considered a super typhoon. The variation of TC genesis is closely related to the intraseasonal oscillation (ISO) over the WNP (e.g., Gray 1979; Camargo et al. 2009; Li et al. 2012; Li and Zhou 2013). Around 70% of the TCs in the WNP form during the active ISO period of June to December (Huang et al. 2011). Also of interest for our study are the East Asian summer monsoon (EASM) circulation which has been weakening since the end of 1970s (Zhou et al. 2009), and the Pacific decadal oscillation (PDO) which became positive in 2014 and has remained significantly positive through July 2015 (Supplemental Fig. S24.3). We examine the relevant mechanisms, and role of climate change, in the long period with no TC occurrence after the temporal clustering of super typhoons in the WNP in 2014, especially in the context of a possible PDO phase transition from negative to positive and multidecadal weakening of the EASM.

Historical context. Using the U.S. National Centers for Environmental Prediction (NCEP) reanalysis dataset (Kalnay et al. 1996), we analyze the atmospheric circulation anomaly in August 2014, including 850-hPa wind, midlevel humidity (600 hPa), low-level relative vorticity (850 hPa), vertical wind shear of horizontal wind (200–850 hPa), moisture flux (850 hPa), and velocity potential (250 hPa). Convection associated with the ISO is based on the interpolated outgoing longwave radiation (OLR) from National Oceanic and Atmospheric Administration (NOAA), which comprise daily data on a 2.5° × 2.5° grid from 1979 to 2014 (Liebmann and Smith 1996). All anomalies used in the study are relevant to the base period of 1970–2010.

In August 2014, anomalous low-level northeasterly flow dominated the northeast sector of the WNP (area "B" indicated in Fig. 24.1c), and turned to easterly around 140°E until 40°E (area "A" indicated in Fig. 24.1c). The strong easterlies mainly prevailed over the tropical WNP and northern tropical Indian Ocean (TIO). Along with these prevailing easterlies, there were the midlevel dry conditions and negative low-level vorticity (Figs. 24.1d,e). The moisture flux field showed that the anomalous midlevel dry conditions were mainly due to the sustained easterly anomaly (Fig. 24.1f). The anomalous wind pattern played an important role in leading to the unfavorable condi-

AFFILIATIONS: Yang, X. Wang, Huang, and D. Wang—State Key Laboratory of Tropical Oceanography, South China Sea Institute of Oceanology, Chinese Academy of Sciences, Guangzhou, China

DOI: 10.1175/BAMS-D-15-00125.1

A supplement to this article is available online (10.1175/BAMS-D-15-00125.2)

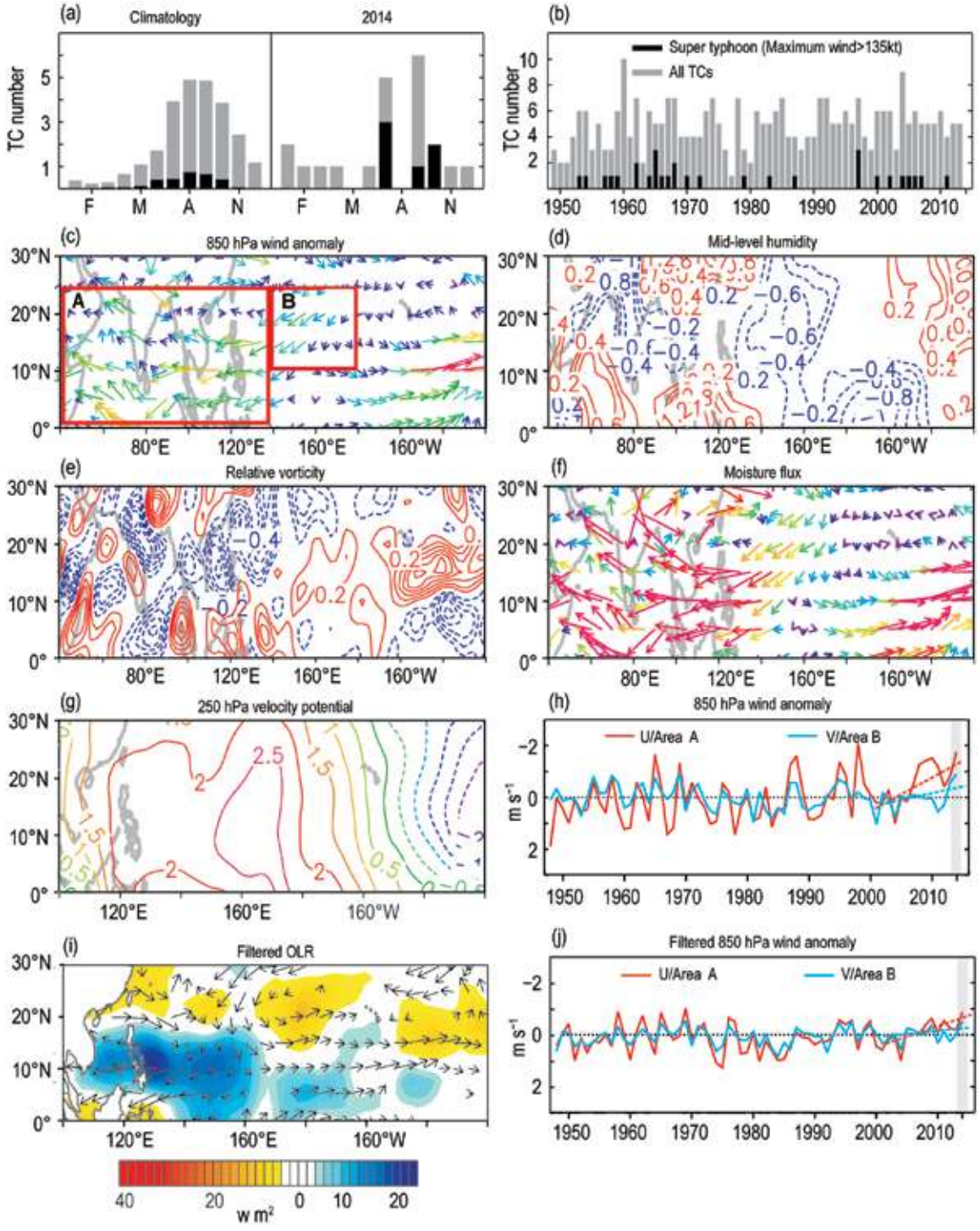

Fig. 24.1. (a) Annual cycle of tropical cyclones in the WNP for climatology and 2014; bars in dark gray (black) represent all TCs (super typhoons). (b) Time series of the tropical cyclone numbers in Aug in the WNP during 1949–2014. (c) 850-hPa wind anomaly (m s^{-1}) for Aug 2014. (d) 600-hPa specific humidity anomaly (g kg^{-1}) for Aug 2014. (e) Low-level relative vorticity anomaly (10^{-5} s^{-1}) for Aug 2014. (f) Moisture flux anomaly (g kg^{-1} m s^{-1}) for Aug 2014. (g) Velocity potential anomaly at 250hPa (10^{-6} m^2 s^{-1}) for Aug 2014. (h) Time series of 850-hPa wind anomaly (m s^{-1}) in Aug during 1948–2014 for U-component over area "A" [indicated in (c)] and V-component over area "B" [indicated in (c)]. (i) 20–100-day filtered OLR (W m^{-2}). (j) As in (h), but for filtered 850-hPa wind anomaly (m s^{-1}). Note that the positive trend lines in (h) and (j) mean further negative values since 2000 and represent increasing easterlies during 2000–14.

tions for TC genesis by continuously transporting dry air from midlatitudes into the WNP and through the western TIO. Correspondingly, a positive velocity potential anomaly at 250 hPa dominated the WNP with a maximum around 160°E, indicating strong divergence and enhanced subsidence in the region (Fig. 24.1g). The vertical wind shear anomaly was not significant and likely had a lesser influence on the anomalous TC genesis (Supplemental Fig. S24.4).

The sustained easterly anomalies over the WNP in August 2014 were unusual. By examining the easterly anomalies in August during 1948–2014, it is found that such strong anomalous easterly flow over the area "A" occurred in only three years: 1988, 1998, and 2014 (Fig. 24.1h and Supplemental Fig. S24.5). Different from those of August 2014, the easterly flows in 1988 and 1998 prevailed from the central Pacific, but weakened and diverged at the eastern TIO (Supplemental Fig. S24.6). It is well known that 1988 and 1998 were strong La Niña years, during which the easterly winds were mostly related to the strong sea surface temperature gradient (SSTG) due to strong cooling in the eastern Pacific (Wang et al. 2000). However, 2014 was a neutral year, according to the Niño 3.4 index (NOAA Climate Prediction Center), and the SSTG was less likely to contribute to the strong easterly anomalies in August 2014. Meanwhile, the average northeasterly flow over the area "B" in August 2014 was anomalously strong, which transported dry air into the WNP and also led to a strong divergence anomaly centered at 160°E, acting together with the strong westerly flow over the eastern North Pacific (ENP). Both the northeasterly and easterly anomalies exhibit strong interannual variability with a positive trend in the recent decade (Fig. 24.1h). The sea level pressure anomaly was slightly positive over the WNP in August 2014, which is different from that in 1998, when the TIO warming after the strong El Niño (1997) induced strong Kelvin wave propagation into WNP, leading to anomalous high pressure over the WNP (Du et al. 2011; Tao et al. 2012; Supplemental Fig. S24.6).

The modulation of the ISO. In contrast to the anomalous atmospheric circulation in the WNP in August 2014, the central North Pacific (CNP) and ENP experienced an almost exactly opposite situation, with strong westerlies, moist midlevels, and increased vorticity and convergence (Figs. 24.1c–g). Correspondingly, more TC activities were recorded in the CNP/ENP during the period. The differences in the atmospheric circulation anomalies and TC activity between WNP and ENP suggest a possible connection to the ISO phase.

In early July of 2014, strong positive convection dominated the WNP and western TIO, while negative convection was located in the CNP and ENP. The positive convection center in the western TIO gradually moved northward into the WNP and combined with the positive center in the WNP. At the end of July, the positive center started to move out of the WNP and split into two branches, one moving northward and one eastward (Supplemental Fig. S24.7) and marking a phase change from positive to negative (negative to positive) in the WNP (ENP). With the continuing northward propagation of the ISO signals, a strong negative convection anomaly center dominated the WNP and lingered until the end of August, leading to unfavorable conditions for TC genesis (Fig. 24.1i).

Did anthropogenic climate change influence the extreme TC activity in August 2014? The variations of TC genesis frequency and intensity in the WNP, from intraseasonal to interdecadal time scales, are related to ISO phases (e.g., Gray 1979; Huang et al. 2011; Li and Zhou 2013; Yang et al. 2015), monsoon trough variability (e.g., Ritchie and Holland 1995; Chen et al. 2004; Wu et al. 2012), the El Niño–Southern Oscillation (e.g., Chan 2005; Du et al. 2011; Kim et al. 2011), and the PDO (e.g., Yang et al. 2012; Liu and Chan 2013). WNP TC genesis frequency depends on the ISO phase (Huang et al. 2011) and might also vary with different climate backgrounds of the EASM (Zhou et al. 2009; Wang et al. 2012) and PDO phase (Liu and Chan 2013). Previous studies suggested that the modulation of TCs by the ISO during July–August of 1979–2008 or 1979–2004 was relatively weak compared to other seasons (Huang et al. 2011; Kim et al. 2008). Here, a strong positive correlation between the ISO and TC frequency in the WNP is found during August 2000–14 (Supplemental Fig. S24.8). Averaged 20–100-day filtered 850-hPa wind anomaly over the WNP in August showed an increasing trend during 2000–14 (under PDO negative phase and possible transition to positive phase), which corresponded well with the decreasing trend in TC frequencies (Fig. 24.1j). During this period, the correlation between filtered easterlies in area "A", northeasterlies in area "B", and OLR anomalies over the WNP (5°–20°N) is 0.75, 0.73, and -0.74, respectively (Fig. 24.2a-c). During the other two PDO phases, negative phase of 1950–76 and positive phase of 1977–99, the correlation was much lower,

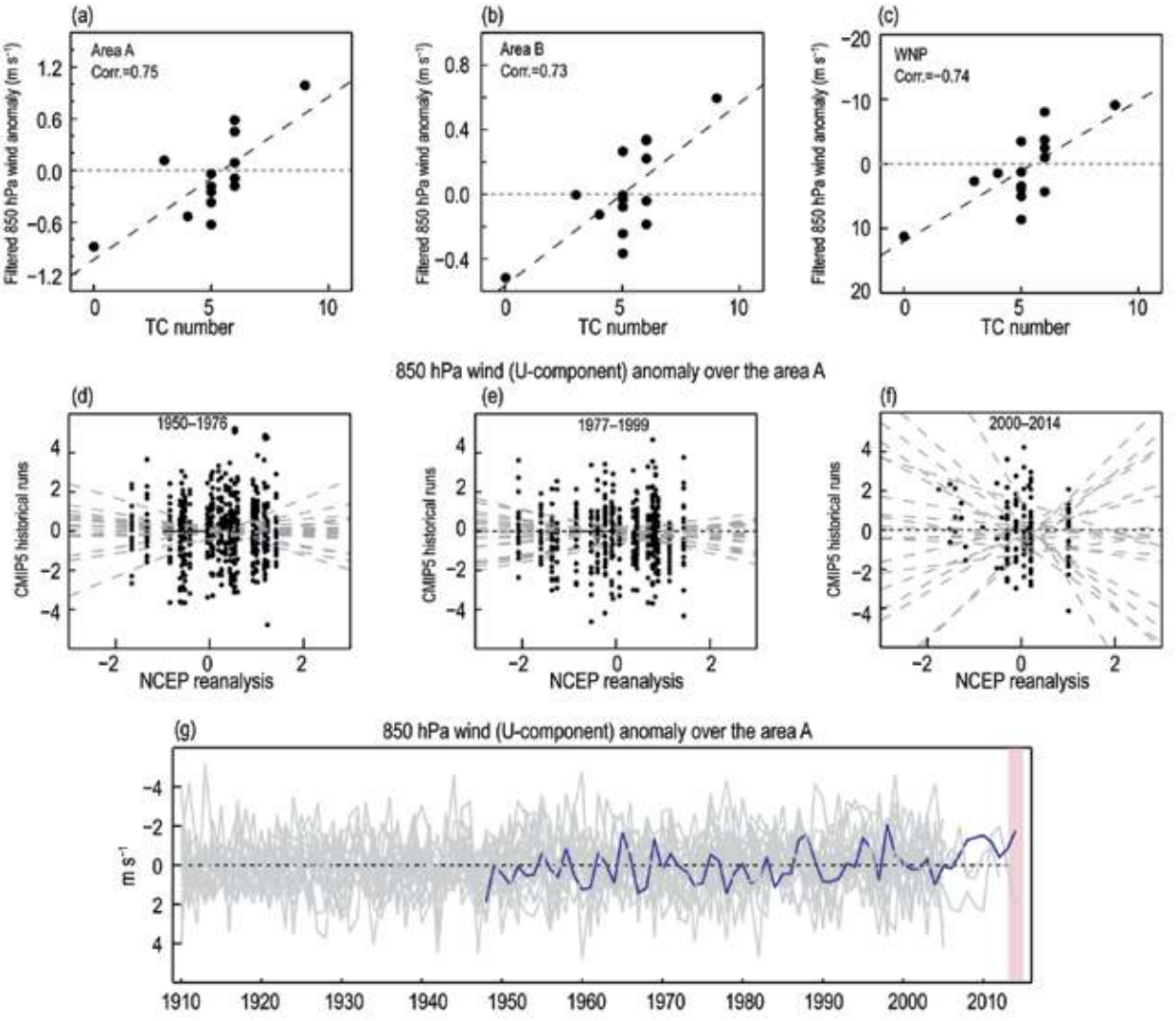

Fig. 24.2. Scatter plot between TC numbers and (a) filtered 850-hPa wind anomaly over area "A". (b) Filtered 850-hPa wind anomaly over area "B". (c) OLR anomaly over WNP during 2000–14. Scatter plot of 850-hPa wind anomaly (U-component; m s⁻¹) between 20 CMIP5 historical runs and NCEP reanalysis for (d) 1950–76, (e) 1977–99, and (f) 2000–14. (g) Time series of 850-hPa wind (U-component) anomaly (m s⁻¹) simulated by CMIP5 historical runs (gray lines) and derived from NCEP reanalysis (blue line). Notes: 1) All figures are for Aug; 2) the positive trend in (c) and (g) represents a further negative value and means increasing convection inhibition and easterlies, respectively, during 2000–14.

with increasing tendency from 1950–76 to 1977–99 (Supplemental Fig. S24.8).

Was the increased correlation with different PDO phases related to the weakening of EASM or climate change induced by anthropogenic forcing? The averaged 850-hPa wind anomaly over the WNP and ENP derived from the historical simulation of 20 Coupled Model Intercomparison Project Phase 5 (CMIP5) models are analyzed. A model is chosen based on its performance in reproducing the averaged 850-hPa wind during 1948–2005. Those with an obvious pattern difference are not selected. Only one model has historical data in 2014 which simulate an opposite pattern of 850-hPa easterly anomaly compared to the reanalysis data: westerly anomaly in the WNP and easterly anomaly in the ENP (Supplemental Fig. S24.9). Scatter plots of 850-hPa wind anomaly between reanalysis and 20 model runs for the three PDO phases since 1948 show a poor correlation (Figs. 24.2d–f). None of the twenty models can simulate a reasonable result for all three periods (Fig. 24.2g). Comparisons during the third PDO phase period are less meaningful due to small samples because there were only two model runs after

2005. The inability of CMIP5 models to replicate the easterly anomaly pattern might be partly due to the inconsistency of PDO phase transition (Zhou et al. 2013) and the variation of EASM with observations. Therefore, the study cannot conclude the role of climate change in the low TC activity in the WNP.

Concluding remarks. The year 2014 was the first since 1949 that no TC formed in the WNP during August, which is climatologically a peak TC month. It is found that ISO played an important role in inhibiting TC genesis in August 2014 by inducing anomalous easterlies, which led to decreased moisture and vorticity, and increased divergence. The strength of the modulation of TC frequency by the ISO over the WNP during August has been increasing since 1948 under three PDO phases with the strongest during the recent negative PDO phase. However, the anomaly pattern as well as the interannual variations of 850-hPa wind anomaly cannot be captured by the CMIP5 models, and therefore, we currently cannot determine whether the significant easterly trend as well as the observed TC activity is part of natural climate variability or climate change induced by anthropogenic forcing. In the future, application of downscaling techniques in atmospheric general circulation models may be needed to diminish the biases in the tropical areas.

ACKNOWLEDGEMENTS. The authors would like to thank three anonymous reviewers and BAMS subject matter editor Dr. Jim Kossin and Chief editor Dr. Jeff Rosenfeld for helpful comments on the earlier version of this manuscript. This work is supported by the Strategic Priority Research Programs of the Chinese Academy of Sciences (No. XDA11010302) and LTOZZ1202. Special thanks go to Dr. Yanluan Lin for the enlightening discussions.

REFERENCES

Camargo, M., C. Wheeler, and A. H. Sobel, 2009: Diagnosis of the MJO modulation of tropical cyclogenesis using an empirical index. *J. Atmos. Sci*., **66,** 3061–3074.

Chan, J. C. L., 2005: Interannual and interdecadal variations of tropical cyclone activity over the western North Pacific. *Meteor. Atmos. Phys*., **89**, 143–152.

Chen, T.-C., S.-Y. Wang, M.-C. Yen, and W. A. Gallus Jr., 2004: Role of the monsoon gyre in the interannual variation of tropical cyclone formation over the western North Pacific. *Wea. Forecasting*, **19**, 776–785.

Du, Y., L. Yang, and S-P. Xie, 2011: Tropical Indian Ocean influence on northwest Pacific tropical cyclones in summer following strong El Niño. *J. Climate*, **24**, 315–322, doi:10.1175/2010JCLI3890.1.

Gray, W. M., 1979: Hurricanes: Their formation, structure, and likely role in the tropical circulation. *Meteorology over the Tropical Oceans*, D. B. Shaw, Ed., Royal Meteorological Society, 155–218.

Huang, P., C. Chou, and R. Huang, 2011: Seasonal modulation of tropical intraseasonal oscillations on tropical cyclone geneses in the western North Pacific. *J. Climate*, **24**, 6339–6352, doi:10.1175/2011JCLI4200.1.

Kalnay, E. and Coauthors, 1996: The NCEP/NCAR 40-year reanalysis project. *Bull. Amer. Meteor. Soc*., **77**, 437–470.

Kim, H-M., P. J. Webster, and J. A. Curry, 2011: Modulation of North Pacific tropical cyclone activity by the three phases of ENSO. *J. Climate*, **24**, 1839–1849, doi:10.1175/2010JCLI3939.1.

Kim, J., C. Ho, H. Kim, C. Sui, and K. Seon, 2008: Systematic variation of summertime tropical cyclone activity in the western North Pacific in relation to the Madden–Julian oscillation. *J. Climate*, **21**, 1171–1191.

Li, R. C.-Y., and W. Zhou, 2013: Modulation of western North Pacific tropical cyclone activity by the ISO. Part I: genesis and intensity. *J. Climate*, **26**, 2904–2918, doi:10.1175/JCLI-D-12-00210.1.

——, ——, J. C. L. Chan, and P. Huang, 2012: Asymmetric modulation of the western North Pacific cyclogenesis by the Madden–Julian Oscillation under ENSO conditions. *J. Climate*, **25**, 5374–5385, doi:10.1175/JCLI-D-11-00337.1.

Liebmann, B., and C. Smith, 1996: Description of a complete (interpolated) outgoing longwave radiation dataset. *Bull. Amer. Meteor. Soc*., **77**, 1275–1277.

Lin, Y., M. Zhao, and M. Zhang, 2015: Tropical cyclone rainfall area controlled by relative sea surface temperature. *Nat. Commun*., **6**, 6591, doi:10.1038/ncomms7591.

Liu, K. S., and J. C. L. Chan, 2013: Inactive period of western North Pacific tropical cyclone activity in 1998–2011. *J. Climate*, **26**, 2614–2630, doi:10.1175/JCLI-D-12-00053.1.

Ritchie, E. A., and G. J. Holland, 1999: Large-scale patterns associated with tropical cyclogenesis in the western Pacific. *Mon. Wea. Rev*., **127**, 2027–2043.

Tao, L., L. Wu, Y. Wang, and J. Yang, 2012: Influences of tropical Indian Ocean warming and ENSO on tropical cyclone activity over the western North Pacific. *J. Meteor. Soc. Japan*, **90**, 127–144, doi:10.2151/jmsj.2012-107.

Wang, B., R. Wu, and X. Fu, 2000: Pacific–East Asian teleconnection: How does ENSO affect East Asian climate? *J. Climate*, **13**, 1517–1536.

Wang, X., W. Zhou, C-Y. Li, and D. Wang, 2012: Effects of the East Asian summer monsoon on tropical cyclone genesis over the South China Sea on an interdecadal time scale. *Adv. Atmos. Sci.*, **29**, 249–262, doi:10.1007/s00376-011-1080-x.

Wu, L., Z. Wen, R. Huang, and R. Wu, 2012: Possible linkage between the monsoon trough variability and the tropical cyclone activity over the western North Pacific. *Mon. Wea. Rev.*, **140**, 140–150, doi:10.1175/MWR-D-11-00078.1.

Yang, L., Y. Du, S. Xie, and D. Wang, 2012: An interdecadal change of tropical cyclone activity in the South China Sea in early 1990s. *Chinese J. Oceanol. Limnol.*, **30**, 953–959, doi:10.1007/s00343-012-1258-9.

——, ——, D. Wang, C. Wang, and X. Wang, 2015: Impact of intraseasonal oscillation on the tropical cyclone track in the South China Sea. *Climate Dyn.*, **44**, 1505–1519, doi:10.1007/s00382-014-2180-y.

Zhou, T., D. Gong, J. Li, and B. Li, 2009: Detecting and understanding the multi-decadal variability of the East Asian Summer Monsoon – Recent progress and state of affairs. *Meteor. Z.*, **18**, 455–467.

——, F. Song, R. Lin, X. Chen, and X. Chen, 2013: The 2012 North China floods: Explaining an extreme rainfall event in the context of a long-term drying tendency [in "Explaining Extreme Events of 2012 from a Climate Perspective"]. *Bull. Amer. Meteor. Soc.*, **94** (9), S49–S51.

25. THE 2014 RECORD DRY SPELL AT SINGAPORE: AN INTERTROPICAL CONVERGENCE ZONE (ITCZ) DROUGHT

John L. McBride, Sandeep Sahany, Muhammad E. E. Hassim, Chi Mai Nguyen , See-Yee Lim, Raizan Rahmat, Wee-Kiong Cheong

The record dry spell over Singapore–Malaysia was caused by the southward contraction of the intertropical convergence zone. Within present evidence, there is no clear attribution to climate change.

Introduction. The 62-day period from 13 January to 15 March 2014 is the longest dry spell in Singapore since the beginning of the official record in 1929. A dry spell is defined as more than 15 consecutive days with less than 1 mm of rainfall registered at a climate station (the Singapore station is now at Changi, 1°13'12"N, 103°35'24"E). The previous longest dry spells by this definition had lasted 42 days in January–February 2009 and 40 days in January–February 2005 (Fig. 25.1a). The climate station has moved several times since its establishment in 1869. With that qualification, February 2014 is the driest for any calendar month since 1869. Continuous multistation networks have been established over Singapore in recent decades. Averaged over eight stations since 1965, February 2014 is the second driest calendar month on record, and averaged over 28 stations since 1980, it is the driest calendar month on record. The drought/dry spell had a large spatial extent covering Malaysia and parts of Indonesia, and fits into the category of intertropical convergence zone (ITCZ) droughts, as discussed later in the text. This paper attempts to examine the record dry spell in the contexts of natural variability and of climate change (section 2) and in terms of plausible physical mechanisms (section 3).

Interannual and climate change perspective. From December through March, the low-level flow over Singapore is Northeasterly, the "Northeast monsoon in the South China Sea." As shown in Fig. 25.1b February has a different rainfall climatology than the rest of the Northeast monsoon, being considerably drier. This is associated with the ITCZ reaching its furthest southward location in that month and thus having less effect on Singapore's rainfall.

Addressing first the natural variability aspect, we analyze records for the single month February rather than the more usual three months, due to the high temporal structure within the Northeast monsoon season and the fact that February has a different climatology. The data in Fig. 25.1a show an increase in dry spell length over the period 1984 to present when the climate station has been in its current location, with an r-squared of 0.12 for the linear correlation with time. However, when the end-point (2014) is removed, the r-squared reduces to .02 and is not significant even at the 10% level. February rainfall averaged over the eight-station network from 1965 is shown in Fig. 25.1c. That series also has a downward trend, but with an r-squared of 0.02, which is also not statistically significant. Thus, over recent decades, there is no evidence for any statistically significant decrease in February rainfall or increase in dry-spell length, other than the single event in 2014.

The climate change context from CMIP5 models used in the Intergovernmental Panel on Climate Change AR5 (IPCC AR5) is a projected decrease in rainfall in the lower range of the distribution. This means that droughts (as defined by negative Standard Precipitation Index or by lowest deciles) will be more severe (Fig. 25.1d). The upper panel is the percentage change in the 25th percentile of rainfall for mid-twenty-first century, while the lower is for end-century, both for the RCP8.5 global warming emissions pathway (Stocker et al. 2013). The figures show differences between 20-year periods for future climate compared with current climate. To determine the significance of this, hatching indicates regions where the magnitude of the change of the 20-year mean is less than one standard deviation of model-estimated present-day natural variability of 20-year mean differences. This measure of natural variability

AFFILIATIONS: McBride, Sahany,* EeqmalHassim, Nguyen, Lim, Rahmat, and Cheong—Centre for Climate Research Singapore, Meteorological Service Singapore, Singapore

* **CURRENT AFFILIATION**: Centre for Atmospheric Sciences, Indian Institute of Technology, Delhi, New Delhi, India

DOI: 10.1175/BAMS-D-15-00117.1

is discussed further in Annex I of IPCC AR5 (Stocker et al. 2013).

Since the Singapore region is under the hatching for midcentury (upper panel) and for other emission

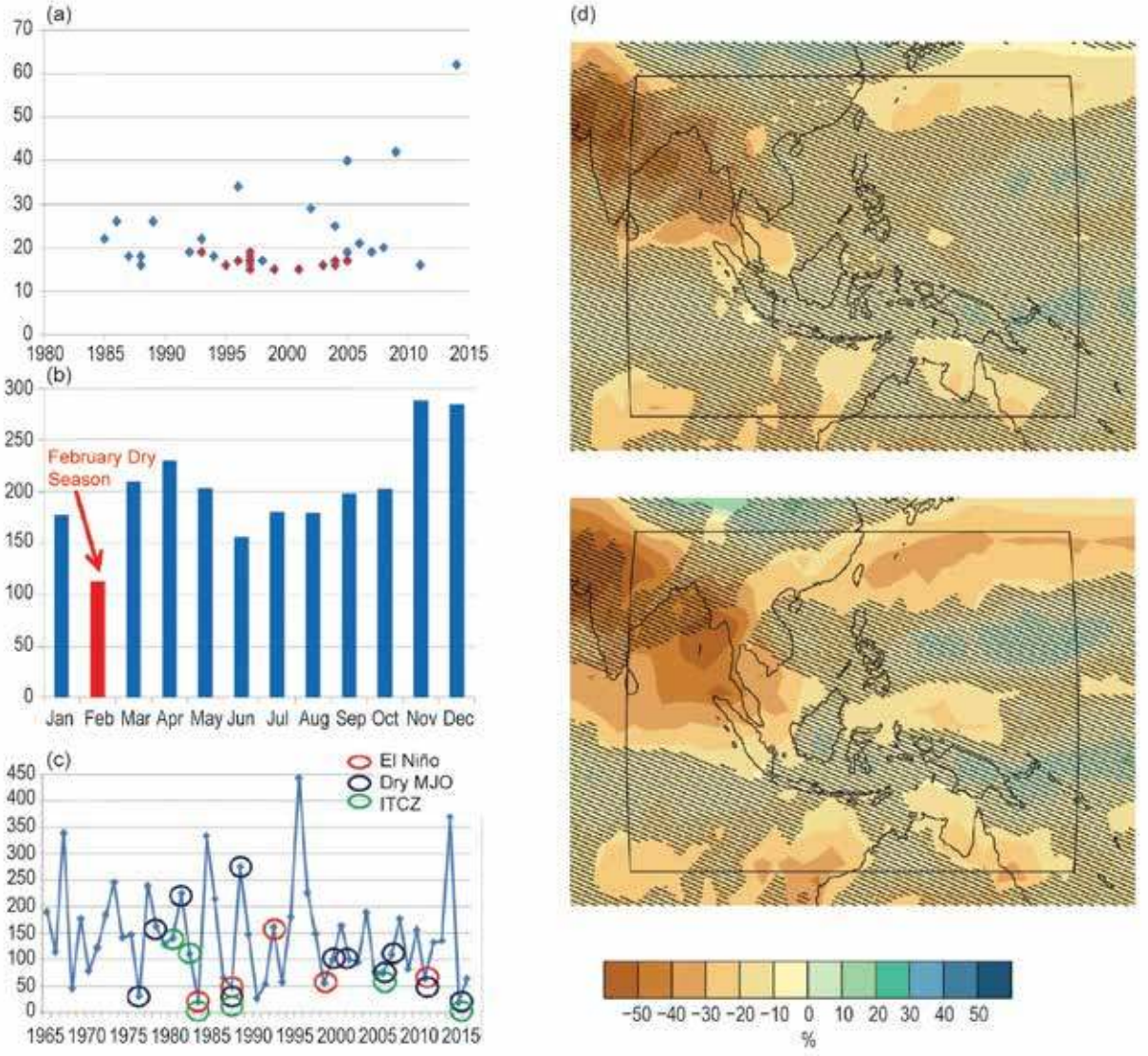

Fig. 25.1. (a) The length of dry spells at the Singapore climate station since being established in its current location in Jan 1984. A dry spell is defined as more than 15 consecutive days with less than 1 mm of rainfall. Blue diamonds are dry spells during the Northeast monsoon months of Dec to Mar. Red are the remaining calendar months. (b) Singapore climatology showing monthly median rainfall (mm) for a network of 28 stations operational since 1980, and highlighting the climatological Feb dry season. (c) Feb rainfall (mm) averaged over an 8 station network since 1965. Red circles denote El Niño conditions. Black circles denote years with greater than 50% time in MJO dry phase (6–8), according to the phase space of Wheeler and Hendon (2004) (available since 1974 at www.bom.gov.au/climate/mjo/). Green circles denote years when the Feb mean location of Northern edge of ITCZ is south of equator. The wet and dry phases of the MJO in terms of influence on Singapore are based on the study by Xavier et al. (2014). (d) IPCC projections of the percentage change in 25th percentile of Feb rainfall over southeast Asia for the midcentury (2041–2060, upper panel) and end of the century (2081–2100, lower panel) as compared to the historical period (1986–2005), for the full CMIP5 ensemble corresponding to the RCP8.5 global warming scenario. The shading shows the percentage change, and the hatching represents areas where the magnitude of the change of the 20-year mean is less than 1 standard deviation of model-estimated present-day natural variability of 20-year means. (Figure produced using online Climate Explorer of the Netherlands Meteorological Service KNMI).

scenarios (e.g., RCP4.5, not shown), it means the model estimates of natural (multidecadal) variability exceed any expected signal at least for the immediate future. This, combined with the time series analysis in the preceding paragraphs, leads to the conclusion that the 2014 dry spell is not an extreme event that can be attributed to any monotonic change associated with anthropogenic warming.

Mechanisms associated with the dry spell. Structurally, the dry spell was characterized by very low moisture content in the lower to middle troposphere, above the planetary boundary layer. This is demonstrated in Fig. 25.2a, which shows time series of monthly specific humidity over Singapore for the 600-hPa level since 1979. As can be seen in the upper panel, February 2014 recorded the lowest value in the time series for any calendar month. The lower panel shows the specific humidity time series for a 10° × 10° latitude-longitude box centered on Singapore, demonstrating the spatial scale of drying.

A second structural characteristic is a narrowing of the ITCZ, which has its center south of the equator at that time of year. As seen in the right panel of Fig. 25.2b, a tongue of downward vertical motion extended from higher latitudes down to the equator and over Singapore. Measuring the northern edge of the ITCZ as the edge of the upward vertical motion at 500 hPa (and similarly for centroid and southern edge) on these cross sections, time series can be constructed as shown in Fig. 25.2c. The arrows on the figure depict the five driest and five wettest February

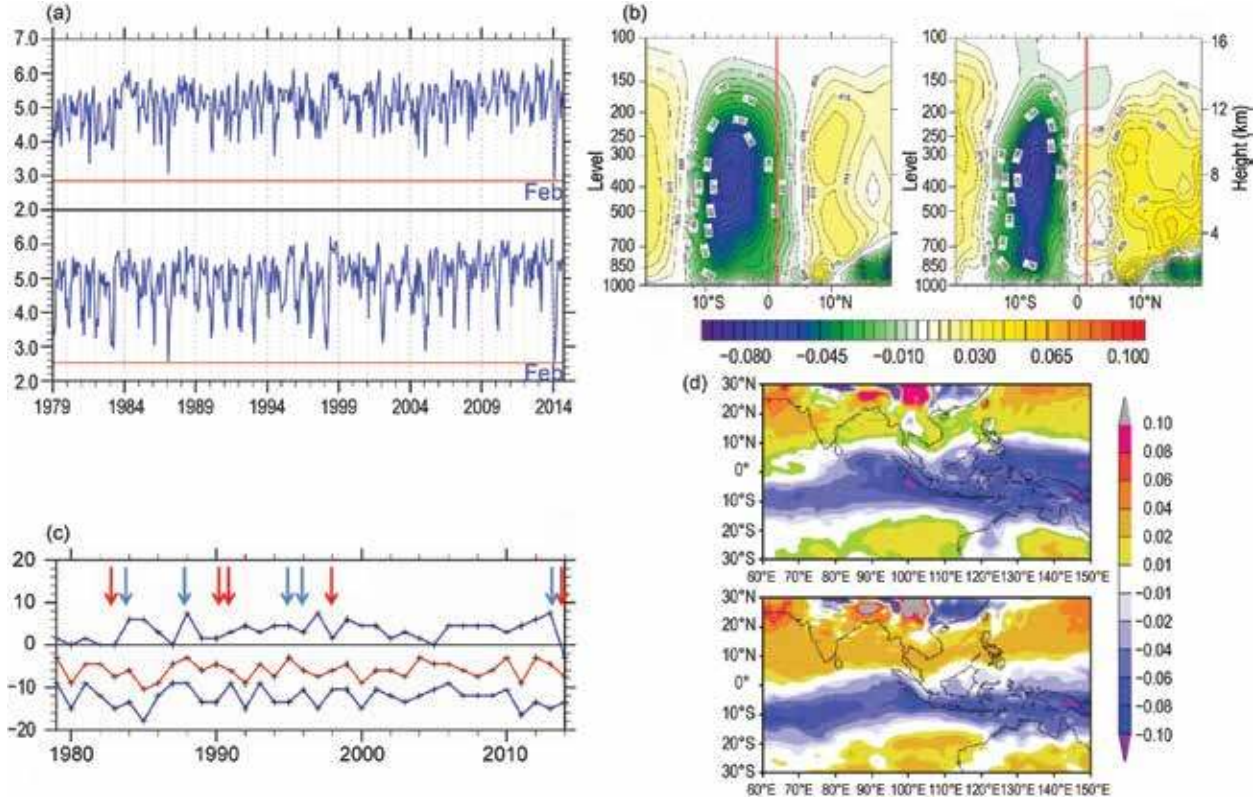

Fig. 25.2. (a) Time series of monthly specific humidity (g kg^{-1}) at 600 hPa from the ERA-Interim analyses (Dee et al. 2011). Upper for Singapore, lower for a 10° × 10° box over Singapore (4°18'S–6°18'N, 98°48'–108°48'E). The larger box demonstrates the large spatial scale of the dry spell. Note Feb 2014 (labelled) has the lowest value on record for any calendar month. (b) North South cross-sections along 105°E of vertical motion (omega, Pa sec^{-1}) averaged between 98°48'E to 108°48'E from ERA-Interim reanalyses, for mean Feb conditions (left) and for Feb 2014 (right). The latitude of Singapore is marked by the vertical red line. The blue upward motion is the location of the ITCZ, climatologically south of Singapore in Feb. (c) Time series of the latitude of the northern edge, maximum value, and southern edge of upward vertical motion at 500 hPa, averaged between 98°48'E and 108°48'E, averaged over the month of Feb, from ERA-Interim analyses. Blue and red arrows respectively denote the years making up the wet and dry composites in part (d) of this figure. (d) Composite analyses from ERA-Interim of the 500-hPa vertical motion (Pa sec^{-1}) averaged over the five wettest Februaries and five driest Februaries since 1979, as defined by average rainfall over the 28-station Singapore network.

rainfall totals in the series. Visually, it can be seen that dry years correspond to a southward contraction of the northern edge of the ITCZ, and that February 2014 is the extreme value in the time series of ITCZ northern edge.

The role of ITCZ contraction in the mechanism for the dry spell is further illustrated in Fig. 25.2d which shows composites of 500-hPa vertical motion for the five wettest and five driest Februaries since 1980. The ITCZ in these figures is represented by the east–west extending band of upward vertical motion (blue shading). The difference in ITCZ width between the two composites is remarkable, with the drier years (lower panel) having a much narrower ITCZ, particularly over the maritime continent, or the central and eastern part of the domain.

The Madden–Julian oscillation (MJO) also played a role in the 2014 January–March dry spell. This can be seen in Fig. 25.1c, where the black circles on the rainfall series are years where the dry phases of the MJO are present for more than 50% of the month. The coincidence of the dry MJO phase with dry Februaries is high, but there are a number of dry-MJO-phase years that experience normal rainfall. Also, the percentage of dry-phase days in 2014 was not an extreme value. Thus, we conclude that while playing a major influence, the MJO event was not the main causal factor bringing about the extreme low rainfall event.

A further factor contributing to low rainfall events in February is the presence of an El Niño event. As represented by the red circles on Fig. 25.1c, El Niño events coincided with a number of the extreme dry years. However, El Niño conditions were not present in January– March 2014. The green circles on Fig. 25.1c show the years where the northern edge of the ITCZ at Singapore longitudes is at the equator or southward, that is, the years of ITCZ contraction.

Discussion. A February dry spell is a seasonal occurrence over Singapore, coinciding with the furthest Southward location of the ITCZ. The 2014 event was characterized by a two-month-long record dry period, associated with a contraction of the ITCZ in its position south of the equator, and a suppressed phase (phases 6–8) of the MJO. The southward contraction of the ITCZ is the extreme value in the recent time series. The mechanism causing the narrowing of the ITCZ is not known. Also, to the authors' knowledge the relationship between the MJO and the width of the ITCZ has not been explored in the literature. Another aspect that is not well understood is the mechanism for the extreme drying, which brought about the lowest value of 600-hPa specific humidity in the past 35 years (Fig. 25.2a). These questions are being investigated in follow-up research.

As discussed in Section 2, the event was of local concern, as it is consistent with climate change projections of a greater intensity to droughts. As discussed, there is no evidence uncovered here that the event is outside the range of natural variability. Still, the fact that it was associated with a displacement of the ITCZ does raise the issue of the vulnerability of the deep tropics to ITCZ displacements. There is some literature on this in the context of paleoclimate (for example Chiang 2009; Stager et al. 2011) and in the context of West African droughts in current climate (Nicholson 2008). The possibility of shifts in ITCZ location in the context of climate change is an active area of research (see for example Kang et al. 2008; Chiang and Friedman 2012; Frierson and Hwang 2012); though the emphasis in these studies is on the zonally averaged ITCZ rather than any longitudinally localized component. As follow-on work, this will be investigated in both data studies and climate model runs in the context of the maritime continent.

ACKNOWLEDGMENTS. The authors acknowledge the valuable discussions with Dr. Chris Gordon Director of the Centre for Climate Change Singapore and with the weather forecast staff of the Meteorological Service Singapore. We also thank the BAMS referees and Jim Kossin (NOAA) for helpful comments that improved the manuscript.

REFERENCES

Chiang, J. C. H., 2009: The tropics in paleoclimate. *Ann. Rev. Earth Planet. Sci*., **37**, 263–297.

——, and A. R. Friedman, 2012: Extratropical cooling, interhemispheric thermal gradients, and tropical climate change. *Ann. Rev. Earth Planet. Sci*., **40**, 383–412, doi:10.1146/annurev-earth-042711-105545.

Dee, D. P., and Coauthors, 2011: The ERA-Interim reanalysis: Configuration and performance of the data assimilation system. *Quart. J. Roy. Meteor. Soc*., **137**, 553–597, doi:10.1002/qj.828.

Frierson, D. M. W., and Y.-T. Hwang, 2012: Extratropical influence on ITCZ shifts in slab ocean simulations of global warming. *J. Climate*, **25**, 720–733, doi:10.1175/JCLI-D-11-00116.1.

Kang, S. M, I. M. Held, D. M. W. Frierson, and M. Zhao, 2008: The response of the ITCZ to extratropical thermal forcing: Idealized slab-ocean experiments with a GCM. *J. Climate*, **21**, 3521–3532.

Nicholson, S. E., 2008: The intensity, location and structure of the tropical rainbelt over west Africa as factors in interannual variability. *Int. J. Climatol.*, **28**, 1775–1785.

Stager, J. C., D. B. Ryves, B. M. Chase, and F. S. R. Pausata, 2011: Catastrophic drought in the Afro-Asian monsoon region during Heinrich Event 1. *Science*, **331**, 1299–1302, doi:10.1126/science.1198322.

Stocker, T. F., and Coauthors, 2013: *Climate Change 2013: The Physical Science Basis.* Cambridge University Press, 1535 pp. [Available online at www.climatechange2013.org/images/report/WG1AR5_ALL_FINAL.pdf.]

Wheeler, M. C., and H. H. Hendon, 2004: An all-season real-time multivariate MJO index: Development of an index for monitoring and prediction. *Mon. Wea. Rev.*, **132**, 1917–1932.

Xavier, P., R. Rahmat, W. K. Cheong, and E. Wallace, 2014: Influence of Madden-Julian Oscillation on Southeast Asia rainfall extremes: Observations and predictability. *Geophys. Res. Lett.*, **41**, 4406–4412, doi:10.1002/2014GL060241.

26. TRENDS IN HIGH-DAILY PRECIPITATION EVENTS IN JAKARTA AND THE FLOODING OF JANUARY 2014

Siswanto, Geert Jan van Oldenborgh, Gerard van der Schrier, Geert Lenderink, and Bart van den Hurk

The January 2014 floods paralyzed nearly all of Jakarta, Indonesia. The precipitation events that lead to these floods were not very unusual but show positive trends in the observed record.

Introduction. In the period 10–20 January 2014, Jakarta and surrounding areas experienced heavy rains causing river overflows and flooding. Thousands of buildings were flooded and much infrastructure was damaged. The Provincial Agency for Disaster Management (BPBD) DKI Jakarta reported that losses reached up to 384 million U.S. dollars (http://koran-jakarta.com/?4767) with 26 reported deaths. Jakarta is regularly affected by flooding during the wet season, but the number of casualties in 2014 was among the highest since 2003, with only 2007 and 2013 more severe in this aspect.

On 11 January 2014 the Indonesian meteorological services (BMKG) recorded heavy precipitation (50 mm day^{-1}) in the larger Jakarta area. The day after, extreme rainfall (100 mm day^{-1}) was observed in the southern part of the city (see Supplemental Table S26.1). These high rainfall amounts were also observed in the TRMM satellite precipitation (Fig. 26.1a). The initial flood on 12 January was associated with heavy storms on 11–12 January over the Ciliwung catchment south of Jakarta and southern Jakarta (Fig. 26.1a and inset), with accumulated precipitation as much as 200 mm. A second flood episode was generated by severe storms on 17–18 January, when most of the precipitation fell in central to northern Jakarta.

The synoptic analyses (wind and relative humidity anomalies at 850 hPa) from the NCEP/NCAR Reanalysis-1 shows an intensified monsoon with the northerly component penetrating more to the south than usual, especially over the South China Sea (Figs. 26.1b,c). The Borneo vortex (Tangang et al. 2008; Trilaksono et al. 2012; Koseki et al. 2014), clearly visible in the 11–14 January wind field of Fig. 26.1b (white arrows), strengthened the cross-equatorial flow and transferred wet and humid air evaporated from the sea to the Sumatera and Java islands where it converged as indicated by the updraft velocity in these areas. The course of events is similar to the case of 2 February 2007 (Trilaksono et al. 2011), which was one of the most extensive floodings in Jakarta. The high humidity values in those areas, up to 15% more than the long-term average, fueled strong activity from convective showers. The event of 17–18 January 2014 was also associated with a stronger than usual northerly monsoon and cross-equatorial flow (Fig. 26.1c). Although the relative humidity and updraft velocity were weaker than the 11–14 January episode, accumulated precipitation was higher at some stations in this second episode of flooding. Figure 26.1d shows that the January 2014 precipitation at Jakarta Obs. reached 699 mm, and ranks fifth since 1900, slightly below the January 1965 value. January 2014 ranks 11th when monthly precipitation from all months is considered.

Figure 26.2a shows a time series of major floodings in Jakarta, for the early period derived subjectively from newspaper articles. Major floodings are defined as extensive inundation of structures and roads or where casualties or significant evacuations of people and/or necessity of transferring property to higher elevations are reported. Recently, major floods were recorded in 2013, 2014, and 2015 after events of extreme precipitation. The swampy plain on which Jakarta is built is a delta of 13 rivers. Rapid urban development of Jakarta makes the area increasingly vulnerable to flooding. About 40% of this area is sinking at rates of 3–10 cm yr^{-1} due to excessive groundwater extraction (Abidin et al. 2011, 2015). A cumulative land subsidence of −4.1 m has been observed over the period 1974–2010 in the northern Jakarta area (Deltares

AFFILIATIONS: Siswanto—Agency for Meteorology, Climatology, and Geophysics (BMKG), Republic of Indonesia, and Royal Netherlands Meteorological Institute (KNMI), Netherlands; van Oldenborth, van der Schrier, Lenderink, and van den Hurk—Royal Netherlands Meteorological Institute (KNMI), Netherlands

DOI:10.1175/BAMS-D-15-00128.1

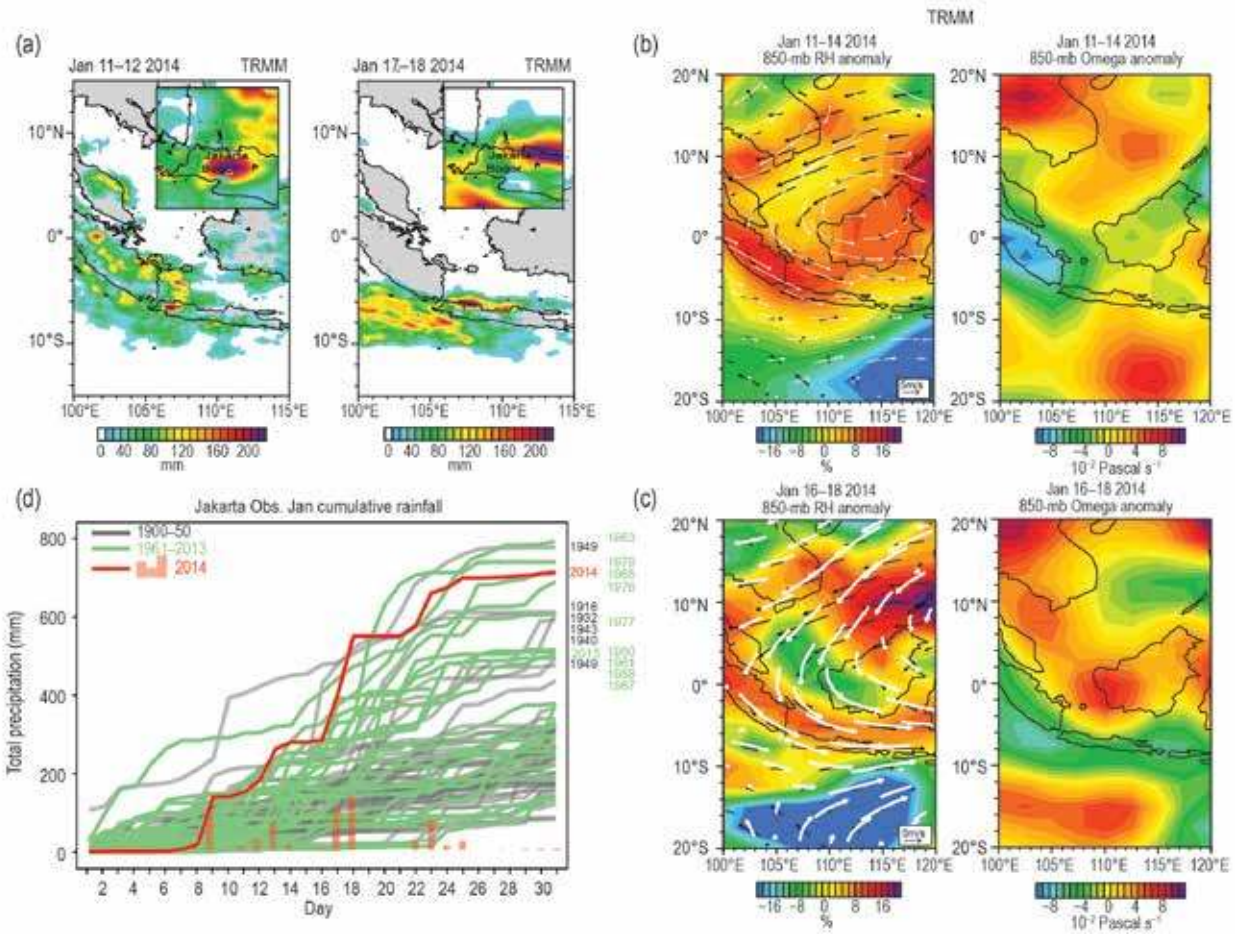

Fig. 26.1. (a) TRMM 3B42 accumulated rainfall for the two heavy rainfall events on 11–12 and 17–18 Jan 2014. (b) 11–14 Jan 2014 composite anomaly of 4-days consecutive (left) 850-hPa wind and relative humidity (%) and (right) omega (10^{-2} Pa s^{-1}) relative to Jan 1981–2010 climatology (shaded). The white (black) vectors denote the 11–14 Jan 2014 composite (climatology) of the wind field (m s^{-1} with reference vector). Negative values of omega indicate convective processes. (c) As in (b), but for 16–18 Jan 2014. (d) The Jakarta Obs. cumulative rainfall for Jan in 2014 (red line) in comparison to historical Jan between 1900–50 (gray lines) and 1961–2012 (green lines). Red bars indicate the daily amount of rainfall in 2014.

2011). There is growing concern that the apparent clustering of major flooding in recent years may not be exclusively related to the location of Jakarta in a slowly sinking delta and other hydrological factors, but that climate change may contribute as well (Firman et al. 2011; Ward et al. 2011, 2014). The aim of this paper is to assess whether the 2014 event became more likely due to trends in extreme precipitation.

Data. A subjective list of 31 major flood occurrences in Jakarta in the period 1900–2015 has been compiled using newspaper sources for 1900–1980 (www.merdeka.com; http://green.kompasiana.com) and since 1981 the official classification of BPBD DKI Jakarta. This is not used to study the trend but only the association of floods with extreme precipitation. We use the long hourly observed precipitation series measured at Jakarta Observatory (hereafter Obs.) from the Digitisasi Data Historis (DiDaH) project (www.didah.org), aggregated to the daily level (Siswanto et al. 2015, manuscript submitted to *Int. J. Climatol.*; Können et al. 1998). We use the data starting at 1900 because of evidence of a discontinuity before that (Siswanto et al. 2015, manuscript submitted to *Int. J. Climatol.*). Precipitation analyses from surrounding stations over the period 1971–2014 were retrieved from the Southeast Asian Climate Assessment & Dataset (SACA&D; http://sacad.database.bmkg.go.id/).

Return Times and Trends. Flooding in Jakarta usually occurs in December to February (DJF) at the peak of the wet season. Analysis of major flood events between 1900 and 2015 as in Fig. 26.2a revealed that 15 of 24 major flooding events for which precipita-

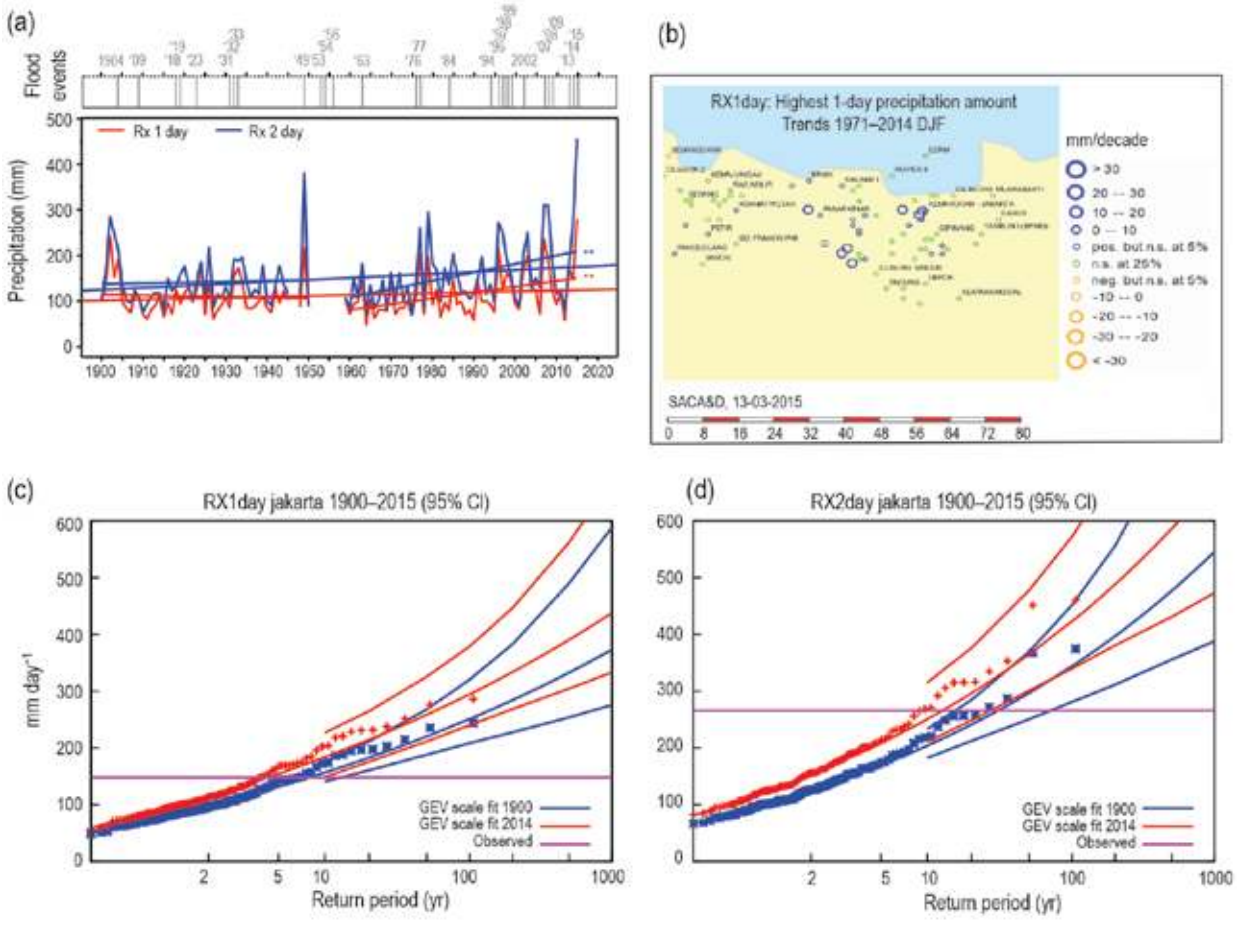

Fig. 26.2. (a, top) Observed major flood events in Jakarta during 1900–2015. The historic data from 1900–80 is gathered from national newspapers; more recent data is recorded by the BPBD DKI Jakarta. (a, bottom) Time series of RX1day (red) and RX2day (blue) including trend assessments for the whole period 1900–2015 and for the last 54 years. Symbols (**) and (*) indicate the significance level for $p < 0.01$ and $p < 0.05$, respectively. (b) The trend map of the DJF highest precipitation amount, RX1day (mm decade^{-1}) for 1971–2014 in the Greater Jakarta and Banten area as retrieved from the SACA&D system. (c) Return period of Jakarta RX1day over 1900–2015. The generalized extreme value (GEV) position and scale parameters (μ, σ) vary together with the smoothed global mean temperature. Blue lines correspond to the fit parameters for the climate of 1900, red lines for 2014 with the 90% confidence interval estimated with a non-parametric bootstrap. The observations are also shown twice: once scaled down with the fitted trend to 1900, and once scaled up to 2014. The purple line represents the observed value of Jan 2014. (d) As in (c), but for RX2day.

tion data is available could be associated with the 24 highest single-day precipitation extremes (flash floods; ADPC 2010), while 11 events are related to the 24 highest 2-day extreme precipitation events (cf. Liu et al. 2015), two of which are not also high 1-day events. The association is weaker in the beginning of the century when the floods are not as well-defined. The 2014 and 2015 floods were associated with two and one 2-day events, respectively; the 2-day precipitation event of 2015 (with 485.5 mm) is the highest in the precipitation history since 1900. Therefore, here we also consider the trend in the 2-day annual maximum. Most of the major floodings relate to excessive precipitation in the Jakarta area itself, while some floods relate to heavy precipitation upstream of the catchment of Jakarta's rivers, which is not recorded in the time series of Fig. 26.2a.

The highest daily rainfall of 2014 (RX1day) is 148 mm day^{-1} and occurred on 17 January. Rainfall on this day ranks 20th of annual highest daily rainfall since 1900. In terms of the maximum 2-day accumulated rainfall (RX2day), 16–17 January 2014 is more exceptional. The 266 mm recorded is the eighth largest 2-day precipitation sum observed at the Jakarta Obs. station since 1900.

The heaviest 1% of all daily precipitation events from the centennial series of Jakarta Obs. shows a positive linear trend over 1866–2010. The number

of days with rainfall exceeding 50 mm day^{-1} and 100 mm day^{-1} has shown a statistically significant increase (Siswanto et al. 2015, manuscript submitted to *Int. J. Climatol.*). The trend is larger for the 1961–2010 period.

Figure 26.2a shows that the annual RX1day and RX2day have increased during the last 112 years. The increasing trend of RX2day is statistically significant at p-value <0.05 (one-sided, as we expect short time-scale extremes to increase in this area; O'Gorman 2012). The trend in annual RX1day and RX2day during the last 54 years shows significant increases with rates of 13 mm decade^{-1} and 18 mm decade^{-1} respectively ($p < 0.01$). Increasing trends of RX1day over 1971–2014 are consistent in the area around Jakarta (Fig. 26.2c).

To compute the return time in the current climate and address the question whether the probability of occurrence of the recent extreme events has increased over time, we fitted the annual RX1day and RX2day data to a GEV distribution with position and scale parameters μ, σ simultaneously varying with the global mean temperature (smoothed with a 5-year running mean to suppress ENSO variability) as a first approximation of possible effects of global warming using a maximum likelihood method (available at http://climexp.knmi.nl; see also Schaller et al. 2014). The dependence is fitted simultaneously. Confidence intervals were estimated using a non-parametric bootstrap. The GEV describes the 1- and 2-day annual maxima better than the normal distribution implied by a least-square fit, and using the smoothed global mean temperature as covariate instead of a linear trend acknowledges that global warming has not been linear over the period 1900–2015. Finally, scaling rather than shifting the distribution is more appropriate for extreme precipitation.

The fit is shown for the parameters in 2014 representing the current climate and in 1900 as the climate of historic times. The observations are also shown twice, scaled with the fitted trend to these years. Figure 26.2c shows that the return period based on modern climate has very likely decreased compared to an analysis based on climate data from the past. The return time of the observed highest daily precipitation (148 mm day^{-1}) associated with the 2014 flood event is found to be about 4 years presently (95% CI: 2–10 years). This would have been 5–13 years in 1900. The ratio of these return times is about 1.8, different from one at $p < 0.1$ (one-sided), in agreement with the linear trend analysis of Fig. 26.2a.

Similarly, for annual RX2day, the return period of 13 years for the 2014 event in the current climate (95% CI: 5–27 years) is shorter than the 30-year (16–70) return period based on data from the past climate (Fig. 26.2d). The ratio of about a factor 2.4 is significant at $p < 0.01$ (one–sided). To conclude, we find increases in both 1-day and 2-day precipitation sums in the historical record that are unlikely due to natural variability. Just like in the seasonal mean rainy season precipitation we do not find a connection between annual maxima Jakarta precipitation and December–February sea surface temperature, in particular with El Niño (van Oldenborgh 2003).

Conclusion. Daily precipitation amounts during the 2014 floods have not been very exceptional, with estimated return periods of roughly 4 to 13 years for the one-day and two-day accumulated precipitation sums respectively. Our analyses give evidence that yearly maximum rainfall amounts, as observed in the 2014 event, have become more likely, both for daily (roughly 1.8 times more likely, $p < 0.1$) and two-day (roughly 2.4 times more likely, $p < 0.05$) rainfall amounts over the last 115 years. It should be stressed that this concerns only the meteorological aspects of the flooding. Subsidence and other hydrological factors that also affect the flooding have not been included. However, the trends in the frequency of the annual maximum of 1- and 2-day precipitation, about a factor two over the last century, do increase the risk of flooding in Jakarta. We have not established whether global warming, the urban heat island, or other effects cause these extreme precipitation trends.

ACKNOWLEDGEMENTS. This study was supported by the Joint Cooperation Program between KNMI, BMKG, PusAir, and Deltares and by the FP7 EUCLEIA project under Grant # 607085.

REFERENCES

Abidin, H. Z., H. Andreas, I. Gumilar, Y. Fukuda, Y. E. Pohan, and T. Deguchi, 2011: Land subsidence of Jakarta (Indonesia) and its relation with urban development. *Nat. Hazards*, **5**, 1753–1771, doi:10.1007/s11069-011-9866-9.

——, ——, ——, and I. R. R. Wibowo, 2015: On correlation between urban development, land subsidence and flooding phenomena in Jakarta. *Proc. IAHS*, **370**, 15–20, doi:10.5194/piahs-370-15-2015.

ADPC, 2010: Safer cities 27: Flood preparedness initiatives of high-risk communities of Jakarta. Asian Disaster Preparedness Center, 8 pp. [Available online at www.adpc.net/igo/category/ID226/doc/2013-c28Jbn-ADPC-Safer_Cities_27.pdf.]

Deltares, 2011: Sinking cities: An integrated approach towards solutions. Deltares–Taskforce Subsidence, 12 pp. [Available online at www.deltares.nl/app/uploads/2015/01/Subsidence-Sinking-cities_Deltares.pdf.]

Firman, T., C. Izhar, I. Surbakti, and H. Simarmata, 2011: Potential climate change related vulnerabilities in Jakarta: Challenges and current status. *Habitat Int.*, **3**, 32–37, doi:10.1016/j.habitatint.2010.11.011.

Können, G. P., P. D. Jones, M. H. Kaltofen, and R. J. Allan, 1998: Pre-1866 extensions of the Southern Oscillation index using early Indonesian and Tahitian meteorological readings. *J. Climate*, **11**, 2325–2339.

Koseki, S., T.-Y. Koh, and C.-K. Teo, 2014: Borneo vortex and mesoscale convective rainfall. *Atmos. Chem. Phys.*, **14**, 4539–4562, doi:10.5194/acp-14-4539-2014.

Liu, J., C. D. Doan, S.-Y. Liong, R. Sanders, A. T. Dao, and T. Fewtrell, 2015: Regional frequency analysis of extreme rainfall events in Jakarta. *Nat. Hazards*, **75**, 1075–1104, doi:10.1007/s11069-014-1363-5.

O'Gorman, P. A., 2012: Sensitivity of tropical precipitation extremes to climate change. *Nat. Geosci.*, **5**, 697–700, doi:10.1038/ngeo1568.

Schaller, N., F. E. L. Otto, G. J. van Oldenborgh, N. R. Massey, S. Sparrow, and M. R. Allan, 2014: The heavy precipitation event of May–June 2013 in the upper Danube and Elbe basins [in "Explaining Extreme Events of 2014 from a Climate Perspective"]. *Bull. Amer. Meteor. Soc.*, **96** (9), S69–S72.

Tangang, F. T., L. Juneng, E. Salimun, P. N. Vinayachandran, Y. K. Seng, C. J. C. Reason, S. K. Behera, and T. Yasunari, 2008: On the roles of the northeast cold surge, the Borneo vortex, the Madden-Julian Oscillation, and the Indian Ocean dipole during the extreme 2006/2007 flood in southern Peninsular Malaysia. *Geophys. Res. Lett.*, **35**, L14S07, doi:10.1029/2008GL033429.

Trilaksono, N. J., S. Otsuka, S. Yoden, K. Saito, and S. Hayashi, 2011: Dependence of model simulated heavy rainfall on the horizontal resolution during the Jakarta flood event in January–February 2007. *SOLA*, **7**, 193–196, doi:10.2151/sola.2011-049.

——, ——, and ——, 2012: A time-lagged ensemble simulation on the modulation of precipitation over West Java in January–February 2007. *Mon. Wea. Rev.*, **140**, 601–616, doi:10.1175/MWR-D-11-00094.1.

van Oldenborgh, G. J., 2003: The influence of El Niño – Southern Oscillation on West Java. *Jakarta Kota Pantai*, **3**, 8–9. [Available online at http://climexp.knmi.nl/publications/westjava.pdf.]

Ward, P. J., M. A. Marfai, Poerbandono, and E. Aldrian, 2011: Climate adaptation in the City of Jakarta. *Climate Adaptation and Flood Risk in Coastal Cities*, J. Aerts et al., Eds., Earthscan, 285–304.

——, and Coauthors, 2014: Jakarta climate adaptation tools (JCAT). Delta Alliance No. 8; KvK Rep. KfC 139/2014, National Research Programme Knowledge for Climate (KvK), 137 pp. [Available online at www.delta-alliance.org/news/delta-alliance-news/10853039/Final-Report-Jakarta-Climate-Adaptation-Tools-JCAT.]

27. EXTREME RAINFALL IN EARLY JULY 2014 IN NORTHLAND, NEW ZEALAND—WAS THERE AN ANTHROPOGENIC INFLUENCE?

Suzanne Rosier, Sam Dean, Stephen Stuart, Trevor Carey-Smith, Mitchell T. Black, and Neil Massey

The risk of an extreme 5-day July rainfall event over Northland, New Zealand, such as was observed in early July 2014, has likely increased due to anthropogenic influence on climate.

Introduction. From 8 to 12 July 2014, Northland, New Zealand, suffered a deluge of rainfall that caused widespread severe flooding; the resulting damage is estimated to have cost NZD 18.8 million in insurance claims (ICNZ 2015). Low pressure to the northwest and high to the southeast resulted in strong northeasterly flows across the upper North Island. The subtropical origin of the air mass produced a conveyor belt of very moist air that fueled the extreme rainfall. High pressure over much of the rest of the country "parked" the low pressure system over Northland for about five days, allowing extremely high rainfall amounts to accumulate (Met Service NZ 2015). Kaikohe (central Northland) received 311% of normal rainfall in July—a record July rainfall total for this location (NIWA 2014). This study investigates whether, and to what degree, there was an anthropogenic influence on July rainfall amounts in Northland such as observed in 2014.

Data and methods. Rainfall observations for the period 1972–2014 were used from the Virtual Climate Station Network (VCSN), which takes measurements from 600 sites around New Zealand and creates a 5 km × 5 km data field using a thin-plate smoothing spline interpolation (Tait et al. 2006).

Extremely large ensembles of simulations of a regional climate model came from the "climate*prediction*.net" project (Allen 1999) running the "weather@home" experiment for the Australia/New Zealand (ANZ) region. This is an ANZ version of the modeling capability described by Massey et al. (2015). In this setup, the Met Office HadAM3P model (Pope et al. 2000) is run globally, providing lateral boundary conditions to the regional model HadRM3P (Jones et al. 2004), which covers a domain spanning Australia, New Zealand, and much of Indonesia at approximately 50-km resolution.

For this study, two experiments were conducted creating very large initial condition ensembles to represent many different realizations of possible weather. The first is of the year 2014 with all forcings included (ALL)—sea surface temperature (SST) from the "Operational Sea Surface Temperature and Sea Ice Analysis", greenhouse gases, aerosol, ozone, solar, and volcanic. A second "natural forcings only" (NAT) ensemble was produced, where the anthropogenic contribution to the 2014 forcings was removed. For the SSTs, patterns of changes were estimated using 10 different Coupled Model Intercomparison Project Phase 5 (CMIP5) models and a multimodel mean. This is the same configuration as described in Schaller et al. (2014) and Black et al. (2015).

How well does the "weather@home ANZ" model simulate this event? VCSN observations in Northland (defined as New Zealand land area north of 36.6°S) were spatially averaged, and 5-day totals were summed starting on consecutive days in July. The maximum of these values for each year is shown in Fig. 27.1a. The 2014 observation of 221 mm (the 5-day total beginning on 8 July 2014) was a very clear record in the time series.

To validate the model performance, the VCSN observations and model rainfall were area-averaged over Northland, and 5-day rainfall totals were calculated. The resulting July maximum values are

AFFILIATIONS: Rosier, Dean, Stuart, and Carey-Smith—National Institute of Water and Atmospheric Research, Wellington, New Zealand; Black—School of Earth Sciences, University of Melbourne, Melbourne, Victoria, Australia; Massey—Environmental Change Institute, University of Oxford, Oxford, United Kingdom

DOI:10.1175/BAMS-D-15-00105.1

A supplement to this article is available online (10.1175/BAMS-D-15-00105.2)

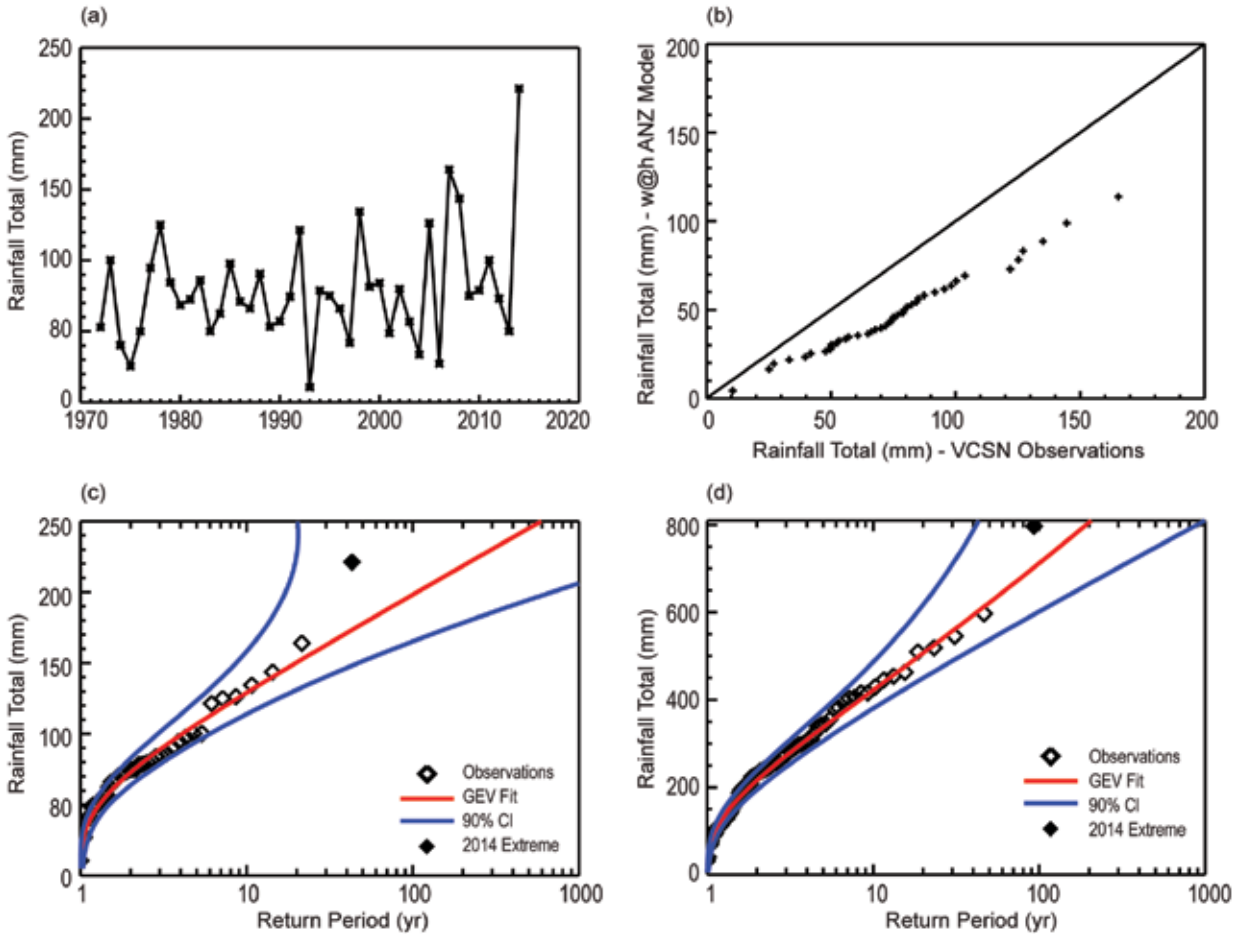

Fig. 27.1. (a) Jul maximum 5-day rainfall totals in Northland from the New Zealand VCSN observations on their 5 km × 5 km grid, plotted against time over the span of the dataset (1972–2014). (b) Quantile–quantile plot of Jul maximum 5-day rainfall total in Northland (crosses), comparing 2772 "weather@home" model ALL simulations (w@h ANZ 2014) against 43 years of VCSN observations. Each cross marks corresponding values of rainfall in the model ensemble and in the observations at the same percentile in the two (different sized) distributions. A perfect match between the model and observations would be indicated if the crosses lay on the line x = y (solid). (c) Black diamonds indicate the return periods of the 43 years of VCSN observations of Jul maximum 5-day rainfall totals in Northland shown in (a). The red line is the generalized extreme value (GEV) fit through these observations, and blue is the 90% confidence interval on this GEV fit. (d) As in (c), but for the Kaikohe station (central Northland) only, for which a longer time series of 93 years is available.

compared in the quantile–quantile plot in Fig. 27.1b. The model exhibits a persistent dry bias; at each percentile, the model is approximately two-thirds as wet as the observations. Similar behavior in the same model, but over Europe, has been noted by Otto et al. (2014), Sparrow et al. (2013), and Schaller et al. (2014). The ANZ model is capable of reproducing July maxima as wet as the 2014 observed extreme but only at a greatly increased return period (Fig. 27.2a). The model dry bias is also consistent with the findings of Ackerley et al. (2012), who used the same model over a smaller domain. Running it with varying boundary conditions, they found the same systematic bias over Northland and that this was removable by tuning a single precipitation parameter.

To assess the 2014 event against the historical record of 43 years, a generalized extreme value (GEV) distribution was fitted to the observations (Fig. 27.1c) following the methodology described in Ailliot et al. (2011). This estimates the 2014 extreme to be close to a 1-in-200-yr event, with 90% confidence of its being between about a 1-in-20-yr and 1-in-1000-yr event. This large uncertainty is narrowed when considering observations from the Kaikohe station only (Fig. 27.1d), for which a longer time series (93 years) is available. In this case, the 2014 event is still close to a 1-in-200-yr event in the GEV fit, but it is between

about a 1-in-40-yr and a 1-in-800-yr event at the 90% confidence interval (CI).

Was this event influenced by global climate change? Figure 27.2a shows rainfall totals from the ALL and NAT model ensembles. The horizontal lines span the 5th–95th percentiles of the distribution of return periods formed by applying a standard bootstrapping technique (random resampling with replacement) to each ensemble 1000 times. Results were robust to an exploration of bootstrapping the ensembles varying numbers of times.

On this measure, the curves are separable over much of the range from approximately the 1-in-20-yr to the 1-in-400-yr event, except around the 1-in-100-yr event (gray blocks in Fig. 27.2a). Over this range of return periods, a given precipitation threshold (amount) occurs more often in the anthropogenic case than under natural forcings only. The GEV estimate for the 2014 event (1-in-200-yr) is within this range, but the long-return period end of the GEV uncertainty range is in the tail of the distribution and thus is not well characterized. A larger ensemble is necessary to address these issues more reliably as it would be expected to characterize the whole distribution better, including the tails. An identical analysis using a larger ensemble available for the year 2013 (Fig. 27.2b) reveals separability of the curves over this whole range. We also repeated the 2014 analysis using more grid points (including ocean points) in the averaging area, and the curves showed consistently more separability over more of the range. Thus, our basic result appears robust, but it may become clearer once a larger ensemble is available for 2014.

We computed the fraction of attributable risk (FAR) proposed by Allen (2003) as FAR = 1 – (Pn / Pa), where Pn and Pa are the relative frequency of the event in the NAT and ALL distributions respectively. The FAR value denotes the fraction of the risk of the event that is attributable to anthropogenic climate change.

We effectively bias corrected the model data by choosing our event threshold to be the 1-in-200-yr event in the ALL ensemble (150 mm) rather than the observed event precipitation amount (221 mm). The corresponding return period in the NAT is then approximately 1-in-350-yr. The FAR at this threshold is 0.47, indicating that 47% of the risk of such an event is attributable to anthropogenic climate change. We estimated the uncertainty in this by computing FAR at all thresholds corresponding to the range of GEV estimates (90% CI) of the "true" return period of the event. The resulting distribution of FAR values ranged from approximately 0.1 to 0.8, with a peak at around 0.27. Hence, we find almost half of the risk of an event such as that of July 2014 to be attributable to anthropogenic influence but not over the full range of uncertainty around the event threshold.

Discussion. Our result is broadly consistent with observed trends (Alexander et al. 2006), theory (Hart-

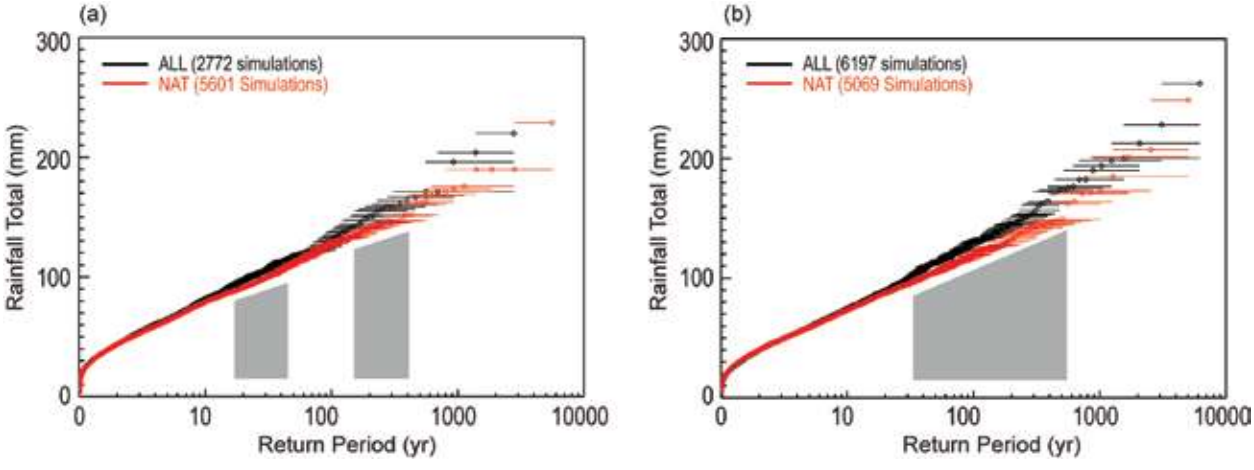

Fig. 27.2. (a) Jul maximum 5-day rainfall totals (mm) in Northland, New Zealand, from the "weather@home ANZ" model, plotted against corresponding return periods (log scale). Black diamonds show the 2772 ALL forcings simulations, and red diamonds the 5601 NAT (natural only) forcings simulations, both for 2014. The horizontal lines span the 5th–95th percentiles of the distribution of return periods computed after applying a standard bootstrapping technique (random resampling with replacement) to each distribution 1000 times. The gray blocks show approximately the range of return periods over which the curves separate on the 5th–95th percentile measure. (b) As in (a), but from runs of a very similar model setup for 2013 (instead of 2014), and having a much larger ALL ensemble (6197 simulations).

mann et al. 2013), other modeling studies (Carey-Smith et al. 2010), future projections (Sillman et al. 2013), and the attribution of extreme precipitation to anthropogenic influence for Northern Hemisphere land areas (Zhang et al. 2013). However, other studies analyzing different regions using a very similar model configuration do not find an anthropogenic influence on extreme precipitation changes, for example, Sparrow et al. (2013) and Schaller et al. (2014). This raises the question of why a stronger signal should be apparent here.

New Zealand's situation as a maritime landmass in the midlatitude westerlies means its precipitation is usually delivered via the eastward progression of low pressure systems and their interaction with orography (Sturman and Tapper 2006). There is some evidence that the most extreme events arise because of "atmospheric rivers" (Zhu and Newell 1998) of exceptionally moist air forced to make landfall in New Zealand. Dean et al. (2013) found that all the most extreme rainfall events in Golden Bay, New Zealand, were associated with very moist air of subtropical origin. Harrington et al. (2015, manuscript submitted to *Geophys. Res. Lett.*) have found that the most extreme precipitation events in Northland coincide almost exclusively with anomalously high moisture fluxes of subtropical origin, and much more so than midlatitude continental regions such as Europe. This suggests New Zealand's maritime position, with unimpeded access to the West Pacific warm pool, may make an anthropogenic signal in extreme rainfall more easily detectable. Further analysis of these ideas with the weather@home model is ongoing and requires the model to be capable of adequately reproducing observed features of the event (see online supplemental material).

Conclusions. Results from very large ensembles of regional model simulations show evidence of increased July maximum 5-day precipitation in Northland, New Zealand, in the anthropogenic world for events with return periods longer than about 1-in-20-yr. An event as extreme as that of July 2014 is estimated to change from approximately 1-in-350-yr in the "natural" world to 1-in-200-yr with anthropogenic influences, with a corresponding FAR of 47%. The results do not, however, exhibit a statistically significant change consistently over the entire range of the estimated uncertainty (90% CI) in the return period of the extreme event; thus, we suggest medium confidence in the exact degree to which anthropogenic factors increased the risk of events such as this one. Results from a larger ensemble (but for 2013) show a significant anthropogenic influence consistently across the full range of event return period uncertainty, suggesting that additional ensemble members might strengthen these conclusions.

ACKNOWLEDGEMENTS. Weather@home ANZ is a collaboration among the University of Oxford, the U.K. Met Office, the ARC Centre of Excellence for Climate System Science (Australia), NIWA (New Zealand), the University of Melbourne, the University of Tasmania and the Tasmanian Partnership for Advanced Computing. We gratefully acknowledge assistance from Oxford eResearch Centre, the New Zealand eScience Infrastructure (NeSI) and Ministry of Business, Innovation and Employment, and the climate*prediction*.net volunteers for their generous donation of computing resources.

REFERENCES

Ackerley, D., S. Dean, A. Sood, and A. B. Mullan, 2012: Regional climate modelling in New Zealand: Comparison to gridded and satellite observations. *Wea. Climate*, **32** (1), 3–22.

Ailliot, P., C. Thompson, and P. Thomson, 2011: Mixed methods for fitting the GEV distribution. *Water Resour. Res.*, **47**, W05551, doi:10.1029/2010WR009417.

Alexander, L. V., and Coauthors, 2006: Global observed changes in daily climate extremes of temperature and precipitation. *J. Geophys. Res.*, **111**, D05109, doi:10.1029/2005JD006290.

Allen, M. R., 1999: Do-it-yourself climate prediction. *Nature*, **401**, 642.

——, 2003: Liability for climate change. *Nature*, **421**, 891–892.

Black, M. T., D. J. Karoly, and A. D. King, 2015: The contribution of anthropogenic forcing to the Adelaide and Melbourne, Australia, heatwaves of January 2014 [in "Explaining Extreme Events of 2014 From a Climate Perspective"]. *Bull. Amer. Meteor. Soc.*, **96** (12), S145-S148, doi:10.1011/BAMS-D-15.00098.1.

Carey-Smith, T., S. Dean, J. Vial, and C. Thompson, 2010: Changes in precipitation extremes for New Zealand: Climate model predictions. *Wea. Climate*, **30**, 23–48.

Dean, S. M., S .M. Rosier, T. Carey-Smith, and P. A. Stott, 2013: The role of climate change in the two-day extreme rainfall in Golden Bay, New Zealand, December 2011 [in "Explaining Extreme Events of 2012 from a Climate Perspective"]. *Bull. Amer. Meteor. Soc.*, **94** (9), S61–S63.

Hartmann, D. L., and Coauthors, 2013: Observations: Atmosphere and surface, Supplementary material. *Climate Change 2013: The Physical Science Basis*, T. F. Stocker et al., Eds., Cambridge University Press, 30 pp. [Available online at www.climatechange2013.org/images/report/WG1AR5_Ch02SM_FINAL.pdf.]

ICNZ, 2015: Cost of disaster events in New Zealand. Insurance Council of New Zealand. [Available online at www.icnz.org.nz/statistics-data/cost-of-disaster-events-in-new-zealand/.]

Jones, R. G., M. Noguer, D. C. Hassell, D. Hudson, S. Wilson, G. J. Jenkins, and J. F. B. Mitchell, 2004: Generating high resolution climate change scenarios using PRECIS. Met Office Hadley Centre, 40 pp. [Available online at http://precis.metoffice.com/docs/PRECIS_Handbook.pdf.]

Massey, N., and Coauthors, 2015: weather@home—development and validation of a very large ensemble modelling system for probabilistic event attribution. *Quart. J. Roy. Meteor. Soc.*, **141**, 1528–1545, doi:10.1002/qj.2455.

Met Service NZ, 2015: The Northland floods of July 2014. Meteorological Service of New Zealand Ltd. [Available online at http://blog.metservice.com/2014/07/the-northland-floods-of-july-2014/].

NIWA, 2014: Monthly climate summary: July 2014. NIWA National Climate Centre. [Available online at www.niwa.co.nz/climate-summary-for-july-2014].

Otto, F. E. L., S. M. Rosier, M. R. Allen, N. R. Massey, C. J. Rye, and J. Imbers Quintana, 2014: Attribution analysis of high precipitation events in summer in England and Wales over the last decade. *Climatic Change*, doi:10.1007/s10584-014-1095-2, Open access.

Pope, V., M. Gallani, P. Rowntree, and R. Stratton, 2000: The impact of new physical parameterizations in the Hadley Centre climate model: HadAM3. *Climate Dyn.*, **16**, 123–146.

Schaller, N., F. E. L. Otto, G. J. van Oldenborgh, N. R. Massey, S. Sparrow, and M. R. Allen, 2014: The heavy precipitation event of May-June 2013 in the Upper Danube and Elbe basins [in "Explaining Extreme Events of 2013 from a Climate Perspective"]. *Bull. Amer. Meteor. Soc.*, **95** (9), S69–S72.

Sillman, J., V. V. Kharin, F. W. Zwiers, X. Zhang, and D. Bronaugh, 2013: Climate extremes indices in the CMIP5 multimodel ensemble: Part 2. Future climate projections. *J. Geophys. Res. Atmos.*, **118**, 2473–2493, doi:10.1002/jgrd.50188.

Sparrow, S., C. Huntingford, N. Massey, and M. R. Allen, 2013: The use of a very large atmospheric model ensemble to assess potential anthropogenic influence on the U.K. summer 2012 high rainfall totals [in "Explaining Extreme Events of 2012 from a Climate Perspective"]. *Bull. Amer. Meteor. Soc.*, **94** (9), S36–S38.

Sturman, A., and N. J. Tapper, 2006: *The Weather and Climate of Australia and New Zealand*. Oxford University Press, 541 pp.

Tait, A., R. Henderson, R. Turner, and X. G. Zheng, 2006: Thin plate smoothing spline interpolation of daily rainfall for New Zealand using a climatological rainfall scheme. *Int. J. Climatol.*, **26**, 2097–2115, doi:10.1002/joc.1350.

Zhang, X., H. Wan, F. W. Zwiers, G. C. Hegerl, and S.-K. Min, 2013: Attributing intensification of precipitation extremes to human influence. *Geophys. Res. Lett.*, **40**, 5252–5257, doi:10.1002/grl.51010.

Zhu, Y., and R. E. Newell, 1998: A proposed algorithm for moisture fluxes from atmospheric rivers. *Mon. Wea. Rev.*, **126**, 725–735, doi:10.1175/1520-0493.

28. INCREASED LIKELIHOOD OF BRISBANE, AUSTRALIA, G20 HEAT EVENT DUE TO ANTHROPOGENIC CLIMATE CHANGE

Andrew D. King, Mitchell T. Black, David J. Karoly, and Markus G. Donat

Climate model simulations for 2014 indicate anthropogenic climate change very likely increased the likelihood of hot and very hot November days in Brisbane by at least 25% and 44% respectively.

Introduction. In mid-November 2014, politicians representing the largest economies in the world gathered for the G20 summit in Brisbane, Australia, a major city on the east coast. Combatting climate change was low on the agenda, but in a speech at the University of Queensland on 14 November, U.S. President Barack Obama spoke of the dangers climate change posed to Pacific nations, Australia, and the wider world. During the G20 summit, there was unseasonably hot weather in Brisbane and southeast Queensland generally as part of Australia's hottest spring on record. The daytime maximum temperatures were well-above average from 14 to 16 November with Saturday (15th) and Sunday (16th) being the main days of the summit. The temperatures on 15 November surpassed 34°C and on the 16th reached close to 39°C. While these were not record hot temperatures they were well-above normal for late spring (the average being approximately 27°C for November in 1911–40) and attracted media attention due to the summit. The aim of this study was to address the question of whether human-induced climate change has increased the odds of abnormally hot November days in Brisbane occurring. Previous attribution studies of heat events in Australia have investigated hot spells on larger spatial and temporal scales (e.g., Perkins et al. 2014; King et al. 2014; Lewis and Karoly 2014). In this study, individual hot days at a local scale are studied.

Data and Methods. The Australian Water Availability Project (AWAP; Jones et al. 2009) dataset of daily maximum temperatures (1911 onwards) was used to investigate the high daytime temperatures in Brisbane in the context of the observational record. The AWAP dataset is a gridded product of temperature and precipitation observations on a 0.05° grid which is more reliable in areas of dense observations (King et al. 2013), such as near Brisbane. The data were regridded onto a 0.5° resolution and the timeseries of November daily maxima for the gridbox over Brisbane was extracted.

Thousands of simulations using the "weather@home" model setup (Massey et al. 2015) over the Australia–New Zealand (ANZ) domain were analyzed to estimate whether a significant change in the likelihood of hot days in November had occurred due to anthropogenic climate change. For extended details of the model setup see Black et al. (2015); a brief description in the context of this study is given here. The weather@home ANZ model is a regional atmosphere-only model (HadRM3P; used in regional climate modelling as described by Jones et al. 2004), at 0.44° resolution, embedded within a coarser global model (HadAM3P; Pope et al. 2000). The model is run tens of thousands of times for a given year, in this case 2014, using volunteers' spare computer time to give a very large ensemble of simulations. Atmospheric simulations representing the climate as it was in 2014 were run with specified observed sea surface temperatures, greenhouse gas concentrations, and aerosols. These were compared with "natural" simulations that were forced with pre-industrial greenhouse gas concentrations and ozone as well as estimates of the natural sea surface temperature (SST) fields derived

AFFILIATIONS: King, Black, and Karoly—ARC Centre of Excellence for Climate System Science, School of Earth Sciences, University of Melbourne, Melbourne, Victoria, Australia; Donat—ARC Centre of Excellence for Climate System Science, Climate Change Research Centre, University of New South Wales, Sydney, New South Wales, Australia

DOI:10.1175/BAMS-D-15-00098.1

A supplement to this article is available online (10.1175/BAMS-D-15-00098.1)

from the historical simulations of ten CMIP5 models (Taylor et al. 2012; see Table S1 of Black et al. 2015 for full list). The use of ten different estimates for the SSTs in the natural case allows for a more comprehensive analysis of uncertainties. In total there were 2787 complete all-forcings simulations of November and 5105 simulations for the natural November case extracted and analysed. The use of such a large ensemble means that robust estimates of the distributions of November daily maxima in Brisbane can be made.

The November daily maximum temperatures from the natural and all forcings ensembles of weather@home simulations were extracted for the land gridbox over Brisbane. The natural forcings ensemble was compared with the AWAP data for the 1911–40 period (Fig. 28.1) when we assume that the anthropogenic influence on Australian temperatures was negligible (Karoly and Braganza 2005). The 1911–40 period is the earliest 30-year period in AWAP, so is most suitable for comparison with the natural simulations. The weather@home data were bias-adjusted by the difference in the means of the natural ensemble and the 1911–40 AWAP data. If this bias adjustment is not performed there is a negligible difference to the final attribution statement.

The fractional attributable risk (FAR; Allen 2003) was then calculated comparing the frequency of hot days above 34°C (like Saturday, 15 November) and very hot days above 38°C (like Sunday, 16 November) in the natural and all forcings maximum temperature data. In the 1911–40 AWAP data, November maxima above 34°C occur 14 times (i.e., a return period of one day in just over two years) and there is only a single November maximum temperature above 38°C.

To account for structural uncertainties (i.e., uncertainties related to model set-up) in our attribution statement, the FAR calculations were performed separately using each natural forcing subensemble where SSTs were derived from ten global climate models (GCMs) to provide ten "best estimate" FAR values. The sampling uncertainty was also accounted for by bootstrapping 50% subsets of each natural subensemble (sampling all 30 November days from a given simulation if it is included) using each of the 10 SST estimates derived from each GCM and calculating 10 000 FAR estimates with all forcings subsets of the same size. These uncertainties were then used to make conservative (10th percentile) estimates of the roles of anthropogenic climate change in the hot and very hot November days in Brisbane during the G20 summit last year.

Results. The all forcings and natural weather@home simulations reproduce the longer warm tail seen in the observations (Fig. 28.1), although with slightly greater spread than in the observed distribution. A discussion of the causes of this difference is included in Supplemental Material. A small bias correction was applied to the weather@home simulations of 0.55°C. The mean of the all forcings simulations is slightly warmer (by 0.79°C) than the mean of the natural forcings simulations.

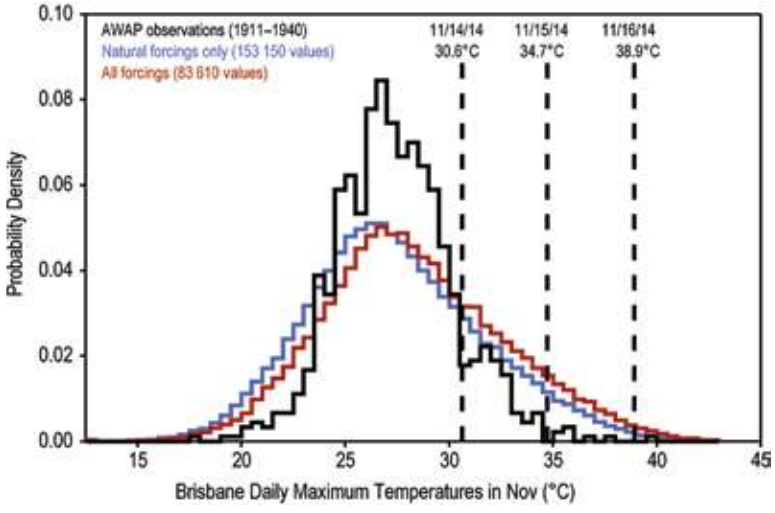

Fig. 28.1. Probability density distributions of Nov daily maximum temperatures for a gridbox over Brisbane in AWAP observations interpolated to 0.5° resolution for the 1911–40 period (black), and the weather@home model run for 2014 with natural forcings only (blue) and all forcings (red). The weather@home distributions have been bias corrected (cooled by 0.55°C). The dashed lines mark the daily maximum temperatures during the G20 period with the dates and temperatures shown.

The FAR values were calculated using the natural simulations forced by the 10 SST estimates separately for a 34°C and 38°C threshold (Fig. 28.2). Ten thousand estimates of the FAR were derived from 50% subsamples as described previously. For both the 34°C and 38°C thresholds, the vast majority of FAR estimates derived using each natural SST estimate are above zero (i.e., there is an increase in the likelihood of hot and very hot days in Brisbane in November associated with the anthropogenic influence on climate). The uncertainties in FAR values associated with the different natural SST estimates are of a broadly similar magnitude as the sampling uncertainties, especially when the

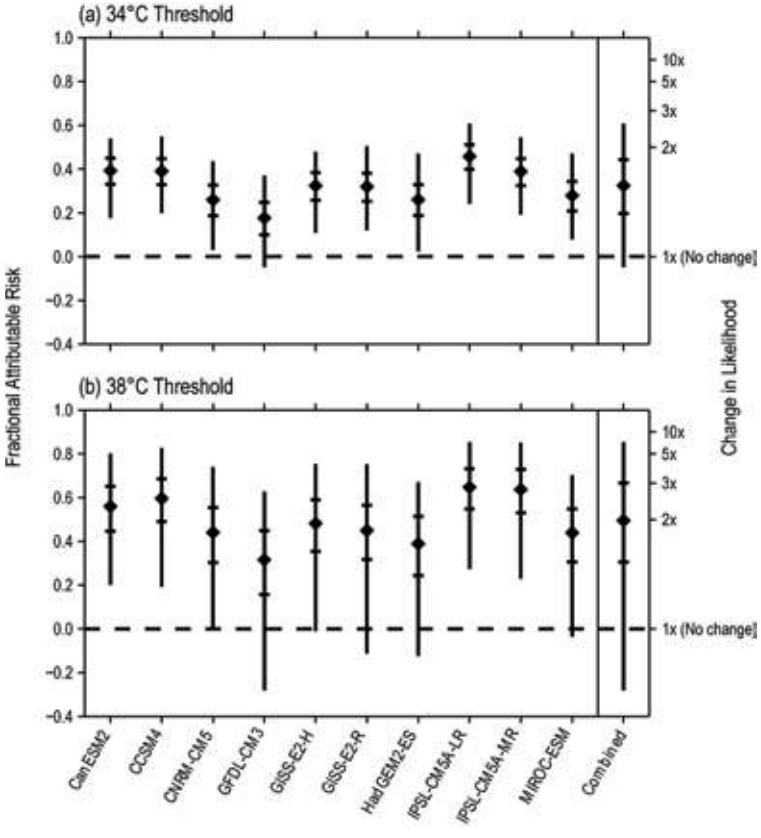

Fig. 28.2. Distributions of 10 000 bootstrapped estimates of FAR (left axes) and change in likelihood (right axes) for each of the 10 natural SST estimates for Brisbane daily Nov maximum temperature above (a) a 34°C maximum temperature threshold and (b) a 38°C maximum temperature threshold. The vertical lines show the full ranges of the bootstrapped FAR/likelihood values, the dashes mark the 10th and 90th percentile FAR/likelihood values, and the diamonds mark the best estimate FAR/likelihood values. The far right column shows the distribution of FAR values compiled by combining the distributions from each GCM with the best estimate, 10th percentile and 90th percentile again marked.

10th and 90th percentile FAR estimates are compared for the different model-derived natural simulations.

The combined FAR distributions, produced by compiling the FAR estimates using the different natural SST estimates, are also shown (Fig. 28.2). These show almost all FAR estimates are greater than zero (99.97% for the 34°C threshold and 99.86% for the 38°C threshold). The 10th percentile FAR estimate for the 34°C threshold is 0.20 which corresponds to a 25% increase in the likelihood of hot November days above 34°C. The 10th percentile FAR estimate for very hot days above the 38°C threshold is 0.30 corresponding to a 44% increase in likelihood. The best estimate FAR values, calculated using the entire samples, are 0.32 for the 34°C threshold and 0.50 for the 38°C threshold, corresponding to increases in likelihood of 47% and 100% respectively.

Conclusions. During the G20 summit in November 2014, Brisbane experienced unusually hot weather, although the temperatures were not unprecedented. Using thousands of atmospheric simulations with a regional climate model representing the climate as it was in 2014 and an estimated 2014 climate without any anthropogenic influences, the role of human-induced climate change on this event was investigated. The likelihood of 2014-like hot days above 34°C (like Saturday, 15 November) was found to have *very likely* (i.e., with 90% confidence) increased by at least 25%. The likelihood of very hot days above 38°C (like Sunday, 16 November) was found to have increased by *very likely* at least 44%. The best estimates for the change in likelihood of hot and very hot days are considerably higher with increases of 47% and 100% respectively. The influences of both structural and sampling uncertainties on the attribution statement were analyzed and found to be of similar magnitudes. Both sources of uncertainty are substantial, but we can still have very high confidence that the FAR values are greater than zero since after accounting for these uncertainties more than 99.9% of FAR estimates are positive. Therefore, in summary, using the weather@home model setup with observed 2014 SSTs we find that anthropogenic climate change has increased the likelihood of hot and very hot November days in Brisbane.

REFERENCES

Allen, M., 2003: Liability for climate change. *Nature*, **421**, 891–892, doi:10.1038/421891a.

Black, M. T., D. J. Karoly, and A. D. King, 2015: The contribution of anthropogenic forcing to the Adelaide and Melbourne, Australia, heatwaves of January 2014 [in "Explaining Extreme Events of 2014 from a Climate Perspective"]. *Bull. Amer. Meteor. Soc.*, **96** (12), S145–S148, doi:10.1175/BAMS-D-15-0098.1.

Jones, D. A., W. Wang, and R. Fawcett, 2009: High-quality spatial climate data-sets for Australia. *Aust. Meteor. Ocean. J.,* **58**, 233–248.

Jones, R., and Coauthors, 2004: Generating High-Resolution Climate Change Scenarios using PRECIS. Met Office Hadley Centre, 40 pp. [Available online at www.metoffice.gov.uk/media/pdf/6/5/PRECIS_Handbook.pdf.]

Karoly, D. J., and K. Braganza, 2005: Attribution of recent temperature changes in the Australian region. *J. Climate*, **18**, 457–464.

King, A. D., L. V. Alexander, and M. G. Donat, 2013: The efficacy of using gridded data to examine extreme rainfall characteristics: a case study for Australia. *Int. J. Climatol.*, **33**, 2376–2387, doi:10.1002/joc.3588.

——, D. J. Karoly, M. G. Donat, and L. V. Alexander, 2014: Climate change turns Australia's 2013 Big Dry into a year of record-breaking heat [in "Explaining Extreme Events of 2013 from a Climate Perspective"]. *Bull. Amer. Meteor. Soc.*, **95** (9), S41–S45.

Lewis, S. C., and D. J. Karoly, 2014: The role of anthropogenic forcing in the record 2013 Australia-wide annual and spring temperatures [in "Explaining Extreme Events of 2013 from a Climate Perspective"]. *Bull. Amer. Meteor. Soc.*, **95** (9), S31–S34.

Massey, N., and Coauthors, 2015: weather@home—development and validation of a very large ensemble modelling system for probabilistic event attribution. *Quart. J. Roy. Meteor. Soc.*, **141**, 1528–1545, doi:10.1002/qj.2455, .

Perkins, S. E., S. C. Lewis, A. D. King, and L. V. Alexander, 2014: Increased risk in Australian heatwave occurrence during 2012–2013 [in "Explaining Extreme Events of 2013 from a Climate Perspective"]. *Bull. Amer. Meteor. Soc.*, **95** (9), S34–S37.

Pope, V. D., M. L. Gallani, P. R. Rowntree, and R. A. Stratton, 2000: The impact of new physical parametrizations in the Hadley Centre climate model: HadAM3. *Climate Dyn.*, **16**, 123–146, doi:10.1007/s003820050009.

Taylor, K. E., R. J. Stouffer, and G. A. Meehl, 2012: An overview of CMIP5 and the experiment design. *Bull. Amer. Meteor. Soc.*, **93**, 485–498, doi:10.1175/BAMS-D-11-00094.1.

29. THE CONTRIBUTION OF ANTHROPOGENIC FORCING TO THE ADELAIDE AND MELBOURNE, AUSTRALIA, HEAT WAVES OF JANUARY 2014

Mitchell T. Black, David J. Karoly, and Andrew D. King

Anthropogenic climate change very likely increased the likelihood of prolonged heat waves like that experienced in Adelaide in January 2014 by at least 16%. The influence for Melbourne is less clear.

Introduction. Southeast Australia experienced one of the most significant heat waves on record in January 2014. A near-stationary high pressure system over the Tasman Sea directed very hot air from the interior of the continent to the southeast, where extreme temperatures persisted from 13 to 18 January. Records were broken for extended periods of heat at a number of locations (Australian Bureau of Meteorology 2014), including the major cities of Adelaide and Melbourne. Adelaide recorded five consecutive days above 42°C (13–17 January), while Melbourne recorded four consecutive days above 41°C (14–17 January). The heat wave became a leading news story worldwide when extreme conditions at the Australian Open Tennis Grand Slam in Melbourne resulted in professional tennis players hallucinating and collapsing on court.

This study investigates how the likelihood of prolonged periods of extreme heat, like those experienced in Adelaide and Melbourne in January 2014, has been changed due to human-induced climate change.

Data and Methods. We use very large ensembles of simulations with the Met Office HadAM3P global atmospheric circulation model (Pope et al. 2000; 1.25° longitude by 1.875° latitude, 19 levels) with a nested regional model (HadRM3P; 0.44° longitude by 0.44° latitude, 19 levels) over the Australasian Coordinated Regional Climate Downscaling Experiment (CORDEX1) domain. These simulations were undertaken as part of the weather@home distributed computing project (Massey et al. 2015). Using this framework, the model was run under two distinct climate scenarios: industrial ("all forcings") and non-industrial ("natural") realizations of the year 2014. The "all forcings" simulations were driven by observed aerosols and greenhouse gas composition, as well as observed sea surface temperatures (SSTs) and sea ice from the Operational Sea Surface Temperature and Sea Ice Analysis (OSTIA) operational analysis (Donlon et al. 2012). The "natural" simulations were driven by preindustrial greenhouse gases and aerosols, sea ice extent corresponding to the year of maximum sea ice extent in each hemisphere of the OSTIA record, and SSTs modified to remove estimates of the warming attributable to historical anthropogenic greenhouse gasses. Estimates of the SST changes due to human influences were separately calculated using 10 available Coupled Model Intercomparison Project Phase 5 models (Taylor et al. 2012; see online supplemental material). Thus, 10 alternative ensembles of the "natural" climate were created. Given this experimental design, the change in likelihood of heat events is conditional upon the main modes of variability represented by the prescribed observed SSTs for 2014. To generate sufficiently large ensembles, the model was run using multiple initial conditions subject to random perturbations. We used all of the ensemble members that were available at the time of writing: 3417 for the "all forcing" scenario and 7998 for the "natural" scenario (constituting at least 780 members for each of the 10 "natural" ensembles).

To ensure that the model is able to reliably represent January daily maximum temperatures at Adelaide and Melbourne (taken as the nearest model land-only grid point values), evaluation was seperately performed for each location. Because the model simulations only span the short period from December 2013 to November 2014, we cannot express the temperatures as anomalies relative to a climatological pe-

[1]www.cordex.org

AFFILIATIONS: Black, Karoly, and King—School of Earth Sciences and ARC Centre of Excellence for Climate System Science, University of Melbourne, Melbourne, Victoria, Australia

DOI:10.1175/BAMS-D-15-00097.1

A supplement to this article is available online 10.1175/BAMS-D-15-00097.2)

riod. Instead, we compare the combined distribution of January daily maximum temperatures from the "natural" model scenario against the observed 1910–39 station temperatures from the high-quality Australian Climate Observations Reference Network–Surface Air Temperature (ACORN-SAT) dataset (Trewin 2013). The Australian surface temperatures do not show a discernable anthropogenic warming signal prior to 1950 (Karoly and Braganza 2005) and thus the early period of the instrumental records (1910–39) may be treated as a proxy for a "natural" climate baseline. Therefore, we correct for model bias by adjusting the mean of the "natural" daily maximum temperature distribution to equal that of the early observations; this bias adjustment is then applied to the "all forcing" distribution. Using this approach, modeled daily maximum temperatures for Adelaide were adjusted (cooled) by 0.97°C, while Melbourne values were cooled by 0.92°C. The resulting modeled and observed daily maximum temperature distributions are remarkably similar in shape and variance (Fig. 29.1a, b). There is a warm shift in the distributions between the "natural" and "all forcing" scenarios: +0.63°C for Adelaide and +0.54°C for Melbourne.

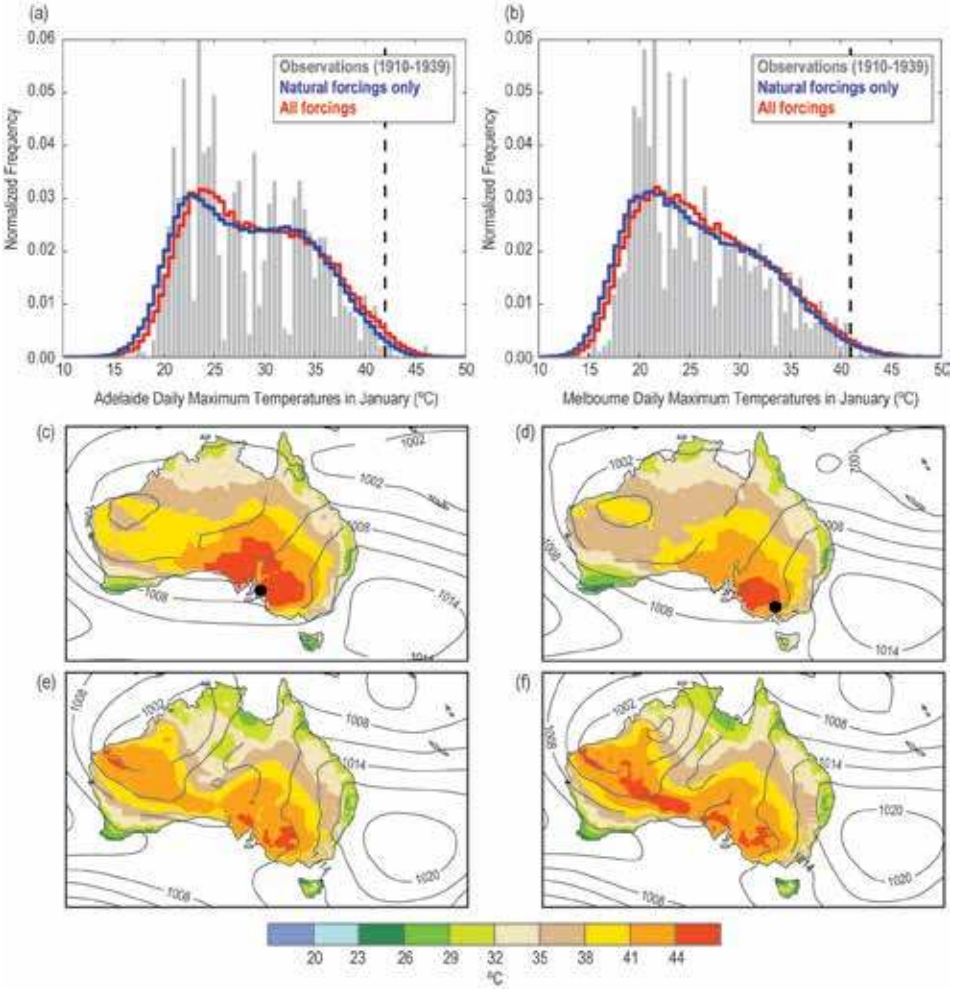

Fig. 29.1. (a) Distributions of January daily maximum temperatures for Adelaide as represented by the ACORN-SAT observational dataset (1910–39; shown in gray) and the climate model scenarios—"all forcing" ensemble (red) and "natural" climate ensemble (blue). The model distributions have been bias-corrected. The vertical dashed line identifies the observed temperature threshold used to define heat wave events. (b) January daily maximum temperatures for Melbourne. (c) Composite maximum temperature (shaded; °C) and mean sea level pressure (contour; hPa) for 29 Adelaide heat waves as represented by the climate model. (d) Composite conditions for 21 Melbourne heat waves as represented by the climate model. (e) Observed conditions during the Adelaide heat wave (13–17 Jan 2014). Maximum temperatures are from the Australian Water Availability Project (AWAP) dataset (Jones et al. 2009) while MSLP is from ERA-Interim reanalysis (Dee et al. 2011). (f) Observed conditions during the Melbourne heat wave (14–17 Jan 2014). The locations of Adelaide and Melbourne are identified by the black dots in (c) and (d), respectively.

For this study we define heat waves to be *n* consecutive January days when the maximum temperature exceeds a very high threshold. For Adelaide, this observed threshold is 42°C (n = 5 days), while for Melbourne the threshold is 41°C (n = 4 days). Heat waves are considered to be non-overlapping events—that is, six consecutive days in Adelaide above 42°C would be counted as a single heat wave event. To test the sensitivity of the results to these temperature and duration thresholds, we also examined heat waves of shorter durations (n = 1 to n = 3 days) and reduced the

observed temperature thresholds to 40°C for Adelaide and 39°C for Melbourne (see online supplemental material).

To estimate the anthropogenic influence in a quantitative manner, we use the fraction of attributable risk (FAR; Allen 2003; Stott et al. 2004) in which the probability of heat waves occurring is compared in the "all forcing" and "natural" scenarios. Here, we aggregate the 10 "natural" ensembles in order to calculate a *best estimate* of FAR, while we consider each of the "natural" ensembles separately in order to better sample the possible range of FAR values and estimate uncertainties. This latter point was undertaken because there is a greater variation in FAR between the different "natural" ensembles (due to the different underlying SST patterns) than within the ensembles (due to the perturbed initial conditions). To assist with the interpretation of results, FAR values are also presented as *estimated increase in likelihood*.

Results. Within the 3417 simulations comprising the "all forcing" ensemble, we identified 29 heat waves at Adelaide with five or more consecutive days above 42°C (return period of 118 years), and 21 heat waves at Melbourne with four or more consecutive days above 41°C (return period of 163 years). Composite mean sea level pressure (MSLP) and maximum temperature conditions for these modeled heat waves are shown in Figs. 29.1c, d, while conditions for actual case events are shown in Figs. 29.1e,f. The model is seen to be capable of representing the large-scale pressure patterns associated with prolonged heat waves in southeast Australia, adding confidence to the resulting attribution statement.

Next, we compare the frequencies of heat waves in the "all forcing" and "natural" climate ensembles to assess the impact of human influence (see Fig. 29.2; a complete listing of heat wave frequencies is provided as online supplemental material). For heat waves at Adelaide with five consecutive days above 42°C, the best estimate of FAR is 0.65 (with a range of 0.14 to 0.85). This corresponds to a 186% increase in likelihood due to anthropogenic climate change (range from 16% to 567% increase in likelihood). For heat waves at Melbourne with four consecutive days above 41°C, the best estimate of FAR is 0.47 (ranging from −0.42 to 1.0); within one of the "natural" ensembles the frequency of heat waves is greater than that for the "all forcing" ensemble, while in another "natural" ensemble the heat wave never occurred. This corresponds to a 89% increase in likelihood due to anthropogenic climate change (range from 30% decrease to >1000% increase in likelihood).

Finally, we examine the sensitivity of the FAR results by relaxing the temperature and duration thresholds used to define heat waves. Overall, the results remain relatively robust (see Fig. 29.2 and Supplementary Fig. S29.3). The "best estimates" of FAR maintain similar positive values when considering events of different durations and magnitudes. Across this sampled space, FAR values calculated for the individual "natural" ensembles were consistently positive for Adelaide heat events, while there remained some negative FAR values for Melbourne events. While we can expect some uncertainty in the FAR values for the warmer, longer heat wave events to be due to their low frequency within the modeled distribution, sample size alone cannot explain all of the uncertainty. For example, the single very hot days in Melbourne (Fig. 29.2) still show a large spread in FAR values despite the relatively higher frequency of

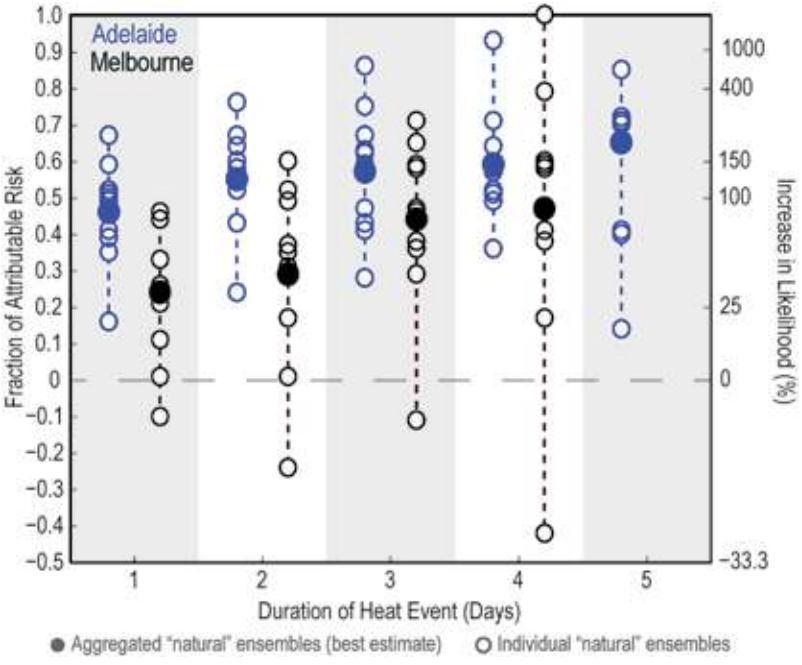

Fig. 29.2. Fraction of Attributable Risk (FAR) and corresponding increase in likelihood calculated for Adelaide (blue) and Melbourne (black) heat waves of different durations. The temperature threshold used to define heat waves was 42°C for Adelaide and 41°C for Melbourne.

such events under both the "natural" and "all forcings" climate scenarios. Therefore, the underlying SST patterns driving the "natural" simulations have an important influence on the resulting FAR values. The negative FAR values for Melbourne and the small FAR values for Adelaide are associated with the smaller estimates of anthropogenic SST increases (see online supplemental material).

Conclusions. This study quantifies the influence of anthropogenic climate change on the likelihood of heat waves like those experienced in Adelaide and Melbourne in January 2014. Using large ensembles of regional climate model simulations of "natural" and "all forcing" scenarios, we find that human influence has increased the likelihood of heat waves in Adelaide (best estimate 186% increase, range from 16% to 567%), while the signal for Melbourne is less clear (best estimate 89% increase, range from 30% decrease to >1000% increase). While the model used in this study is shown to be capable of correctly representing the conditions associated with heat waves in southeast Australia, the overall analysis would benefit from larger ensemble sizes. The results are sensitive to the underlying SST patterns driving the "natural" scenarios, which is not surprising given that we are considering single-model grid cells at locations close to the coastline. Therefore, the study would benefit from further consideration of uncertainties in "natural" SST patterns. This study is an important step towards a comprehensive understanding of the Adelaide and Melbourne heat waves of January 2014.

ACKNOWLEDGEMENTS. The authors have been supported by funding from the ARC Centre of Excellence for Climate System Science (Grant CE110001028). Weather@home ANZ is a collaboration between the University of Oxford, the UK Met Office, the ARC Centre of Excellence for Climate System Science in Australia, NIWA in New Zealand, the University of Melbourne, the University of Tasmania and the Tasmanian Partnership for Advanced Computing. We thank the volunteers who donated their computing time to run weather@home.

REFERENCES

Allen, M., 2003: Liability for climate change. *Nature*, **421**, 891–892.

Australian Bureau of Meteorology, 2014: Special climate statement 48: One of southeast Australia's most significant heatwaves. Bureau of Meteorology, 18 pp. [Available online at www.bom.gov.au/climate/current/statements/scs48.pdf.]

Dee, D. P., and Coauthors, 2011: The ERA-Interim reanalysis: Configuration and performance of the data assimilation system. *Quart. J. Roy. Meteor. Soc.*, **137**, 553–597, doi:10.1002/gj.828.

Donlon, C. J., M. Martin, J. Stark, J. Roberts-Jones, E. Fiedler, and W. Wimmer, 2012: The Operational Sea Surface Temperature and Sea Ice Analysis (OSTIA) system. *Remote Sens. Environ.*, **116**, 140–158, doi:10.1016/j.rse.2010.10.017.

Jones, D., W. Wang, and R. Fawcett, 2009: High-quality spatial climate data-sets for Australia. *Aust. Meteor. Oceanogr. J.*, **58**, 233–248.

Karoly, D. J., and K. Braganza, 2005: Attribution of recent temperature changes in the Australian Region. *J. Climate*, **18**, 457–464.

Massey, N., and Coauthors, 2015: weather@home—development and validation of a very large ensemble modelling system for probabilistic event attribution. *Quart. J. Roy. Meteor. Soc.* **141**, 1528–1545, doi:10.1002/qj.2455.

Pope, V. D., M. L. Gallani, P. R. Rowntree, and R. A. Stratton, 2000: The impact of new physical parametrizations in the Hadley Centre climate model: HadAM3. *Climate Dyn.*, **16**, 123–146.

Stott, P. A., D. A. Stone, and M. R. Allen, 2004: Human contribution to the European heatwave of 2003. *Nature*, **432**, 610–614.

Taylor, K. E., R. J. Stouffer, and G. A. Meehl, 2012: An overview of CMIP5 and the experiment design. *Bull. Amer. Meteor. Soc.*, **93**, 485–498, doi:10.1175/BAMS-D-11-00094.1.

Trewin, B., 2013: A daily homogenized temperature data set for Australia. *Int. J. Climatol.*, **33**, 1510–1529, doi:10.1002/joc.3530.

30. CONTRIBUTORS TO THE RECORD HIGH TEMPERATURES ACROSS AUSTRALIA IN LATE SPRING 2014

Pandora Hope, Eun-Pa Lim, Guomin Wang, Harry H. Hendon, and Julie M. Arblaster

The record warm Australian spring of 2014 would likely not have occurred without increases in CO_2 over the last 50 years working in concert with an upper-level wave train.

The Event. Australia experienced in 2014 its highest springtime mean maximum temperature (Tmax) since records began in 1910. The Australian-mean Tmax was 2.32°C above the 1961–90 mean, and 0.26°C warmer than the previous record set in 2013 (Bureau of Meteorology 2014). While September was very warm, both October and November had the hottest Australia-average Tmax on record, with maximum temperatures 2.76°C and 2.18°C above their 1961–90 means, respectively, and the south-east was particularly warm (Fig. 30.1a). Here we focus on the causes of the October–November extreme Tmax anomaly.

Increasing CO_2. The previous monthly records in October and November were found to be six or seven times more likely in the current modelled climate than in the modelled climate with only natural forcing using the fraction of attributable risk (FAR) method of Lewis et al. (2014). Thus it is highly likely that anthropogenic forcing, especially increasing CO_2, played a role in the extreme heat of this event. While the FAR method is useful, below we describe results using a new method that allows for the influence of increasing CO_2 to be assessed within a coupled seasonal forecast framework.

The Australian Bureau of Meteorology's seasonal forecast model POAMA (Cottrill et al. 2013; Hudson et al. 2013) was used and the design of the forecast sensitivity experiments is described in the online supplemental material. The control forecast was initialized with observed atmosphere, ocean, and land initial conditions for 2014 and the CO_2 concentration was set to current levels (400 ppm). The extreme heat across Australia was captured well (Fig. 30.1b).

The response of the climate system to enhanced levels of CO_2 occurs on a number of time scales: a rapid adjustment in the atmosphere and longer term warming of the ocean. The immediate atmospheric adjustment is accounted for by re-running the control ensemble, but with CO_2 levels set at 1960 levels (315 ppm). The Tmax ensemble mean anomaly across Australia from the 400-ppm forecast experiment is warmer compared to the 315-ppm experiment (Fig. 30.1c), but this change is not significant and the ensemble has large spread [compare the red and light blue bars in the probability distribution function (PDF) in Fig. 30.1g]. To assess the impacts of the long-term changes in the ocean due to rising levels of CO_2, a "preCO2" experiment was conducted. The atmospheric CO_2 was set to 1960 levels and the CO_2 forced component of ocean temperatures and salinity since 1960 (termed oceanCO2anom, see online supplemental material) was also removed from the initial conditions. Removing oceanCO2anom from the 2014 ocean initial conditions had a far greater impact on predicted Australian temperatures (Fig. 30.1d) than did changing the atmospheric CO_2 alone. Figure 30.1e represents the contribution to Australian October–November temperatures in 2014 from changing atmospheric CO_2 and the ocean temperature response to the last 50 years of CO_2 change and shows widespread warmth across the continent. Figure 30.1f shows the predicted anomaly if the same initial conditions (i.e., synoptic state of the atmosphere) occurred under 1960 CO_2 levels and associated ocean conditions. Although the warmth was significantly reduced in the preCO2 experiment (Fig. 30.1f) the predicted conditions in October–November 2014 in the absence of increased

AFFILIATIONS: Hope, Lim, Wang, and Hendon—Research and Development Branch, Bureau of Meteorology, Melbourne, Victoria, Australia; Arblaster—Research and Development Branch, Bureau of Meteorology, Melbourne, Victoria, Australia, and National Center for Atmospheric Research, Boulder, Colorado

DOI:10.1175/BAMS-D-15-00096.1

A supplement to this article is available online (10.1175/BAMS-D-15-00096.2)

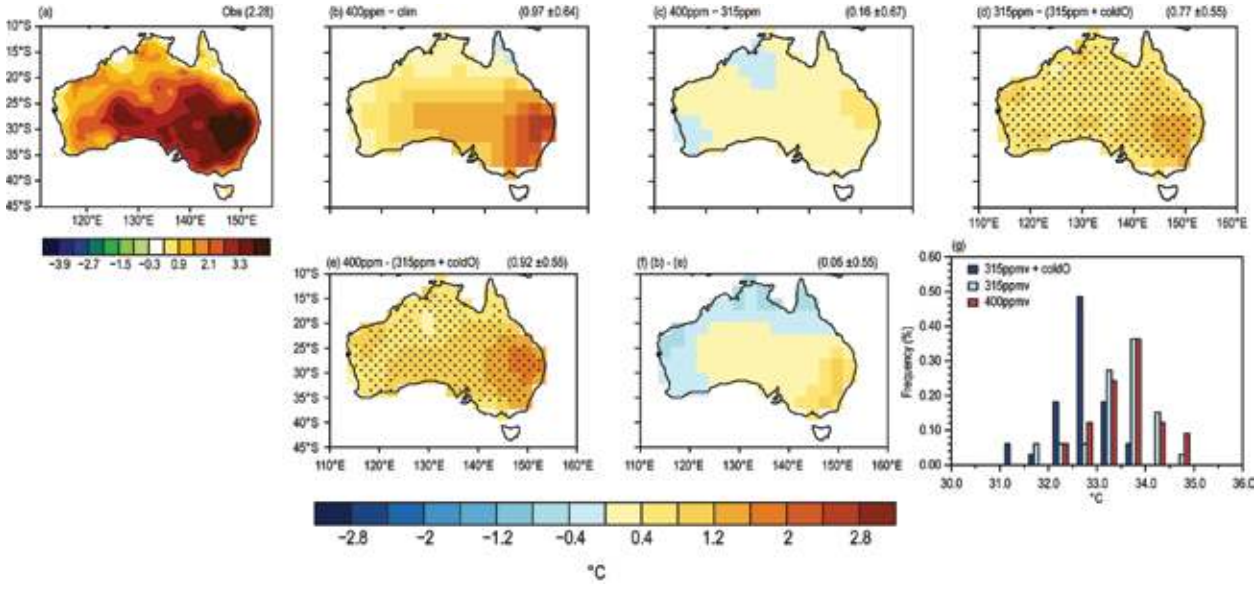

Fig. 30.1. (a) Observed anomaly of Oct–Nov mean Australian Tmax in 2014 relative to 1981–2010 climatology; (b) control forecast Tmax anomaly (with respect to the hindcast climatology) for Oct–Nov, initialized on 21, 25, and 28 September 2014, and with CO_2 levels set at 400 ppm; (c) difference in the forecasts under 400 ppm vs 315 ppm CO_2 concentration; (d) difference in the forecasts made using 2014 realistic initial conditions vs the same conditions but from which oceanCO2anom is removed under 315 ppm CO_2 (preCO2); (e) difference between the control forecast (with CO_2 set at 400 ppm) and the forecast with 315 ppm CO_2 and the adjusted ocean initial conditions (oceanCO2anom removed), which indicates the Tmax associated with increased CO_2 since 1960; (f) difference between (b) and (e), which indicates the Tmax that would have occurred without the influence of increased CO_2 since 1960; (g) PDFs of Australian-average Tmax of 33 ensemble members from the control (400-ppm), 315-ppm, 315-ppm_coldOcean (preCO2) experiments. The number in parenthesis in the top right corner of (a) is the observed Australian-average Tmax anomaly; in (b)–(f) it is Australian-average Tmax anomaly of the ensemble mean forecast anomaly (or difference between experiments) with an indication of the ensemble spread. Differences with statistical significance greater than 90% confidence level are indicated with stippling. All temperature anomalies in °C.

CO_2 would have still been conducive to a warm event occurring over the far south east of the country.

Compared to the hindcast climatology, forecast Australian late spring temperatures in 2014 were warmer than one standard deviation above the mean in more than half of the control ensemble members (Fig. 30.1g, red bars), but only in 2 of the 33 members from the preCO2 experiment (Fig. 30.1g, dark blue bars). Given that 2014 was a record event of more than two standard deviations above the mean, no member of the preCO2 experiment achieved this heat, even while the pattern across Australia reflected anomalously warm conditions in the south-east. Sampling and modelling errors may influence these results. However, the forecast spread of POAMA's prediction for Australian seasonal Tmax has been shown to encompass the forecast error at short lead times (Hudson et al. 2013) and the clear shift seen in the PDFs between the control and preCO2 experiments suggest that this result is robust. Other contributors to the extremity of this event could have arisen from anomalous land conditions in 2014, other large-scale climate drivers, or aspects of the synoptic situation. These are explored below.

Large-scale climate drivers. In order to elucidate the causes of the record heat that worked in concert with increased CO_2, we explicitly describe the contribution from factors known to influence Australian spring temperatures (e.g., Marshall et al. 2013; White et al. 2013) using multiple linear regression (as described in Arblaster et al. 2014). We use three predictors that represent the large-scale climate drivers—ENSO (NINO3.4 index), Indian Ocean dipole (IOD), and the southern annular mode (SAM index)—as well as global mean temperature and antecedent Australian upper level soil moisture. The association of these individual predictors with Australian temperatures is demonstrated here by the regression pattern between Australian Tmax and SST/MSLP (Supplemental Fig.

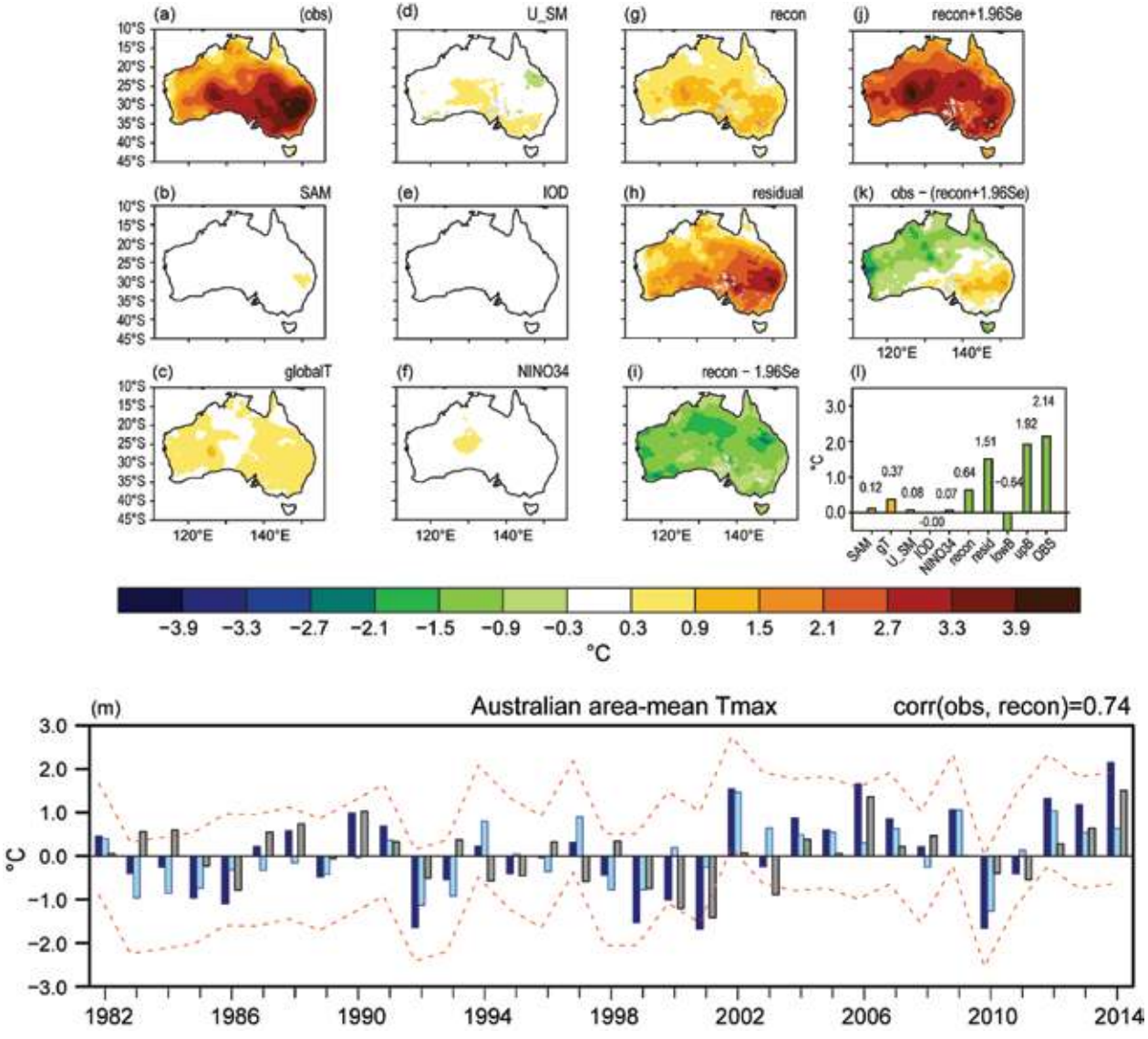

Fig. 30.2. (a)–(l) Patterns of Oct–Nov mean maximum temperature anomaly (°C) of 2014 from (a) observations, and the contribution of individual predictors from a multiple linear regression using (b) the southern annular mode, (c) global mean temperature, (d) 2014 September upper-layer soil moisture, (e) the Indian Ocean dipole index, and (f) Niño3.4 SSTs, where each regression map has been multiplied by the size of the predictor in Oct–Nov 2014. (g) The total reconstructed anomaly (sum of panels b–f); (h) the residual, that is, the difference between the observed (a) and reconstructed anomalies (g); (i) the reconstructed anomaly minus the 95% prediction interval; (j) the reconstructed anomaly plus the 95% prediction interval; and (k) difference between (a) and (j). (l) The observed Australian-average maximum temperature anomaly and the contribution by each of the predictors (orange), the total predicted anomaly, the residual, and the predicted anomaly accounting for the 95% prediction interval (green). Anomalies are relative to the 1982–2013 base period. (m) The observed (dark blue), reconstructed (light blue), and residual (gray) Tmax (°C) obtained from the multiple linear regression model described in Arblaster et al. (2014) and in the text. Red lines indicate 95% prediction intervals.

S30.3), with signatures of El Niño, positive IOD, and a strong negative SAM associated with warm Australian temperatures.

The observed October–November Australian average Tmax was clearly extreme—it fell outside the bounds of the 95% prediction interval of the regression model (which accounts for the uncertainty in the strength of the historical relationships Fig. 30.2m). The SST anomaly pattern of late austral spring 2014 (Supplemental Fig. S30.2a) was consistent with weak El Niño, and the tropical Indian Ocean and the far western Pacific Ocean were anomalously warm due

to a warming trend in the last 34 years. However, the regression model reproduces only 30% of the observed warmth across Australia, with global mean temperature being the dominant predictor (Fig. 30.2l). The observed antecedent soil moisture also contributed to the warmth captured by the regression model (Fig. 30.2d), particularly across the south. The pattern of the reconstruction reflects the observed anomalies across the country (Fig. 30.2g), however the magnitude of the 2014 event was much warmer in the east (Fig. 30.2h), and is outside the prediction interval of the regression model (Figs. 30.2j,k). Thus the contribution from large-scale climate drivers such as ENSO, IOD, and SAM as well as antecedent soil moisture to this extreme warm event appears to have been small but positive, and the result of this regression analysis confirms the importance of global mean temperature to this event.

Synoptic situation. While the regression analysis reveals that the large-scale drivers such as ENSO did not contribute strongly to the magnitude of this event, the forecast experiments indicate that there was a predictable contribution to this event over and above the response to global warming (Fig. 30.1f). To explore this further we examine aspects of the observed conditions in October–November 2014. The anomalous circulation at the surface (Supplemental Fig. S30.2b) and in the upper level of the atmosphere (Supplemental Fig. S30.2c) in late austral spring 2014 strongly resemble those typically related to high Tmax over Australia (Supplemental Figs. S30.3c,d). At the surface, an anticyclonic circulation over the Australian continent and cyclonic circulations to its southeast and southwest were evident although they were not part of the SAM in 2014. The upper-level features are characterized by a strong signal of northwest to southeast Rossby wave propagation, which was likely to emanate from the tropical Indian Ocean, positioning high geopotential height anomalies over Australia (e.g., Supplemental Fig. S30.3c).

The degree to which these synoptic conditions are distinct from the large-scale climate drivers was assessed using the reconstruction from the regression model above. Regressing the 200-hPa geopotential height onto the time series of reconstructed Tmax from Fig. 30.2m (Supplemental Fig. S30.4a) does not capture the high geopotential height anomaly described above, while regression onto the residual (Supplemental Fig. S30.4b) highlights the high geopotential height over the country. This suggests that in the upper atmosphere, the synoptic situation of late spring 2014 was largely uncaptured by the five predictors of the regression model. At the surface, this distinction is less clear, and the regression of MSLP onto the reconstructed Tmax (Supplemental Fig. S30.4c) has some similarity with the regression onto the observed series (Supplemental Fig. S30.3d) while the residual has less. This highlights that this upper-level feature is important in explaining the extremity of this warm event.

Further analysis reveals this Rossby wave train was likely to be promoted by the anomalously high rainfall in the tropical central Indian Ocean (Supplemental Fig. S30.2d). Regression of global 200-hPa geopotential height and rainfall onto the tropical central Indian Ocean rainfall (red box in Supplemental Fig. S30.5a,b) that is independent of IOD, reveals a similar wave train pattern and rainfall anomaly pattern to those of late spring 2014 (Supplemental Fig. S30.5 compared to Supplemental Figs. S30.2c,d). Significant trends in rainfall in this region have been inferred in observations (e.g., Deser and Phillips 2006) over the late 20th century, suggesting a potential trend in this type of synoptic system, but that is a topic for further study.

Conclusions. The record late spring temperatures over Australia in 2014 were analysed using both regression analysis and experiments with a seasonal forecast system. These varied approaches to defining the contributors to the warmth across Australia in late spring 2014 have proved complementary. The impact from ENSO, IOD, and SAM were minor and the antecedent land surface conditions played only a small role, but anomalous Rossby wave train activity was believed to be important to building heat across Australia. The immediate atmospheric adjustment to the changes in CO_2 levels over the last 50 years contributed to the heat, but the major driver of the Australian late spring 2014 heat was the long-term response to CO_2 levels over that time as expressed by an upward trend in oceanic temperature. No members of the preCO2 experiments achieved the heat of late spring 2014. In summary, each season's warmth will be determined by a combination of anthropogenic forcing and internal variability, in 2014 the enhanced levels of CO_2 likely helped build the heat associated with an anomalous Rossby wave train into a record breaking event.

ACKNOWLEDGMENTS. We thank Matthew Wheeler, Debbie Hudson, David Karoly, Thomas Peterson and two anonymous reviewers for their

constructive comments on this manuscript. This work has been undertaken as part of the Australian Climate Change Science Programme, funded jointly by the Australian Department of the Environment, the Bureau of Meteorology and CSIRO.

REFERENCES

Arblaster, J. M., E.-P. Lim, H. H. Hendon, B. C. Trewin, M. C. Wheeler, G. Liu, and K. Braganza, 2014: Understanding Australia's hottest September on record [in "Explaining Extremes of 2013 from a Climate Perspective"]. *Bull. Amer. Meteor. Soc*., **95** (9), S37–S41.

Bureau of Meteorology, 2014: Special climate statement 50: Australia's warmest spring on record. Bureau of Meteorology, 9 pp. [Available online at www.bom.gov.au/climate/current/statements/scs50.pdf.]

Cottrill, A., and Coauthors, 2013: Seasonal forecasting in the Pacific using the coupled model POAMA-2. *Wea. Forecasting*, **28**, 668–680, doi:10.1175/WAF-D-12-00072.1.

Deser, C., and A. S. Phillips, 2006: Simulation of the 1976/1977 climate transition over the North Pacific: Sensitivity to tropical forcing. *J. Climate*, **19**, 6170–6180.

Hudson, D., A. G. Marshall, Y. Yin, O. Alves, and H. H. Hendon, 2013: Improving intraseasonal prediction with a new ensemble generation strategy. *Mon. Wea. Rev.*, **141**, 4429–4449, doi:10.1175/MWR-D-13-00059.1.

Lewis, S., D. Karoly, and M. Yu, 2014: Quantitative estimates of anthropogenic contributions to extreme national and state monthly, seasonal and annual average temperatures for Australia. *Aust. Meteor. Oceanogr. J.*, **64**, 215–230.

Marshall, A. G., D. Hudson, M. Wheeler, O. Alves, H. H. Hendon, M. J. Pook, and J. S. Risbey, 2013: Intra-seasonal drivers of extreme heat over Australia in observations and POAMA-2. *Climate Dyn*., **43**, 1915–1937, doi:10.1007/s00382-013-2016-1.

White, C. J., D. Hudson, and O. Alves, 2013: ENSO, the IOD and the intraseasonal prediction of heat extremes across Australia using POAMA-2. *Climate Dyn*., **43**, 1791–1810, doi:10.1007/s00382-013-2007-2.

31. INCREASED RISK OF THE 2014 AUSTRALIAN MAY HEATWAVE DUE TO ANTHROPOGENIC ACTIVITY

Sarah E. Perkins and Peter B. Gibson

Anthropogenic activity has increased the risk of Australian heatwaves during late autumn similar to the 2014 event by up to 23-fold, compared to climate conditions under no anthropogenic influence.

Introduction. The year 2014 was the hottest globally on record (Deng 2015), and the third hottest on record for Australia (Bureau of Meteorology 2015). From 8–26 May, Australia experienced a 19-day heatwave, with the continentally averaged maximum temperature 2.52°C above the monthly mean (Bureau of Meteorology 2014). An intense and persistent high pressure system centered over the Tasman Sea (east of Australia), coupled with exceptional warmth contributed to this event (Bureau of Meteorology 2014; see Supplemental Fig. S31.2). This system was typical of synoptic patterns associated with Australian heatwaves, which advect hot air from the continental interior to the region(s) affected (Pezza et al. 2012).

The start of May, which is late in the austral autumn, initially brought cool conditions to the Australian continent (Bureau of Meteorology 2014), however the original onset of the high pressure system returned temperatures to average seasonal conditions. After the passage of a weak front, the system reestablished, where it strengthened and remained stationary for over two weeks (Bureau of Meteorology 2014). The persistence of the re-established system was exceptional, as similar systems over this region typically last less than a week, before being permanently dislodged by a propagating frontal system (Marshall et al. 2014).

Heatwaves are generally regarded as summertime events, however there is evidence that warm extremes during cooler times of the year are increasing faster than those during warmer seasons (e.g., Alexander et al. 2006; Perkins et al. 2012). While impacts on human systems are likely minimal, anomalously warm events in cooler seasons can have vast impacts on agriculture (e.g., Lanning et al. 2011), which currently contributes to 12% of Australia's gross domestic product. Moreover, increasingly frequent and elevated temperatures are expected throughout all times of the year, as anthropogenic influence on the climate continues to increase (Cowan et al. 2014). This study employs the fraction of attributable risk (FAR) method (Stone and Allen 2005) to ascertain whether anthropogenic climate change has increased the likelihood of the 2014 Australian May heatwave.

Data and Methods. The Australian May heatwave was defined as the area-averaged maximum temperature (tmax) anomaly for 8–26 May 2014. This period was selected as it was a time of anomalously warm conditions over much of Australia. Observed anomalies were calculated with respect to 1961–90 using the Australian Water Availability Project (AWAP) temperature dataset (Jones et al. 2009) interpolated onto a two-degree grid. Figure 31.1a shows the average anomaly across Australia, which, when continentally averaged, equates to +2.52°C.

The FAR framework was used to analyze changes in the risk of a 19-day May heatwave due to increases in anthropogenic greenhouse gases. This requires conditions under no anthropogenic influence, and where greenhouse gas concentrations account for observed and projected anthropogenic emissions. A 21-member ensemble of the Community Earth System Model (CESM; Fischer et al. 2013) is employed. The ensemble is generated through perturbations of atmospheric temperature initial conditions on the order of 10^{-13}°C (see Fischer et al. 2013), yet with identical external forcings. The historical simulations (1950–2005) are forced by observed changes

AFFILIATIONS: Perkins and Gibson—Australian Research Council Centre of Excellence for Climate System Science, Climate Change Research Centre, University of New South Wales, Sydney, New South Wales, Australia

DOI: 10.1175/BAMS-D-15-00074.1

A supplement to this document is available online (10.1175/BAMS-D-15-00074.1)

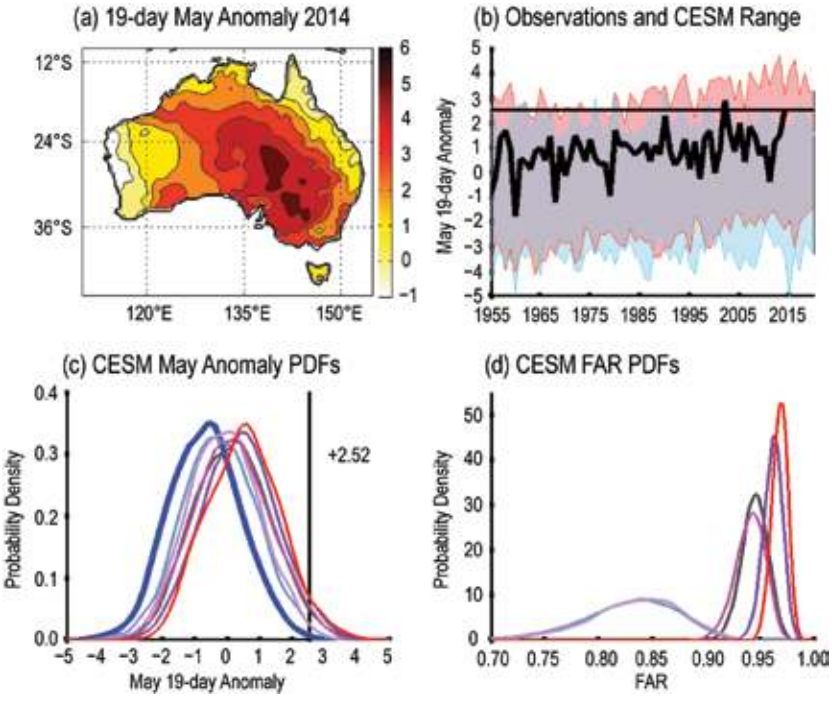

Fig. 31.1. (a) The 19-day average tmax anomaly (°C) over Australia from 8–26 May 2014 calculated from the AWAP dataset, respective to 1961–90. (b) The yearly range between the highest and lowest spatially averaged 19-day May tmax anomalies across the CESM forced ensemble (red) and 14 non-overlapping 66-year periods in the control (blue), and the yearly maximum from AWAP. (c) PDFs of 19-day May tmax anomalies from the CESM ensemble for the control (blue), 1955–74 (light blue), 1965–84 (light purple), 1975–94 (magenta), 1985–2004 (dark purple), 1995–2020 (red) and 1955–2014 (gray). The event analyzed is marked by a black vertical line. (d) PDFs of FAR estimates from 10 000 bootstrapped samples for each of the forced time periods in (c) for a 19-day average anomaly of +2.52°C.

in greenhouse gases, whereas RCP8.5 (2006–2100) assumes increasing greenhouse gas emissions under a business as usual scenario (Taylor et al. 2012). A 982-year control run was employed to represent the climate under no human influence.

The historical period from 1955–2005 was merged with 2006–20 from RCP8.5. Anomalies in the forced and control simulations are with respect to 1961–90. To increase sample size, all 19-day anomalies for the month of May (13 values per year) from the control and forced simulations were computed. Figure 31.1b displays that the observed range of 19-day May anomalies is well-captured by the CESM ensemble. This study is dependent on a single model, and while this does not consider inter-model uncertainty, it does capture remarkably well the uncertainty due to internal climate variability (Fischer et al. 2013; Perkins and Fischer 2013), as implemented by changes in the initial conditions. This model setup allows for the sampling of internal climate variability that is not available from other fully coupled (multi-) model GCM ensembles, thus supplying a range of plausible climates under identical external forcing and model physics. It also was shown to perform reasonably well in capturing the synoptics relevant to this heat event (see supplemental material).

A range of overlapping periods were analyzed to understand the transient nature of changes in the FAR and risk of the 2014 May heatwave (1955–74; 1965–84; 1975–94; 1985–2004; 1995–2020; 1955–2014). Bootstrapping was performed 10 000 times per period, which respectively sampled (with replacement) 50% of all 19-day May anomalies from the control and forced simulations. Bootstrapping is commonplace in FAR assessments (e.g., Stott et al. 2004; Lewis and Karoly 2013), estimating the uncertainty surrounding the FAR value. Only 50% of anomalies in both experiments are resampled to account for uncertainty in sample size. Per iteration, the probability of a +2.52°C is computed in the respective experiments, where the FAR is calculated by:

$$FAR = 1 - \left(\frac{P_{cntrl}}{P_{forced}}\right) \qquad (1)$$

A distribution of the 10 000 FAR values is then obtained. A conservative approach is taken by focusing the 10th percentile. Thus, it is very likely (i.e., 90% confidence, see Lewis and Karoly 2013) that the true FAR value (i.e., the measurable human influence) as represented by the CESM climate model is greater than this 10th percentile. From this, the change in the risk is computed by:

$$Risk = \frac{1}{(1 - FAR)} \qquad (2)$$

A sensitivity analysis on FAR values computed for combinations of event length and magnitude is given in the supplemental material.

Results. Figure 31.1c presents area-averaged 19-day May tmax anomalies in the CESM ensemble over different temporal periods. The event in 2014 was the second hottest recorded across all 19-day May anoma-

Table 31.1. Very likely (>90% confidence) FAR values and associated changes in risk of exceeding a 19-day average tmax anomaly of +2.52°C during the month of May over Australia. Values were estimated from the 21-member CESM model ensemble, where each member is forced by observed anthropogenic emissions, and projected emissions from the RCP8.5 scenario. A 982-year control run was used to represent climate conditions without anthropogenic influence.

	1955–2014	1955–74	1965–84	1975–94	1985–2004	1995–2020
FAR	0.93	0.77	0.77	0.92	0.98	0.96
Risk	13.99	4.27	4.4	12.82	19.81	23.85

lies since 1955 (Fig. 31.1b). Throughout the periods of the simulations (i.e., with greater anthropogenic forcing), the right tail of the probability density function (PDF; Fig. 31.1c) shifts further right, including more exceedances of the 2.52°C threshold. All forced PDFs in Fig. 31.1c are centered on positive anomalies. A Kolmogorov–Smirnov test at the 5% level indicates that the PDF of anomalies in the control are significantly different from those of all distributions sampled from the historical period.

Figure 31.1d presents PDFs of the FAR values per time period of a 19-day anomaly in May of +2.52°C. Again it is clear that with greater anthropogenic forcing, there is an increased risk of prolonged extreme temperatures in May. FAR estimates from 1955–2014 are very similar to the middle of the historical period (1975–94), with near-identical distributions of the two earlier periods (1955–74; 1965–84). However there is very little overlap between earlier and later periods (1985–2004 and 1995–2020), indicating a large increase in the risk of May heatwaves attributable to human influence over a relatively short time in the historical record. This is not clear from simply looking at distributions of anomalies in Fig. 31.1c, where all historical PDFs considerably overlap. The FAR PDFs in Fig. 31.1d show a dramatically large increase in the extreme right-hand tail of the distributions in Fig. 31.1c, as marked by the 2.52°C threshold.

Table 31.1 presents the very likely (>90% confidence) FAR values for each temporal period, as well as the corresponding changes in risk. It is very likely that during the 1950s–70s, the risk of a 19-day May heatwave of +2.52°C increased by 4-fold compared to conditions under no anthropogenic influence. The risk increases to 12-fold in the middle of the historical period, as well as for 1955–2014 overall, however the risk increases by 23-fold when considering the latter part of the historical period extending up to 2020. This means that the current change in risk of experiencing a prolonged May heatwave is not only higher than anticipated without anthropogenic influence on the climate, but is also over five times greater than the change of risk estimated during middle of the 20th century. Thus, even higher levels of risk of an event of similar intensity and duration than the Australian 2014 May event can be anticipated in the future. However, it is worth noting that even under the current inflated changes, the 2014 May heatwave is still reasonably rare, occurring approximately once every 30 years over 1995–2020 (compared to approximately once every 750 years in the control).

Conclusions. Using a 21-member ensemble of the CESM model, changes in the risk of the prolonged 2014 May heatwave over Australia were analyzed. An increased risk of 13-fold was found for the historical period (1955–2014), which increases to 23-fold when considering a later segment (1995–2020), due to anthropogenic activity. Analysis of temporal slices of 20 years indicates that changes in risk are transient, suggesting further increases in risk of a similar event during the 21st century.

ACKNOWLEDGMENTS. Sarah Perkins is supported by the Australian Research Council grant number DE140100952.

REFERENCES

Alexander, L. V., and Coauthors, 2006: Global observed changes in daily climate extremes of temperature and precipitation. *J. Geophys. Res.*, **11**, D05109, doi:1029/2005JD006290.

Bureau of Meteorology, 2014: Special climate statement 49: An exceptionally prolonged autumn warm spell over much of Australia. Bureau of Meteorology, 16 pp. [Available online at www.bom.gov.au/climate/current/statements/scs49.pdf.]

——, 2015: Annual climate report 2014. Commonwealth of Australia, 26 pp. [Available online at www.bom.gov.au/climate/current/annual/aus/.]

Cowan, T., A. Purich, S. Perkins, A. Pezza, G. Boschat, and S. Sadler, 2014: More frequent, longer, and hotter heatwaves for Australia in the 21st Century. *J. Climate*, **27**, 5851–5871, doi:10.1175/JCLI-D-14-00092.1.

Deng, B., 2015: 2014 was the hottest year on record. *Nature News*, doi:10.1038/nature.2015.16674.

Fischer, E. M., U. Beyerle, and R. Knutti, 2013: Spatial aggregation reveals robust projections in climate extremes. *Nat. Climate Change*, **3**, 1033–1038, doi:10.1038/NCLIMATE2051.

Jones, D. A., W. Wang, and R. Fawcett, 2009: High-quality spatial climate data-sets for Australia. *Aust. Meteor. Oceanogr. J.*, **58**, 233–248.

Lanning, S. B., T. J. Siebenmorgen, P. A. Counce, A. A. Ambardekar, and A. Mauromoustakos, 2011: Extreme nighttime air temperatures in 2010 impact rice chalkiness and milling quality. *Field Crop Res.*, **124**, 132–136.

Lewis, S. C., and D. J. Karoly, 2013: Anthropogenic contributions to Australia's record summer temperatures of 2013. *Geophys. Res. Lett.*, **40**, 3705–3709, doi:10.1002/grl.50673.

Marshall, A. G., D. Hudson, M. C. Wheeler, O. Alves, H. H. Hendon, M. J. Pook, and J. S. Risbey, 2014: Intra-seasonal drivers of extreme heat over Australia in observations and POAMA-2. *Climate Dyn.*, **43**, 1915–1937, doi:10.1007/s00382-013-2016-1.

Perkins, S. E., and E. M. Fischer, 2013: The usefulness of different realizations for the model evaluation of regional trends in heat waves. *Geophys. Res. Lett.*, **40**, 5793–5797, doi:10.1002/2013GL057833.

——, L. A. Alexander, and J. R. Nairn, 2012: Increasing frequency, intensity and duration of observed global heatwaves and warm spells. *Geophys. Res. Lett.*, **39**, L20714, doi:10.1029/2012GL053361.

Pezza, A. B., P. Van Rensch, and W. Cai, 2012: Severe heat waves in Southern Australia: Synoptic climatology and large scale connections. *Climate Dyn.*, **38**, 209–224, doi:10.1007/s00382-011-1016-2.

Stone, D. A., and M. R. Allen, 2005: The end-to-end attribution problem: From emissions to impacts. *Climatic Change*, **71**, 303–318.

Stott, P. A., D. A. Stone, and M. R. Allen, 2004: Human contribution to the European heatwave of 2003. *Nature*, **432**, 610–614.

Taylor, K. E., R. J. Stouffer, and G. A. Meehl, 2012: An overview of CMIP5 and experiment design. *Bull. Amer. Meteor. Soc.*, **93**, 485–498, doi:10.1175/BAMS-D-11-00094.1.

32. ATTRIBUTION OF EXCEPTIONAL MEAN SEA LEVEL PRESSURE ANOMALIES SOUTH OF AUSTRALIA IN AUGUST 2014

Michael R. Grose, Mitchell T. Black, James S. Risbey, and David J. Karoly

It is likely that human influences on climate increased the odds of the extreme high pressure anomalies south of Australia in August 2014 that were associated with frosts, lowland snowfalls and reduced rainfall.

Introduction. August 2014 saw very strong monthly positive mean sea level pressure (MSLP) anomalies and intense daily to multiday MSLP events south of Australia and in the Tasman Sea (Fig. 32.1a). To the west of Tasmania there were monthly anomalies of over 10 hPa (2.4 standard deviations from the mean), the highest on record since 1979 using ERA-Interim reanalysis (ERAint; Dee et al. 2011), or from 1850 using the Hadley Centre Sea Level Pressure analysis (HadSLP2r; Allan and Ansell 2006). Atmospheric blocking west of Tasmania on 10–15 August (Figs. 32.1b,c) featured the highest daily August MSLP anomaly in either record in that location. Blocking was seen in the south Tasman Sea later in the month, including the highest daily MSLP anomaly on record at that location. The spatial distribution of the monthly MSLP anomalies resembles a wave-3 pattern (Fig. 32.1a).

The strong MSLP anomalies were associated with severe frosts in southeast Australia throughout August, snow down to 200 m in parts of Tasmania on 10–11 August ahead of the particularly strong high, drier than average monthly rainfall in some regions of southern Australia, with <20% average rainfall in places (Bureau of Meteorology 2015), and a prolonged dry spell in the South Island of New Zealand from mid-August (NIWA 2015). A long-term increase in Southern Hemisphere midlatitude MSLP has already been partly attributed to anthropogenic influence (Gillett et al. 2013), and here we undertake the first event attribution of high monthly MSLP that we are aware of. We use the fraction of attributable risk (FAR) framework as adapted for climate work by Allen (2003), with August 2014 MSLP as a case study.

AFFILIATIONS: Grose and Risbey—CSIRO Oceans and Atmosphere, Hobart, Tasmania, Australia; Black and Karoly—School of Earth Sciences and ARC Centre of Excellence for Climate System Science, University of Melbourne, Victoria, Australia

DOI:10.1175/BAMS-D-15-00116.1

A supplement to this article is available online (10.1175/BAMS-D-15-00116.2)

Methods. We used the atmospheric model framework provided by *weather@home*; see Massey et al. (2015) and Black et al. (2015) for more details. We used this framework rather than coupled global climate models (GCMs) as previous studies have shown that coupled models underestimate the MSLP response to external forcings (Gillett et al. 2003, 2005; Gillett and Stott 2009; Barkhordarian 2012; Bhend and Whetton 2013) and underestimate atmospheric blocking (Scaife et al. 2010; Flato et al. 2013). Models with lower biases, including atmosphere-only models, have been shown to perform better (Scaife et al. 2010; Risbey et al. 2011).

We examined *weather@home* global simulations (1.25° latitude × 1.875° longitude resolution) forced by observed sea surface temperatures (SST) and atmospheric greenhouse gas, ozone, and aerosol concentrations labelled "all forcing" (2765 simulations). We compare these to simulations using 2014 observed SST with the mean estimated anthropogenic warming signal subtracted and estimated pre-industrial concentrations of greenhouse gases, ozone, and aerosols, labelled "natural". We examine eleven sets of "natural" simulations, produced using the anthropogenic signal estimated from each of ten GCMs (CanESM2, CCSM4, CNRM-CM5, GFDL-CM3, GISS-E2-H, GISS-E2-R, HadGEM2-ES, IPSL-CM5A-LR, IPSL-CM5A-MR, and MIROC-ESM) and the multimodel mean (MMM) of those ten. There were 490–511 simulations in each "natural" group. Ensembles were created using perturbed initial conditions of atmospheric variables and soil moisture.

Variability in August MSLP in the 2765 "all forcing" simulations, zonal wind at 200 hPa, and the longitudinal profile of the Bureau of Meteorology

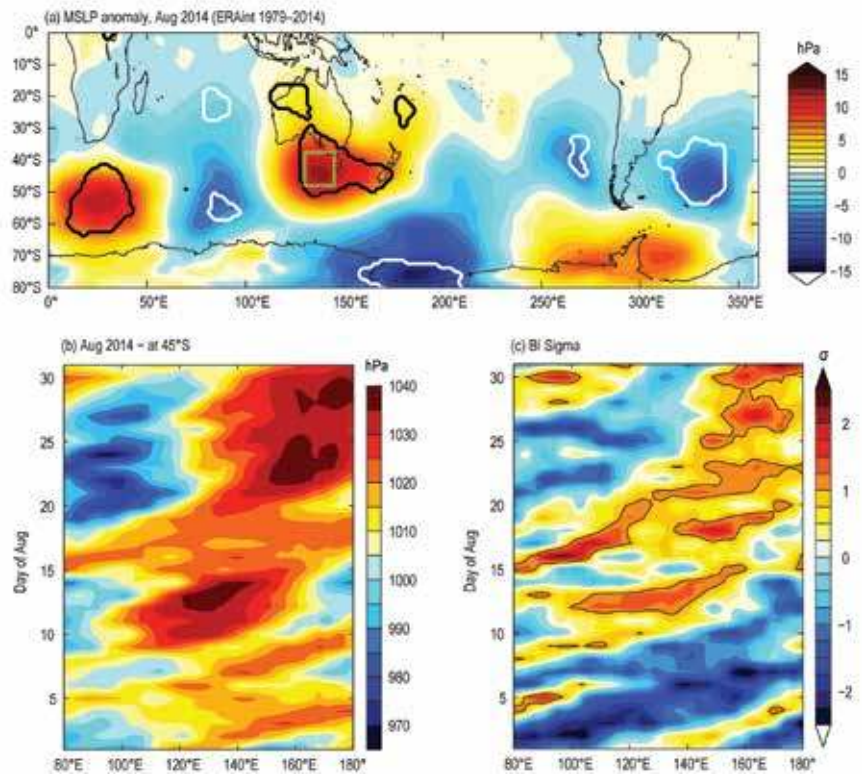

Fig. 32.1. Mean sea level pressure during Aug 2014: (a) MSLP monthly anomaly in ERAint showing where 2014 was highest in the record (black) and lowest in the record (white) and the analysis box (green); (b) Hovmöller plot of daily MSLP in at 45°S (hPa); (c) Hovmöller plot of the daily Bureau of Meteorology blocking index (BI) plotted as standard deviations (σ) with >1 σ outlined by a black line

blocking index (Pook and Gibson 1999) from 90° to 200°E in the "all forcing" simulations was compared to ERAint. This was not a formal evaluation, as it compared multiple simulations of 2014 to a climatology of multiple years, but was done to gauge the general model performance in terms of variability and circulation.

To avoid uncertainty in the extreme tail of distributions, event attribution studies typically use the second highest extreme rather than the actual extreme value as the threshold for FAR (e.g., Lewis and Karoly 2013). Here we used the second highest monthly MSLP in the analysis box from 1914 in HadSLP2r, 1021.0 hPa (2014 was 1025.5 hPa). We calculate FAR = 1 − Natural/All forcing and Likelihood Ratio = All forcing/Natural using pressure at this magnitude.

Results. The standard deviation of monthly mean August MSLP in "all forcing" simulations is broadly similar to ERAint over southern Australia (Figs. 32.2a,b). The standard deviation of MSLP in the analysis box in "all forcing" simulations it is 3.8 hPa, which lies between 4.7 hPa in ERAint in 1979–2014, and 2.4 in HadSLP2r in 1850–2014. The model also shows a similar depiction of jets and the wintertime split jet over the Tasman Sea to ERAint (Figs. 32.2c,d) and the longitudinal profile of the Bureau of Meteorology blocking index is also similar to ERAint (not shown). The model produces internal variability of August mean MSLP comparable with observed interannual variability and contains the basic components of southern hemisphere circulation similar to reanalyses.

MSLP is more than 1 hPa higher in the mean of "all forcing" compared to "natural (MMM)" simulations over the subtropical jet region in both the mean and more than 2 hPa lower over parts of the Antarctic coast (Fig. 32.2e). In the analysis box the mean difference is 1.2 hPa (range of 0.01–2.4 hPa using different "natural" simulations). There is a similar pattern in the difference of 90th percentiles of MMM, and there is a slightly different spatial pattern in each of the sets of "natural" simulations (Supplemental Figs. S32.1, S32.2). Also, geopotential height at the 500-hPa level is more positive over the positive MSLP region, zonal wind at the 500-hPa level simulations is more negative and rainfall is lower to the north of the region with negative zonal wind and positive rainfall anomalies to the south (not shown). The mean difference between "natural" and "all forcing" simulations is more zonally symmetric than the observed 2014 anomalies (Fig. 32.1a), indicating that there was a component of forced response but also a component of natural internal variability leading to the wave-3 pattern observed.

The "natural" and "all forcing" monthly data for the box (MMM shown in Fig. 32.2f) are statistically different (Kolmogorov–Smirnov test with 0.05 significance) in all cases except for the simulations using the GISS-E2-H signal. Using a generalised

extreme value (GEV) distribution for the MMM simulations, FAR for the 1021.0-hPa threshold is 0.63 and the Likelihood Ratio is 2.7 (170% more likely). The FAR estimate is quite insensitive to the choice of distribution (e.g., Beta gives 0.70, Pearson gives 0.51), or to the threshold of MSLP (e.g., 1020 hPa gives 0.65, 1022 hPa gives 0.70). In the different "natural" simulations, FAR is 0.42–0.86 (mean 0.67) and Likelihood Ratio is 1.7–6.3 (mean 3.9), excluding the non-significant GISS-E2-H results (where FAR = 0.3 and Likelihood = 1.4).

Discussion and Conclusion. Here we have performed the first case of event attribution of extreme monthly mean MSLP anomalies that we are aware of. The results suggest that the monthly MSLP anomaly of the intensity observed south of Australia in August 2014 was about twice as likely (at least 70%) given the climate change we have seen since pre-industrial times. Or to phrase it another way, the MSLP anomaly would have been about 1 hPa less intense without the anthropogenic influences. However, attribution was not significant using one model. For the others the attributions are modest but statistically significant, so the attribution is meaningful.

The MSLP anomalies were associated with low rainfall in southeast Australia, consistent with

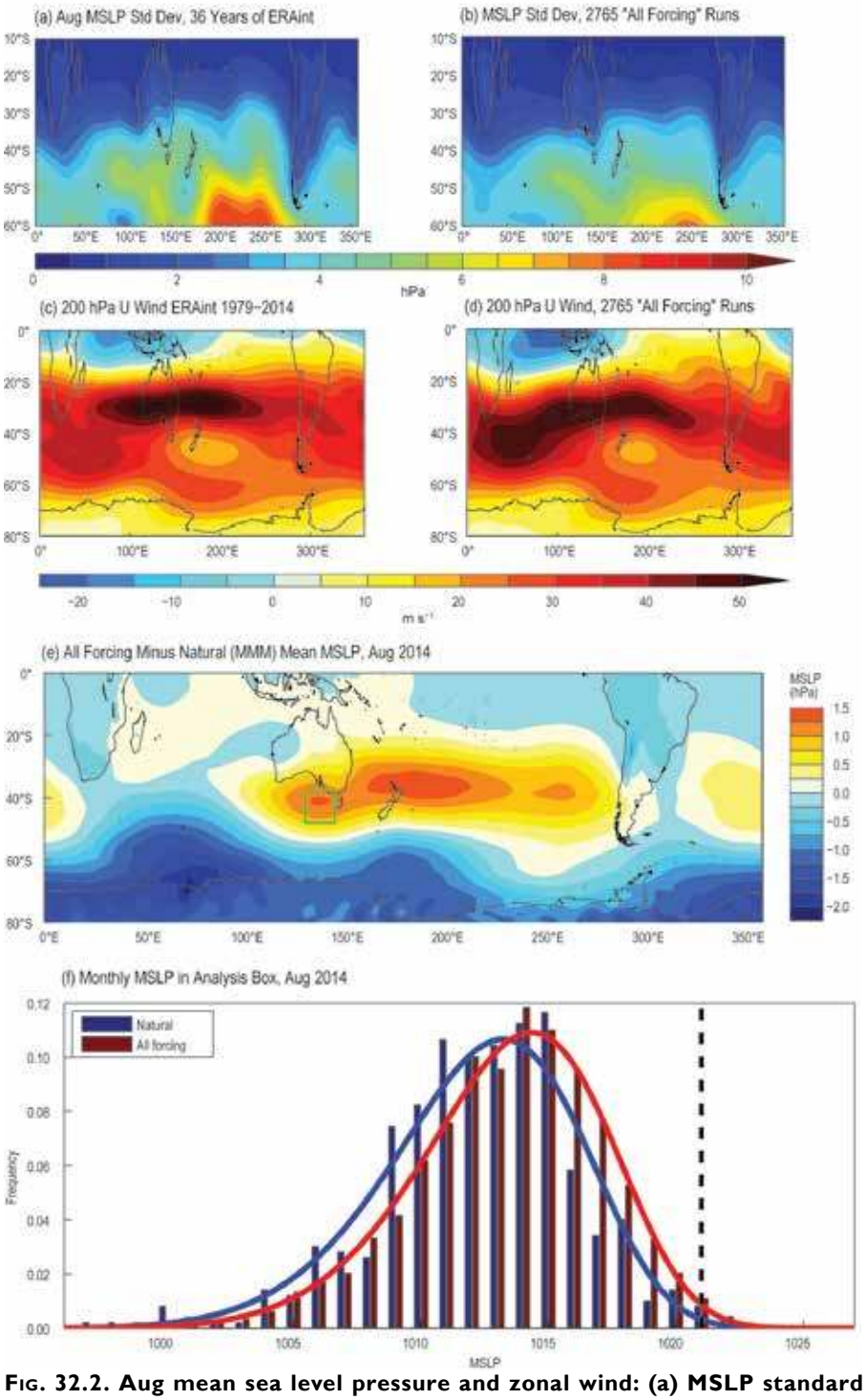

Fig. 32.2. Aug mean sea level pressure and zonal wind: (a) MSLP standard deviation in NCEP1 1948–2014; (b) MSLP standard deviation in 2765 "all forcing" simulations; (c) zonal wind at the 200-hPa level in ERAint 1979–2014; (d) zonal wind at the 200-hPa level in the mean of "all forcing" simulations; (e) difference in MSLP between "all forcing" and "natural (MMM)" simulations (analysis box shown in green); (f) histogram and fitted GEV distribution of August MSLP in "natural" and "all forcing" simulations in the analysis box (normalized by number of simulations), dashed line marks the second highest MSLP value reached in HadSLP2r (1021 hPa) used for the FAR calculation.

climate projections due to anthropogenic forcing. The MSLP anomalies were also linked to severe frosts in southeast Australia and snow down to low levels in Tasmania, so this attribution implies that human influence has contributed to an increase in the likelihood of frost, offsetting the influence of long-term warming. Also, some other notable events were possibly linked, at least in part, to the strong MSLP anomalies of August 2014 such as high temperature anomalies in parts of Western Australia and higher than average rainfall on the Australian eastern seaboard with 400% of average rainfall in places (Bureau of Meteorology 2015).

The *weather@home* modelling system provided a method for examining changes due to anthropogenic climate change while possibly avoiding many of the problems associated with coupled models such as their bias in atmospheric blocking and possible under-estimation of response to forcings. The use of a very large ensemble of atmospheric model simulations allowed us to estimate the uncertainty from initial conditions. However, the limitations of the methods used must be acknowledged. The system uses one atmospheric model and so does not sample the structural uncertainty from different models. It also assumes that removing an estimate of the climate change signal from the observations of a particular year creates a meaningful proxy for pre-industrial conditions.

This event attribution in MSLP is consistent with a wider change in the mean state of atmospheric circulation expected as greenhouse gas forcing increases, including an expansion of the Hadley Cell and poleward shift in storm tracks (Collins et al. 2013). Recent decreases in MSLP at high latitudes have already been partly attributed to greenhouse and aerosol forcings (Gillett et al. 2003, 2005; Hegerl et al. 2007) and some studies also attribute MSLP increases over the Mediterranean in winter (Gillett et al. 2003; Gillett and Stott 2009; Barkhordarian 2012). External forcing from greenhouse gasses, aerosol, and stratospheric ozone depletion each have a distinct seasonal and geographic signature on MSLP, all contributing to MSLP increase over southern Australia in winter but greenhouse gases contributing the most (Gillett et al. 2013). The results can be contrasted with Dole et al. (2011) who finds no greenhouse attribution for blocking in the Russian heatwave of 2010. The consistency in different atmospheric variables and shift in the mean climate adds physical understanding and therefore confidence to the results.

ACKNOWLEDGEMENTS. We thank Weather@Home at Oxford University, the Australian Detection and Attribution workshop (Will Hobbs and Nathan Bindoff), Andrew Marshall, Terry O'Kane, Peter McIntosh and Mike Pook. Michael Grose was supported by ACCSP and the Weather and Climate Extremes project, James Risbey was supported by ACCSP and GRDC. The Weather@Home ANZ simulations, and Mitchell Black and David Karoly were supported by the ARC Centre of Excellence for Climate System Science (Grant CE110001028).

REFERENCES

Allan, R., and T. Ansell, 2006: A new globally complete monthly historical gridded mean sea level pressure dataset (HadSLP2): 1850–2004. *J. Climate*, **19**, 5816–5842.

Allen, M. R., 2003: Liability for climate change. *Nature*, **421**, 891–892.

Barkhordarian, A., 2012: Investigating the influence of anthropogenic forcing on observed mean and extreme sea level pressure trends over the Mediterranean region. *Sci. World J.*, 2012, Article 525303, doi:10.1100/2012/525303.

Bhend, J., and P. Whetton, 2013: Consistency of simulated and observed regional changes in temperature, sea level pressure and precipitation. *Climatic Change*, **118**, 799–810, doi:10.1007/s10584-012-0691-2.

Black, M. T., D. J. Karoly, and A. D. King, 2015: The contribution of anthropogenic forcing to the Adelaide and Melbourne, Australia, heatwaves of January 2014 [in "Explaining Extreme Events of 2014 from a Climate Perspective"]. *Bull. Amer. Meteor. Soc.*, **96** (12), S145–S148, doi:10.1175/BAMS-D-15-00098.1.

Bureau of Meteorology, 2015: Annual climate report 2014. Commonwealth of Australia, 26 pp. [Available online at www.bom.gov.au/climate/current/annual/aus/.]

Collins, M., and Coauthors, 2013: Long-term climate change: Projections, commitments and irreversibility. *Climate Change 2013: The Physical Science Basis*, T. F. Stocker et al., Eds., Cambridge University Press, 1029–1136.

Dee, D. P., and Coauthors, 2011: The ERA-Interim reanalysis: Configuration and performance of the data assimilation system. *Quart. J. Roy. Meteor. Soc.*, **137**, 553–597, doi:10.1002/gj.828.

Dole, R., and Coauthors, 2011: Was there a basis for anticipating the 2010 Russian heat wave? *Geophys. Res. Lett.*, **38**, L06702, doi:10.1029/2010GL046582.

Flato, G. M., and Coauthors, 2013: Evaluation of climate models. *Climate Change 2013: The Physical Science Basis*, T. F. Stocker et al., Eds., Cambridge University Press, 741–866.

Gillett, N. P., and P. A. Stott, 2009: Attribution of anthropogenic influence on seasonal sea level pressure. *Geophys. Res. Lett.*, **36**, L23709, doi:10.1029/2009GL041269.

——, F. W. Zwiers, A. J. Weaver, and P. A. Stott, 2003: Detection of human influence on sea-level pressure. *Nature*, **422**, 292–294.

——, R. J. Allan, and T. J. Ansell, 2005: Detection of external influence on sea level pressure with a multimodel ensemble. *Geophys. Res. Lett.*, **32**, L19714, doi:10.1029/2005GL023640.

——, J. C. Fyfe, and D. E. Parker, 2013: Attribution of observed sea level pressure trends to greenhouse gas, aerosol, and ozone changes. *Geophys. Res. Lett.*, **40**, 2302–2306, doi:10.1002/grl.50500.

Hegerl, G. C., and Coauthors, 2007: Understanding and attributing climate change. *Climate Change 2007: The Physical Science Basis*, S. Solomon et al., Eds., Cambridge University Press, 663–745.

Lewis, S. C., and D. J. Karoly, 2013: Anthropogenic contributions to Australia's record summer temperatures of 2013. *Geophys. Res. Lett.*, **40**, 3705–3709, doi:10.1002/grl.50673.

Massey, N., and Coauthors, 2015: weather@home—development and validation of a very large ensemble modelling system for probabilistic event attribution. *Quart. J. Roy. Meteor. Soc.*, **141**,1528-1545, doi:10.1002/qj.2455, .

NIWA, 2015: Annual climate summary. NIWA National Climate Centre, 27 pp. [Available online at www.niwa.co.nz/sites/niwa.co.nz/files/2014_Annual_Climate_Summary.pdf.]

Pook, M. J., and T. T. Gibson, 1999: Atmospheric blocking and storm tracks during SOP-1 of the FROST Project. *Aust. Meteor. Mag.*, **48**, 51–60.

Risbey, J. S., P. C. McIntosh, M. J. Pook, H. A. Rashid, and A. C. Hirst, 2011: Evaluation of rainfall drivers and teleconnections in an ACCESS AMIP run. *Aust. Meteor. Oceanogr. J.*, **61**, 91–95.

Scaife, A. A., T. Woollings, J. Knight, G. Martin, and T. Hinton, 2010: Atmospheric blocking and mean biases in climate models. *J. Climate*, **23**, 6143–6152, doi:10.1175/JCLJ3728.1.

33. THE 2014 HIGH RECORD OF ANTARCTIC SEA ICE EXTENT

F. Massonnet, V. Guemas, N. S. Fučkar, and F. J. Doblas-Reyes

The record maximum of Antarctic sea ice resulted chiefly from anomalous winds that transported cold air masses away from the Antarctic continent, enhancing thermodynamic sea ice production far offshore.

Introduction. Antarctic sea ice extent exceeded the symbolic level of 20 million km² for the first time since 1978, when reliable satellite measurements became available. After the successive records of 2012 and 2013, sea ice extent in 2014 once again reinforced the positive trend observed since the late 1970s. Previous studies have interpreted this trend as the result of powerful atmosphere– and ocean–sea ice feedbacks (Zhang 2007; Goosse and Zunz 2014), freshwater forcing from continental ice-sheet melting (Bintanja et al. 2013), or changes in wind regimes (Holland and Kwok 2012), although this trend was found to be compatible with internal variability (Polvani and Smith 2013). We conduct here a dedicated study to elucidate the origins of a major, and perhaps the most intriguing, climatic event of 2014.

Winter 2014 Antarctic conditions in context. The average September 2014 Antarctic sea ice extent reached 20.10 million km² according to the National Snow and Ice Data Center Sea Ice Index (Fetterer et al. 2015). This value represented a significant upward departure from the observed positive trend in total sea ice extent (Fig. 33.1a). The 2014 sea ice extent anomaly was the result of a circumpolar increase in sea ice concentration near the ice edge, except in the Amundsen–Bellingshausen Seas (Fig. 33.1b). The spatial patterns of 2014 anomalies thus matched well the spatial trends in observed sea ice concentration over the past decades (Parkinson and Cavalieri 2012).

Wind is a primary driver of autumn and winter Antarctic sea ice variability at decadal time scales (Holland and Kwok 2012; Holland et al. 2014) through enhanced transport and divergence of sea ice (dynamic contribution), or near-surface air temperature advection, i.e., transport of near-surface air across a temperature gradient (thermodynamic contribution). In 2014, positive sea ice concentration anomalies in September were associated with anomalous southerly winds in the preceding austral winter in the Indian and Ross Sea sectors (Fig. 33.1b). Meanwhile, anomalous northerly winds blew in the Amundsen–Bellingshausen Seas where ice concentration anomalies were negative. Elsewhere around the hemisphere, the link between sea ice anomalies and the meridional component of the wind was less obvious.

While the link between 2014 winds and sea ice concentration seems solid in several regions of the Southern Ocean, three questions remain: 1) Is this link causal? 2) Are sea ice anomalies the result of anomalous dynamic or thermodynamic forcing? 3) Have other factors contributed to the record, namely preconditioning from the ocean in summer, anomalies in precipitation, or freshwater discharge from the Antarctic ice-shelves? To answer these questions, we implement a sensitivity analysis with a state-of-the-art ocean–sea ice general circulation model.

Attribution of the 2014 maximum through model experiments. We perform 10 (2005–14) 8-month-long simulations, labeled "CTRL" in Fig. 33.2, with the Louvain-la-Neuve sea ice model (LIM3; Vancoppenolle et al. 2009) embedded in the Nucleus for European Modelling of the Ocean (NEMO3.3; Madec 2008) ocean model forced by the ERA-Interim atmospheric reanalyses (Dee et al. 2011) following

AFFILIATIONS: Massonnet—Georges Lemaître Centre for Earth and Climate Research, Earth and Life Institute, Université catholique de Louvain, Louvain-la-Neuve, Belgium, and Climate Forecasting Unit, Catalan Institute of Climate Sciences, Barcelona, Spain; Guemas—Climate Forecasting Unit, Catalan Institute of Climate Sciences, Barcelona, Spain, and Centre National de Recherches Météorologiques, Toulouse, France; Fučkar—Climate Forecasting Unit, Catalan Institute of Climate Sciences, Barcelona, Spain; Doblas-Reyes—Climate Forecasting Unit, Catalan Institute of Climate Sciences, and Catalan Institution for Research and Advanced Studies, and Barcelona Supercomputing Center-Centro Nacional de Supercomputación, Barcelona, Spain

DOI:10.1175/BAMS-D-15-00093.1

A supplement to this article is available online (10.1175/BAMS-D-15-00093.2)

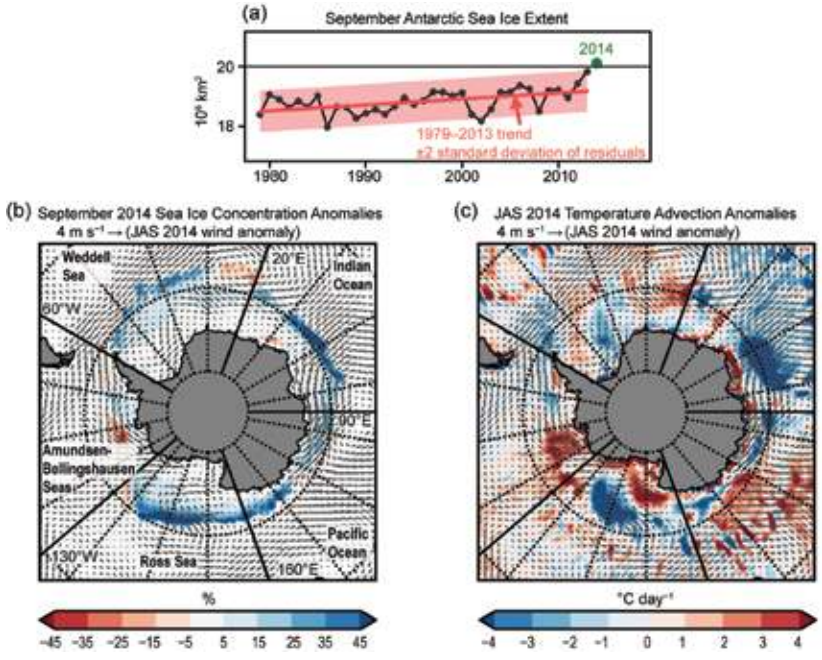

Fig. 33.1. Winter 2014 Antarctic conditions in context. (a) Sep Antarctic sea ice extent as retrieved from satellite imagery (Fetterer et al. 2015). Sea ice extent is defined throughout the text as the cumulative area of oceanic grid cells containing at least 15% of ice. The trend line (least-squares regression) across the period is shown as the red line, and the red shadow is the interval corresponding to two standard deviations of the residuals of the fit. (b) Anomalies of Sep 2014 sea ice concentration relative to 1979–2013 (Eastwood 2014) overlaid by 2014 austral winter [Jul–Aug–Sep (JAS) mean] wind anomalies from the ERA-Interim reanalysis (Dee et al. 2011) relative to the 1979–2013 average. (c) Anomaly of winter 2014 advection of near-surface temperatures relative to 1979–2013. Advection for 1979–2013 and 2014 is estimated as $-\vec{u}\cdot\nabla T$, i.e., the scalar product between the 10-m JAS ERA-Interim winds and the 2-m JAS mean temperature gradient. The gradient operator is itself estimated using a 6-point centered difference scheme along the meridional and zonal directions, respectively.

the bulk formulae of Large and Yeager (2004). The simulations are initialized on 1 March of each year from the Nucleus for European Modelling of the Ocean Variational data assimilation system–Ocean Reanalysis System 4 (NEMOVAR–ORAS4) oceanic reanalysis (Balmaseda et al. 2013) and from a sea ice reconstruction described in the online supplemental material. To account for uncertainty in the atmospheric forcing and initial conditions (ICs), we run ensembles of five members for each year (see online supplemental material). Since the skill of CTRL simulations depends in part on the realism of the atmospheric forcing, it is desirable to know that the ocean–sea ice model responds in a reasonable way to the forcing used in this study. This aspect is also discussed in the online supplemental material.

The CTRL experiment performs well in all sectors of the Southern Ocean except the Pacific Ocean sector (Fig. 33.2), for reasons that are still to be investigated. Therefore, we exclude this sector from subsequent analyses. Spurious sea ice variability over 2007–10 in the Pacific Ocean sector contaminates the skill of simulated total Antarctic sea ice extent and partly explains why September 2014 is not a maximum in the model. Figure 33.2 also illustrates why the correlation of total Antarctic sea ice extent can be a misleading metric of performance. Maps of gridpoint correlations over the period of interest reveal that more than 50% of the observed variance in sea ice concentration near the ice edge is explained by the model (Supplemental Fig. S33.2). We therefore argue that the model is adequate to conduct our attribution study given the spatial patterns of sea ice concentration anomalies in September 2014 (Fig. 33.1b). In addition to the CTRL experiment, we run four sensitivity experiments initialized on 1 March 2014. Each sensitivity experiment differs from CTRL by one aspect only. This approach, already implemented in an attribution study of the 2012 Arctic sea ice minimum (Guemas et al. 2013), has the advantage of systematically isolating the role of individual factors that could have explained the 2014 record.

We run a first sensitivity experiment called "WND LOW," in which we substitute surface winds of 2014 for those from earlier years corresponding to the lowest total Antarctic sea ice extents in the model (2007, 2008, 2011, 2012, and 2013, referred to as "low" years hereafter). All other parameters (ICs, near-surface air temperatures, precipitation) are left to their default values for 2014. As shown in Fig. 33.2, the replacement of winds has no significant effect on sea ice extent (that is, the new interval includes the CTRL value) except in the Pacific Sector, which we discard due to suspicious model performance. Because winds in the model only impact the sea ice mass budget through transport and divergence, we exclude the possibil-

ity that they have contributed dynamically to the 2014 record high.

This, however, does not exclude an indirect *thermodynamic* contribution of winds to the record by anomalous atmospheric heat advection. To explain the observed close association between winds and sea ice concentration in winter 2014 (Fig. 33.1b), we diagnose the rate of observed near-surface temperature change by advection. This diagnostic suggests that, in 2014, winds have played a role in bringing relatively cold air masses in the Indian Ocean and Ross Sea sectors far offshore, where ice eventually grew more than usual (Fig. 33.1c).

To confirm this hypothesis, we run a second sensitivity experiment, labeled "T2M LOW" in Fig. 33.2, in which we substitute only near-surface air temperatures of 2014 for those from "low" years. This single change in air temperatures results in a significant decrease of 0.41 million km² in total sea ice extent. More than the half of this decrease is due to a significant response of simulated sea ice in the Indian Ocean sector (where ice concentration reached anomalously high levels, Fig. 33.1b). Whether the same process was at play in the Ross Sea sector is less clear, given the lack of model response to surface temperature change in this sector. We conclude that the 2014 anomalous near-surface thermal conditions, resulting themselves from anomalous winds, favored the record high in 2014, since sea ice extent could have been lower than 2012 and 2013 otherwise.

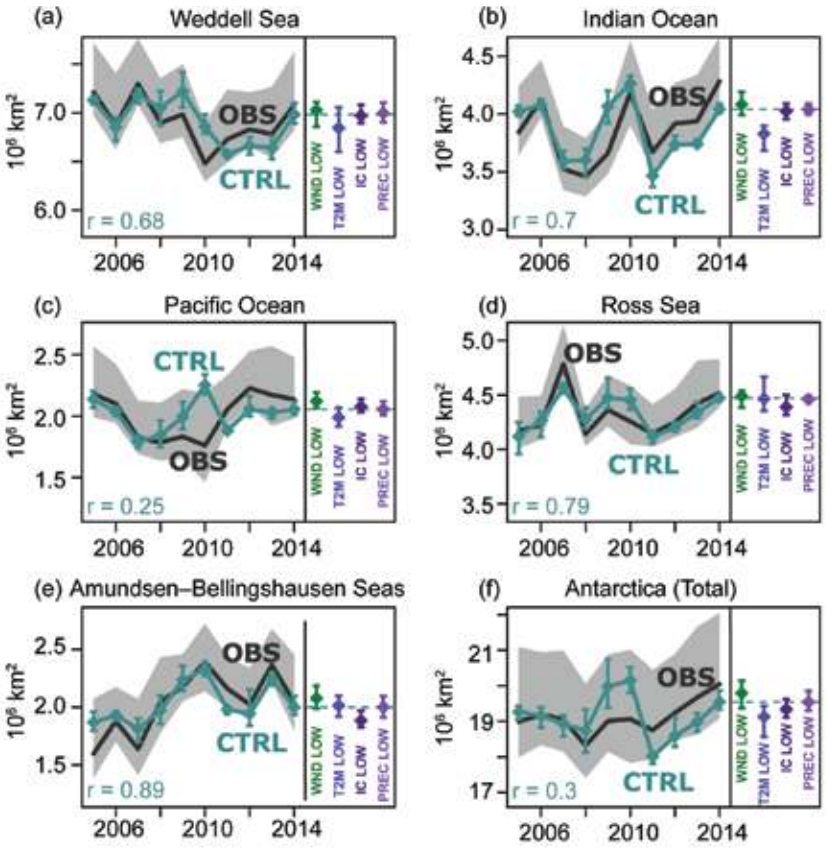

Fig. 33.2. Model sensitivity analyses. Sea ice extent as observed (black line; Eastwood 2014) and simulated (colors) by the NEMO–LIM3 ocean–sea ice model in various sectors of the Southern Ocean, corresponding to those identified in Fig. 33.1b. The CTRL simulation runs from 2005 to 2014 with initial conditions and atmospheric forcings from these years. The CTRL time series have been recentered on the time-mean of observed time series to account for systematic biases due to differences in land–sea masks. The correlations between the CTRL and observed time series are reported in the lower left corner of each panel. Gray shading corresponds to the estimated uncertainty in sea ice extent, based on a 14% nominal error in sea ice concentration typical of winter conditions (see the reprocessed products of Eastwood et al. 2014). In the right part of each panel, box plots refer to the four sensitivity experiments for 2014 described in the text: disabling the 2014 winds (WND LOW), near-surface air temperatures (T2M LOW), initial conditions (IC LOW), and precipitation (PREC LOW). The horizontal dashed line is the 2014 level for comparison. All error bars represent the range (minimum to maximum value) of the five-member ensembles, and diamonds represent the mean.

We are aware that the experimental setup proposed has limitations. The atmospheric state forcing the model is no longer in dynamical balance when either temperatures or winds are replaced. We find, however, the two effects to be additive: a simulation where both wind *and* temperatures were replaced would give a total sea ice extent response consistent with the cumulated responses of the individual simulations (not shown here).

In a third experiment ("IC LOW"), we substitute the 1 March 2014 oceanic and sea ice ICs with those from "low" years. No significant reduction is found except in the Amundsen–Bellingshausen Seas sector. In this sector, modeled sea surface temperatures were in fact colder by up to 1.5°C than for "low" years in

March 2014. We conclude that oceanic preconditioning did not play a fundamental role in explaining the sea ice record of September 2014.

We finally test whether anomalous hydrological conditions could have explained the 2014 anomaly. We first investigate the role of the *atmospheric* hydrological cycle: we replace the 2014 solid and liquid precipitations by those of "low" years. Increased precipitation could reduce upper-ocean density and convective overturning, thereby decreasing sea ice melt (Zhang 2007). However, we find no evidence that this factor has played a significant role in driving sea ice extent to a record in 2014 (Fig. 33.2). Regarding the role of the *continental* hydrological cycle, we have to acknowledge that the model is forced with climatological runoff data. That is, proper ocean-ice-sheet interactions are absent, making a clean sensitivity experiment impossible. Applying a 0.1 PSU decrease in the 1 March 2014 ocean salinity IC in the top 50 m and south of 55°S increased the total Antarctic sea ice extent of September 2014 by 0.20 million km^2 (not shown here). However, we cannot conclude that this mechanism was responsible for the 2014 record since, to our knowledge, no robust estimates of the freshening distribution of the upper-ocean due to Antarctic melt are available for 2014.

Conclusion: What drove the 2014 record of Antarctic sea ice extent? Following the results of both observational (Fig. 33.1) and model sensitivity (Fig. 33.2) analyses, we find that the primary cause for the 2014 record is anomalous thermodynamic sea ice growth near the ice edge in the Indian Ocean due to anomalous southerly advection of cold air there (Fig. 33.1c). Anomalous winds over winter 2014 are themselves the consequence of a strong dipole of mean sea level pressure anomaly at the boundaries of this sector (Supplemental Fig. S33.3). Oceanic preconditioning appears to have a secondary, but not negligible, influence on the total 2014 sea ice anomaly.

The 2014 Antarctic sea ice extent record can be explained as the superposition of a long-term, positive trend with a large positive anomaly for that particular year (Fig. 33.1a). Unlike the Arctic where the imprint of anthropogenic climate change can be detected in the multidecadal sea ice loss (Min et al. 2008), a rigorous attribution statement is not as straightforward for the long-term observed increase in Antarctic sea ice extent. Recent studies using coupled models of different complexity and at various resolutions (Sigmond and Fyfe 2012, 2014; Bitz and Polvani 2012; Ferreira et al. 2014) found evidence of a *negative* response of total Antarctic sea ice extent to stratospheric ozone depletion at multidecadal time scales. Shorter timescale variability of sea ice extent and concentration has been linked to large-scale atmospheric variability, such as the Southern Annular Mode (SAM; Lefebvre et al. 2004; Stammerjohn et al. 2008; Simpkins et al. 2012). However, in 2014, the winter (JAS) index of the SAM did not display a particular polarity (not shown here). Furthermore, anomalies in mean sea level pressure for winter 2014 (Supplemental Fig. S33.3) did not display a SAM-like signature. In light of our results and those from earlier studies, it is therefore difficult to formulate a robust attribution statement for explaining the 2014 record of Antarctic sea ice extent.

ACKNOWLEDGMENTS. We wish to thank Editor-in-Chief J. Rosenfeld, Editor T. Peterson and two anonymous reviewers for handling and commenting on our manuscript. François Massonnet is a F.R.S. – FNRS Post-Doctoral Researcher. The research leading to these results has also received funding from the EU Seventh Framework Programme FP7 (2007–2013) under grant agreements 308378 (SPECS) and 607085 (EUCLEIA) and CGL2012-31987 (PICA-ICE).

REFERENCES

Balmaseda, M. A., K. Mogensen, and A. T. Weaver, 2013: Evaluation of the ECMWF ocean reanalysis system ORAS4. *Quart. J. Roy. Meteor. Soc.*, **139**, 1132–1161, doi:10.1002/qj.2063.

Bintanja, R., G. J. van Oldenborgh, S. S. Drijfhout, B. Wouters, and C. A. Katsman, 2013: Important role for ocean warming and increased ice-shelf melt in Antarctic sea-ice expansion. *Nat. Geosci.*, **6**, 376–379, doi:10.1038/ngeo1767.

Bitz, C. M., and L. M. Polvani, 2012: Antarctic climate response to stratospheric ozone depletion in a fine resolution ocean climate model. *Geophys. Res. Lett.*, **32**, L20705, doi:10.1029/2012GL053393.

Dee, D. P., and Coauthors, 2011: The ERA-interim reanalysis: Configuration and performance of the data assimilation system. *Quart. J. Roy. Meteor. Soc.*, **137**, 553–597, doi:10.1002/qj.828.

Eastwood, S., Ed., 2014: Sea ice product user's manual. Ocean and Sea Ice Satellite Application Facilities, 38 pp. [Available online at http://osisaf.met.no/docs/osisaf_ss2_pum_ice-conc-edge-type.pdf.]

Ferreira, D., J. Marshall, C. M. Bitz, S. Solomon, and A. Plumb, 2015: Antarctic Ocean and sea ice response to ozone depletion: A two-time-scale problem. *J. Climate*, **28**, 1206–1226, doi:10.1175/JCLI-D-14-00313.1.

Fetterer, F., K. Knowles, W. Meier, and M. Savoie, 2015: Sea ice index. National Snow and Ice Data Center, Boulder, CO, digital media. [Available online at http://nsidc.org/data/docs/noaa/g02135_seaice_index/.]

Goosse, H., and V. Zunz, 2014: Decadal trends in the Antarctic sea ice extent ultimately controlled by ice-ocean feedback. *Cryosphere*, **8**, 453–470, doi:10.5194/tc-8-453-2014.

Guemas, V., F. J. Doblas-Reyes, A. Germe, M. Chevallier, and D. Salas y Mélia, 2013: September 2012 Arctic sea ice minimum: Discriminating between sea ice memory, the August 2012 extreme storm, and prevailing warm conditions [in "Explaining Extreme Events of 2012 from a Climate Perspective"]. *Bull. Amer. Meteor. Soc.*, **94** (9), S20–S22.

Holland, P. R., and R. Kwok, 2012: Wind-driven trends in Antarctic sea-ice drift. *Nat. Geosci.*, **5**, 872–875, doi:10.1038/ngeo1627.

——, N. Bruneau, C. Enright, M. Losch, N. T. Kurtz, and R. Kwok, 2014: Modeled trends in Antarctic sea ice thickness. *J. Climate*, **27**, 3784–3801, doi:10.1175/JCLI-D-13-00301.1.

Large, W. G., and S. G. Yeager, 2004: Diurnal to decadal global forcing for ocean and sea-ice models: The data sets and flux climatologies. NCAR Tech. Note NCAR/TN-460+STR, 105 pp., doi:10.5065/D6KK98Q6.

Lefebvre, W., H. Goosse, R. Timmermann, and T. Fichefet, 2004: Influence of the Southern Annular Mode on the sea ice-ocean system. *J. Geophys. Res.*, **109**, C09005, doi:10.1029/2004JC002403.

Madec, G., 2008: NEMO ocean engine. Note du Pôle de modélisation de l'Institut Pierre-Simon Laplace 27, 357 pp. [Available online at www.nemo-ocean.eu/About-NEMO/Reference-manuals.]

Min, S.–K., X. Zhang, F. W. Zwiers, and T. Agnew, 2008: Human influence on Arctic sea ice detectable from early 1990s onwards. *Geophys. Res. Lett.*, **35**, L21701, doi:10.1029/2008GL035725.

Parkinson, C. L., and D. J. Cavalieri, 2012: Antarctic sea ice variability and trends, 1979–2010. *Cryosphere*, **6**, 871–880, doi:10.5194/tc-6-871-2012.

Polvani, L. M., and K. L. Smith, 2013: Can natural variability explain observed Antarctic sea ice trends? New modeling evidence from CMIP5. *Geophys. Res. Lett.*, **40**, 3195–3199, doi:10.1002/grl.50578.

Sigmond, M., and J. Fyfe, 2010: Has the ozone hole contributed to increased Antarctic sea ice extent? *Geophys. Res. Lett.*, **37**, L18502, doi:10.1029/2010GL044301.

——, and ——, 2014: The Antarctic sea ice response to the ozone hole in climate models. *J. Climate*, **27**, 1336–1342, doi:10.1175/JCLI-D-13-00590.1.

Simpkins, G. R., L. M. Ciasto, D. W. J. Thompson, and M. H. England, 2012: Seasonal relationships between large-scale climate variability and Antarctic sea ice concentration. *J. Climate*, **25**, 5451–5469, doi:10.1175/JCLI-D-11-00367.1.

Stammerjohn, S., D. G. Martinson, R. C. Smith, X. Yuan, and D. Rind, 2008: Trends in Antarctic annual sea ice retreat and advance and their relation to El Niño–Southern Oscillation and Southern Annular Mode variability. *J. Geophys. Res.*, **113**, C03S90, doi:10.1029/2007JC004269.

Vancoppenolle, M., T. Fichefet, H. Goosse, S. Bouillon, G. Madec, and M. A. Morales Maqueda, 2009: Simulating the mass balance and salinity of Arctic and Antarctic sea ice. 1. Model description and validation. *Ocean Modell.*, **27**, 33–53.

Zhang, J., 2007: Increasing Antarctic sea ice under warming atmospheric and oceanic conditions. *J. Climate*, **20**, 2515–2529.

34. SUMMARY AND BROADER CONTEXT

Stephanie C. Herring, Martin P. Hoerling, James P. Kossin,
Thomas C. Peterson, and Peter A. Stott

This special supplement on explaining extreme events has now published 79 papers over the past four years. Over half of these papers have shown that human-caused climate change influenced an event's frequency and/or intensity in a substantial manner. It could be argued that because all of these events occurred in the context of a warmer world, there are impacts on all extremes whether or not the influence is detectable with current methods and available observations. While potentially true, to make attribution results informative to adaptation decisions, scientists must take on the questions of whether the risk or magnitudes of such events have increased or decreased, by how much, and what level of confidence supports the claims. This is the challenge the authors who have contributed to this report have taken on. The summary table (Table 34.1) is provided to give readers a general overview of their results. However, it is a highly simplified categorization of the results and does not include information about the size of the signal detected and the confidence in the results. This information is present within each individual report, and provides essential context for understanding and interpreting results for any individual event.

This year's report covers an unprecedented geographic range that looks at events from North America, South America, Europe, the Middle East, Africa, Asia, the western Pacific, Australia, and Antarctica. Also, this year event types include tropical cyclones, sea level pressure, sea surface temperature, forest fires, and Antarctic sea ice extent in addition to heat, cold, floods, and drought. We are pleased to see both the geographic distribution and event types continuing to expand.

Perhaps most importantly, this report and the field of event attribution science continue to provide evidence that human influences on climate have changed the risk of a wider class of extreme events. This year's report shows increasing risk of event types including forest fires in California and snow storms such as the one in Nepal. The analysis of California forest fire showed fires have been increasing recently in part because of drought. While the direct mechanism linking the 2014 fires to warming is not made, the authors do show that global warming likely will exacerbate fire intensity and risk in California in the future. This result is consistent with the most recent national climate assessment which concluded that western forests in the United States will be increasingly affected by large and intense fires that occur more frequently due to climate change (Melillo et al. 2014).

As in past years, results for heat events continue to overwhelmingly show the impact of human caused climate change. Heat events in this report—from Argentina, Europe, China, Korea, Australia, and the northern Atlantic and Pacific Oceans—showed a climate change signal. Over the past four years only one (Cattiaux and Yiou 2012) out of 22 papers that looked at extreme heat events did not find a detectable climate change influence. While these reports represent a small and non-random sampling of extreme events from around the world, these results add to the preponderance of evidence that the climate change impact on heat waves is pronounced (Field et al. 2012; Melillo et al. 2014).

At the other end of the event spectrum, North America had a very unusual pattern of winter storms in 2013/14, in which there were far fewer storms than normal along the West Coast of the United States and more storms than normal in a region extending from central Canada down to the midwestern United States. This pattern of storm activity was linked to unusual winds in the tropical Pacific and not anthropogenic climate change. Analysis of specific features of the cold North American winters of 2013/14 showed different links to climate change. The daily variability of temperatures over the Midwest and eastern United States was found to be neither increas-

AFFILIATIONS: Herring—NOAA/National Centers for Environmental Information, Boulder, Colorado; Hoerling—NOAA/Earth System Research Laboratory, Boulder, Colorado; Kossin—NOAA/National Centers for Environmental Information, Madison, Wisconsin; Peterson—NOAA/National Centers for Environmental Information, Asheville, North Carolina; Stott—Met Office Hadley Centre, Exeter, United Kingdom

DOI: 10.1175/BAMS-D-15-00210.1

ing nor decreasing as a result of climate change. Also, the seasonal extremes during the past winter were not unusual historically. However, it was found that seasonal mean cold conditions such as occurred over the greater Upper Midwest in 2013/14 are now 20–100 times less likely than in the late 19th century due to long-term warming.

Drought continues to be an event type where the results require significant context, and easy answers often remain elusive because of the many meteorological, hydrological, and societal drivers that combine to cause drought. In particular, conclusions about the influence of human-caused climate change could depend on whether authors looked at the role of temperature or precipitation on the drought. An analysis of precipitation deficits related to the devastating drought in southeastern Brazil did not find that human influences on climate played a role. Two analyses of the East Africa drought, using different methods, arrived at different conclusions regarding how human-caused climate change affected the reduced rainfall in 2014. Other drought mechanisms, especially human-induced surface warming, may have increased the drought's intensity. While no role for human-caused climate change was found in the large drought covering the Middle East and central–southwest Asia, the drought in Syria was determined to have been made worse because climate change reduced rainfall. No role for human-caused climate change was found for the droughts in northeast Asia or the record dry spell in Singapore.

This year only two events examining extreme precipitation showed climate change increased the strength and/or likelihood of the event (Table 34.1). Over the past four years this supplement has published 20 attribution studies on precipitation, and they are split between events that did and did not find human influences on precipitation events. Changes in precipitation trends are anticipated to vary by location (Field et al. 2012).

This year we are also excited to have several contributions on tropical cyclones (TC). The very active TC season in the Hawaiian region was shown to be substantially more likely due to human-caused factors, but was also affected by ENSO. The transition of Hurricane Gonzalo into a very strong extratropical storm that affected Europe was found to lie within the range of natural variability. However, one of these studies reflects the challenges with doing attribution work on these complex events. The anomalous TC behavior during the 2014 western North Pacific typhoon season could not be confidently linked to human factors with CMIP5 models because of the models' inability to capture the relevant environmental features.

Improving the communication of attribution research. As we have noted in past years, being able to deliver scientifically robust attribution statements about an extreme event in a timely manner is an important first step in supporting informed decision making. This year, in an effort to further improve the communication and understanding of attribution results, we have added some detail to the summary table (Table 34.1). Authors have identified whether their results show human influences changed the intensity and/or frequency of the event, because these results often have different implications for improving resilience to extremes. While the summary table is valuable for providing a high level view of the results in this report there is a great deal of information not included in the table. Each of the authors has been asked to provide a summary capsule of their findings which is included at the head of each contribution and provides a starting point for interpretation of their results. Also, it is important to point out that a conclusion of "no influence" may be because the methodology or observations are not sufficient to detect the influence. Despite the need to dig deeper into the individual analysis to make the most effective use of attribution results, the overarching result is clear: because of the on-going strengthening of human-caused climate change, investigations of the extreme weather we are experiencing around the world are increasingly likely to have a detectable human fingerprint found at the scene.

Future directions. As we look ahead to the future of this report a few very exciting opportunities are evident to the editors. Firstly, event attribution has the ability to become increasingly relevant to society by also considering other human-caused drivers of extreme events beyond the usual radiative drivers. For example, flooding in the Canadian prairies was found to be more likely because of human impacts on precipitation as well as land use changes that affect drainage mechanisms. Similarly, the Jakarta floods may have been compounded by land use change via urban development and associated land subsidence. These types of mechanical factors reemphasize the various pathways beyond climate change by which human activity can increase regional risk of extreme events. This type of information about the various ways in which human actions impact extreme events is critical for decision making.

Table 34.1. ANTHROPOGENIC INFLUENCE

ON EVENT STRENGTH †			
	INCREASE	**DECREASE**	**NOT FOUND OR UNCERTAIN**
Heat	**Australia** (Ch. 31) **Europe** (Ch.13) **S. Korea** (Ch. 19)		**Australia, Adelaide & Melbourne** (Ch. 29) **Australia, Brisbane** (Ch.28)
Cold		**Upper Midwest** (Ch.3)	
Winter Storms and Snow			**Eastern U.S.** (Ch. 4) **N. America** (Ch. 6) **N. Atlantic** (Ch. 7)
Heavy Precipitation	**Canada**** (Ch. 5)		**Jakarta**** (Ch. 26) **United Kingdom***** (Ch. 10) **New Zealand** (Ch. 27)
Drought	**E. Africa** (Ch. 16) **E. Africa*** (Ch. 17) **S. Levant** (Ch. 14)		**Middle East and S.W. Asia** (Ch. 15) **N.E. Asia** (Ch. 21) **Singapore** (Ch. 25)
Tropical Cyclones			**Gonzalo** (Ch. 11) **W. Pacific** (Ch. 24)
Wildfires			**California** (Ch. 2)
Sea Surface Temperature	**W. Tropical & N.E. Pacific** (Ch. 20) **N.W. Atlantic & N.E. Pacific** (Ch. 13)		
Sea Level Pressure	**S. Australia** (Ch. 32)		
Sea Ice Extent			**Antarctica** (Ch. 33)

† Papers that did not investigate strength are not listed.

†† Papers that did not investigate likelihood are not listed.

* No influence on the likelihood of low rainfall, but human influences did result in higher temperatures and increased net incoming radiation at the surface over the region most affected by the drought.

** An increase in spring rainfall as well as extensive artificial pond drainage increased the risk of more frequent severe floods from the enhanced rainfall.

*** Evidence for human influence was found for greater risk of UK extreme rainfall during winter 2013/14 with time scales of 10 days

**** The study of Jakarta rainfall event of 2014 found a statistically significant increase in the probability of such rains over the last 115 years, though the study did not establish a cause.

	ON EVENT LIKELIHOOD ††			Total Number of Papers
	INCREASE	DECREASE	NOT FOUND OR UNCERTAIN	
Heat	**Argentina** (Ch. 9) **Australia** (Ch. 30, Ch. 31) **Australia, Adelaide** (Ch. 29) **Australia, Brisbane** (Ch. 28) **Europe** (Ch. 13) **S. Korea** (Ch. 19) **China** (Ch. 22)		**Melbourne, Australia** (Ch. 29)	7
Cold		**Upper Midwest** (Ch.3)		1
Winter Storms and Snow	**Nepal** (Ch. 18)		**Eastern U.S.**(Ch. 4) **N. America** (Ch. 6) **N. Atlantic** (Ch. 7)	4
Heavy Precipitation	**Canada**** (Ch. 5) **New Zealand** (Ch. 27)		**Jakarta**** (Ch. 26) **United Kingdom***** (Ch. 10) **S. France** (Ch. 12)	5
Drought	**E. Africa** (Ch. 16) **S. Levant** (Ch. 14)		**Middle East and S.W. Asia** (Ch. 15) **E. Africa*** (Ch. 17) **N.E. Asia** (Ch. 21) **S. E. Brazil** (Ch. 8) **Singapore** (Ch. 25)	7
Tropical Cyclones	**Hawaii** (Ch. 23)		**Gonzalo** (Ch. 11) **W. Pacific** (Ch. 24)	3
Wildfires	**California** (Ch. 2)			1
Sea Surface Temperature	**W. Tropical & N.E. Pacific** (Ch. 20) **N.W. Atlantic & N.E. Pacific** (Ch. 13)			2
Sea Level Pressure	**S. Australia** (Ch. 32)			1
Sea Ice Extent			**Antarctica** (Ch. 33)	1
			TOTAL	32

Also, in the past four years we have seen huge strides in the ability of event attribution methodologies to be carried out in a routine manner. In particular, attribution of heat events now relies on several established methodologies. And much like other routine analysis, such as an operational seasonal forecast, statements made about heat events using these methods do not necessarily need to go through the peer-reviewed literature to be considered credible (Met Office 2014). However, heat events are unique in this respect and we hope this report can continue to drive analyses of other extreme event types in this same direction.

Finally, of the 79 papers from the past four years, 32 are in this year's report. The annual growth in the report speaks to both the increasing interest and broadening scope of attribution science. As we look ahead to future explaining extreme events reports, we will continue to look for opportunities to serve the detection and attribution community, and help the results of this body of research become increasingly relevant to society.

REFERENCES

Cattiaux, J., and P. Yiou, 2012: Contribution of atmospheric circulation to remarkable European temperatures of 2011 [in "Explaining Extreme Events of 2011 from a Climate Perspective"]. *Bull. Amer. Meteor. Soc.*, **93**, 1054–1057.

Field, C. B., and Coauthors, Eds., 2012: *Managing the Risks of Extreme Events and Disasters to Advance Climate Change Adaptation*. Cambridge University Press, 582 pp.

Melillo, J. M., T. C. Richmond, and G. W. Yohe, Eds., 2014: *Climate Change Impacts in the United States: The Third National Climate Assessment*. U.S. Global Change Research Program, 841 pp., doi:10.7930/J0Z31WJ2.

Met Office, 2014: Human influence important factor in possible global and UK temperature records. Press release. [Available online at www.metoffice.gov.uk/news/releases/archive/2014/2014-global-temperature.]